THE FIRST HIGH-STRENGTH BAINITIC STEEL DESIGNED FOR HYDROGEN EMBRITTLEMENT RESISTANCE
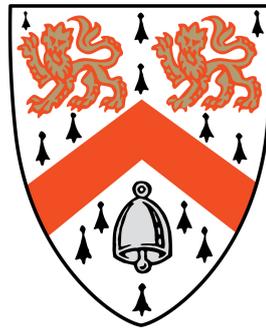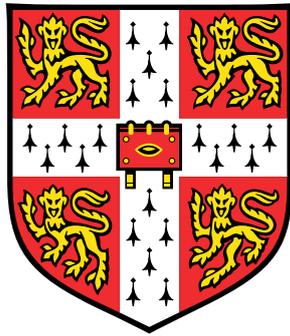
Joachim Octave Valentin Dias

Wolfson College

Department of Materials Science and Metallurgy

University of Cambridge

This dissertation is submitted for the degree of

Doctor of Philosophy

March 2018

Abstract

The phenomenon of hydrogen embrittlement in steel has been known for over 150 years. Hydrogen-resistant alloys have been developed to mitigate this effect and three types of alloys with optimised structures have been enhanced over the years: nickel alloys, stainless steels, and quenched and tempered martensitic low alloy steels. Nevertheless, those alloys are limited in terms of strength and ductility.

The aim of the work presented in this thesis was to design bainitic alloys with hydrogen embrittlement resistance, and with a better combination of strength and ductility than conventional alloys.

In the novel alloys, two microstructural features were produced to mitigate the damaging effects of hydrogen:

1. A percolating austenite structure, in which hydrogen diffusion is orders of magnitude lower than in bainitic ferrite. This feature was introduced to impede the ingress of hydrogen through the structure.

2. Iron carbide traps, which can form at the bainite transformation temperature. This feature was introduced to trap diffusible hydrogen and prevent it from causing damage.

The alloys, designed with the aid of computer models and phase transformation theory, contained a volume fraction of retained austenite above its percolation threshold, theorised as 0.1, which was proven to form an efficient barrier to hydrogen ingress. The effective diffusivity of hydrogen, measured using an electrochemical permeation technique, was shown

to decrease with increasing austenite fraction up to the percolation threshold. It was seen to plateau for austenite fractions comprised between 0.1 and 0.18, and to decrease further for fractions above 0.18.

The compositions of the alloys were precisely selected to allow for iron carbides to precipitate during the bainitic transformation reaction. Until the present work, only alloy carbides V_4C_3, TiC and NbC had been reported to strongly trap hydrogen. The literature was very inconsistent regarding the trapping ability of cementite, with reported trap binding energies ranging from 11 to 66 kJ mol^{-1}. The carbides produced in the alloys were identified as cementite. The cementite fraction was measured to be 0.001 ± 0.0001 for one of the designed alloys, which is the lowest ever reported carbide fraction in steel measured using a simple X-ray diffraction technique. Experimental thermal desorption spectroscopy data were used to determine the binding energy of hydrogen to cementite to be 37.5 kJ mol^{-1}, suggesting that cementite is not a strong hydrogen trap. Further tests performed after room temperature hydrogen degassing displayed insignificant amount of trapped hydrogen, thus confirming the reversible nature of cementite traps. The comparison of two successive transients using the electrochemical permeation technique confirmed that result.

The influence of the heat treatments on the microstructures and on the mechanical properties of the designed alloys was extensively studied. The novel alloys met all the set requirements, and successfully outperformed conventional alloys in terms of strength and ductility. They did not meet the NACE TM0316-2016 standard requirement for operation in hydrogen-rich environments, likely owing to the inadequate trapping ability of cementite. Future work should focus on exploring the possible use of alternative carbides for hydrogen trapping in bainitic structures.

Declaration

This dissertation is the result of my own work and includes nothing which is the outcome of work done in collaboration except as specified in the text.

It is not substantially the same as any that I have submitted, or, is being concurrently submitted for a degree or diploma or other qualification at the University of Cambridge or any other University or similar institution. I further state that no substantial part of my dissertation has already been submitted, or, is being concurrently submitted for any such degree, diploma or other qualification at the University of Cambridge or any other University or similar institution.

It does not exceed the prescribed word limit of 60,000 words.

Joachim Octave Valentin Dias

March 2018

Acknowledgements

I would first like to deeply thank my academic supervisor, Harry Bhadeshia, for all his invaluable qualities. It was a great relief to always find help, assistance and advice whenever I needed it. His incredible knowledge and experience allowed me to progress in my Ph.D. at an enjoyably fast pace. It is only after hearing horror stories of Ph.D. supervisors that I realise how lucky I have been with my own. I thank him for the trust he has given me with regards to this whole project.

I would like to thank all the people who have helped me with my academic work, within the department of materials, as well as in Manchester, and without whom this thesis would not be what it is today. I would like to thank my sponsors for funding fundamental scientific research generously, and allowing me to produce high quality work without being financially hindered, as well as for consistently showing interest and trust in my management of the project. I would like to thank Steve Ooi in particular, for introducing me to most experimental techniques from the first days of this Ph.D. I would also like to thank Mary Vickers for brightening my many days spent working on XRD. Her breadth of knowledge, experience and expertise in that field were extremely useful and working with her was a truly captivating scientific experience. She also had many great stories that were very welcome for staying motivated when nothing seemed to work and when disasters kept on striking. Finally, my special thoughts go to Gaurav Joshi, who has not only taught me all I know about electrochemistry, but whose calm, sturdy and intelligent attitude to the many problems faced in the lab are a source of inspiration in all aspects of my life. It was a great pleasure to have him by my side during the hard time I went through in Manchester.

A friend once told me that, if you want to know who someone is, you just have to look at their friends. Over time, they influence each other and modify one another's personalities by gaining from each other and adopting aspects of each other's personalities. I don't think that could be more accurate, and I would therefore like to thank all of my friends, from the bottom of my heart, for making me who I am today. I am extremely grateful to have been accompanied in life by such high quality individuals, who keep on amazing me, making me die of laughter and inspiring me to surpass myself. Progressing through life with a group of individuals that I value immensely is a beautiful experience, and I cannot wait to see what we will all achieve soon. And because good times are only good because bad times exist, I am also incredibly grateful to be able to rely on them when I am not strong, and to be able to find fresh perspectives and great advice regarding problems that I simply cannot seem to figure out. Every single one of my friends is uniquely important to me, and I hope and believe that they all know how much they count for me.

It is hard for me to give my family the gratitude they deserve. I am incredibly lucky to have been brought up in such a supportive and loving environment. Their unconditional love is my strength, and I hope my unconditional love can be theirs. Today, and as always, I truly feel, too blessed to be stressed.

How could I forget Dr. B., who has shared my life over the last months, and provided immense support in the rather stressful writing up stage of this Ph.D. I am grateful I have been found by someone so unique. I wish for our honeymoon period never to end.

I would like to thank chance for the crazy adventure that my life during this Ph.D. turned out to be. An emotional roller coaster ride that kept getting more intense as the years progressed. I want to always remember the lessons learned over the last few years: Never to take current situations for granted. Always to question. Always to be curious. Always to strive for

understanding. Always to favour progress over perfection. Always to be honest. Never to allow snakes in my circle.

Table of contents

Nomenclature

α Ferrite

α' Martensite

α_b Bainitic ferrite

ε Epsilon carbide, $Fe_{2.4}C$

γ Austenite

γ_r Retained austenite

ρ Dislocation density

θ Cementite

θ_L Fraction of lattice sites occupied by hydrogen

θ_T Fraction of trap sites occupied by hydrogen

ε Strain

a_γ Austenite lattice parameter

b Burgers vector

B_S Bainite-start temperature

C_0 Initial sample hydrogen concentration sub-surface

D_0 Hydrogen lattice diffusion pre-exponential factor

D_L Lattice hydrogen diffusivity

D_{Eff} Effective hydrogen diffusivity

E_B Trap binding energy

E_{B_C} Cementite binding energy

E_{B_D} Dislocation binding energy

E_{B_I} Ferrite/austenite interface binding energy

L Specimen thickness

M_S Martensite-start temperature

N_L Hydrogen lattice site density

N_{T_C} Cementite trap density

N_{T_D} Dislocation trap density

N_{T_I} Ferrite/austenite interface trap density

p_{H_2S} Partial pressure of hydrogen sulphide

Q Lattice diffusion activation energy

T_0 The temperature at which the free energy of ferrite and that of austenite of a unique composition are equal

T_0' The temperature at which the free energy of ferrite and that of austenite of a unique composition are equal, when the stored strain energy is accounted for

t_b Breakthrough time

t_{lag} Time-lag time

V_{α_b} Volume fraction bainite

V_{γ} Austenite volume fraction

CCT   Continuous cooling transformation

EDX   Energy-dispersive X-ray spectroscopy

SEM   Scanning electron microscopy

SSC   Sulphide stress cracking

TDS   Thermal desorption spectroscopy

TEM   Transmission electron microscopy

TRIP   Transformation-induced plasticity

TTT   Time-temperature-transformation

UTS   Ultimate tensile strength

XRD   X-ray diffraction

YS   Yield strength

Introduction

After the discovery of hydrogen embrittlement, its causes and effects were extensively explored. The deeper understanding of the mechanisms governing hydrogen embrittlement led to the development of three types of hydrogen resistant alloys: nickel alloys, stainless steels, and low alloy steels. The mechanical properties of those alloys have been progressively improved and optimised in order to meet the industrial needs for increasingly stronger alloys, while preserving their hydrogen resistance in operating conditions that were becoming more extreme. Recently, the strength of those alloys has reached values close to the inherent limit imposed by the crystal structures of their matrix phases.

Duplex and austenitic stainless steels and nickel alloys have large fractions of austenite, which has a face-centred cubic structure, and is more ductile but has an innate lower strength than ferritic phases. Martensitic stainless steels and low alloy steels have a tempered martensitic structure. Martensite is formed through a diffusionless, displacive transformation and acquires a body-centred tetragonal crystal structure. It is due to the inability of carbon to diffuse out of the carbon-supersaturated martensitic phase formed, preventing it from reaching the equilibrium body-centred cubic ferritic phase. The tempering step is therefore needed to increase the ductility of this strong and brittle phase, but causes a decrease in strength.

In order to circumvent those inherent strength limitations, the ability of other alloys, such as titanium or bainitic alloys, to resist hydrogen embrittlement was recently explored. It is known that fully austenitic alloys are good for preventing hydrogen embrittlement because

of the slow hydrogen diffusivity in that phase. Some carbides are also known to strongly trap hydrogen, thus preventing it from causing embrittlement. The present work describes the design of a new alloy containing slender plates of carbide-containing bainitic ferrite dispersed in a matrix of carbon-enriched retained austenite, that could be produced in a single isothermal phase transformation. This alloy could theoretically benefit from the advantages procured by the austenitic phase, and from the presence of carbides. One aspect of the work presented in this thesis was to clarify the efficacy of iron carbides as hydrogen traps, because of the many contradictory results presented in the literature. The bainitic transformation differs from the martensitic one in that it occurs at higher temperature and permits the diffusion of carbon out of the supersaturated ferritic phase, either enriching the neighbouring austenite phase, or precipitating as carbides. The presence of both untempered phases in the final microstructure leads bainite to exhibit simultaneously high strengths and high ductility.

A general introduction to the behaviour of hydrogen in steels is first presented, in Chapter 1, as well as a description of commercial hydrogen-resistant alloys and of iron carbides that can form in steels. Using this knowledge, and with the aid of computer models, an alloy design is proposed in Chapter 2. A set of characterisation techniques is defined as the most suited for this project and described in Chapter 3. The characterisation of laboratory scale alloys is presented in Chapter 4, and optimised compositions are suggested for large-scale alloys. The work presented in Chapters 5, 6 and 7 focuses on characterising the two large-scale alloys, with special focus on microstructural characterisation, hydrogen behaviour and mechanical properties respectively. The main results are summarised in Chapter 8 and suggestions for future work are presented.

Chapter 1

Literature review

1.1   Introduction

The aim of the work presented in this chapter is to show that novel steels can be used for mitigating the hydrogen embrittlement effect and its damaging consequences. This research is designed to explore new opportunities for hydrogen resistance in bainitic steels, using both the austenite phase to provide a barrier to hydrogen ingress and iron carbides to trap hydrogen. The literature review is composed of four sections:

- The first section explores the current knowledge about the problematic hydrogen embrittlement of steels.

- The second one examines the transport of hydrogen in steel and shows what methods have been reported for measuring it. Simultaneously, it investigates how microstructural features in steels, called hydrogen traps, can be used to prevent diffusible hydrogen from causing embrittlement.

- The third one describes commercial hydrogen-resistant alloys and illustrates the opportunity offered by bainitic alloys to become a new class of hydrogen-resistant alloys.

- The final section describes structure of iron carbides, a type of hydrogen traps, and their growth in bainitic alloys.

1.2 Hydrogen Embrittlement

1.2.1 First observation

Hydrogen embrittlement commonly refers to the deterioration of toughness, elongation and strength as a result of hydrogen ingress into metallic alloys. This effect in steels has been known for more than 150 years. It was initially investigated in an experiment by Johnson, where iron samples were dipped into hydrochloric or sulphuric acid for several minutes and displayed a dramatic deterioration of their toughness and strain to failure [1]. Johnson reported that this degradation in mechanical properties was only temporary and could be recovered with time. Hydrogen was suggested to be responsible for the observed behaviour because there was no significant change in the mechanical properties of the samples when iron was dipped into acids that wouldn't cause hydrogen evolution on the surface of the samples.

This discovery had serious consequences for the steel industry, since the mere presence of hydrogen or hydrogen generating sources in a given environment could prove potentially devastating, by causing steels to fail unexpectedly, much below their uncontaminated yield points. A great effort has therefore been put into trying to understand hydrogen embrittlement in as much detail as possible. Yet, the specific mechanisms are not fully agreed upon [2]. This is partly due to the very small scale over which mechanisms happen, and the very high speed at which hydrogen can diffuse rendering experimental work complex [3]. There is currently no experimental design which allows analysis of the atomic-scale behaviour of embrittlement at the crack tip at the extremely fast speed at which it occurs, and no atomistic or larger scale simulation can be accurate enough to give insights into specific mechanisms [4]. Additionally, experiments are usually run on complex systems, in complex environments, because those are more relevant for engineering applications. As a result, the very nature of the processes cannot be investigated in depth and a fundamental understanding of hydrogen embrittlement

remains challenging. In order to understand the mechanisms of hydrogen embrittlement, three important characteristics of hydrogen in metals have been identified:

1. It is atomic hydrogen that is present in the metallic lattice and not dihydrogen gas. The gaseous phase can be present in steels, but only in specific cases where, for example, many hydrogen atoms have gathered at a void and recombined into a gas [5].

2. There are two different "states" in which hydrogen can be found in metals; either trapped at a specific site in the structure and thus immobile, or mobile through the alloy, in which case it is referred to as diffusible hydrogen. Only diffusible hydrogen causes embrittlement through mechanisms that are explained in detail in Section 1.2.2 [2]. The state of a given hydrogen atom at a given point can be assessed using several methods, which are described in Section 1.3.

3. The effect of embrittlement can be observed even if hydrogen is present in concentrations as low as one part per million in weight [3].

Unique behaviour of the hydrogen atom

The reason why hydrogen embrittles metals in a unique way lies in its very nature. Being the first element of the periodic table, composed of a single proton and a single electron, it can diffuse in ferrite from an interstitial site to another extremely quickly and can also display quantum mechanical tunnelling [3]. Slater calculated that its atomic radius is significantly smaller than that of other interstitials, and Table 1.1 shows that, as a consequence, its diffusivity is many orders of magnitude higher than that of other interstitials at room temperature. Hydrogen is the only element whose diffusivity is not very sensitive to temperature change compared to other interstitials [6–9]. This ability to diffuse through the ferrite lattice much faster than other interstitial atoms means thermodynamic equilibrium is reached very quickly, even at room temperature. It also occupies interstitial vacancy sites differently than other interstitial atoms: instead of bonding with the atoms on either side of the vacancy, and being located close to the centre of it, hydrogen atoms tend to preferentially sit at the edge of the vacancy, thus only binding with one metallic atom [10]. This non-bridging bonding is very

detrimental to the mechanical properties and is a cause of failure in some embrittlement mechanisms reported in the literature [11]. Both behaviours make hydrogen embrittlement of great concern while no other element in the periodic table causes any similar issues.

1.2.2 Embrittlement mechanisms

Many mechanisms have been suggested in order to explain the nature of the embrittlement generated by the presence of hydrogen. Depending on the conditions, different mechanisms are at play. Only the most widely accepted mechanisms are reported here.

1. Pfeil observed in 1926 a decrease in cleavage strength when iron was stressed in tension perpendicular to the cleavage planes and in the presence of hydrogen. He concluded that hydrogen lowers the cohesion strength along cleavage planes, whereas hydrogen has close to no effect on slip. This is known as hydrogen enhanced decohesion (HEDE) [11]. He also noticed that grain boundaries were the regions most vulnerable to hydrogen embrittlement, because such areas have more many interstitial sites hydrogen can occupy due to incoherency between adjacent grains. As a result, iron samples with large grains, and thus few heavily weakened boundaries, were a lot more susceptible to hydrogen embrittlement than those with small grains, where the many boundaries were each less affected. This was observed as a tendency for samples to display intragranular fracture when grains were small and intergranular fracture when grains were large.

Table 1.1: Comparison of the room temperature diffusivity of four interstitial elements found in ferrite. The diffusivity of hydrogen is many orders of magnitude higher than that of other interstitials. The atomic radii reported were calculated by Slater, and can help explain the unique behaviour [12].

Element	atomic radius / Å	Diffusivity at room temperature / $\text{m}^2\,\text{s}^{-1}$	Reference
Hydrogen	0.25	10^{-8}	[6]
Boron	0.85	10^{-22}	[7]
Carbon	0.70	10^{-20}	[8]
Nitrogen	0.65	10^{-20}	[9]

2. The second mechanism involves the formation of brittle hydrides (HYFO, for hydride formation) as a way to lower the free energy of alloys containing hydrogen and transition metals from the 4th and 5th group of the periodic table, such as niobium, vanadium or zirconium. These hydrides tend to form preferentially at stress-concentration areas such as crack tips, and eventually crack under applied stress because of their brittle nature. The process of hydride formation and fracture is repeated as cracks grow and causes macroscopic failure of the alloys [13]. This process is not of concern in this project since the alloying elements that form hydrides do not provide enough advantages to be added to the steel designed.

3. Beachem demonstrated in 1972 that hydrogen can lead to local plastic deformation below the macroscopic yield stress through a process called hydrogen enhanced localised plasticity (HELP) [14]. This has later on been confirmed by in-situ TEM fracture analysis in iron, in which it was proven that hydrogen enhanced motion and emission of screw, edge and mixed dislocations [15, 16]. In this case, hydrogen atmospheres accumulate near stress fields, such as dislocations. They in turn lower the stress field's interaction with neighbouring stress fields from point defects for example, meaning that the thermal activation energy for slip of the dislocation is lowered. As the dislocation travels through the lattice, the hydrogen atmosphere, attracted to its stress field, tends to follow it, and continue providing the enhanced plasticity effect. Consequently, this mechanism only occurs close to room temperature. Hydrogen atmospheres are usually not observed at high temperatures and cannot have a significant effect on slip. This mechanism leads to slip band fracture surfaces.

4. Whereas all the previously described mechanisms rely on hydrogen dissolved inside the alloy, this mechanism relies on the hydrogen that is adsorbed on the surfaces of the cracks. The surface here refers to the three first layers of atoms, as they have been reported to be able to accommodate a lot more hydrogen than could otherwise be present in the bulk of the alloy. Adsorbed hydrogen presence is seen to facilitate dislocation emission from the crack tip by breaking the interatomic iron bonds, therefore allowing

the crack to grow as a direct result from dislocation emission. The process is referred to as adsorption-induced dislocation emission (AIDE). This is seen as an intergranular dimple fracture surface [17].

5. Conversely, Song and Curtin described, using molecular dynamics simulations, that absorbed hydrogen could also prevent dislocation emission at the crack tip [18]. In this mechanism, the hydrogen presence is seen to cause a phase transformation at the crack tip, thus impeding the slip mechanism and preventing dislocation emission from the crack tip. Brittle failure then occurs because of the lack of plasticity. This mechanism has the advantage of quantitatively predicting the threshold for hydrogen embrittlement in ferritic steels, based on the diffusivity of hydrogen to the crack tip region, the average hydrogen concentration in the alloy and the mechanical loading. The model has been proven to agree well with experimental data [18–20].

6. Finally, it has been demonstrated that hydrogen presence stabilises vacancies in ferritic iron [5]. As a result, voids within the strain field ahead of crack tips have been observed to coalesce with vacancies and neighbouring voids before the crack propagation itself, thus accelerating propagation of crack once it started growing. This is called hydrogen-enhanced stress-induced vacancy mechanism (HESIV). The hydrogen in this case has a very high solubility on the surfaces of the voids, can recombine into molecular hydrogen, and can cause significant stress at high pressures of hydrogen gas. Nagumo observed such behaviour in TEM, by showing a defect rich, amorphous region of iron just beneath the crack [5]. This mechanism can explain the observed behaviour that, in a few specific cases, the mechanical properties cannot be recovered after hydrogen degassing, even though it is the case when other mechanisms are dominating.

It is complicated to differentiate between the mechanisms at play in practice, and it is likely that combinations of the described mechanisms would be taking place simultaneously.

Hydrogen embrittlement in industrial applications

Hydrogen embrittlement is a problem in many engineering applications. The fundamental

investigation presented in this thesis describes the development of bainitic alloys with mechanical properties specified for use as structural materials in environments containing H_2S. Due to the versatility of the bainitic structure, they could be adapted to other applications where hydrogen embrittlement is an issue. Failure in H_2S environments is usually referred to as sulphide stress cracking (SSC), in which H_2S reacts with metallic atoms to form hydrogen and other corrosion by-products. Sulphur is a hydrogen recombination poison, which means it prevents atomic hydrogen adsorbed on the steel surface from recombining as a gas and escaping into the environment. Consequently, the concentration of atomic hydrogen on the surface of the steel increases and drives diffusion into the alloy. Additionally, it also encourages the iron dissolution rate. Once the hydrogen is present in a large quantity in the alloy, the mechanisms described previously lead to the embrittlement [21].

It has long been reported that high strength steels are more susceptible to hydrogen embrittlement than softer steels, although the precise reasons for this are not clear [22]. Some studies suggest that the higher resistance to plastic flow in such alloys mean that stress cannot be relieved as easily as in other alloys and consequently crack growth leading to brittle fractures is more likely to dominate. This is worsened by the fact that hydrogen embrittlement also affects body-centred cubic structures more than face-centred cubic phases [6].

After the damaging effects of hydrogen having been reviewed, three approaches to mitigating hydrogen embrittlement could be identified:

1. Reducing iron corrosion rates that generate the hydrogen at the surface of the steel. For this, either chemical inhibitors or coatings can be used, both of which are outside the scope of this Ph.D., and are not discussed further.

2. Preventing ingress of hydrogen into the structure. Two effective ways of achieving this goal are the use of coatings, and the design of alloys that possess an optimised, tortuous austenite structure.

3. Neutralising diffusible hydrogen present in the steel. For this, hydrogen traps have been suggested. Section 1.3 focused on assessing diffusion and trapping of hydrogen in complex microstructures.

1.3   Hydrogen transport and trapping

Since hydrogen embrittlement is a significant problem in the steel industry, a great amount of work has attempted to describe the kinetics of hydrogen transport and thermodynamics of hydrogen trapping. The concepts of trap and binding energy were clarified, as some confusion exists in the literature. The different thermodynamic and kinetic based models for characterising traps were reviewed with their advantages and drawbacks. Eventually, a comprehensive table of all the values suggested for trap binding energies of usual microstructural features that are used for trapping was produced.

1.3.1   Physical definition of hydrogen trapping

A simple way to visualise traps is to imagine the potential energy trace of the microstructure in which the hydrogen atom can fit. Fig. 1.1, inspired from Oriani, shows a simplified schematic potential trace of a trap in one dimension, in which the different activation energies can be visualised [23]. The minima correspond to sites that can be occupied by a single hydrogen atom. Q is the lattice diffusion activation energy, E_B is the trap binding energy and $Q + E_B$ is the detrapping activation energy.

In the simplest case, that of a single crystal with no defects, the potential energy is composed of an array of dips and saddles, all with the same energy barrier, corresponding to the activation energy for lattice diffusion. The more defects are present in the structure, the more this basic potential trace changes. The presence of a vacancy would cause a dip in the potential, because this feature is the most basic trap that can be encountered in a structure. Dislocations have a similar effect, but because of the strain field generated by the dislocation, not only is the potential lower at the location of the dislocation, but it is also modified in the vicinity of the dislocation. Consequently, as hydrogen atoms approach the dislocation, the lattice diffusion becomes gradually easy to overcome. With more complex structures, such as grain boundaries, the traces are more complicated, but with the same concept that there are a combination of dips in potential energy and as such, traps for hydrogen to occupy. Fig. 1.2,
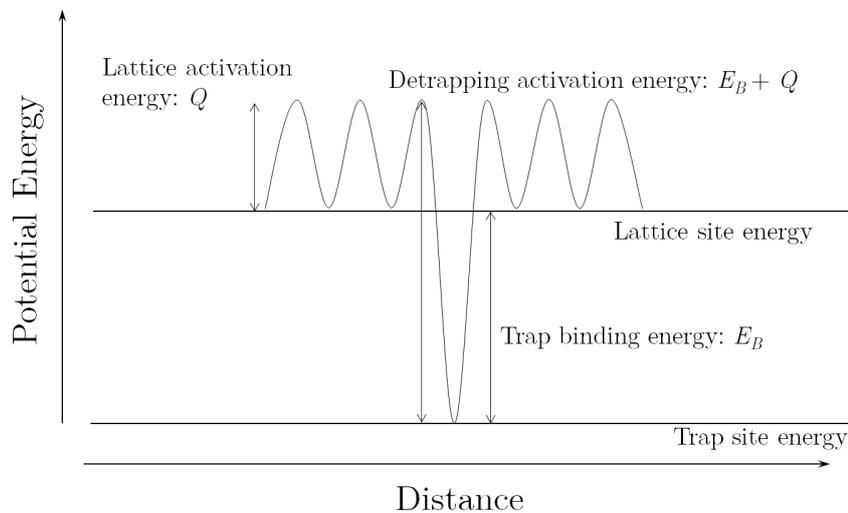
Fig. 1.1: Physical representation of hydrogen traps as potential energy minima, inspired by Oriani [23].

reproduced from Kirchheim illustrates this relation between microstructural features and trap potential trace [3].

Attractive and physical traps

Traps like dislocations are called attractive traps, because the energy barrier is progressively lowered as hydrogen approaches the trap. This attractive nature can be generated in two ways:

1. Electronically, in which case an electron vacancy due to a defect in the structure, such as impurity elements, can attract the electron from an hydrogen atom.

2. From stress fields, in which case lattice stress field induces this effect, as is the case for dislocations, grain boundaries or coherent precipitates.

Alternatively, some traps are purely physical and do not display a progressive change in potential energy. Such traps are, for example, high angle grain boundaries, or incoherent particles. The nature of the trap has a very important impact on the efficacy with which it can prevent diffusible hydrogen from causing embrittlement in the structure. The process of trapping is statistical and depends on the jump frequency of the hydrogen atoms from site to site, and it is important to realise that the frequency at which the atom can jump towards a

Material	Structure	Potential trace
Single crystal		
Single crystal + point defect		
Single crystal + dislocation		
Single crystals + grain boundary		
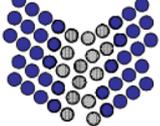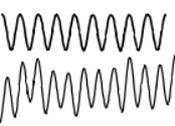
Fig. 1.2: Representation of the potential trace of some hydrogen traps in metals, from Kirchheim [3].

trap is the same as the frequency that would make it leave the trap.

The advantage of attractive traps is the ease with which hydrogen can enter them. The main drawback is that hydrogen can also leave the traps easily, and such traps can sometimes become hydrogen sources that end up worsening embrittlement [24]. Physical traps do not allow hydrogen to escape easily, but the probability that hydrogen atoms enter them is low, since atoms have to randomly fall into the traps. In practice, most traps tend to have components of attractive and physical traps. Intuitively, it is possible to conceive that ideal hydrogen traps would display both attractive and physical characteristics. Indeed, a slow initial decrease in potential energy followed by a very deep trap, as displayed schematically in Fig. 1.3, would enable such mixed trap to gather hydrogen from a wide region and trap it strongly to its core. It has been revealed that some carbides, such as V_4C_3, behave as described, first by attracting hydrogen with the coherent strain field from their interface with the matrix, and then by providing a strong trap within the carbide itself due to carbon vacancies [25]. Additionally, the traps would need to be homogeneously dispersed and rela-

tively close together in order to be able to trap the largest amount of hydrogen possible [26]. The best option to achieve this, through the use of carbides, was investigated deeper in Section 1.3.4.

Internal and external hydrogen

When designing hydrogen traps, a factor to consider is the amount of hydrogen that can be generated from the manufacturing processes, called internal hydrogen, and the amount that can ingress during the lifetime of the part in the field, called external hydrogen. A lot of processes like electroplating of protective coatings have been reported to generate large amounts of internal hydrogen, of the order of 1-5 part per million per weight (ppmw), that cannot be removed fully by heat treating the sample since the coating applied forms a barrier to hydrogen egress [19]. In such alloys, weak carbide traps M_2C, where M is a metallic alloying element, have been reported to actually act as a source for diffusible hydrogen, and therefore to cause embrittlement, because they trap internal hydrogen and release it during operation. In this project, the manufacturing process only involve either continuous cooling from austenitising temperature or cooling with isothermal holding at a bainitic transformation temperature. As a result, internal hydrogen is not an issue for the current project.

1.3.2 Experimental methods for trap characterisation

Many methods have been reported for assessing the trapping of hydrogen in steels. A list of the most widely reported in the literature, along with their advantages and disadvantages, is reported. First, destructive methods are reviewed [3]:

- Hot extraction – Melting of samples in vacuum or in an inert atmosphere, combined with gas mass spectrometry can give very accurate information on low levels of hydrogen present, and is therefore a technique very applicable to steels. It gives very accurate values for the total hydrogen concentration in the steel. Yet, specific local concentrations of hydrogen at trap sites cannot be measured precisely with this technique because it is destructive on a too large scale.
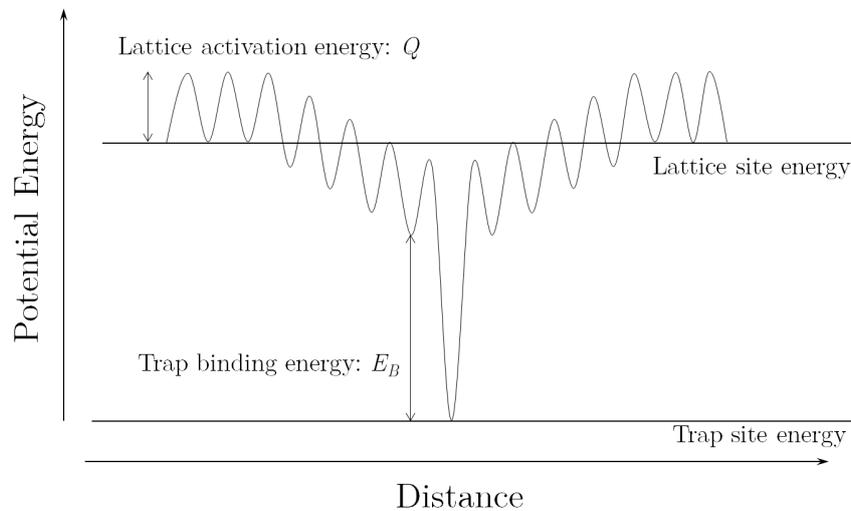
Fig. 1.3: Schematic representation of an ideal hydrogen trap: a slow progressive decrease in lattice potential energy, combined with a large trap binding energy at the core of the trap.

- Secondary ion mass spectrometry (SIMS) – Sputtering of samples and mass spectrometry can give qualitative information on hydrogen content in the structure, but is usually not quantifiable. On top of that, a problem that has been reported during the sputtering process is that the newly created surface attracts hydrogen present in the layers below it very strongly, thus complicating the differentiation between hydrogen trapped by real features and hydrogen seemingly trapped because of this effect. Gemma has proven it can be mitigated by incorporating a specific set of parameters to the data analysis [27]. This technique is particularly used for investigation of thin films and multilayers.

- Atom probe tomography – With this technique, a small region, of the order of 100 nm, at the tip of a sharp needle is field evaporated, or laser pulse evaporated in the case of non-conductive samples like oxides, and the mass-to-charge ratio is obtained through time of flight, thus revealing a precise elemental distribution in the sample. This technique has been reported to have a lateral resolution of about 1 nm and a depth resolution of the size of an atom. Very precise quantitative elemental maps can therefore be obtained, as depicted in Fig. 1.4. As for SIMS, hydrogen diffusion to the newly created surface is an issue and has to be mitigated. In order to prevent quantum tunnelling between interstitial sites, and to differentiate trapped hydrogen from contamination,

deuterium is used instead of hydrogen during the charging step. Performing the analysis at cryogenic temperatures also prevents deuterium diffusion. Additional parameters have to be used to account for the difference in melting temperatures of the different phases, for example carbides compared to the matrix in steels. In that case, the matrix is removed more easily, leading the carbides to only be evaporated later and appear deeper in the sample than they actually are, and therefore display inaccurate deuterium localisation. This technique was not used in this project because it is clear from the literature that hydrogen can be effectively trapped at carbides and other point defects on a small scale [25, 28, 29]. This project is trying to use this behaviour and obtain quantitative data on trapping on a larger scale. Additionally, this technique is expensive and not readily available.

Thermodynamic approach

A precise way to assess hydrogen presence in metals is through thermal desorption spectroscopy (TDS), which was used extensively in this project. This technique involves heating a sample in an inert carrier gas towards a gas chromatography detector, where the hydrogen detected is monitored. There are two schools of thoughts regarding the use and effectiveness of this technique. It is sometimes the case that TDS is used for surface analysis where several different traps are present, in which case several distinct peaks can be observed depending on the trapping energy of the different defects [3]. The more common application, which was performed in this project, is to have a thicker sample, of about 1 or 2 mm in thickness, in which a single or several broad peaks can be observed [6, 30]. The major advantage of this technique is that it accurately measures the amount of hydrogen present and trap binding energy can be deduced from a variety of TDS data. Other parameters that can be obtained are the trap density, and the ratio of filled to unfilled traps. The main disadvantage that is usually overlooked, is that no other information can be obtained, and therefore the microstructure has to be known extremely well in order to attempt to explain results from TDS. It is not uncommon in the literature that TDS is used and hydrogen trapping contribution arbitrar-
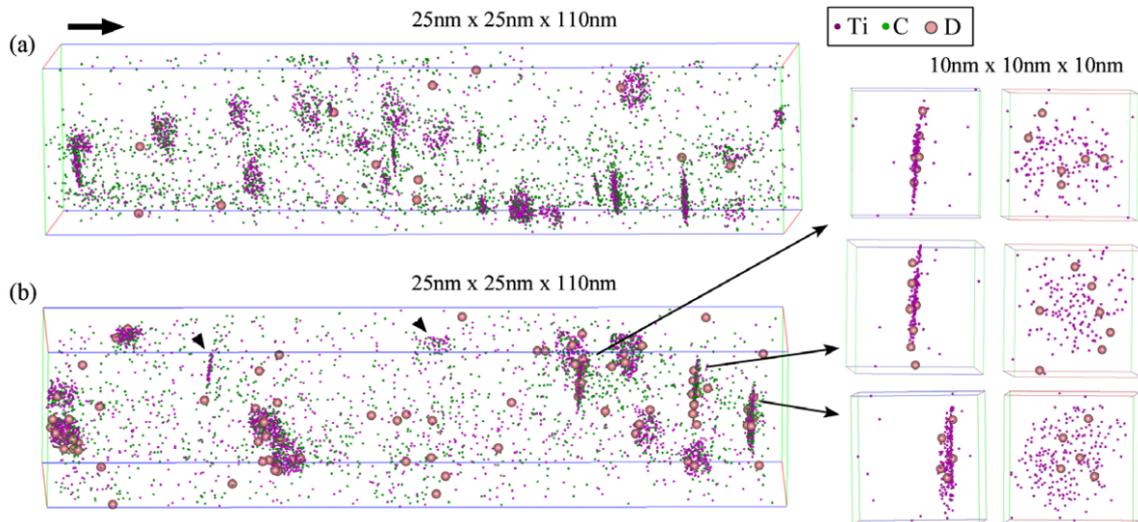
Fig. 1.4: Atom probe tomography results presented by Takahashi [28]. TiC are visible as clusters of Ti and C atoms. Deuterium is visibly more present in the vicinity of such carbides than in the matrix. The black arrow indicates the scan direction.

ily attributed to the phase of interest, without attempting to consider other microstructural features [31–33].

Kinetic approach

Electrochemical permeation is a method complimentary to TDS. The setup was first described by Devanathan and Stachurski in 1962 for study of hydrogen in palladium [34]. For this macroscale technique, a sample of approximately 1 mm thick is placed between two electrolytes and hydrogen is evolved on the cathode. Through application of a potential, hydrogen is forced to travel through the cell to reach the anode, at which point a rise in current is detected. As it is the case for TDS, permeation gives a macroscopic average and it is not trivial to obtain trapping information for specific features. The trap binding energy can be deduced from the slope of the rise of the current detected at the anode with time. This method was used in this project. Similarly to TDS analyses, the literature has examples of trap binding energy calculations without taking into account the complexity of the microstructures investigated [35–37].

Experimental challenges

The main parameters that are used to characterise traps are the trap binding energy and the number density of traps. From those, it is theoretically possible to predict the ability of a structure to trap hydrogen, since the trap occupancy can be estimated from the concentration of hydrogen in the structure. The main experimental challenge to find such parameters is the measurement of the concentration of hydrogen sub-surface, C_0, and of the lattice diffusivity D_L, both of which must be known before the models can be used to interpret any data. The way data have been analysed in the literature is usually inaccurate because there always are non-unique solutions to all the permeation or TDS curve fitting [23, 38]. In other words, there are too many unknowns to obtain any single reliable value for any of the parameters investigated. In the past, D_L has been estimated in iron in several experiments and those values tend to be used for estimating C_0 to analyse the data, using $J_{SS} = DC_0/L$, where J_{SS} is the permeation steady-state current and L the thickness of the sample [39–43].

A parameter that often is reported is the effective diffusivity of hydrogen in the material, D_{Eff}, as it gives an indication on how fast hydrogen diffusion is in a structure, although it is not a material parameter but depends upon the experimental conditions. For example, a change in the charging current affects the hydrogen concentration sub-surface of the sample, which in turns affects D_{Eff}, as displayed in Fig. 1.12 [43].

1.3.3 Quantification of results

Four major models have been reported in order to quantify the TDS and permeation results.

1. The first method is based on Kissinger's differential thermal analysis (DTA) experiment in 1956 and 1957 [44, 45]. In this case, the reaction is investigated at different heating rates, and a sample's behaviour is compared with an inert reference. The nature of the reaction investigated is solid $\rightarrow$ solid + gas. The difference between the two behaviours is attributed to the differences in structures of the materials studied. Using the fact that the maximum deflection from the reference, i.e. the summit of the DTA peak, occurs

when the reaction rate is maximum, and by running the experiment at different rates, Kissinger deduced the thermal activation energy for specific reaction. His model only takes into account thermal activation for the rate of reaction:

$$\frac{d(\ln \frac{\phi}{T_m^2})}{d(\frac{1}{T_m})} = \frac{-(E_B + Q)}{R} \tag{1.1}$$

where T_m is the temperature at which the DTA peak is maximum, ϕ is the heating rate, R is the gas constant and the sum $E_B + Q$ is the detrapping activation energy.

It is possible to see a few ways in which this model fails to represent the scenario investigated in TDS. First, it is assumed that all the material that undergoes the reaction solid $\rightarrow$ solid + gas stays as a gas, which holds for his experiments, but is not the case here, as it is well known that hydrogen can be reabsorbed by a trap directly after having escaped it. Secondly, with this technique, only one thermally activated process can be calculated at a time. In order for that to hold, the microstructure investigated should be extremely simple, such as a single crystal and a single type of trap, be it dislocation, vacancies or others. This model is used extensively in the literature and many values of trapping activation energies are reported, but it is very hard to estimate how far off the real values are. Additionally, sample geometry is not accounted for, and it has been shown computationally that for equivalent microstructures, an increase in sample thickness would lead to a decrease in calculated trap binding energy when Kissinger's model is used [46]. Furthermore, Du showed that at low trap density, Kissinger's model leads to an underestimate of the trap binding energy because traps are not homogeneously filled and therefore hydrogen evolution does not reflect well the trap occupancy [47].

2. Consequently, McNabb and Foster investigated a novel method for assessing the specific case of hydrogen desorption behaviour in steels [38]. They theorised that hydrogen in steel could not simply be solved by an application of Fick's laws of diffusion because of inconsistencies in the literature when that was done. Darken and Smith

observed in 1948 that samples charged with hydrogen using fixed boundary conditions in which the hydrogen concentration was kept at 0 and an arbitrary C_0 value on both ends of the sample, did not display a linear change in the hydrogen concentration from C_0 to 0 as would be expected from Fick's law [48]. Additionally, if the concentration of hydrogen at both ends of the sample was kept at C_0, in other words that at the steady state, saturation is achieved, the ratio between the total amount of hydrogen between the first and second case should be 0.5. Instead experimental measurements showed that it was actually close to 0.8, meaning the concentration of hydrogen did not obey Fick's law. The hydrogen concentration in samples is schematically represented in Fig. 1.5. A and B show the concentration of hydrogen obeying Fick's law, where the boundary conditions are $C = 0$ and $C = C_0$ on the samples surfaces in A and $C = C_0$ on both surfaces in B. It is clear that the ratio of hydrogen concentrations between A and B is 0.5. C and D show the actual hydrogen distribution, with the same boundary conditions, hence a ratio closer to 0.8.

They based their model on the existence of two different types of lattice sites, normal sites and traps, which slow down the normal diffusion process. They deduced this behaviour from another result by Darken and Smith, who observed that it was faster for hydrogen to ingress a sample than it was for it to egress it, under the same boundary condition. They derived a set of partial differential equations to represent the problem, assuming a random walk type mechanism; one to assess the diffusion, equation (1.2) and one for the trapping and detrapping local equilibrium, equation (1.3).

$$\frac{\partial C}{\partial t} + N_T \frac{\partial n}{\partial t} = \mathrm{div}(D\,\mathrm{grad}\,C) \qquad (1.2)$$

where C is the total hydrogen concentration, i.e. the density of diffusing atoms per unit volume, t is time, N_T is trap density, n is the fraction of traps occupied and D is the hydrogen diffusion constant in the alloy.

$$\frac{\partial n}{\partial t} = kC(1-n) - pn \tag{1.3}$$

where k is the trapping probability per second and p is the detrapping probability per second.

3. The problem with that model is its complex mathematical aspect, which renders it complicated to apply to experimental data. In 1970, Oriani proposed a simpler model, solely based on equilibrium between trapped and diffusible hydrogen [23]. He showed that, when traps are not close to saturation, the diffusivity of mobile hydrogen can be deduced from the trap density and the trap binding energy. This is only true when the time required for the trap equilibrium to be reached, as described by equation (1.4), happens faster than the concentration of hydrogen at the trap location can change through diffusion. In practice, this depends on the hydrogen attempt jump frequency, which typically is of the order of 10^{13} s^{-1}, and this assumption is valid up to values of approximately 400°C [38].

$$\frac{\theta_T}{\theta_L(1-\theta_T)} = \exp\left(\frac{-E_B}{RT}\right) \tag{1.4}$$

where θ_T and θ_L are the fraction of occupied trap and lattice sites respectively, E_B is the trap binding energy, R is the gas constant and T is the temperature.

4. An additional model was therefore developed recently by Song, in which finite element modelling of the process of hydrogen desorption is used [49]. This model is based on the kinetic equations of McNabb Foster and the local equilibrium of Oriani's models. All models initially describe two types of sites, normal lattice sites and trap sites. All the trap sites are assumed to be equivalent, so they are referred to as "one kind of trap" and can be thought of as traps from a unique microstructural feature like dislocations [3]. Conversely, Song's model was designed for use in ferritic steels, and allows for several traps with different binding energies and trap densities to be modelled simultaneously, reflecting the complex structures of steels. Additionally, it is
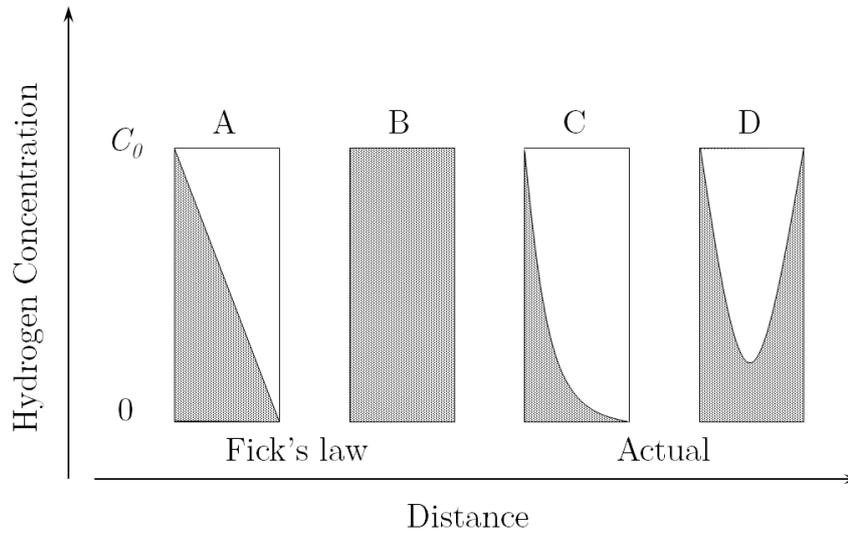
Fig. 1.5: Concentration of hydrogen in a sample as predicted by Fick's law (A and B), and as observed experimentally (C and D). For samples A and C, the hydrogen concentration is kept at C_0 on the left side and at 0 on the right side. For sample B and D the hydrogen concentration is kept at C_0 on both sides.

valid regardless of the fraction of occupied traps. Since TDS was used with saturated samples, it was imperative to use a model that was valid in such conditions. For all those reasons, this model was used to quantify the TDS data obtained. This model was only designed to be used for analysis of TDS data and hence cannot be applied without modification to electrochemical permeation data.

Limitations

All the described models have been designed to study single phase systems, and the diffusion laws they are based on are only valid for such systems. As a result, trying to interpret data for steels with two significantly different phases such as austenite and ferrite is very challenging. Turnbull and Hutchings suggested that the best way to deal with this case is to multiply the diffusion constant of the phase in which diffusion is the fastest (in steels, ferrite rather than austenite) by a moderating factor that has to be estimated experimentally [50]. It is not clear how to determine this factor and depending on its value, the trap characteristic at the austenite/ferrite will be affected, but the general trends of the parameters should stay consistent. This method was used when fitting the TDS data.

Special case of austenite

Austenite is sometimes reported as a trap in the literature. This concerns only blocky austenite, since the interface between bainitic ferrite and thin retained austenite is reported as a trap of interfacial nature. There are two factors that lead to austenite being considered a trap in bainitic structures: the comparatively very low hydrogen diffusivity and very high solubility of hydrogen in austenite compared to ferrite. Fig. 1.6 illustrates the measured values for diffusion constants of hydrogen in austenite and ferrite in function of temperature [2].

Those differences arise from the crystal structures of those phases. Ferrite is body-centred cubic hence pseudo close-packed, while austenite is face-centred cubic, which is close-packed. The higher solubility in austenite can be explained conceptually by calculating the size and number of interstitial sites in both structures. The addition of an interstitial atom to a host lattice induces strain which causes an increase in the total free energy of the system [52]. Calculating the ratio of the radius of interstitial to host atoms for both tetrahedral and octahedral interstitial sites in austenite and ferrite, assuming atoms as hard spheres, indicates the size of each interstitial site. The values calculated for all four sites are summarised in Table 1.2, as well as the number of interstitial sites available. Fig. 1.7 illustrates the location of those sites. It appears that the octahedral site in austenite is bigger than the other three interstitial sites, and is therefore more likely to be occupied than any other site. This was confirmed by calculating the dissolution energy of hydrogen in the octahedral and tetrahedral interstices for both ferrite and austenite from first principles, as displayed in Table 1.3 [53]. The dissolution energy of hydrogen in the octahedral site in austenite is only 0.07 eV, while it is 0.19 eV in the tetrahedral site in ferrite, which is the most likely site to be occupied in ferrite. Both results explain why hydrogen has a higher solubility in austenite. The number of sites available is not directly relevant since the fraction of occupied sites compared to available sites is low.

Hydrogen diffusivity on the other hand is lower in austenite by several orders of magnitude compared to ferrite, at room temperature. This is because there is no diffusion path in
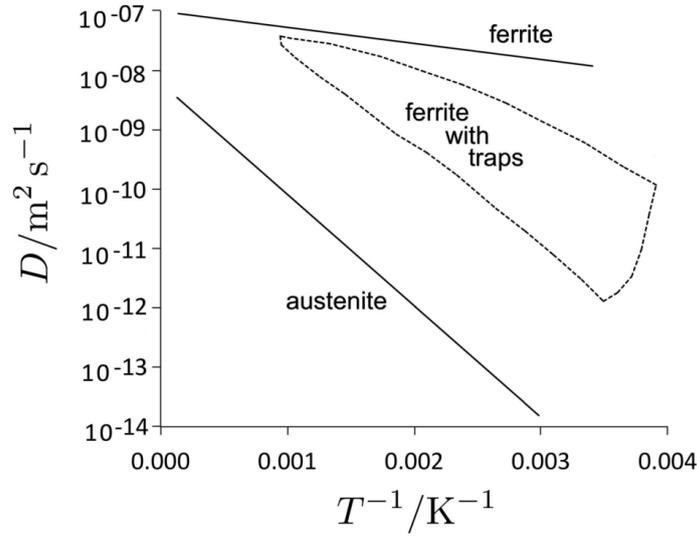
Fig. 1.6: Hydrogen diffusivity in austenite, ferrite, and ferrite in which traps are present [51]. At room temperature ($T^{-1} = 0.0034$), the diffusivity of hydrogen is many orders of magnitude lower in austenite compared to ferrite.

austenite that allows hydrogen to always occupy octahedral sites. Those sites are at the centre of the unit cell, as displayed in Fig. 1.7, and in order for hydrogen atoms to diffuse through austenite, they temporarily need to occupy tetrahedral sites before reaching neighbouring octahedral sites. Because of the high hydrogen dissolution energy of 0.51 eV at such sites, hydrogen diffusivity in austenite is slow. Conversely, for ferrite, there are six tetrahedral interstitial sites that can be occupied by hydrogen per iron atom, as opposed to a single octahedral site in austenite, as a result, hydrogen atoms can always occupy such sites as they diffuse through ferrite.

Table 1.2: Calculated octahedral and tetrahedral interstitial size in austenite (face-centred) and ferrite (body-centred). The site size is calculated as the ratio between the radius of the interstitial and the lattice atom, and is therefore unitless. The octahedral site in austenite is significantly larger than other sites, which is consistent with the higher solubility of hydrogen in austenite than in ferrite [51].

	Ferrite	Austenite
Octahedral site size	0.155	0.414
Tetrahedral site size	0.291	0.225
Number of octahedral sites per iron atom	3	1
Number of tetrahedral sites per iron atom	6	2
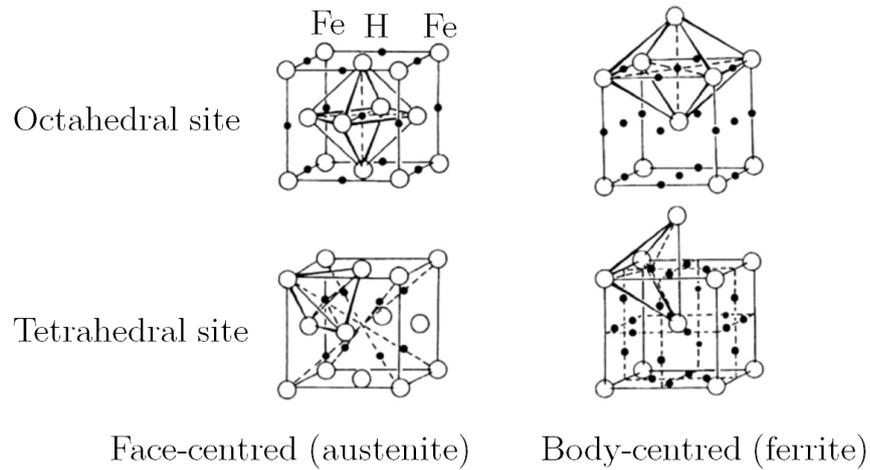
Fig. 1.7: Locations of octahedral and tetrahedral interstitial sites in face-centred and body-centred crystals [52]. Lattice sites, where Fe atoms sit, are white, and interstitial sites, where hydrogen atoms can sit, are black.

Table 1.3: Dissolution energy of hydrogen in the octahedral and tetrahedral interstitial sites in austenite and ferrite calculated by Song [53]. This explains the higher solubility of hydrogen in austenite than in ferrite.

	Ferrite	Austenite
Octahedral site dissolution energy / eV	0.34	0.07
Tetrahedral site dissolution energy / eV	0.19	0.51

Need for simple microstructures

Since those models are more reliable when they assess one trap type, it is essential that experiments that hope to obtain precise values for trap binding energies should be as simple as possible and make use of models that hold true under the conditions investigated. For example, systems of single crystals with precisely measured dislocation density should be used to investigate dislocation as a trap site. Systems with equiaxed grains containing as few defects as possible should be used to investigate grain boundaries as a trap, and so forth. It is worth noting that point defects, such as impurity atoms or vacancies have also been reported to act as traps [6]. Since their characterisation is extremely hard, and the chance of a hydrogen atom encountering such defect compared to other larger traps like carbides or dislocations is low, it was assumed in this study that their contribution to the overall trapping effect is negligible, and they were not reviewed in depth. Additionally, surfaces have also been reported to be strong traps, but since their number density compared to the bulk material is insignificant, their trapping potential was not investigated further [3].

Importance of vacancies

Vacancies are one of the most basic and smallest of defects in crystal structures. They are extremely complicated to characterise or to quantify. Recent work by Nazarov, from first principles, has revealed that vacancies are responsible for the trapping behaviour in carbides, in the case of nickel in particular [54]. It was shown that in perfect structures, it was highly unfavourable for hydrogen atoms to be added to either the interface or the core of many types of carbides. On the contrary, if vacancies existed in carbides, the drop in free energy for adding hydrogen atoms would decrease in carbides to extents much greater than for vacancies present in the lattice. The same behaviour was subsequently confirmed by Kawakami for the specific case of TiC and V_4C_3 carbides. It was shown from ab-initio calculations that a hydrogen atom occupying an interstitial site in TiC and V_4C_3 would actually lead to a significant increase in the free energy of the system, of about 60 kJ mol^{-1} in TiC and 100 kJ mol^{-1} in V_4C_3, and that it is only favourable for hydrogen to occupy carbon vacancies in the structure, or the interface between the matrix and the carbides [55].

1.3.4 Trap binding energies reported in the literature

Table 1.4 has been created with two aims: first, to give an overview of the current knowledge in terms of trapping characterisation of different structures and how consistent or inconsistent the values reported are, and second, to be able to identify an opportunity in using novel nanostructured bainite with retained austenite and carbides as a way of combing as many traps as possible and achieving strong hydrogen trapping. This is the most complex structure ever investigated with the standard methods described earlier. Many inclusions such as MnS or Al_2O_3 have been reported to trap hydrogen, but in order to make the table as clear, concise and relevant to the current project as possible, they were not reviewed [30, 56]. Consequently, only features that can be present in the steel designed and the carbides that display strongest trapping and can offer insight into the mechanisms behind trapping were reviewed. TiC and V_4C_3 cannot be formed with the proposed heat treatment in this project but were reviewed due to their excellent trapping behaviour, in the hope that mechanisms that make them efficient can be applied to other carbides.

Dislocations

The trapping ability of dislocations has been studied extensively, and it has been suggested that the stress field around dislocations can act as an attractive trap, and that the hydrogen atoms can then bind to the core of the dislocations. The most rigorous work was performed by Foster and McNabb, and they obtained values for the trap binding energy of 25 kJ mol^{-1} in a steel with 0.23 wt% C [23]. As shown in Table 1.4, many more experiments were performed in order to confirm this result. Choo and Lee's work is usually taken as a reference because they assessed dislocations in pure iron with changing grain size, so that they could distinguish between grain boundary and dislocation contributions [57]. They ensured the samples all had the same density, as a proof that the microvoid contribution should also be consistent between samples. They interpreted their result using Kissinger and therefore the binding energies obtained are not precise. Hagi's work is not rigorous in the sense that a few arbitrary values were selected for the tentative trap binding energy while ignoring the effect of grain boundaries [35]. The number of trap sites from the arbitrarily chosen trap

Table 1.4: Summary of the trap binding energies associated with dislocations, grain boundaries, microvoids, interfaces, and selected carbides reported in steels. A detailed description and analysis of those results is provided in the text. The compositions are expressed in weight percent. E_B is the trap binding energy.

Trap	Alloy	Method	E_B / kJ mol^{-1}	Reference
Dislocation	Fe	TDS, Kissinger	19	Hagi [35]
Dislocation	Fe	Permeation, Oriani	27	Choo, Lee [57]
Dislocation	Fe	Permeation, McNabb	55	Kumnick [36]
Dislocation	Fe	Modelling	26 and 38	Ramasubramaniam [58]
Dislocation	0.16C	TDS, Oriani	18-25	Johnson, Hill [23]
Dislocation	0.16C	TDS, Oriani	36-40	Johnson, Hill [23]
Dislocation	0.23C	Immersion in water, McNabb	25	Foster [23]
Grain boundary	Fe	TDS, Kissinger	10	Choo, Lee [57]
Grain boundary	0.15Ti	Tensile strength	30	Bernstein [59]
Microvoid	Fe	TDS, Kissinger	28	Choo, Lee [57]
Microvoid	Fe	Permeation, McNabb	55	Kumnick [36]
α/γ interface	Duplex, 44% austenite	Permeation, McNabb	52	Turnbull [50]
α/γ interface	0.063C	TDS, Kissinger	55	Park [31]
TiC (coherent)	0.42C-0.3Ti	TDS, Kissinger	45-60	Wei [60]
TiC (incoherent)	0.42C-0.3Ti	TDS, Kissinger	70-115	Wei [60]
TiC (incoherent)	0.05C-0.22Ti-2Ni	TDS, Kissinger	85	Wei [60]
TiC	0.15Ti, carburised	Permeation, Mc Nabb	95	Pressouyre [61]
TiC	0.63Ti, carburised	Permeation, Mc Nabb	95	Pressouyre [61]
TiC	1.5Ti, carburised	Permeation, Mc Nabb	95	Pressouyre [61]
TiC	Fe	Modelling	48 and 125	Kawakami [55]
V_4C_3	0.25C-0.3V	TDS + permeation, Kissinger	33	Asahi [32]
V_4C_3	0.25C-1V	TDS + permeation, Kissinger	33	Asahi [32]
V_4C_3	Fe	Modelling	116	Kawakami [55]
Fe_3C	0.49C, pearlite	Permeation, McNabb	11	Hong [62]
Fe_3C	0.82C, martensite	TDS, Kissinger	18	Kim [33]
Fe_3C	0.82C, pearlite	TDS, Kissinger	66	Kim [33]
Fe_3C	0.84C, bainite	TDS, Kissinger	23	Takai [63]
Fe_3C	0.84C, cold-worked	TDS, Kissinger	65	Takai [63]
Fe_3C	0.43C, coarse cementite	Permeation, McNabb	36	Robertson [37]
Fe_3C	0.43C, pearlite	Permeation, McNabb	18	Robertson [37]
Fe_3C	Fe	Modelling	41 and 47	Kawakami [64]

binding energy was then deduced so that the model fits as best as possible the data observed for the effective diffusivity of hydrogen. Understandably, many fits can exist and little information is gained from such experiment. Johnson's work was carried out rigorously but they calculated an increase in the trap binding energy of dislocations as their number density increased, due to higher cold-work deformation [23]. Simultaneously, they calculated a decrease in trap density by about an order of magnitude, although this does not make physical sense. This leaves some doubt over the reliability of their analysis. Kumnick suggests a binding energy of 55 kJ mol^{-1}, several times the values obtained in other work, but this is dubious [36]. Indeed, in their results, the trapping behaviour is very similar between annealed samples and cold-worked samples, indicating that either grain boundaries or microvoid effects dominate, although they were both completely ignored. Ramasubramaniam proposes binding energies of 26 and 38 kJ mol^{-1} for screw and edge dislocations respectively, from density functional theory (DFT) modelling [58]. This work seems reliable, although it is only a model and some imperfection effects might lead to different effects in real samples.

The dislocation trapping depends on the carbon concentration in the steel. It is well known that carbon in steel tends to segregate to the dislocation core, and it has been pointed out that the carbon presence lowers the binding energy of hydrogen at the dislocations [65]. For this reason, the trap binding energy is expected to decrease as the carbon concentration increases. This is consistent with Ramasubramaniam's DFT simulation for pure iron, that dislocations have a stronger binding energy than in Foster's result.

Grain boundaries

The only work in pure iron with grain boundaries being the only parameter varied has been performed by Choo, and is analysed using Kissinger: it therefore is not reliable. Additionally, only relatively large grain sizes are investigated, from 180 to 16 μm in diameter. Fig. 1.8 displays features of a typical TDS curve. In this specific case, the first peak is due to grain boundaries and the second peak is due to dislocations. For grain size of 180 μm, a negligible contribution to trapping is visible. The binding energy is reported by Choo as 10 kJ mol^{-1}.

Ono demonstrated that varying grain size from 450 to 130 µm had little effect on trapping behaviour [66]. Consistently with Choo, it is noticeable that as the grain size diminishes, more hydrogen can be trapped. Conversely, where Choo noted insignificant trapping for grain size of 180 µm, Ono found that in all the polycrystalline samples analysed, irrespective of grain size, three times more hydrogen was trapped compared to single crystal samples. Beck presented a result somewhat consistent with Choo, that the hydrogen diffusivity between pure single crystal iron and polycrystal iron were very close, with values of 6.25 and $8.25 \times 10^{-9} \, \mathrm{m^2 \, s^{-1}}$ at room temperature for single and polycrystal respectively [40]. No information is given on the grain size, it is therefore impossible to try and assess the grain boundary behaviour in this work, since no quantitative analysis was performed. Wei's results also tend to outline the weak effect of grain boundaries as a trap. TDS was performed using many quenched and tempered martensitic samples, with tempering temperatures varied from 300 to 700°C. Their results show that at 700°C, above recovery temperature, there is a clear decrease in trapping. Between 300 and 650°C, there are competing effects of dislocation annihilation, recrystallization and recovery that are at play, and it is not simple to differentiate between them since no information is available on either the grain structure or the dislocation density.

Bernstein suggests a grain boundary-hydrogen interaction energy of 30 kJ mol^{-1}, although this is achieved through mechanical assessment [59]. Samples with varying grain sizes were subjected to a tensile stress with and without hydrogen, and by using the Hall-Petch relationship, described in equation (1.5), and literature values for grain boundary-carbon interactions, the interaction energy for grain boundary-hydrogen could be calculated.

$$\sigma_A = \sigma_O + Kd^{-1/2} \tag{1.5}$$

where σ_A is the applied stress, σ_O is the lattice frictional stress, K is the Hall-Petch slope and d the average grain diameter.

It is not entirely clear if this is reliable or can be applied in terms of trapping in non-
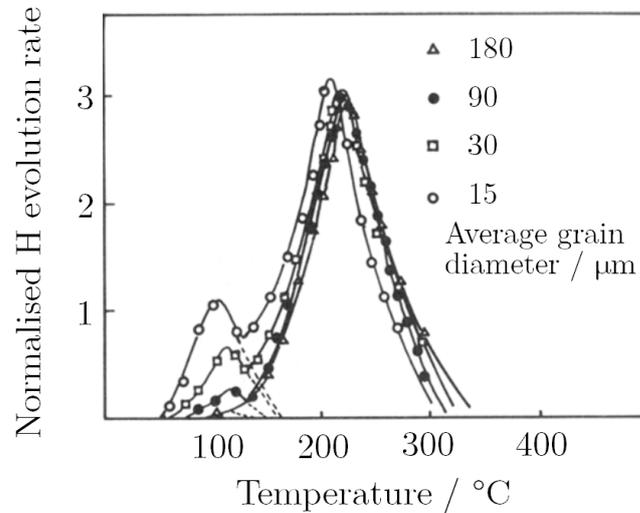
Fig. 1.8: TDS analysis of pure iron samples with varying grain sizes, as presented by Choo [57]. The peaks in the spectra correspond to hydrogen evolved from the sample, and can be fitted to determine a specific trap binding energy and trap density. In the current example, the peak at 100°C is due to the hydrogen trapped at grain boundaries being released and the peak at 210°C is due to hydrogen trapped at dislocations being released.

stressed samples since mechanisms that could dominate trapping under stress could be different without stress. In light of all those results, the binding energy for grain boundaries was considered to be within the range 10-30 kJ mol^{-1}.

Austenite phase

Turnbull proposed that in the case of duplex steels, the solubility and diffusivity of hydrogen in the austenite phase were not directly relevant to the observed diffusivity [50]. A duplex steel with composition 0.06C-21.6Cr-6.3Ni-2.51Mo-0.87-Si wt% was tempered and quenched in order to achieve different austenite contents. Five different values were investigated: 0%, 5%, 14%, 33% and 44% austenite. In such alloys, the austenite is visibly not percolating through the structure. Yet, Turnbull was able to see a decrease in the effective diffusivity from the sample with 44% and 0% austenite by a factor of 400. As a result, it was indicated that only the interface between the phases could be leading to such results, with binding energy calculated to be 52 ± 5 kJ mol^{-1}. As mentioned previously, the McNabb and Foster model was designed for single phase alloys, and therefore Turnbull had to add a factor to correct for it in the analysis. This is why little work has been reported in the literature on dual-phase alloys.

Park also reports large binding energy for the austenitic phase, although in this case, the hydrogen is only observed in TDS at temperatures above which the austenite decomposes, it is therefore not strictly speaking a trap binding energy that is estimated, it is simply hydrogen dissolved in austenite that becomes diffusible after the austenite decomposition [31].

TiC

Titanium carbides were the first carbides reported to have excellent trapping ability. Pressouyre estimated a binding energy of 95 kJ mol^{-1} by analysing the differences between first and subsequent permeation transients for three steels with Ti content 0.15, 0.63 and 1.5 wt% and with carburised surface to produce carbides [61]. The trap binding energy calculated was consistent in all three cases. Other defects like dislocations and grain boundaries that provide weaker traps were also taken into account in this work. Wei and Tsuzaki investigated the impact of size on the trapping ability of TiC, and noted that there was a significant increase in trapping as the carbide size increased from few nanometres to 100s nm in length. Due to the carbides being coherent with the matrix at very small scales, they deduced that the strain field of the carbide with the matrix would lead to trapping initially, and as the carbides grew larger and lost coherency, the carbide-matrix interface or carbon vacancy inside the carbide would lead to much stronger trapping [60]. The quantitative results in their work are based on Kissinger and are therefore inaccurate, but still consistent with Pressouyre. They calculate a trap binding energy of 70-115 kJ mol^{-1} for incoherent larger carbides, depending on tempering conditions. Kawakami simulated interactions from ab-initio calculations and calculated an interfacial energy of 48 kJ mol^{-1} when the matrix and precipitate are coherent, which is applicable for precipitate sizes approximately up to 8 nm in length [65], and 125 kJ mol^{-1} for carbon vacancies within the precipitate [55]. It is not common in such carbides to have a significant carbon vacancy population, and interfacial effects are expected to dominate. This was confirmed by Asaoka [67]. Interstitial sites in TiC were found to have an energy of -58 kJ mol^{-1} and being therefore very unfavourable sites for H to occupy.

V$_4$C$_3$

Kawakami also investigated the trapping behaviour of vanadium carbides based on first

principles. The interstitial site energy was calculated to be -106 kJ mol^{-1}, the coherent interface energy -6 kJ mol^{-1} and the carbon vacancy energy 116 kJ mol^{-1} [55]. This is of significant importance in this case, since V_4C_3 has a NaCl type structure, but in order to keep the stoichiometry of the phase correct, there has to be approximately 25% carbon vacancies. As a result, vanadium carbides are excellent for trapping. Similarly as for TiC, it was observed using atom probe tomography that for very small, coherent carbides, the trapping effect was negligible [25]. Both results are very consistent together. At larger scales, atom-probe studies showed very clear attraction of deuterium to the carbides. Atom probe showed that dislocation cores at the incoherent precipitate-matrix interface were significant for the overall trapping behaviour, as well as carbon vacancies within the carbides. Yokota also showed strong trapping using TDS; vanadium carbides peaks appeared between 500 and 600°C although the binding energies were not quantified in that study [68]. Asahi quantified the binding energies of V_4C_3 using permeation and TDS but using Kissinger and found trap binding energies of 33 and 44 kJ mol^{-1}. Additionally, the TDS was only performed until 400°C, although it has been seen that peaks from deep traps in such carbides can appear beyond 500°C so it is expected that much of the real nature of trapping for those carbides may not have been revealed during this study.

Fe$_3$C

Out of all the traps investigated here, the literature is most inconsistent with trapping due to cementite. A large number of binding energies have been reported, with values ranging from 11 to 66 kJ mol^{-1}. Kawakami calculated from first principles binding energies of 41 and 47 kJ mol^{-1} for the octahedral interstitial site in cementite, the largest and most likely to be occupied site, and the ferrite-cementite interface respectively [64]. The interface is once again assumed coherent for the purpose of the calculation so that value obtained might not be meaningful. Robertson's work here seems to be the most experimentally rigorous. Values of trap binding energies were found in a low alloy steel with 0.43 wt% C [37]. A pearlitic and a tempered martensitic structure were investigated through means of permeation, and interpreted with McNabb Foster. The binding energies were found to be 18 and 36 kJ mol^{-1}

in the pearlitic structure and in the tempered martensite respectively. Cementite appeared as coarse spheroidised precipitates in the tempered martensite as opposed to $1\,\mu m$ thick lamellae in pearlite. The difference between both values is not clear. This analysis was performed using only one type of trap, although it is probable that in such complex structures this is incorrect. Kim did a similar comparison between tempered martensite and pearlitic structures in a 0.82 wt% C alloy. In that case, TDS was used and results were quantified using Kissinger. They found binding energies of 18 and 66 kJ mol^{-1} for the cementite precipitated in martensite and pearlite respectively [33], which is inconsistent with the results presented by Robertson, in which case the cementite binding energy in pearlite is lower than in tempered martensite. The cementite lamellae in the work presented by Kim were about 20 nm thick. One possible explanation for such a difference might be related to the very high number of interfaces between cementite and ferrite, and to the tortuosity of the structure, which would affect the diffusion of hydrogen, and be perceived as a higher trap binding energy than it actually is. Hong reported that the binding energy for the cementite-ferrite interface in a 0.49 wt% C pearlitic structure was 11 kJ mol^{-1} [62]. This value was found by assuming that the number of cementite and ferrite interfaces in a 0.12 wt% C and a 0.49 wt% C alloy was identical, which has to be rejected since it is visible from micrographs of those alloys, that this is very inaccurate. Finally, Takai reported that cementite precipitated within bainitic ferrite laths had trapping energy of 23 kJ mol^{-1}, using Kissinger to interpret TDS data [63]. When identical samples were cold worked up to 85% reduction in area and re-heated to 200°C to remove the dislocation contribution to trapping, a 65 kJ mol^{-1} trapping site at the interface between ferrite and cementite was observed. The trend observed is interesting as it should indicate that the cementite ferrite interface can indeed provide significant trapping, although it is not clear why that should not be the case when the cementite is present within the ferrite. Part of the problem relates to the inability, using Kissinger, to differentiate the impact of trap sites density and trap binding energy, which could have a significant impact in structures with very high amount of cementite-ferrite interfaces, as this leads to a significant increase in trap density.

Epsilon carbide (Fe$_{2.4}$C, transition iron carbide)

Other transition iron carbides, such as epsilon carbide, have been suggested as potential carbides for trapping hydrogen. Very little quantitative work has been performed for those carbides. Zhu noted that in a Fe–0.22C–1.40Si–1.80Mn wt% alloy, epsilon carbide contribution to trapping was seen as a TDS peak around 400°C, as seen in Fig. 1.9 [29]. The trap binding energy wasn't quantified, but the total trapping capacity was quite low, probably due to the low carbon content. The total quantity of trapped hydrogen seems almost insignificant, as can be seen by their mechanical results: samples charged with hydrogen for 1 minute showed an improvement in the total elongation to failure compared to samples without epsilon-carbide charged, but for any longer charging time, both samples behaved similarly. All epsilon carbide traps could be saturated in that time. Zhu also showed the potential efficacy of epsilon-carbide in trapping hydrogen using atom probe measurements [29]. Altogether, the lack of consistency and reproducible quantitative analyses for iron carbides means there is potential for further investigation. Furthermore, formation of iron carbides have the advantage of only relying on the diffusion of carbon, and silicon for cementite, and can therefore precipitate at much lower temperatures than other carbides.
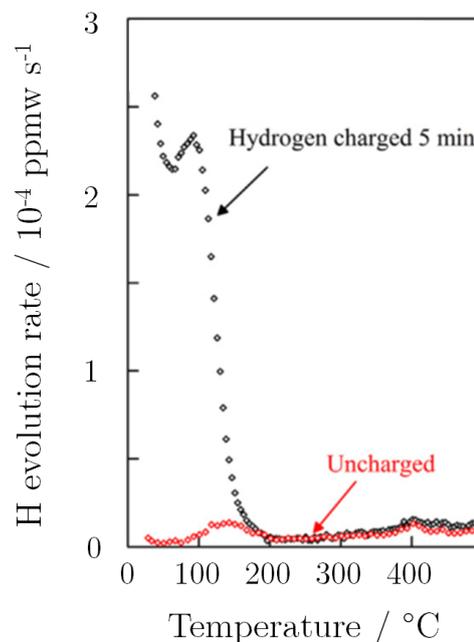
Fig. 1.9: TDS spectra showing a peak at 400°C, attributed to epsilon carbides [29].

Consequences for industrial applications

Creating a base fundamental knowledge of trap binding energies is important but is not directly useful to engineering applications. A quantitative understanding of the effect of trap binding energy and number density on the retardation of hydrogen embrittlement in such alloys in the operating conditions is needed. Two factors limiting this understanding have been identified:

1. Knowledge of hydrogen generation rate and equilibrium concentration of hydrogen at the subsurface of the alloy in use is required in order to predict the rate of ingress of hydrogen in the alloy. The lack of accessible data renders those characteristics extremely hard to investigate.

2. The extent to which the traps can be allowed to be filled before the equilibrium between trapped and diffusible hydrogen can cause embrittlement is unclear. In many experimental assessment of traps, hydrogen is inserted into alloys with concentrations much beyond any realistic case, and show failure mechanisms without assessing the real advantage offered by the traps.

Knowledge of such data would allow a prediction of the additional expected lifetime alloys would gain by possessing traps.

1.4 Hydrogen-resistant structural alloys used in hydrogen sulphide environments

1.4.1 Introduction

This section introduces the typical types of alloys used in industry, to help identify the challenges faced by such alloys in H_2S-containing environments, called sour environments, which are typical in the petroleum industry [69]. It was suggested that bainitic ferrite, although never investigated, could be a potential successful alternative to the currently used alloys.

There have been two major approaches used in order to mitigate the corrosion problems in sour environments. On one hand, corrosion-resistant alloys have been developed, although with limited yield and ultimate tensile strength. Additionally, those alloys are expensive due to the use of large concentrations of nickel and chromium. In contrast, high-strength low alloy steels have also been developed. They are a lot cheaper since they possess fewer alloying elements, and can reach higher strengths, providing careful heat treatment is performed. However, they lack inherent corrosion resistance, it is therefore necessary to use corrosion inhibitors, or use coatings to prevent corrosion. In order to assess the impact of H_2S on hydrogen embrittlement, "sour service" domain maps, which categorise the severity of an environment based on pH and partial pressure of H_2S, are used. Fig. 1.10 is an example of such a map [70]. All circles represent in-situ four-point bend tests, with black circles indicating failure and white ones that no fracture occurred. All tests need to be run according to the NACE TM0316-2016 standard in order to obtain consistent sour domain maps [71]. The corrosion mechanism in such environments is called sulphide stress cracking (SSC) and is a form of hydrogen embrittlement that occurs below the yield strength of the material. In this case, the alloy tested, P-110, can be used safely, for conditions that would be located in the top left corner of the domain map. The partial pressure of H_2S is a critical factor when determining the suitability of an alloy to be used in the field. Not only it generates H^+, that can penetrate and embrittle the alloys, but it is also a poison that prevents H^+ recombination

into H_2, which cannot penetrate into alloy microstructures. The pH is a less important factor, because buffers such as $COOH/COO^-$ can be used to stabilise it [72]. There is no consistent way of anticipating how the materials behave at varying partial pressures of H_2S and varying pH, and every single alloy designed has to pass tests in all the different domains to have an idea of their suitability for use in the field.

1.4.2   Corrosion resistant alloys

Four main types of microstructures have been investigated. Two of those are nickel-based alloys, while two others are stainless steels. The compositions of those alloys have been summarised in Table 1.5. For the Ni-based alloys, the matrix phase has a yield strength of approximately 450 MPa and is strengthened through either cold-working or precipitate hardening. In the latter case, the addition of Ti, Al and Nb has been proven to form Ni_3M precipitates, where M is any of those solutes, that dramatically improve the mechanical properties, and can also be beneficial for mitigating hydrogen embrittlement as long as their morphology and homogeneity in size and dispersion in the parent matrix is controlled accordingly [70]. For instance, if the heat treatment performed or the composition leads to a nucleation of those precipitates at the grain boundary, it has been observed that they become preferential sites for crack initiation due to their brittle nature. Subsequently, intergranular cracking is observed [73].

For the stainless steels, the structure can either be duplex, with reported optimal mechanical performance when the alloys contain close to 50% of each of the ferritic and austenitic phase,

Table 1.5: Compositions in wt% of four common structural corrosion-resistant alloys used in H_2S environments [70].

Alloy	C	Fe	Cr	Ni	Mo	Nb
Cold-worked Ni-based C-276	0.01	6	16	56	16	-
Precipitation-hardened Ni-based 718	0.02	19	19	52	3	5
Duplex stainless steel 22 Cr	0.02	Bal.	22	5.5	3	-
Martensitic stainless steel AISI 410	0.15	Bal.	13	-	-	-
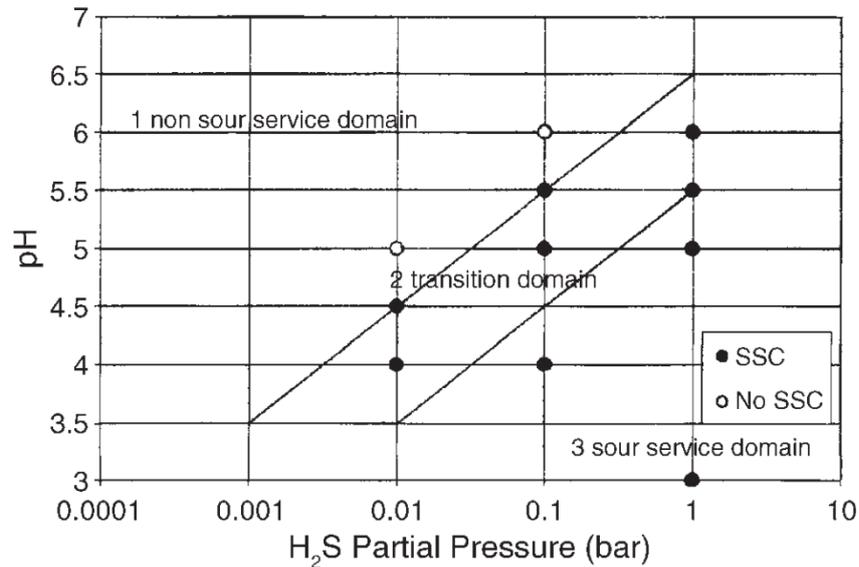
Fig. 1.10: Example of a sour domain map, for low alloy steel P-110. Each circle represents an in-situ four-point bend test. White circles indicate the samples passed the test, black ones indicate failure during the test. Failure occurs through a hydrogen embrittlement mechanism that is referred to as sulphide-stress cracking [70].

or tempered martensitic. The austenitic phase in both cases has been reported to provide a significant sink for hydrogen because of its very high solubility in that phase. For martensitic steels, the addition of nickel is used to stabilise the austenite fraction above 0.1, with accompanying increase in the sulphide stress corrosion resistance of those alloys [74, 75]. It is believed that above that threshold, the austenite percolates the structure, and forms a definitive barrier to hydrogen penetration in the steel, as well as providing trapping sites [76]. Chromium in alloys with carbon contents higher than 0.05 wt% promotes the formation of many different carbides at the grain boundaries, including bulky $M_{23}C_6$ carbides, in which M represents metal atoms such as Cr, Fe or other alloying elements. The formation of large carbides lowers the Cr content in neighbouring regions, thus preventing passivation [77]. A way to mitigate this effect is the addition of Ti or Nb, which are strong carbide formers and produce small homogeneously dispersed TiC and NbC, and prevent the formation of $M_{23}C_6$. This applies particularly to welded steels, in which the heat-affected zone is most sensitive to this process, but also to quenched and tempered martensitic steels, which is why their carbon contents are always kept very low. Forming such carbides is therefore not of concern in the current project.

The most important challenge for those alloys is localised corrosion such as crevice corrosion or pitting, which can occur after mechanical erosion of the surface of those alloys. It is important to ensure that such alloys are able to achieve repassivation before corrosion can take place. In all four types of alloys, Mo increases the breakdown potential, E_{pit}, shown in Fig. 1.11, almost linearly with concentration [78]. The higher the breakdown potential, the more resistant to pitting the alloy is, so alloy selection can be determined by the Mo content depending on the pitting risk in a specific environment.

Use of effective diffusivity

In this field, the measurement of effective diffusivity of hydrogen D_{Eff} is used as a practical and simple approach to estimate the potential of an alloy for hydrogen embrittlement resistance. It is suggested that alloys with faster hydrogen effective diffusivity tend to be more susceptible to embrittlement [70]. Measurement can be performed through simple permeation experiments. It does not assess trapping as described in the previous section, and therefore can only be indicative, as emphasised by Turnbull [79]. It nevertheless is used because it is simple to measure, and other standardised specialised mechanical in-situ tests are required in order to explore the sour domains maps. The typical effective diffusivities reported for the four alloys presented in Table 1.5 are displayed in Table 1.6 [70]. They highlight the much faster diffusivity of hydrogen in martensitic alloys compared to austenitic alloys. The diffusivity of three low-alloy steels are also presented, in Fig. 1.12, for comparative purposes. Their compositions are described in Section 1.4.3 [43].

Table 1.6: Values of effective diffusivity of four common structural corrosion-resistant alloys used in H_2S environments [70].

Alloy	D_{Eff} / m^2 s^{-1}
Cold-worked Ni-based C-276	2×10^{-15}
Precipitation-hardened Ni-based 718	4×10^{-15}
Duplex stainless steel 22Cr	3×10^{-15}
Martensitic stainless steel AISI 410	1×10^{-11}
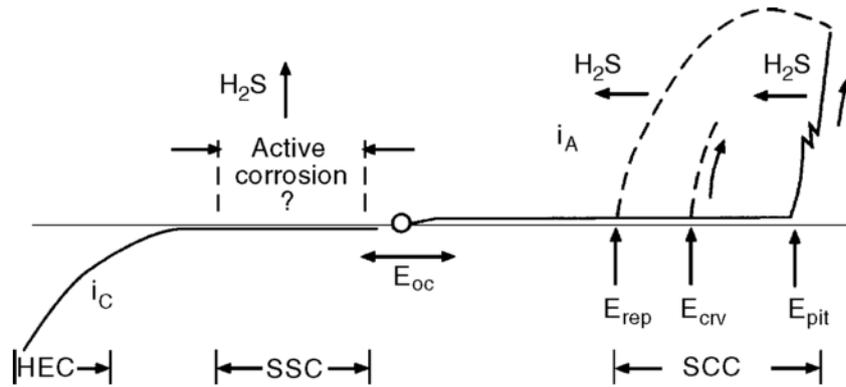
Fig. 1.11: Example of a polarization curve of corrosion-resistant alloys in solution containing Cl^- and H_2S. This curve shows the change in current density i with applied voltage E. Samples are passivated when the current density is constant. Active corrosion takes place when it increases. HEC, SSC and SCC stand for hydrogen embrittlement, sulphide stress and stress corrosion cracking respectively, and are all failure mechanisms due to hydrogen embrittlement [72].
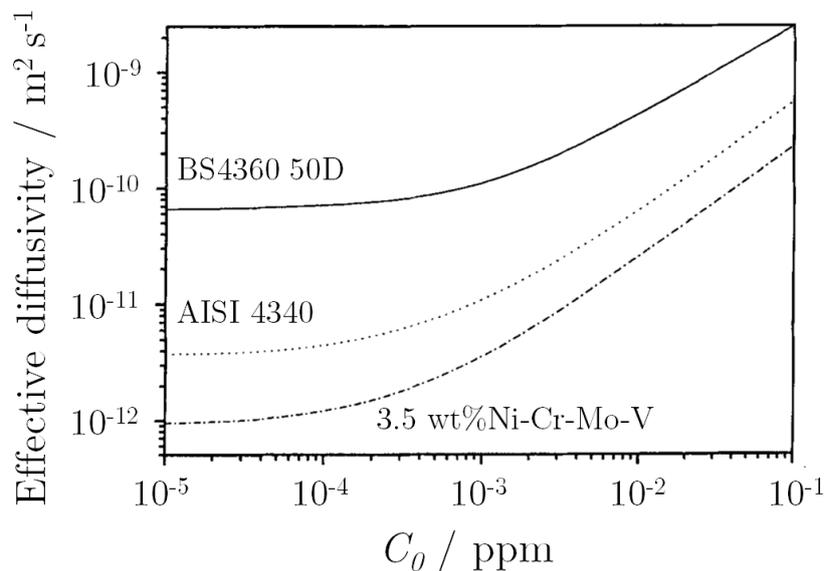
Fig. 1.12: Effect of the hydrogen concentration sub-surface C_0 on the effective diffusivity in three low alloy steels. The values of diffusivity in such alloys are several orders of magnitude lower than in corrosion-resistant alloys with austenitic structures, such as Ni-based or duplex stainless steels [43].

1.4.3 Low-alloy steels

The compositions of the most commonly used and highest-strength low-alloy steels have been summarised in Table 1.7. All low-alloy steels have the similar quenched and tempered martensitic microstructure. As a result, many of the problems observed in martensitic stainless steels also apply here. Asahi reported that the carbon weight percent should be kept between 0.15 and 0.3 wt% to ensure good hardenability but prevent cracking during the initial quenching [80]. Lower carbon contents would not have good enough hardenability and higher carbon contents would be prone to cracking. Boron can also be added in small quantities up to 20 ppm to improve hardenability. It is reported that 10ppm B has a similar hardenability effect as 1 wt% Mn [80]. It segregates at austenite grain boundaries but this has not proved detrimental to the mechanical properties because of the very low weight fraction present. The relation between alloy microstructures and susceptibility to sulphide stress cracking (SSC) are well established. It is seen that the most common factor for SSC failure in low-alloy steels is the formation of carbides at the prior austenite grain boundaries during the tempering step, as described by Eschaniz or Watkins [81, 82]. These brittle precipitates favour crack propagation along the grain boundaries, seen as intergranular fractures observed by Asahi and Omura [80, 83]. Samples with higher Mn content than 1.5 wt% tend to have less homogeneous compositions at the grain boundary and seen to have a diminished resistance to SSC. Craig observed embrittlement from impurity P at the grain boundary and demonstrated the efficacy of using Mo to combat it [84]. The addition of Mo was observed to improve the resistance to SSC by reducing the mobility of diffusing substitutional atoms to the grain boundaries and therefore limiting the local carbide nucleation or growth. The same behaviour was revealed by Omura using vanadium [85]. In this case, the chromium content had to be lowered to 0.5 wt% to prevent the formation of $M_{23}C_6$ brittle carbides. It was shown that the addition of vanadium led to much more homogeneous dispersion of carbides, and no preferential nucleation at the grain boundary. Torii also indicates, in the specific cases of alloy L80 and C80, the possibility of adding Ti and Nb to form TiC and NbC carbides, described in the previous chapter [86]. The use of such carbides can be applied to other

alloys. The results are consistent with previously mentioned trapping ability of such carbides, and the SSC resistance is improved significantly as Ti and Nb are added to alloys and small homogeneously dispersed carbides are nucleated.

Table 1.7 shows compositions very close to one another, indicating a mature field in which compositional changes leading to improved mechanical properties are difficult to realise. Consequently this Ph.D. project aimed at developing a new type of low alloy steel with a unique novel bainitic structure in order to improve significantly those mechanical properties, without hindering the SSC resistance. Using a bainitic structure permits using carbon concentration is excess of 0.3 wt%, because bainite is not susceptible to cracking during cooling. Consequently, higher strength can be achieved easily in bainitic alloys compared to martensitic ones [87].

The most critical challenge for low alloy steels is the formation of hydrogen through reduction of the hydrogen ions present in the acidic solution at the surface of the steel and the subsequent ingress of atomic hydrogen in the alloys, that leads to hydrogen embrittlement. It is therefore necessary to try and limit hydrogen ingress in the structure and attempt to trap hydrogen at specific site to lessen the damaging effect of diffusible hydrogen.

Table 1.7: Compositions in wt% of common structural low alloy steels used in H_2S environments, with Fe balance. For alloys named by a combination of a letter and a number, the latter indicates the yield strength of the material in ksi (80 ksi is 550 MPa and 125 ksi is 860 MPa).

Alloy	C	Si	Mn	Cr	Ni	Mo	Reference
BS 4360 50D	0.17	0.35	1.35	0.10	0.10	-	[88]
Ni-Cr-Mo-V	0.25	-	-	1.70	3.70	0.40	[89]
AISI 4340	0.42	0.28	0.70	0.79	1.83	0.24	[41]
L-80	0.1-0.4	0.1-0.4	0.75-1.5	-	-	0.1-0.4	[90]
P-110	0.24	0.26	1.44	0.82	-	0.10	[91]
C-110	0.32	0.23	0.46	1.00	-	0.85	[92]
C-125	0.27	0.29	0.49	0.52	-	0.69	Private
Q-125	0.20	0.24	1.58	1.03	-	-	[72]

1.4.4   Bainite as an alternative to tempered martensite in low-alloy steels

Bainitic steels have never been used in this field because the strength of the alloys selected originally was satisfactory. Additionally, alloys are only selected for use after in-depth investigation of their properties and observed successful performance of similar alloys in the field over many years. As the maturity of the quenched and tempered steels is preventing any significant improvement in mechanical properties, it is important to consider alternatives. Bainite is a common phase in steel, and was not be reviewed, since a very comprehensive and detailed book concerning bainite in steels has been written by Bhadeshia, and can be consulted [93]. Bainitic steels have three major advantages over martensitic steels:

1. They are produced by air-cooling, or by isothermal holding during cooling. In other words, there is no necessary tempering step that adds to the manufacturing cost and also lowers the maximum strength achievable by coarsening the microstructure.

2. Bainitic transformation allows diffusion of carbon, unlike the martensitic transformation. It follows that the bainitic ferrite becomes depleted of carbon. Subsequently, the neighbouring austenite becomes enriched in carbon and stabilised by it. Ultimately, when the bainitic reaction stops, retained austenite with high carbon content is present in the final structure. This means the bainitic phase is not only less brittle than the martensitic phase due to lower residual stress from carbon, but the presence of thin retained austenite regions provide toughness to the whole structure. In this case, the transformation-induced plasticity (TRIP) effect is at play; under loading, the austenite phase can transform to martensite to relive the stress.

3. Carbides can be nucleated within the bainitic ferrite laths during the isothermal or air cooling treatment and can provide trapping without compromising the structural integrity of the steel, since they do not nucleate preferentially at grain boundaries.

Gomez designed, produced and characterised in 2009 the first carbide-free bainitic steel with similar mechanical properties as low-alloy steels used in sour environments, which could be manufactured by air-cooling. Its composition is displayed in Table 1.8 [94]. This alloy was

not designed to be corrosion-resistant, but to prove the concept of a simpler manufacturing method. The purpose of each of the alloying elements is as follows:

- Carbon – It determines the martensite and bainite start temperatures as well as the scale of the structure, hence the strength of the alloy. Higher carbon contents allow the martensite start temperature to be suppressed to lower temperatures, which in turn allow finer microstructure.

- Silicon – The purpose of silicon is to prevent the brittle cementite phase formation. Silicon solubility in cementite being extremely low, it has to diffuse away from carbides for cementite to be able to form. In continuous cooling, the temperatures are too low for silicon to diffuse enough to allow cementite formation.

- Manganese – The Mn content is kept as low as possible because it is known to segregate within the bainitic structure upon cooling. As a result, Mn-rich regions tend to retard the bainitic transformation and can lead to martensite formation during continuous cooling.

- Chromium – The chromium content is kept low in order to have more control over the retained austenite fraction depending on cooling rate.

- Nickel – Nickel improves the hardenability of the steel. It also contributes to an improvement of the toughness of the ferritic phase.

- Molybdenum – As reported before, the main role of Mo is to prevent the grain boundary embrittlement caused by the presence of impurity P.

Table 1.8: Composition of the bainitic steel designed by Gomez [94].

Fe	C	Si	Mn	Cr	Ni	Mo
Bal.	0.30	1.40	0.10	1.00	3.60	0.25

1.5 Carbide structure and growth in bainite

1.5.1 Introduction

After having revealed the opportunity provided by developing a bainitic structure as opposed to a martensitic structure, and after having identified the possible benefits of forming iron carbides and cementite at a small scale and within the bainite laths, this section of the literature review ties both ends together by investigating the thermodynamics and kinetics of iron carbide precipitation in bainite.

Transition metal carbides like TiC or V_4C_3 have the best hydrogen trapping ability and have been used in the design of hydrogen resistant quenched and tempered steels. Their precipitation can be precisely controlled because they form at temperatures of approximately $600°C$, and rely on the diffusion of the substitutional metal atoms. This way, annealing heat treatments can be used to achieve a well defined dispersity and size of precipitates [95]. In this project, high temperature treatment is not an option, and carbides have to be formed during the isothermal holding step or during continuous cooling. The literature was investigated in order to identify relevant compositions and transformation temperatures to obtain a bainitic structure with carbides present in it.

Advantage of lower bainite over upper bainite

The structure of bainite is differentiated between upper and lower bainite [93]. The structure obtained depends on the composition, and most importantly factors that affect the bainite start and martensite start temperatures, such as carbon composition. The main structural difference between those two structures is that in upper bainite, which forms at higher temperatures, the carbon present in the ferrite phase can diffuse out into the austenite faster than it is able to form carbides within the ferrite laths. As a result, upper bainitic structures have carbon-rich austenite that offers many heterogeneous nucleation sites for cementite along the interface between austenite and ferrite. Consequently, cementite is observed to grow as films along those boundaries and is very detrimental to the toughness. Conversely, in lower bainite, the

mechanisms of carbon diffusion out of the ferrite and the carbide formations are occurring simultaneously, because of the lower carbon mobility at lower temperature. Carbides are therefore generated within the ferrite, tend to be much finer and have not been reported to impact the toughness or strength of the alloys [93].

Carbides in lower bainite tend to have complicated structures because of the lack of iron mobility and the need to observe specific orientation relationships. Thus, many different carbide phases have been observed in lower bainite, as summarised by Bhadeshia, and shown in Table 1.9 [93]. This review focuses on the two most commonly observed phases, epsilon carbide, a metastable transition carbide and cementite, the most stable carbide in steels. Eta, c and chi carbides were all observed in high-silicon steels (approximately 2 wt%) as transition phases before the more stable cementite, but their presence has not been consistently observed in bainitic steels [96, 97]. Kappa carbide has been observed to form in a few high-carbon steels from the austenitic phase before transforming to cementite [93].

1.5.2   Carbide structures

Epsilon carbide has an hexagonal close-packed structure, with the carbon atom occupying some of the octahedral interstitial sites. There are the same number of octahedral interstices and lattice sites in hexagonal lattices and as a result at least half of those sites should be empty so that the observed stoichiometry of the carbide, which varies between Fe_2C and Fe_3C, can be achieved [98]. Fig. 1.13 is a schematic representation of this structure, in which the small spheres are iron atoms and the larger spheres carbon atoms. The dotted spheres represent sites that can be occupied by carbon atoms in order to reach the correct stoichiometry. It was suggested by Nagakura that the carbide has a $P6_322$ space group, and carbon atoms can therefore be speculatively placed in the structure according to the symmetry elements required by that space group [99]. Cementite has an orthorhombic crystal structure in which the iron atoms are almost close-packed, and where the carbon atoms have been observed to be coordinated by the six neighbouring iron atoms with a triangular prism geometry [98]. It has been confirmed to have the Pnma space group using both X-ray and neutron diffraction of

Table 1.9: Summary of all iron carbides observed and characterised in lower bainitic structures [93].

Carbide	Crystal System	Fe, M/C	Reference
κ	Hexagonal $a = 6.9\ c = 4.8$ Å	1.37	Deliry (1965) Pomey (1966)
ϵ	Hexagonal $a = 2.735\ c - 4.339$ Å	2.4–3	Jack (1950, 1951) Hofer *et al.* (1949)
χ	Monoclinic $a = 11.563\ b = 3.573$ Å $c = 5.058\ \beta = 97.44°$	2.2 or 2.5	Hägg (1934)
η	Orthorhombic $a = 4704\ b = 4.318$ Å $c = 2.830$	2	Hirotsu and Nagakura (1972)
Fe_3C	Orthorthombic $a = 4.525\ b = 5.087$ Å $c = 6.743$	3.0	
M_7C_3	Orthorhombic $a = 4.526\ b = 7.010$ Å $c = 12.142$	7/3	Morniroli *et al.* (1983)
$(Fe, Si)C_X$	Orthorhombic $a = 8.8\ b = 9.0\ c = 14.4$ Å		Konoval *et al.* (1959)
$(Fe, Si)C_X$	Orthorhombic $a = 6.5\ b = 7.7\ c = 10.4$ Å		Schissler *et al.* (1975)
$(Fe, Si, Mn)C_X$	Orthorhombic $a = 14.8\ b = 11.4\ c = 8.5$ Å		Schissler *et al.* (1975)
$M_{23}C_6$	Cubic F $a = 10.621$ Å	23/6	
M_6C	Cubic F $a = 11.082$ Å	6	
c	Triclinic $a = 6.38\ b = 5.05\ c = 4.59$ Å $a = 90.0°\ \beta = 70.1°\ \gamma = 84.7°$		Sandvik (1982b)

pure single crystals. Fig. 1.15 and 1.16 show the cementite structure schematically looking at the b and c directions. The smaller ellipsoids are iron atoms and the larger ones carbon atoms. The 6-coordination of carbon atoms as a triangular prism is possible to visualise looking down the b axis.

Carbide lattice parameters have been observed to vary from those ideal cases when precipitated in steels for two main reasons, described by Yakel [98]:

1. The crystal sizes are extremely small, of the order of a few nm to a few 100 nm, and need to accommodate the strains at the interface with the matrix, thus increasing or decreasing the lattice parameter in the structure depending on the orientation relationship.

2. Other transition metals present in the steel can be substitutional metal atoms in the carbides and because of the change in the metallic bond length the overall lattice parameters of the carbides are modified.

Ferrite-carbide orientation relationships

It has been observed that carbides in a single lower bainitic lath form in a unique crystal orientation [93]. It has been reported to be approximately 60 degrees away from the bainite growth direction, and differs from martensite, in which many orientations of the carbides are visible within a single bainite lath. Those orientation relationships between the parent and carbide phases have been studied extensively, and can be used to identify with certainty the nature of the carbides observed experimentally. The following orientation relationship has been characterised by Jack between epsilon carbide and ferrite [101]:

$$(101)_\alpha \parallel (10\bar{1}1)_\varepsilon$$
$$(2\bar{1}1)_\alpha \parallel (10\bar{1}0)_\varepsilon$$
$$(011)_\alpha \parallel (0001)_\varepsilon$$
$$(\bar{1}\bar{1}1)_\alpha \parallel (1\bar{2}10)_\varepsilon$$
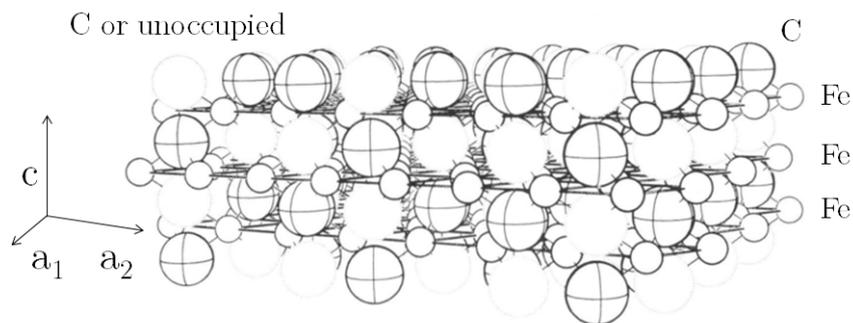
Fig. 1.13: Structure of epsilon carbide. The larger spheres are carbon atoms and the smaller ones are iron atoms. The dotted spheres can be occupied by carbon or vacant depending on the specific stoichiometry [98].
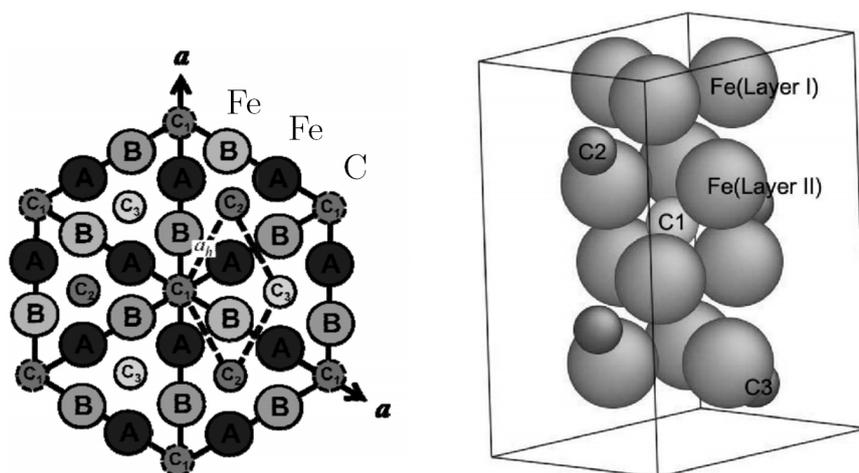
Fig. 1.14: Projected representation of the structure of epsilon carbide. The larger spheres are iron atoms and the smaller ones are carbon atoms [100].
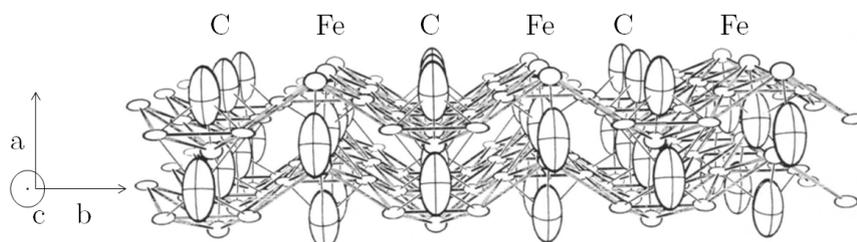
Fig. 1.15: Structure of cementite. Large ellipsoids are carbon atoms and the smaller ones are iron atoms [98].
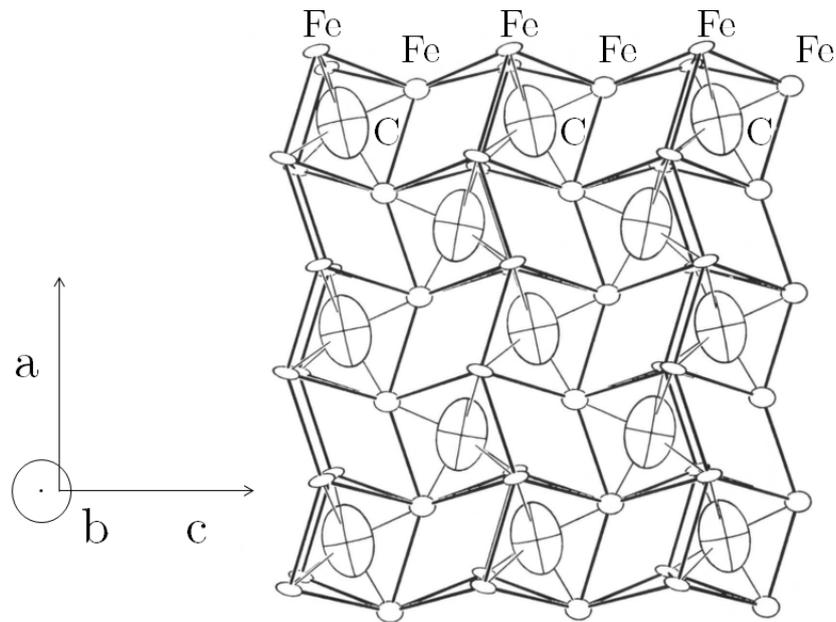
Fig. 1.16: Structure of cementite, with the b axis pointing towards the viewer. Large ellipsoids are carbon atoms and the smaller ones are iron atoms. This is a more conventional way of representing cementite, but does not allow an easy comparison with the structure of epsilon carbide [98].

Between ferrite and cementite, several orientation relationships have been characterised in tempered martensite [93]:

$$\{211\}_\alpha \parallel \{001\}_\theta$$
$$< 0\bar{1}1 >_\alpha \parallel < 100 >_\theta$$

$$\{\bar{2}\bar{1}5\}_\alpha \parallel \{001\}_\theta$$
$$< 3\bar{1}1 >_\alpha \text{ within } 2.6° \text{ of } < 100 >_\theta$$
$$< 131 >_\alpha \text{ within } 2.6° \text{ of } < 010 >_\theta$$

The Isaichev orientation relationship was the main relationship reported in bainite [102]:

$$\{101\}_\alpha \parallel \{103\}_\theta$$
$$< 1\bar{1}\bar{1} >_\alpha \parallel < 010 >_\theta$$

Fig. 1.17 shows those results as a stereogram [103]. Those relations are observed consistently because they induce the lowest energy state possible for the carbide/ferrite interface, and are summarised from several sources [101, 103–105].

Fig. 1.17: Orientation relationships between ε-carbide, cementite and ferrite seen as a stereographic projection [103].

Carbide morphology for hydrogen trapping

As mentioned in Section 1.3, carbon vacancies in carbides are excellent trap locations. Their presence in cementite and epsilon-carbide was investigated. Non-stoichiometric cementite has indeed been reported many times in the literature, but it is always focusing on pearlitic structures [106]. Since cementite in eutectoid pearlitic steels occupies a significant volume in the structure many experiments assessing the modification of the stoichiometry of the cementite phase through mechanical deformation have been reported. Reports show that the cementite stoichiometry can even be reduced in the most extreme cases from 25 at% to 16 at% [107]. Other methods of introducing carbon vacancies in cementite include very fast cooling. It is demonstrated that annealing above 200°C causes the cementite to return to a stoichiometric chemical composition [108]. As a result, those processes are not realisable in the bainitic structure designed here, where long isothermal holds at higher temperatures are needed as part of the manufacturing process.

For the case of epsilon carbide transforming into cementite, as the particles become semi-coherent, a steady-state of vacancy supersaturation is generated at the interface due to the addition of low-angle boundaries to accommodate the increasing lattice strain between the precipitate and the matrix [109]. It would therefore be ideal to obtain a structure that possesses both epsilon carbides and cementite, with as many semi-coherent carbides as possible. Craig suggests that this phase change should be avoided to optimise trapping, claiming that, when coherency is lost, the strain field attraction of hydrogen to the trap is lost too. This is true but using the interface strain fields for trapping would imply the carbides would only be weak reversible traps, no stronger than dislocations. In this project, a stronger trapping ability is sought out for those carbides, and therefore the coherency loss should be required, and be compensated by a homogeneous dispersity of the carbides within the bainite laths.

Additionally, it has been reported once in the literature, from a source not published in a peer-reviewed journal, and not accessible apart from the secondary reference from Craig [109], that hydrogen forms the compound Fe_2HC in epsilon carbide, suggesting epsilon carbides may be strong traps, although this has not been confirmed anywhere else.

Epsilon carbide alone forms until about 200°C in steels with C content above 0.2 wt% and it is seen to transform to cementite at temperatures up to 400°C, depending on silicon content [109]. The cementite initially grows as needles, and gradually becomes incoherent with the matrix as it grows. When temperatures reach above 400°C, the cementite is seen to coarsen and spheroidise, meaning the number density of carbides and the interfacial area between ferrite and the carbides decrease dramatically [37]. This is exactly the opposite of what should be done to optimise trapping. As a result, the isothermal holding steps were not performed above 350°C in the large scale alloys.

1.5.3   Carbide growth in bainite

Steel compositions for ε-carbide formation

Numerous reports of ε-carbide formation in lower bainite have been summarised by Bhadeshia and are shown in table 1.10 [93]. This should provide an idea of the composition a new alloy should aim to approach, in order to ensure formation of the desired phases. Most of these alloys are high-carbon steels, which are not suitable for the application in this thesis. The only two compositions of interest here are from Lai and Miihkinen, with carbon weight percent of 0.4 wt% [110, 111]. It has been suggested that at such low carbon contents, carbon should be able to partition in the austenite faster than the carbides can form, and this has been proven true for a lot of cases. The presence of nickel is the reason why carbides are observed regardless in those alloys. Nickel is a rather weak carbide former but reports have nevertheless shown that epsilon can be formed in tempered martensitic structures with carbon contents as low as 0.27 wt%, but with 5 wt% Ni [112].

Effect of Si

In order to control the epsilon carbide to cementite phase change, the use of silicon is key. Indeed, Silicon is soluble in epsilon carbide, but extremely insoluble in cementite, consequently, it needs to diffuse out of the originally formed epsilon carbides in order for the cementite to be able to grow. At the low temperatures investigated, the diffusion of silicon is extremely low and the overall effect is a significant reduction in the driving force for cementite growth. At high weight percent such as 2% and above, it is usually the case that either no carbide forms at all, or that only epsilon carbide can be formed. Sandvik indicated that epsilon carbide only was formed during transformation of a 0.74C-2.4Si wt% at 380°C for 30 min or at 320°C for 3 h to 5 days [113]. Matas observed similar results in a steel with composition 0.6C-2Si wt% transformed at 260°C or 315°C for up to 50 hours [114]. Yet, Bhadeshia and Edmonds presented contradictory results [115]. In fact an alloy with composition 0.43C-3Mn-2.12Si wt% only contained cementite after transforming at 250°C or even for a few minutes at 300°C. A possible explanation for this unexpected behaviour is

Table 1.10: Compositions in wt% of steels in which epsilon carbide has been observed and characterised, with Fe balance [93].

C	Si	Mn	Ni	Cr	Mo	V	Reference
0.87	–	–	–	–	–	–	Austin and Schwartz, 1952, 1955
0.95	0.22	0.60	3.27	1.23	0.13	–	Matas and Hehemann, 1961
0.60	2.00	0.86	–	0.31	–	–	Matas and Hehemann, 1961
1.00	0.36	–	0.20	1.41	–	–	Matas and Hehemann, 1961
0.58	0.35	0.78	–	3.90	0.45	0.90	Matas and Hehemann, 1961
1.00	2.15	0.36	–	–	–	–	Deliry, 1965
0.60	2.00	0.86	–	0.31	–	–	Oblak and Hehemann, 1967
0.60	2.00	–	–	–	–	–	Hehemann, 1970
0.41	1.59	0.79	1.85	0.75	0.43	0.08	Lai, 1975
0.54	1.87	0.79	–	0.30	–	–	Huang and Thomas, 1977
0.85	2.55	0.3	–	–	–	–	Dorazil and Svejcar, 1979
0.74	2.40	0.51	–	0.52	–	–	Sandvik, 1982a
1.3	3.09	0.17	–	–	–	–	Dubensky and Rundman, 1985
0.40	2.01	–	4.15	–	–	–	Miihkinen and Edmonds, 1987a

the high weight fraction of Mn, which is a strong cementite former [116]. In order to ensure the possible formation of cementite, the silicon content needs to be kept below 2 wt%.

Kinetics of reaction

Despite the large amount of work in the literature, the kinetics of carbide precipitation in bainite are still impossible to predict [98]. This is because the phase changes do not occur at equilibrium, and are extremely dependant on alloy composition, and transformation temperature and time. Another factor affecting this is the dislocation density. It has been proven that carbon segregates at dislocation cores in bainitic ferrite, and therefore, carbide precipitation can effectively be hindered given the dislocation density is high enough and the carbon content low enough. This effect does not seem to be taking place in alloys with carbon content above 0.2 wt%, but it might be occurring locally [106].

1.6   Conclusions

The review of the literature first summarised the phenomenon of hydrogen embrittlement in steels. It then identified the opportunity for bainitic steels to be used as an alternative to martensitic low-alloy steels for structural applications where hydrogen embrittlement is a problem. The bainitic alloys would be cheaper to manufacture, and could easily outperform the martensitic alloys in terms of ductility and strength. They would also possess a fraction of austenitic phase that could be used as a barrier to hydrogen ingress. The inconsistencies of the reported cementite binding energy indicated the need for rigorous investigation, which was pursued in order to assess whether cementite could be used within bainitic ferrite as a hydrogen trap. The review demonstrated that the thermal desorption spectroscopy technique interpreted quantitatively using the model developed by Song was the most accurate way to identify the cementite binding energy precisely.

Chapter 2

Alloy design

2.1 Introduction

Having identified the opportunity for the use of bainitic steels in applications where hydrogen embrittlement is a problem, the process of alloy design is described in this chapter. First, a list of mechanical properties outperforming the current strongest hydrogen-resistant structural alloys used in sour environments is established. Several modelling methods are then described and their suitability to this project is assessed. Subsequently, the most suited method is used in order to demonstrate how the chemical composition of the designed alloy may achieve the desired properties. Initially, two 50 g laboratory scale alloys were manufactured and subjected to elementary tests in order to confirm some expectations. From their behaviour, two 100 kg industrial scale alloys were manufactured. In this section, only the effect of alloying elements is investigated, leading to the suggestion of two laboratory scale alloys. The characterisation of those alloys is detailed in Chapter 4 of this thesis.

2.2   Alloy property requirements

The following attributes are necessary for the successful design of the novel alloy and need to be simultaneously taken into account when determining its composition:

- As mentioned in Section 1.4, the current best performing alloys in the field have a yield strength of approximately 860 MPa. It is therefore necessary to design an alloy that can easily be heat treated to achieve higher yield strengths.

- The alloy also needs to have a high toughness and elongation to failure, in order to prevent catastrophic failure in operating conditions. Requirements were set for the elongation to failure to be larger than 15 % and for the fracture Charpy energy to be larger than 25 J at room temperature.

- The alloy must have an austenite fraction higher than 0.1, because this has been observed to be the percolation threshold [76, 117]. Percolation of this phase is necessary to resist hydrogen ingress.

- The alloy must have a high fraction of bainitic ferrite to limit the size of residual regions of retained austenite, called blocky austenite. This relatively coarse form is responsible for reduced toughness and because it is less stable than films of austenite that have higher carbon contents. It is prone to deform to brittle martensite through stress-induced transformation [93, 116, 118, 119]. In order to minimise the amount of austenite but ensure that the volume fraction exceeds the percolation threshold, the objective is to obtain a volume fraction of austenite in the range of 0.1 to 0.2.

- Carbides must not be present between the bainitic ferrite laths, since their brittle nature would compromise the mechanical properties of the alloy [84, 120, 121]. Instead they should precipitate within the bainitic ferrite laths, where they are known not to cause any change to the mechanical properties due to a more coherent interface with the parent matrix [93, 112, 122].

Strength of designed alloy

In order to ensure a high enough strength is achieved, the isothermal transformation temperature is a key factor. Indeed, the relation between composition, isothermal temperature transformation and strength is well established [93]. In general, transformations are slower at lower temperatures, which means the microstructure is finer and the strength achieved is greater. Alloying elements that increase hardenability, through lowering of the free energy change for the austenite to ferrite phase transformation, such as carbon, nickel or manganese can be used to lower the temperatures at which bainite and martensite can start forming, called B_S and M_S, and in turn allow isothermal transformation at low temperatures. Alloying elements like cobalt or aluminium have the opposite effect, and are known to cause a coarsening of the structure.

Fig. 2.1 was used to find the usual relationship between yield strength (YS) and ultimate tensile strength (UTS) for bainitic steels [93]. In bainitic low alloy steels, a value of the ratio of YS to UTS close to 0.7 has been reported, meaning the minimum UTS requirement for the alloy is 1230 MPa [94]. In order to find the relationship between UTS and transformation temperature, the literature was reviewed and Fig. 2.2 was produced [93, 120, 123–125]. Using this, it was estimated that transformation at 380°C or less should satisfy the strength requirement.

Toughness of designed alloy

The relationship between strength and toughness in steels usually is inversely proportional. This is understandable because strength arises from prevention of deformation through mechanisms such as precipitate strengthening and grain size refinement leading to inhibition of dislocation movement. Conversely, toughness arises from the ability of a phase to deform plastically in order to absorb energy during crack growth, and is achieved by having large regions of easily deformable, hence low yield strength material ahead of a crack tip [116]. In bainitic alloys, this relationship is less pronounced, due to the presence of retained austenite, which has a lower yield strength than ferrite, and effectively improves the toughness to
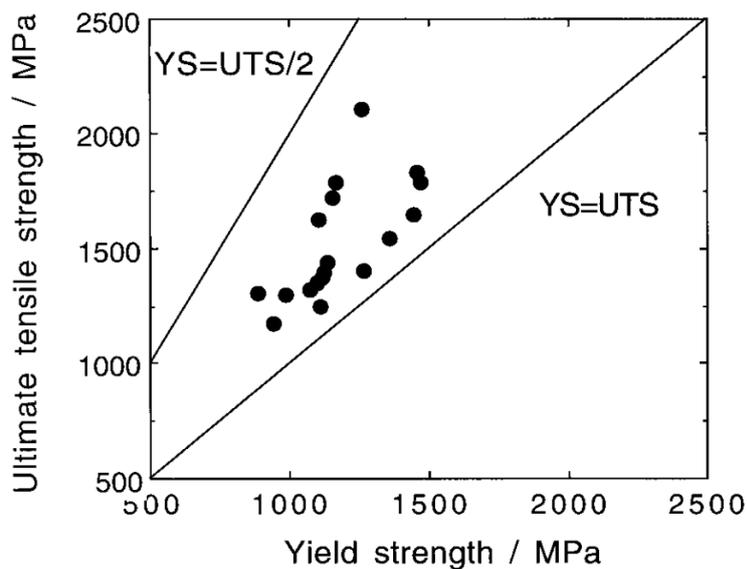
Fig. 2.1: Observed relationship between yield strength (YS) and ultimate tensile strength (UTS) in bainitic steels, from Bhadeshia [93].
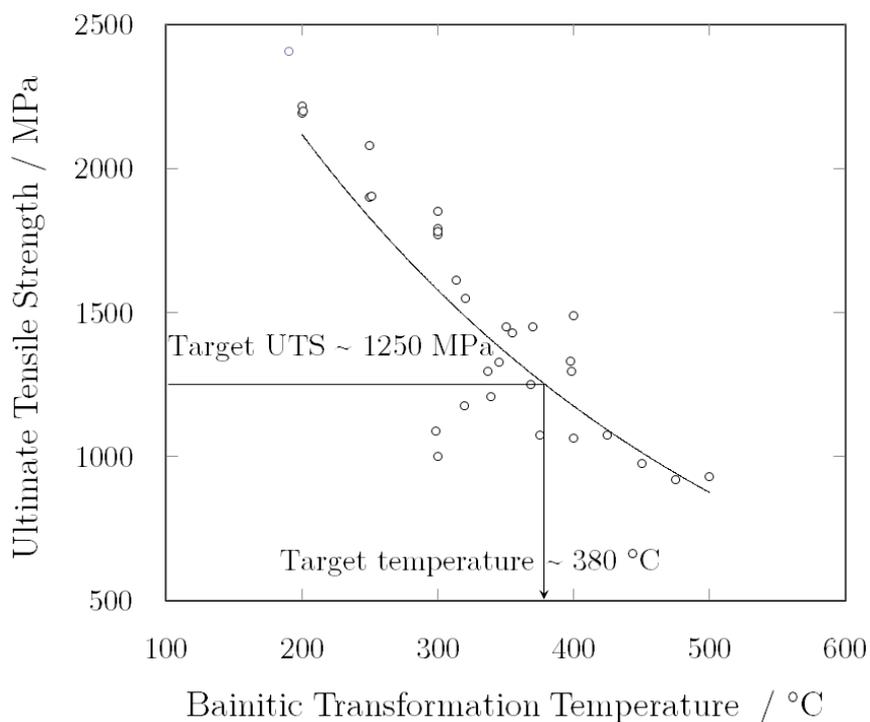
Fig. 2.2: Observed relationship between ultimate tensile strength and isothermal transformation temperature in bainitic steels. Using a polynomial fit of all the values reported, the target minimum UTS was used to find an indicative maximum transformation temperature. The data were collected from [93, 120, 123–125].

the alloy. Fig. 2.3 shows how superior bainitic steels are in terms of toughness, shown as elongation to failure, and in strength compared to standard tempered martensitic steels. The austenite fraction requirement of the designed alloy is expected to be sufficient to achieve the requirement in terms of toughness. It has been shown that the austenite stability is critical in ensuring transformation to martensite only occurs under high stress, and that this stability can come from an increase in the carbon concentration in the austenite [126]. Additionally, toughness in bainitic alloys can be improved by austenite grain refinement during the austenitising of the alloys, through methods described by Hulme-Smith, and can therefore be improved independently of composition [116].

Retained austenite volume fraction

In order to predict the volume fraction of retained austenite that will be present in an alloy, thermodynamic simulations can be used. Because of the nature of the austenite to bainite phase transformation, the equilibrium interpretation of the phase transformation does not apply. Instead, a diffusionless, displacive austenite to ferrite transformation occurs initially, followed by the diffusion of carbon out of the bainitic ferrite phase in which its solubility is very low, into the neighbouring austenite. When the free energy of the austenite and the ferrite phase becomes equal, due to this carbon enrichment of the austenite, the reaction stops. This is known as the incomplete reaction phenomenon, and this carbon concentration in austenite is displayed schematically as an additional line, T_0, in the Fe-C phase diagram, as shown in Fig. 2.4 [93]. Additionally, the shape change resulting from the transformation of austenite to bainite introduces a strain energy. For this reason, the T_0 line can be adjusted so that those internal strains are taken into account, and this is represented as the T_0' line. From it, the fraction of both phases at the end of the reaction can be estimated using the lever rule, as displayed in Fig. 2.5 [127]. In practice, such calculations are not precise. The lack of precision arises from the very nature of the bainite phase. Where it was long believed that bainite was a cubic phase in steel like ferrite, recent work has shown repeatedly that the structure of bainite is actually tetragonal [128–130]. This has significant implications regarding the solubility of carbon in bainite and therefore the equilibrium concentration of
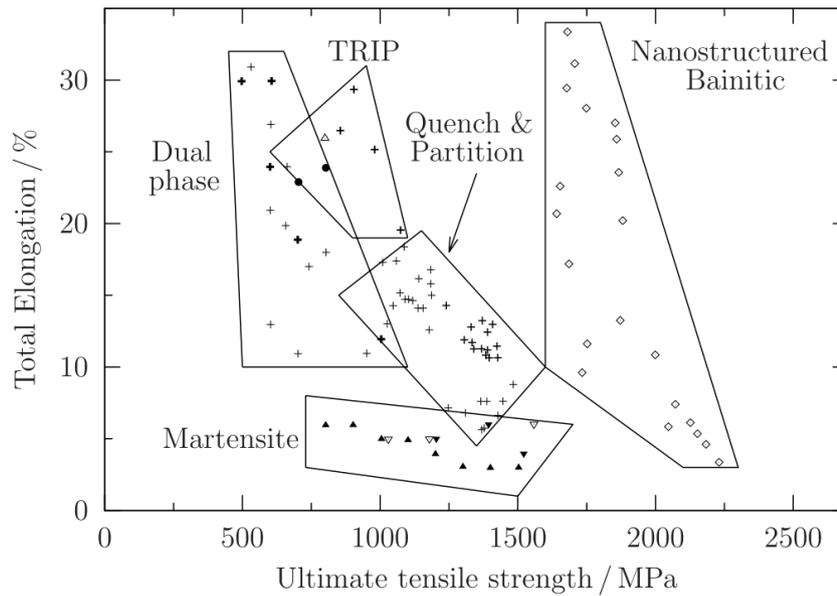
Fig. 2.3: Elongation to failure versus ultimate tensile strength for different types of steels. A combination of higher toughness and strength can be achieved with bainitic compared to martensitic steels [116].

carbon in bainite after partitioning. Assuming a cubic structure, the carbon solubility is close to 0 at temperatures below 400°C, but taking into account the tetragonal nature of the phase, the solubility of carbon can reach up to 0.42 wt% C at 400°C, as seen in Fig. 2.6 [131]. Jang calculated the carbon solubility in cubic ferrite, α, and in tetragonal ferrite (martensite, for example), α', in pure Fe-C steel were calculated from first principles. In practice, The very small difference in lattice parameters between cubic and tetragonal bainite should not lead to such a large solubility difference, but this result highlights the uncertainty of carbon solubility in bainite and therefore the inaccuracy in predicting austenite phase fractions.

Carbide precipitation

Carbide precipitation has been extensively covered in the literature review and is hard to predict. Since no predictive model has been suggested to assess iron carbide precipitation in bainite, the dependence of carbides on composition was used to try and achieve the correct structure. More details were given in Section 2.4, dedicated to the composition determination of the novel alloy.
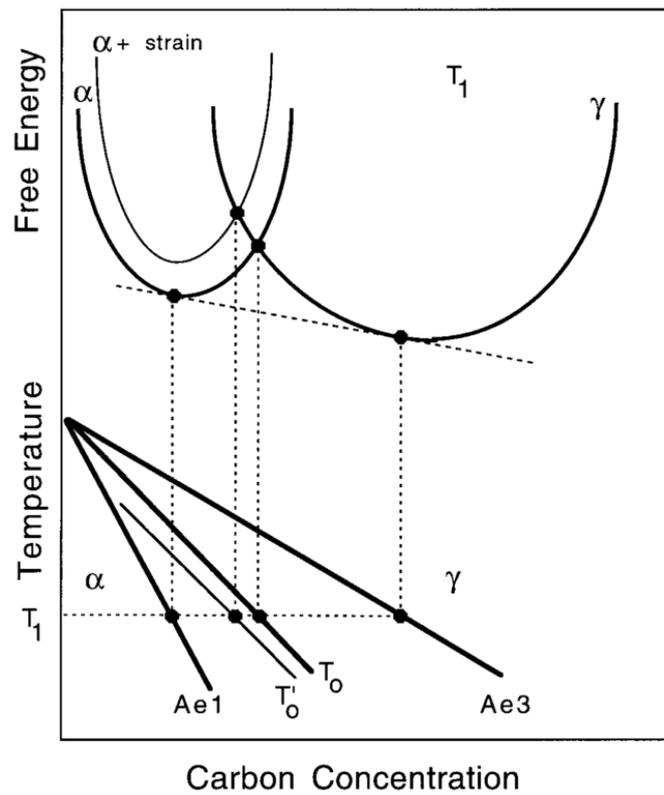
Fig. 2.4: Schematic representation of the T_0 and T_0' lines in the Fe-C phase diagram. They indicate the point at which there is no driving force for the austenite (γ) to ferrite (α) phase change, and therefore when the reaction stops. This point occurs when the carbon concentration in austenite reaches the T_0' line. Ae_1 is defined as the temperature below which only ferrite can exist at equilibrium, while Ae_3 is the temperature above which only austenite can exist at equilibrium [93].

$$V_{\alpha_b} = \frac{x_{T_0'} - \overline{x}}{x_{T_0'} - x_\alpha}$$
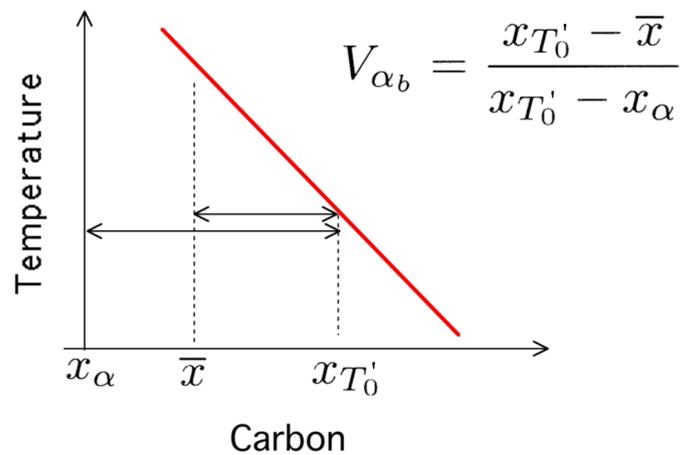
Fig. 2.5: Lever rule used to estimate the volume fraction of bainite, V_{α_b}, formed during isothermal bainitic transformation. $x_{T_0'}$ is the concentration of carbon in austenite when the transformation finishes, $\overline{x}$ is the average carbon concentration of the alloy and x_α is the equilibrium carbon concentration in ferrite, after partitioning into the austenite [93].
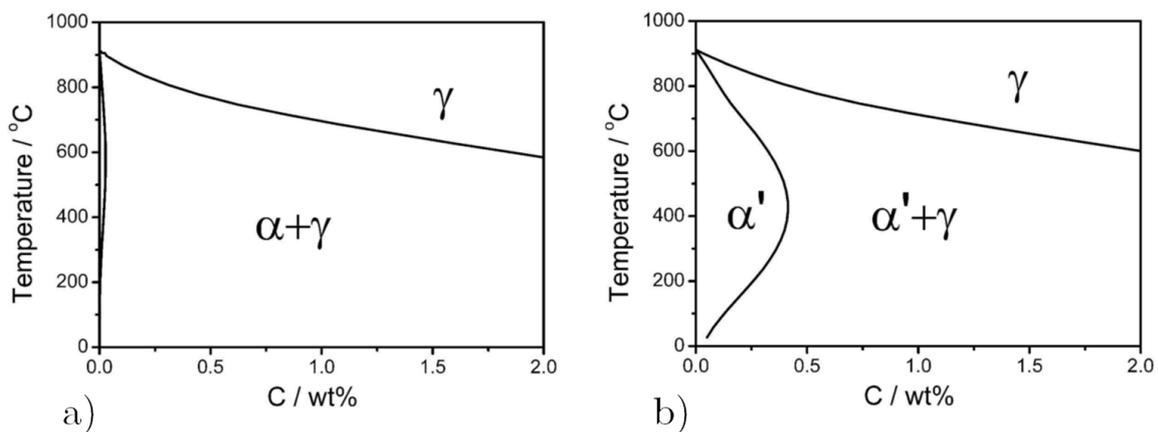
Fig. 2.6: Phase diagrams showing significant differences in the calculated carbon solubility in cubic ferrite, α and tetragonal ferrite, α' [131]. They lead to uncertainties when using the lever rule to calculate the expected volume fraction of bainite formed isothermally.

2.3   Suitability of available modelling programs

Several programs are commonly used when designing novel alloys. Their suitability in this project was assessed, and ultimately only one, MUCG, was used.

Neural networks and genetic algorithms

Such models are non-linear regression models that act as a set of artificial neurones, each representing the input data, and interacting non-linearly onto intermediary undefined nodes in order to obtain the desired output. The weight of each input onto the final output is this way allowed to vary and to be optimised [132]. The most significant advantage of such models is that they allow predictions to be made accurately in extremely complex systems where normal modelling is inapplicable either because the scale would be too small for the model to predict any macro-scale behaviour, or the models would have to be over simplified in order to predict macro-scale behaviour but would not be representative of the atomic scale behaviour. By training a program to determine correlations between input and output, neural networks can bridge the gap between atomic interactions and macro-scale properties, while avoiding the need for understanding and modelling the mechanisms at play [133]. The model will iteratively find the best possible fit, using training data. The last advantage is that, by extrapolation, neural networks can predict behaviours away from the region of the training data, and this has enabled the successful design novel steels [123]. The main drawback of those models is the need for an appropriately large training and testing database that is not always available.

If a neural network were to be used in this project, the input would be the following parameters: composition and heat treatment. The desired output would be the following: volume fraction austenite, toughness, strength and carbide precipitate morphology. It is already possible to notice an imbalance between inputs and outputs. When investigating the available literature in order to generate a training database, the lack of data becomes obvious. Much work on bainitic alloys either focus exclusively on mechanical properties or on carbide morphology but virtually no work has combined both aspects in depth. Consequently, it

was impossible to generate a dataset to train or test a neural network and this route was not pursued for the design of the alloy.

MatCalc - kinetic assessment of carbide growth

MatCalc relies on equilibrium thermodynamic data to estimate the kinetics of nucleation and growth of precipitates. It assumes the validity of standard nucleation theory for all estimations of precipitate growth and is used extensively for steels alloyed with transition metals, which form carbides during tempering steps. In that case, the standard nucleation theory applies and the tempering temperatures and diffusivity of elements are well established and accurate predictions of precipitate morphology can be made [134, 135]. In this project, the standard theory does not apply since there are two simultaneous competing processes at play; the partitioning of excess carbon from the bainitic ferrite into the austenite and the precipitation of carbides within the ferrite. In paraequilibrium conditions, the diffusivity of substitutional atoms cannot be used to make predictions and instead the diffusion of carbon is the rate-determining factor for the precipitate growth. The competing nucleation and partitioning of carbon are significantly affected by the presence of alloying elements that affect the chemical potential of carbon in both ferrite ans austenite, such as silicon, nickel or manganese. Because their effect cannot be computed using MatCalc, it cannot effectively predict the carbide morphology and was not used [93].

MTDATA - thermodynamic assessment of structure

MTDATA is a program that relies exclusively on interaction parameters between species present in the phases of interest. Large databases are available and can be used to calculate the equilibrium phase fraction which minimises the overall Gibbs free energy of a system defined by the user, with respect to temperature [136]. The advantage of this program is that it can allow a large number of phases to co-exist simultaneously. In this project, the phase transformation to bainite and the precipitation of carbides do not take place at equilibrium, so this software cannot be used in that respect.

MUCG - kinetic prediction of microstructure

MUCG is a program written by Bhadeshia, and contains a thermodynamic database and algorithms that can predict the phase transformation kinetics for the austenite to ferrite phase transformation as well as the equilibrium carbon composition in the austenite [137]. It relies on the classical nucleation theory, in which the free energy change for the phase transition is maximised using the parallel tangents construct depicted in Fig. 2.7, which in turn determines the carbon composition of the newly formed phase [137]. The model then predicts the time required for this nucleation to start as a function of temperature using polynomial expressions derived from previous experimental data, representing the displacive and reconstructive transformations. This is not perfect because the classical nucleation theory does not describe accurately the bainitic transformation. For example, there is no information on the coherency between the new and the parent phase, while this information is required in the nucleation theory. Still, this program has proven many times to predict with a satisfactory level of accuracy the kinetics of phase transformation in steels [116, 137, 138]. Fig. 2.8 illustrates the close fit between experimental data and calculated time-temperature-transformation (TTT) diagram using MUCG, from Bhadeshia [137]. The fit is not perfect for the reasons stated previously but the accuracy in the temperatures when martensite and bainite start forming is satisfactory. The strength of this program is that it relies solely on the average alloy composition as the input. Because the database is included in the program, it limits the range of compositions that can be investigated, but it is satisfactory for this project.
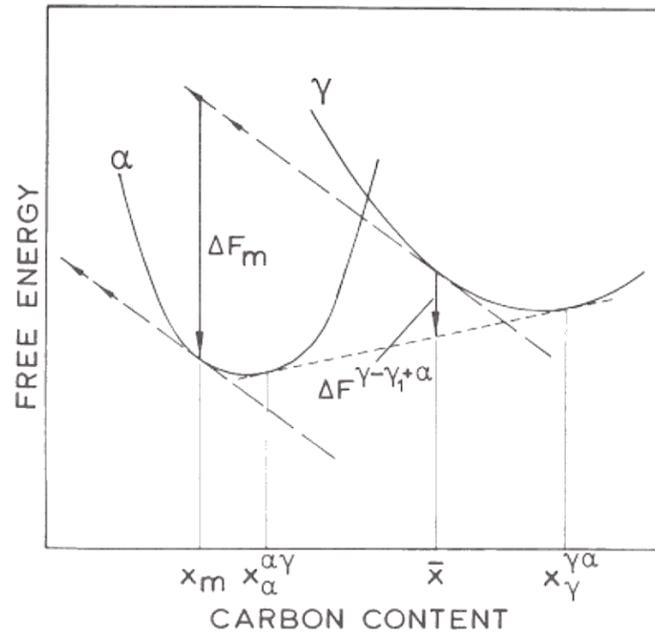
Fig. 2.7: Illustration of the process of austenite to ferrite driving force maximisation performed in MUCG. ΔF_m is the maximised free energy change in the case of ferrite (α) nucleating in the austenite (γ) phase, without a significant austenite composition change. x_m is the carbon concentration in bainite nucleated according to the maximisation of the free energy, $\bar{x}$ is the average carbon concentration of the alloy, $x_\alpha^{\alpha\gamma}$ is the carbon concentration in ferrite at equilibrium with austenite and $x_\gamma^{\gamma\alpha}$ is the carbon concentration in austenite at equilibrium with ferrite. $\Delta F^{\gamma-\gamma_1+\alpha}$ shows the smaller free energy change resulting from austenite transforming into a mixture of austenite and ferrite at equilibrium [137].
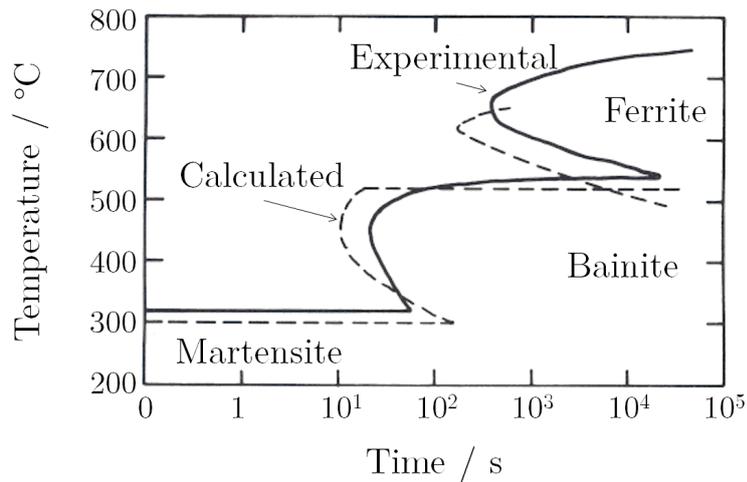
Fig. 2.8: Comparison between a time-temperature-transformation (TTT) diagram calculated using MUCG, and experimental data. The regions where martensite, bainite and ferrite form are indicated [137].

2.4   Chemical composition determination of the novel alloy

After having reviewed the applicability of programs for the design of the novel alloy, the chemical composition of the alloy was selected. The composition of the steel developed by Gomez and presented in Section 1.4.4 was used as a starting point, and modified to reach the final alloy composition [94].

Using the MUCG program, the influence of the most common alloying elements, C, Si, Mn, Cr and Ni was investigated by Hulme-Smith and Bhadeshia [116, 139]. The results presented by Hulme-Smith, displayed in Fig. 2.9, reveal that carbon is the element that has the strongest effect on the change in bainite and martensite start temperatures, B_S and M_S, per weight fraction. Mn, Cr and Ni follow in that order. Bhadeshia indicates that in the case of nickel, one of the most useful alloying elements, the increase in weight fraction leads to a faster drop in B_S compared to M_S, as shown in Fig. 2.10. The opposite behaviour is observed with carbon, especially above 0.5 wt%. A large temperature gap between both should be observed in the final alloy since that allows transformation at a wider range of temperatures, and can be used to determine optimal transformation temperatures. Fig. 2.9 shows that many different compositions of C, Mn, Cr and Ni can be used in order to design an alloy with B_S close to 380°C. The individual advantages of alloying elements is presented in the next paragraph and from them, the final composition was selected to be Fe-0.4C-2Si-0.1Mn-3Ni-0.25Mo-1Cr wt%. This final composition is used as the base alloy when presenting the effect of varying the weight fraction of alloying elements.

Alloying elements for hardenability - V, Mn, Mo, Cr, Ni
All those substitutional elements lower B_S and M_S, as well as the T_0' line. In order to keep the alloy composition as simple as possible, as few elements as possible were used. Vanadium is an expensive element and is used to form vanadium carbides during tempering at high temperatures [140]. Because it does not provide advantages compared to cheaper alloying elements, there is no use for V in this alloy.
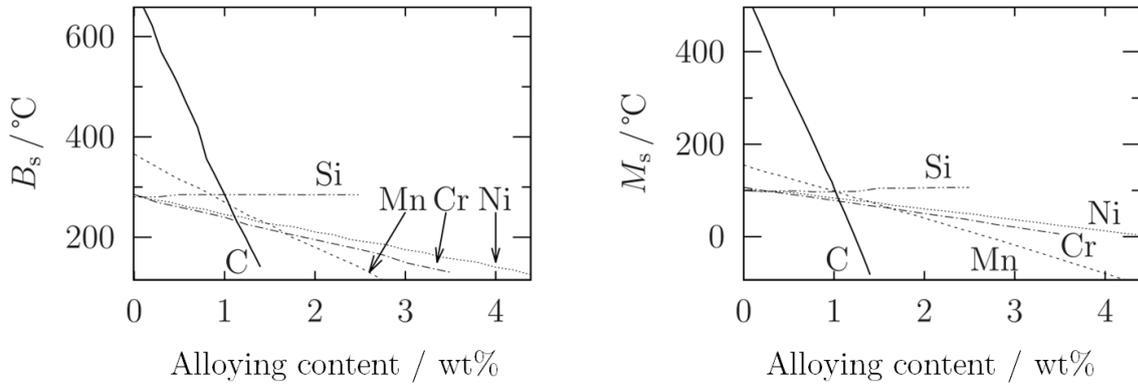
Fig. 2.9: MUCG calculated B_S and M_S temperatures for a 1C-1.25Mn-2.5Si-1Al-0.1V wt% alloy. The effect of varying the content of individual alloying elements on B_S and M_S can be visualised. The effect is most pronounced for carbon and insignificant for silicon [116].
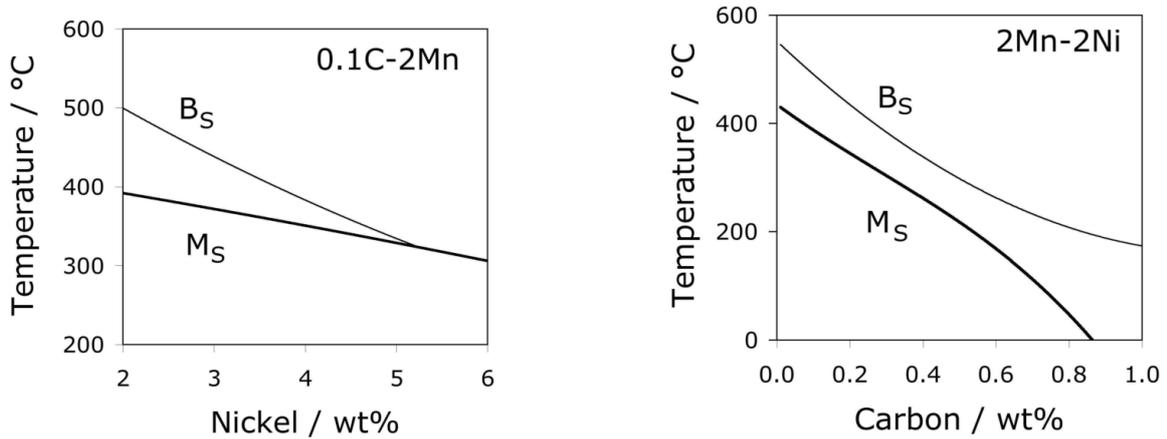
Fig. 2.10: MUCG calculated B_S and M_S temperatures for a 0.1C-2Mn wt% alloy as a function of nickel weight percent, and for a 2Ni-2Mn wt% alloy as a function of carbon weight percent. Nickel reduces the difference between B_S and M_S while carbon increases it, when present in excess of 0.5 wt% [139].

Manganese has the most important hardenability effect [141], but has two major draw-backs that mean it has to be kept to a minimum. First, it is more soluble in cementite than in ferrite [142–144], and it has been seen to favour the formation of cementite instead of epsilon carbide in high-Mn steels transformed for very short times or at low temperatures [145]. Second, it has been reported to segregate within the microstructure, and to prevent austenite to transform to bainite in those regions [94]. As a result, unexpectedly large blocky austenite regions can be generated. However, Mn has been reported to fix impurity sulphur present in alloys from the manufacturing processes, and a composition of 0.1 wt% Mn was reported to be the lowest composition that can prevent sulphur embrittlement [116]. This is therefore the composition selected for Mn for this alloy.

Molybdenum also has a strong hardenability effect. It is used to bind to the impurity phosphorus that is present in steels from manufacturing processes and embrittles grain boundaries. In order to combat this P embrittlement, a composition of 0.25 wt% has proven optimal [146]. At higher concentration, Mo can cause too large regions of blocky austenite to be present because it lowers the T_0' line significantly [147]. 0.25 wt% Mo was chosen for this alloy.

Chromium is very soluble in carbides [148], and is known for causing sensitisation-induced corrosion in the form of brittle carbides formation at grain boundaries, where chromium is more mobile [77]. Even though this is only true at high temperatures, and is not a significant issue in this project, the fact that chromium can favour the formation of cementite at the interlath boundary is a real threat and has to be minimised. In order to achieve a good level of hardenability while limiting the ability for cementite to form, Gomez reported a composition of 1 wt%, to provide strength and hardenability, while not affecting the T_0' line significantly [149]. This composition was used in this design.

Nickel is undoubtedly the most useful of all elements that improve hardenability. It has been

reported to favour the formation of ε-carbide in tempered martensite, in steels with as low as 0.22 wt% C [29]. In bainite, no ε-carbide presence has been reported in alloys with carbon composition inferior than 0.4 wt%, in which case, the nickel content was 4 wt% Ni [111]. In alloys without nickel, the alloy with the lowest carbon weight percent in which ε-carbide has been identified, had 0.54 wt% C [102]. When present in solid solution, nickel is also known to increase the toughness of the ferritic phase [122, 150]. It is also known to stabilise the austenite while not lowering the T_0' line to undesired levels [116]. All those factors make nickel the most important alloying element for this design. Using MUCG, the weight percent of nickel was allowed to change between 1 and 3.5 wt% and TTT diagrams were drawn. The results are presented in Fig. 2.11. Since the target isothermal transformation should be up to 380°C, the bainite start temperature should be just above this value and the martensite start temperature should be as low as possible. With 1 and 2 wt% Ni, the bainite start temperature is too high. 3 wt% Ni and 3.5 wt% Ni seem to be ideal, with possible isothermal transformation temperature ranging from 305 to 420°C and 290 to 375°C respectively. Consequently, the two laboratory scale alloys manufactured had those Ni compositions.

Alloying elements for ε-carbide precipitation - Al, Si

Both aluminium and silicon have been reported to favour the precipitation of ε-carbide over cementite, although the mechanisms behind both effects are different. Hoon calculated from first principles that the substitution of an iron atom by an aluminium atom in cementite and ε-carbide lowered the enthalpy of formation of both carbides by 14 and 21 kJ mol^{-1} respectively, indicating aluminium favours both transformations thermodynamically [144]. Additionally, aluminium is a ferrite stabiliser, which means it increases the driving force for the austenite to ferrite phase transformation, leading to coarser microstructures because of faster reaction kinetics [117, 151]. It raises B_S and M_S, which is the opposite effect of what was achieved through addition of nickel [147]. It is also known to oxidise during casting, generating some dross in the cast that has to be discarded [116]. For the many reasons enumerated, aluminium was not used in the alloys designed.
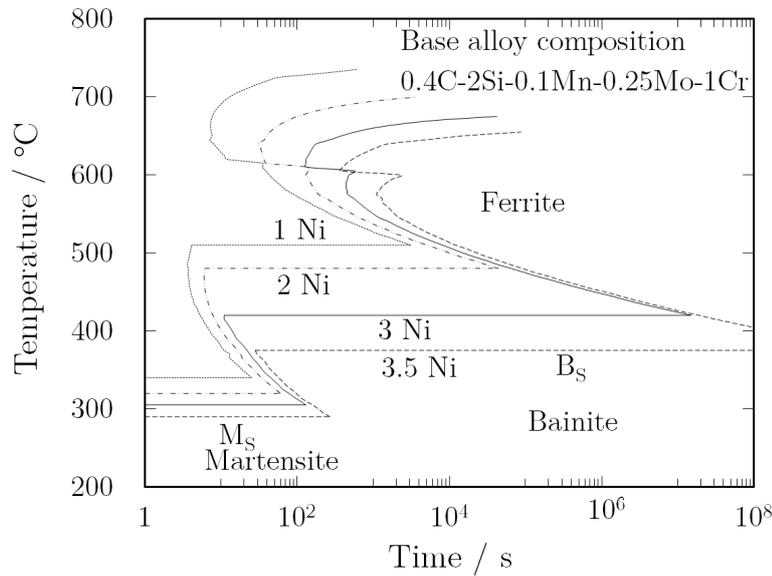
Fig. 2.11: MUCG calculated TTT diagrams for a 0.4C-2Si-0.1Mn-0.25Mo-1Cr steel with varying nickel composition. The Ni compositions of the preliminary alloys were chosen to be 3 and 3.5 wt% respectively.

Silicon on another hand retards kinetically the formation of both carbides, especially when precipitating from austenite, enabling the precipitation of carbides within the bainite and preventing it at the interlath. Owen describes this mechanism as the rejection of silicon from the carbide during precipitation, thus enriching the neighbouring ferrite and increasing the chemical potential of carbon in it [152]. The net effect is the reduction of carbon diffusion towards the carbide because diffusion occurs down chemical potential gradient of the diffusing species. Caballero proved using atom probe tomography that Si is actually present in the carbides when they precipitate and only slowly diffuses out of them with time [153]. Furthermore, Jang calculated from first principles that silicon raises the enthalpy of formation of cementite by 37 or 52 kJ mol^{-1} depending on which iron atom is substituted by a silicon atom [154]. Hoon showed that silicon raises the enthalpy of formation of ε-carbide by 48 or 130 kJ mol^{-1}, which seem to indicate that silicon should effectively thermodynamically favour the formation of cementite over ε-carbide [144]. Experimentally, there are many reports of high-Si alloys containing in which only ε-carbide is present [113, 114], and this is explained because ε-carbide is a transition carbide that forms before cementite because it has a better coherency with the bainitic ferrite phase. Additionally, Si modifies the lattice

parameter of ε-carbide so that it further improves its coherency with the matrix. Fig. 2.12 depicts the small impact the silicon weight fraction has on the transformation kinetics of the alloy, as calculated using MUCG. In order to find the effect of silicon on carbide morphology the silicon contents selected for the two preliminary alloys were 1 and 2 wt%. 2 wt% was chosen as the maximum since it has been reported that at this composition, bainitic alloys sometimes do not have the ability to form cementite at all [113, 114].

Alloying element for strength and carbide precipitation - Carbon

Last but not least, carbon is naturally the most important alloying element in steel, and in the large scale alloy manufacturing two different carbon compositions were investigated. At the laboratory scale, the effect of Ni and Si are already investigated, and as a result, a consistent carbon content is necessary so there are not too many simultaneous composition variables. Carbon strongly affects the B_S and M_S, and the kinetics of the paraequilibrium phase transformation. This in turn determines the scale of the structure and the strength of the alloy. Higher carbon contents lead to finer scales because carbon partitioning is slower and limited by the faster enriched retained austenite phase, and therefore lead to higher strengths [87, 124, 155]. Carbon also determines the maximum volume fraction of bainite formed using the T_0' line. Carbon is known to stabilise the austenitic phase [126]. Using MUCG, the effect of varying the carbon weight percent was investigated and is presented in Fig. 2.13. As for nickel, the carbon concentration that permits isothermal transformation at and below 380°C is selected, in this case, 0.4 wt% C.

The final compositions of the two laboratory scale alloys are summarised in Table 2.1.

Table 2.1: Nominal compositions in wt% of the two laboratory scale novel bainitic steels designed.

Alloy	C	Si	Mn	Ni	Mo	Cr
Alloy 1	0.4	2	0.1	3	0.25	1
Alloy 2	0.4	1	0.1	3.5	0.25	1
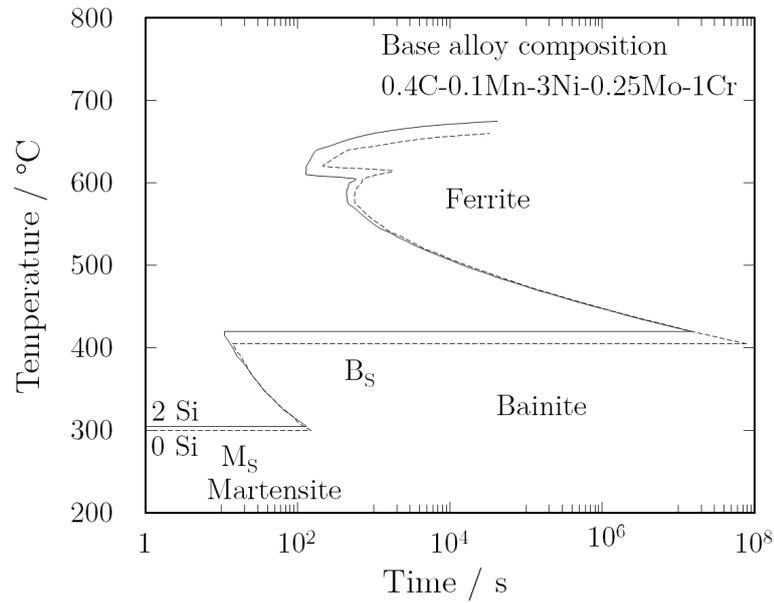
Fig. 2.12: MUCG calculated TTT diagrams for a 0.4C-0.1Mn-3Ni-0.25Mo-1Cr wt% steel with varying silicon composition. The Si compositions of the preliminary alloys were chosen to be 1 and 2 wt% respectively.
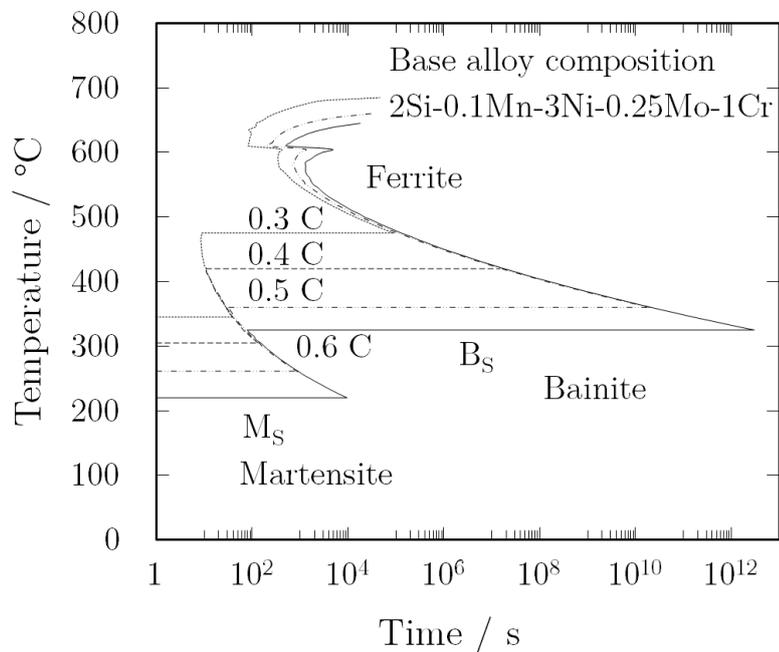
Fig. 2.13: MUCG calculated TTT diagrams for a 2Si-0.1Mn-3Ni-0.25Mo-1Cr wt% steel with varying carbon composition. The C composition of the preliminary alloys was chosen to be 0.4 wt%.

Retained austenite estimation

The volume fraction of retained austenite that can be expected in the two designed alloys was investigated using MUCG, and as described earlier, the accuracy of such measurement makes the calculations unreliable. Still, the results for Alloy 1 are presented in Fig. 2.14. Because no information is available on the solubility of carbon in the bainitic phase formed in this alloy, the lever rule can give completely different results depending on what value is attributed to it. Here, the two most extreme cases are presented, in which the solubility is expected to be either 0 wt%, as would be the case in cubic ferrite, or is as defined by Jang [131]. At 420°C, the solubility of carbon defined by Jang is higher than the average carbon content in Alloy 1, therefore the average carbon content was used as the solubility limit. The volume fraction bainite at 420°C is calculated to vary between $a_{420}/b_{420} = 1$ and $a_{420}/(b_{420} + c_{420}) = 0.22$. The volume fraction bainite at 305°C is calculated to vary between $a_{305}/b_{305} = 0.92$ and $a_{305}/(b_{305} + c_{305}) = 0.52$. Additionally, the particular tetragonality changes and ultimately tends towards a cubic structure. The numerical values calculated are not able to assist in the prediction of the volume of retained austenite, but from the amount of austenite-stabilising alloying elements present in the alloy, a volume fraction of austenite higher than 0.1 is expected. The trend that can nevertheless be confirmed from those calculations is that the volume fraction bainite can be maximised by transforming the alloys at lower temperatures.
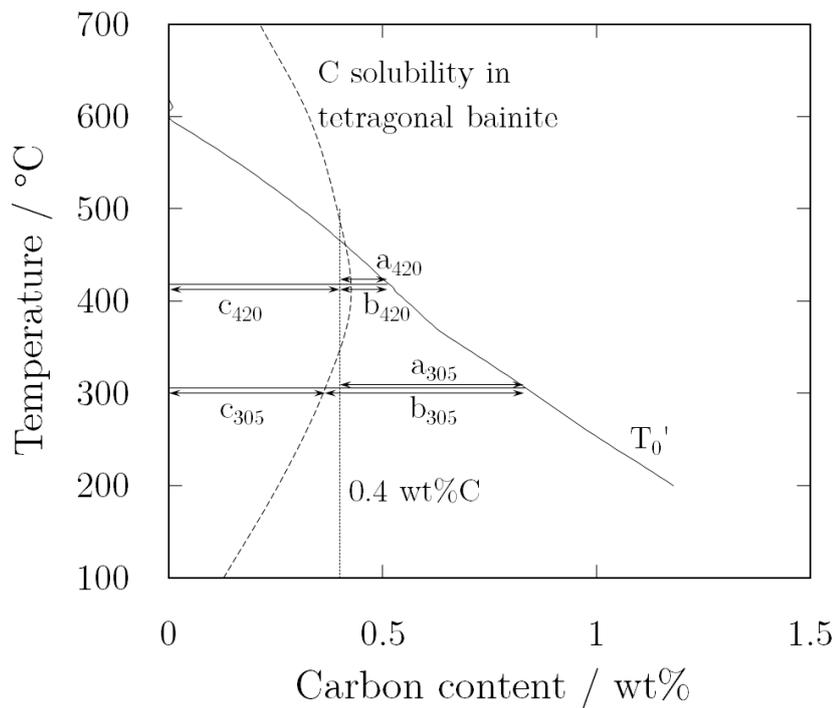
Fig. 2.14: MUCG calculated TTT diagrams for Alloy 1. The maximum and minimum volume fractions of bainite at 305 and 420°C were calculated using the lever rule, described in Fig. 2.5. Those are the lowest and the highest temperatures at which bainite is expected to form in Alloy 1, as shown in Fig. 2.13, in which the 0.4 C curve represents the TTT diagram for Alloy 1.

Chapter 3

Experimental methods

3.1 Introduction

In order to assess the property requirements set in Chapter 2, several characterisation techniques are described, indicating the specific relevant data that can be acquired from each.

1. Bainite structure – dilatometry and scanning electron microscopy (SEM) were used for characterisation of the structure, and of the bainite lath thickness.

2. Austenite fraction – X-ray diffraction (XRD) using Reitveld refinement was used to quantify the austenite phase fraction to a precision of approximately $\pm\,1\%$.

3. Carbides – XRD was used to identify and quantify the phase fractions of carbides. Transmission electron microscopy (TEM) was used to identify the carbides when the XRD signal did not permit carbide identification, and it was also used to determine the carbide morphology.

4. Strength and toughness – for laboratory scale alloys, standardised mechanical tests could not be performed because the alloys were not produced in sufficient quantity. Instead, the Vickers hardness was measured and the ultimate tensile strength was estimated to be approximately 3.3 times the Vickers hardness, since this linear relationship has been observed empirically in bainitic and martensitic steels [127, 156, 157].

The results obtained from those techniques are presented in the four subsequent chapters, as summarised in Table 3.1. Other specialised techniques were also used, and are described in the relevant chapters.

Table 3.1: Summary of the characterisation techniques used in this thesis.

Chapter	Dilatometry	Hardness	SEM	TEM	XRD
4 - Characterisation of laboratory scale novel alloys	x	x	x	x	x
5 - Characterisation of large scale novel alloys	x	-	x	x	x
6 - Hydrogen behaviour in large scale novel alloys	-	-	-	x	x
7 - Mechanical properties of novel alloys	-	-	-	-	x

3.2 Dilatometry

A thermomechanical simulator, the Thermecmastor Z, was used for dilatometry experiments. Cylindrical samples of 8 mm in diameter and 12 mm in length were prepared by electric discharge machining. R-type thermocouples were spot welded onto the sample, which was then induction heated in vacuum. The change in dimension of the sample during heating and cooling was measured by a laser with a precision of $\pm$ 5 μm. Initial continuous cooling runs were performed using He as coolant, in order to determine the martensite and bainite start temperatures. Once this information was obtained, bainitic isothermal transformations were performed after austenitising, and the time and strain associated with a complete transformation were recorded. Comparing the strain due to transformation at several temperatures gave an indication of the extent of bainite transformation achieved in each case. Additionally, slow heating runs were used to detect the Ae_1 and Ae_3 temperatures, which indicate the start and the finish austenite transformation temperatures. This knowledge provided a guidance for subsequent austenitising heat treatments, to limit grain coarsening.

3.3 Hardness

Samples were first cut with a Brilliant 220 machine using a SiC rotating wheel at a controlled speed of 0.03 $\mathrm{mm\,s}^{-1}$. They were then hot mounted on bakelite and ground gradually using P600, P1200 and P2500 grit SiC paper. They were polished using a 6 μm diamond paste followed by a 1 μm diamond paste. The Vickers hardness was then measured on a Q60 microhardness machine. It is established that cutting as well as grinding can cause stress-induced transformation of the austenitic phase into martensite [158], but this effect was not problematic in the hardness measurements, and reproducible results were always achieved.The macroscopic hardness of the laboratory scale alloys was determined from ten measurements using a 30 kg load, and an equivalent strength was suggested based on the empirical relationship between hardness and strength described by Bhadeshia [159].

3.4   Scanning electron microscopy (SEM)

Identical sample preparation as for hardness was performed for SEM, ensuring conductive bakelite was used. The only difference was a final etching step, performed to reveal the microstructure, using a solution of 2% nitric acid in alcohol (2% nital). A FEI Nova NanoSEM FEG and a Philips XL30 FEGSEM were used. Three data collection modes were used:

- Backscattered electron imaging – backscattered electrons are electrons from the primary beam that are scattered through the sample and emitted from the sample. The scattering processes depend on the elements and phases present in the sample, hence backscattered electron imaging was used for low-resolution phase imaging.

- Secondary electron imaging – the primary beam also knocks off electrons from atoms in the sample, which are called secondary electrons. They have lower energies than backscattered electrons and a biased metallic mesh is used to attract them to the detector. As a result, secondary electrons are better for topographic imaging. Secondary electron imaging was used for high resolution imaging, since the etching process creates a clear topographic difference between ferrite and austenite by preferentially etching ferrite.

- Energy dispersive X-ray spectroscopy – as a consequence of electrons being knocked off their shells by the primary beam, other electrons fill those shells, emitting quantised X-rays specific to the elements present in the alloy in the process. This technique was used to determine the local composition in regions where segregation was visible.

3.5   Transmission electron microscopy (TEM)

Samples were initially cut as 150 μm thin sheets using a Brilliant 220 machine. 3 mm disc samples were punched out of them. The disc samples were then ground using P2500 grit SiC paper, using a rubber as support, until they reached a thickness of 50 μm. Samples were then electropolished in a Struers TenuPol-5 machine. The temperature was kept at $10°C$ and a 5% perchloric acid, 25% glycerol and 70% ethanol solution was used. The optimal operating voltage and flow rate were determined for each setup. A JEOL 4000EX-II TEM, with an accelerating voltage of 400 kV, was used for high resolution imaging, and the FEI Tecnai F20 FEG TEM, FEI Tecnai F30 FEG TEM and FEI Tecnai Osiris FEG TEM, which all have accelerating voltages of 200 kV, were used for carbide identification. Reflections due to carbides were identified in the diffraction pattern, and the morphology of the carbides was revealed with dark field imaging, which consists of imaging using only the reflection from the carbides. The crystal structure was then determined using the Crystal program, written by Bhadeshia at the University of Cambridge [160], the ImageJ software [161], and the CrystalMaker SingleCrystal v2.3 software. The Crystal program was used to index reflections in the diffraction pattern using the distance and angle between them measured with ImageJ. The SingleCrystal software was then used to calculate an identical ideal diffraction pattern, which was compared to the original data. The orientation relationship between ferrite and the carbide phases was compared to that described in the literature.

3.6   X-ray diffraction (XRD)

A Bruker AXS D8 diffractometer equipped with a Lynxeye XE position sensitive detector was used. It possesses good energy resolution, which permits signal filtering, thus eliminating fluorescence contribution to the final signal and prevents the need for a monochromator to be used, which would otherwise lower significantly the intensity detected. A divergent beam with fixed illumination length of the size of the sample was used in order to maximise signal to noise ratio. Cu $K\alpha_1$ radiation, a 40 kV voltage and 40 mA current were used. The Cu $K\alpha_1$ radiation is not optimised for work on steels due to its high absorption by iron, as well as leading to fluorescence. Cobalt radiation is known to penetrate steels deeper and cause much less fluorescence [162]. Only Cu sources were available in the department of materials in Cambridge, and no Co source was found to be readily available, as a result Cu sources were used. Samples were first cut with a Brilliant 220 machine using a SiC rotating wheel at a controlled speed of $0.03 \, \mathrm{mm \, s^{-1}}$. They were ground gradually using P600, P1200 and P2500 grit SiC paper. They were polished using a 6 μm diamond paste followed by a 1 μm diamond paste. In order to limit the impact of austenite stress-induced transformation during sample preparation on the final results, samples were etched lightly in 2% nital, and polished gently with a 0.25 μm diamond paste [163]. The austenite to ferrite ratio was initially calculated at every step, and this method was chosen for the reproducible results obtained from it. Samples were mounted on Si wafer to keep background noise to a minimum. The sample stage was rotated 30 revolutions per minute and the step size was chosen to be 5 to 10 times smaller than the width of the smallest peak expected in the data, in order to optimise software analysis and data collection time.

The surface treatment is critical for XRD because the Cu $K\alpha_1$ radiation used does not penetrate steel samples deeply. Fig. 3.1 schematically shows the relation between X-ray path length and penetration depth in a sample. Using the Lambert Beer law (3.1) for X-ray absorption in samples, the penetration depth was estimated [162]:
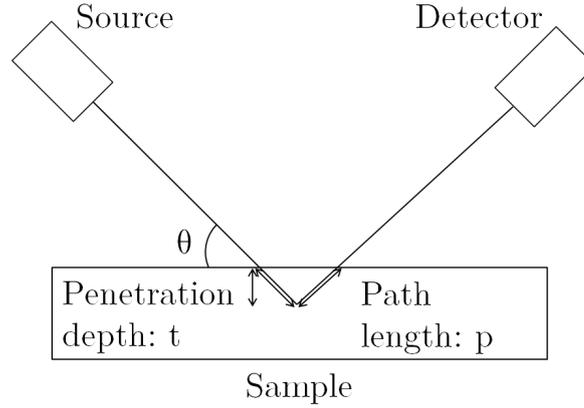
Fig. 3.1: Schematic penetration depth and path length in XRD.

$$I = I_0 \, e^{-\mu p} \qquad (3.1)$$

where I is the intensity of the signal at depth t, I_0 is the total intensity, p is the path length in the sample and μ is the linear absorption coefficient.

Rearranging (3.1), the path length becomes:

$$p = \frac{-\ln(I/I_0)}{\mu}$$

The linear absorption coefficient of Cu Kα_1 in iron is the product of the mass absorption coefficient of Cu Kα_1 in iron and the density of iron. Both values were reported in Cullity: $\mu = 304.4 \times 7.87 = 2396 \, \text{m}^{-1}$ [162]. The slight alloying of the alloys designed have a negligible effect on this parameter. From geometry, the penetration depth can be deduced:

$$t = \frac{p \sin \theta}{2} \Leftrightarrow t = \frac{-\ln(I/I_0) \sin \theta}{2\mu}$$

At the smallest and largest angles of the XRD scans, 25 and 125 degrees, the penetration depth of 90% of the signal, for which $I/I_0 = 0.1$, meaning that 10% of the signal detected penetrated deeper into the sample, was calculated to be approximately 1 and 4.3 µm respectively. The value of 90% was chosen arbitrarily, to give a numerical approximation of the

penetration depth of most of the XRD signal.

XRD was used to obtain the following information:

1. Austenite to ferrite volume fraction – using a 35-125° range, 0.05° step, 0.5 second dwell time, and a 0.012 Ni filter. The main focus during experimental preparation was on repeating the grinding/polishing and etching processes to ensure an undeformed surface was analysed, as described by Garcia-Mateo [161].

2. Unit cell parameters – using the same setup. The carbon content in austenite was calculated from it using the empirical formula suggested by Dyson [164].

3. Carbide crystal structure and volume fraction – using a 25-70° range since carbides have stronger peaks at lower angles, 0.03° step, 20 second dwell time and a 0.02 Ni filter. The ICSD, ICDD and CrystMet databases were used for phase identification.

4. Dislocation density – using using a 35-125° range, 0.05° step, 0.5 second dwell time, and a 0.012 Ni filter and the Williamson-Hall method [165].

For the three first results, the Reitveld refinement method was used to interpret the data, using the Highscore + software, based on Wiles and Young [166]. It is a least square analysis method, in which the sum of the squared difference between the model and the data is minimised at every step of the refinement process [167]. The simulated data are calculated using crystallography and setup information, as well as fitting the experimental data by refining the following parameters in this order:

- Background.

- Lattice parameter, or peak position.

- Scale, or weight fraction of the phases present.

- Peak shape, in which three parameters describe the pseudo-Voigt peak shape fit, which has been proven to be the best fit for ferrite and austenite XRD peaks [168, 169].

- Preferred orientation.

Chapter 4

Characterisation of laboratory scale novel alloys

4.1   Introduction

The purpose of the work presented in this chapter is to confirm experimentally some of the behaviour expected from both of the experimental alloys with compositions described in Chapter 2 and to optimise their compositions for large scale manufacture. First, dilatometry was used to determine the martensite-start and bainite-start temperatures, and isothermal heat treatments were performed in order to form lower bainite. The microstructure was then characterised using SEM, and XRD was used to determine the fractions of austenite and ferrite. Vickers hardness was measured in order to be able to estimate the ultimate tensile strength. Both TEM and XRD were used to identify the carbides present in the alloys, and XRD was used to quantify their volume fractions. Thermal desorption spectroscopy (TDS) was performed in order to assess the hydrogen trapping ability of both alloys.

Alloy manufacture

Both alloys were produced as 50 g elliptic cylindrical casts by vacuum arc remelting of a mixture of pure elements in powder form, using a Edmund Bühler GmbH arc melter AM. This method is known to cause significant solute segregation [116]. In order to remove the

initial dendritic structure and to homogenise the carbon content, both alloys were vacuum sealed in an argon environment and annealed at 1200°C for 48 h. Their actual compositions were determined using optical emission spectroscopy, with the carbon content determined by combustion analysis. The measured compositions together with those intended are summarised in Table 4.1. The substitutional solute compositions are close to the design values, but there is a significant discrepancy between the intended and actual carbon content.

Time-temperature-transformation (TTT) diagram prediction

Using the compositions in Table 4.1, TTT diagrams were calculated using the MUCG program, described in Chapter 2. They are displayed in Fig. 4.1, and suggest that both alloys could be transformed isothermally in the range of 350 to 450°C. This range corresponds exactly to the target transformation temperature proposed in Chapter 2.

Table 4.1: Nominal and actual compositions in wt% of the two laboratory scale novel bainitic steels designed.

Alloy	C	Si	Mn	Cr	Ni	Mo
Alloy 1 - nominal	0.4	2	0.1	1	3	0.25
Alloy 1 - actual	0.36	1.88	0.14	0.99	3.01	0.25
Alloy 2 - nominal	0.4	1	0.1	1	3.5	0.25
Alloy 2 - actual	0.31	1.03	0.11	0.99	3.57	0.22
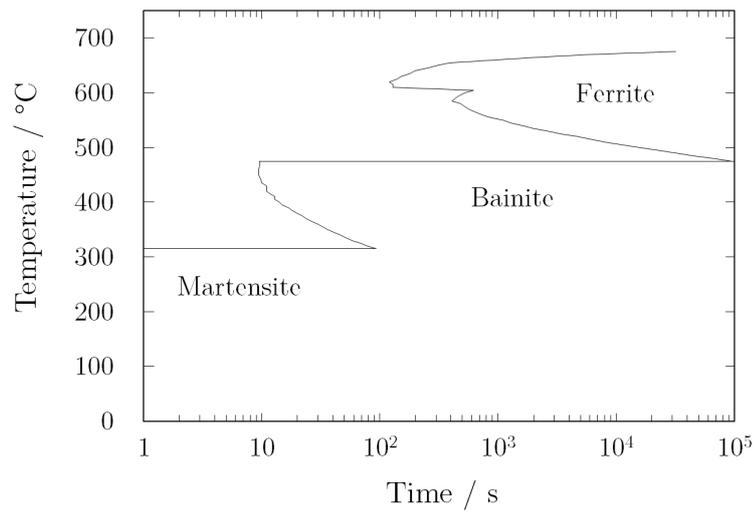
(a) Alloy 1
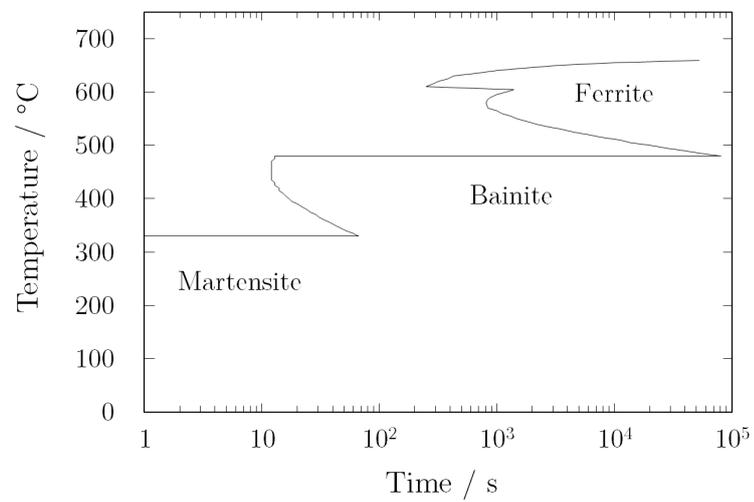
(b) Alloy 2

Fig. 4.1: MUCG calculated TTT diagrams for Alloy 1 and 2.

4.2 Dilatometry

4.2.1 Continuous cooling transformation diagram determination

Dilatometry was initially used to obtain experimental continuous cooling transformation (CCT) diagrams, which were used to verify the accuracy of the TTT diagrams calculated with MUCG. Five cylindrical samples of both alloys were austenitised at 850°C and subsequently cooled at different constant rates: 30, 10, 1, 0.1 and 0.05°C s^{-1}. The austenitising temperature was chosen after heating at 10°C s^{-1} revealed that austenisation was complete above approximately 840°C, as illustrated in Fig. 4.2. The continuous cooling curves obtained for Alloy 1 at 10 and 0.1°C s^{-1} are illustrated in Fig. 4.3. The phase change from austenite to ferrite during cooling causes an expansion of the sample because the ferrite has a lower density than austenite. Using the offset method, which is analogous to the method used for identifying the proof strength for samples that yield continuously during tensile tests, the temperature at which the phase change occurs could be identified [170]. This process was repeated for each cooling rate. At faster cooling rates, the strain change was due to the austenite to martensite transformation, whereas at slower cooling rates, it was due to the austenite to bainite transformation. The changes in strain due to martensite and bainite formation were different in three ways: the temperature at which they occurred, their absolute value, and their shape, all visible in Fig. 4.3. After having identified the martensite-start and bainite-start temperatures, M_S and B_S, they were plotted versus the time at which they occur, for each of the five continuous cooling experiments in order to obtain a CCT diagram for each alloy. Those experimental CCT diagrams show the initiation of reactions, and were compared to the TTT diagrams predicted using MUCG, Fig. 4.4 and 4.5. Only the M_S and B_S should be consistent between the two different types of graphs because TTT diagrams show the equilibrium start of the phase transformation and CCT diagrams show the moment at which the phase transformation causes a noticeable macroscopic strain difference.

There was an unexpectedly large difference in the measured M_S between Alloy 1 and

2, which could not be exclusively due to the small difference in carbon between the alloys. The large difference between the predicted and actual M_S in Alloy 2 could be due to the presence of large prior austenite grains in its microstructure. Several mechanisms relating the refinement of the prior austenite grain size to the lowering of the M_S have been demonstrated experimentally in low alloy steels [171]. The fact that M_S and B_S are higher for Alloy 2 is consistent with the MUCG prediction. Despite being predicted for both alloys, the start of a reconstructive phase transformation is only visible experimentally in the slowest cooling traces in Alloy 2, due to its lower carbon content. The values of both B_S were accurately predicted by MUCG. The overall consistency between the predicted and experimental diagrams was satisfactory. In order to obtain the desired microstructure, an isothermal transformation was required, within the temperature ranges identified as 300-450°C and 410-480°C for Alloy 1 and 2 respectively.

4.2.2   Isothermal transformations

In order to comply with the strength requirements, the isothermal transformation temperatures were chosen as 400°C and 430°C for Alloy 1 and 2 respectively. The heat treatments realised for the alloys are illustrated in Fig. 4.6. The isothermal transformation time was chosen to ensure the bainite reaction would have sufficient time to cease. With the low carbon contents and high transformation temperatures, the reactions were not expected to last more than an hour, but longer transformation times are not expected to affect the bainitic structure formed, once the reaction ceases [93]. The strain change during the isothermal transformations was recorded with respect to time and is shown in Fig. 4.7. A typical S-shape curve was observed for Alloy 1, whereas the transformation started too rapidly in Alloy 2. Both transformations ceased within 20 minutes. The volume fraction of bainite can be calculated from the strain change from this transformation and from the coefficient of thermal expansion of austenite and ferrite [172]. In practice, the results obtained from those calculations are inconsistent with data from XRD [169]. In this project, only XRD was used to determine the volume of bainite and austenite present, since this technique is more accurate and reliable [169].
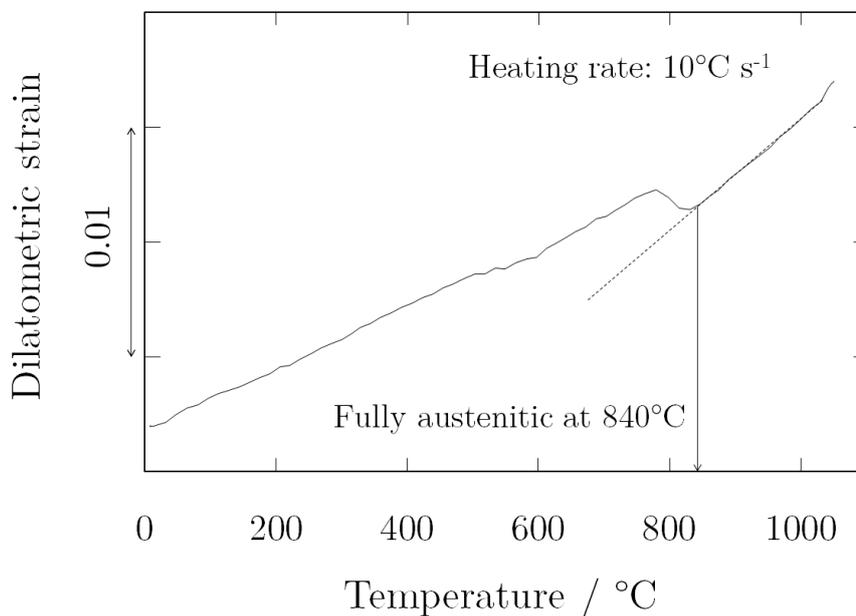
Fig. 4.2: Continuous heating trace at $10°C\,s^{-1}$ for Alloy 1. The phase change from ferrite to austenite was seen to terminate at 840°C.
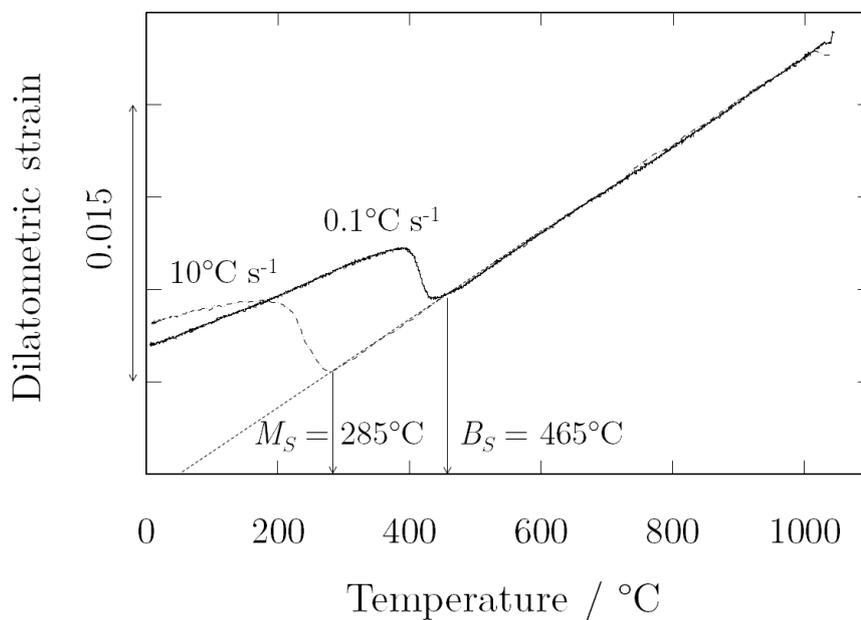
Fig. 4.3: Continuous cooling traces at 10 and $0.1°C\,s^{-1}$ for Alloy 1. The phase change from austenite to martensite and to bainitic ferrite occurred at the M_S and B_S respectively.
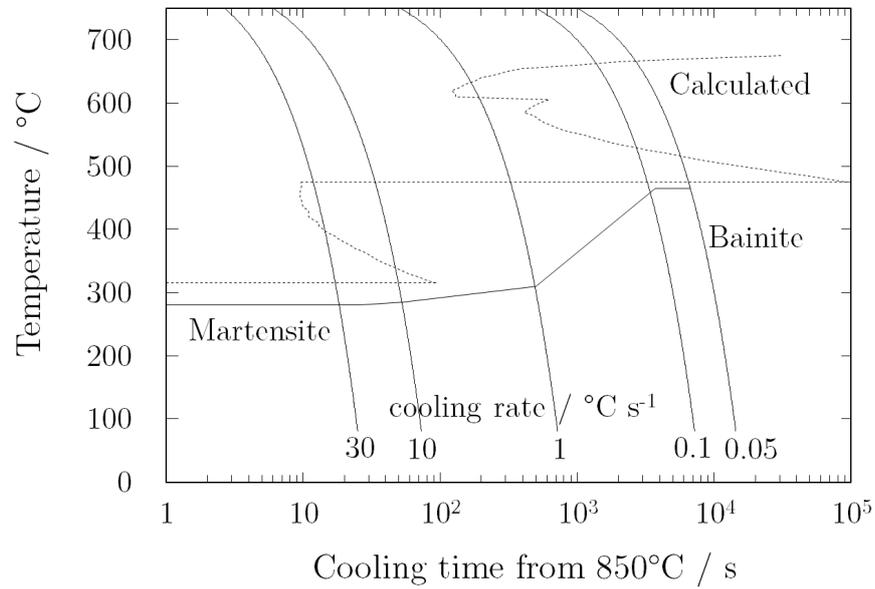
Fig. 4.4: Experimental CCT diagram compared with the calculated TTT diagram for Alloy 1.
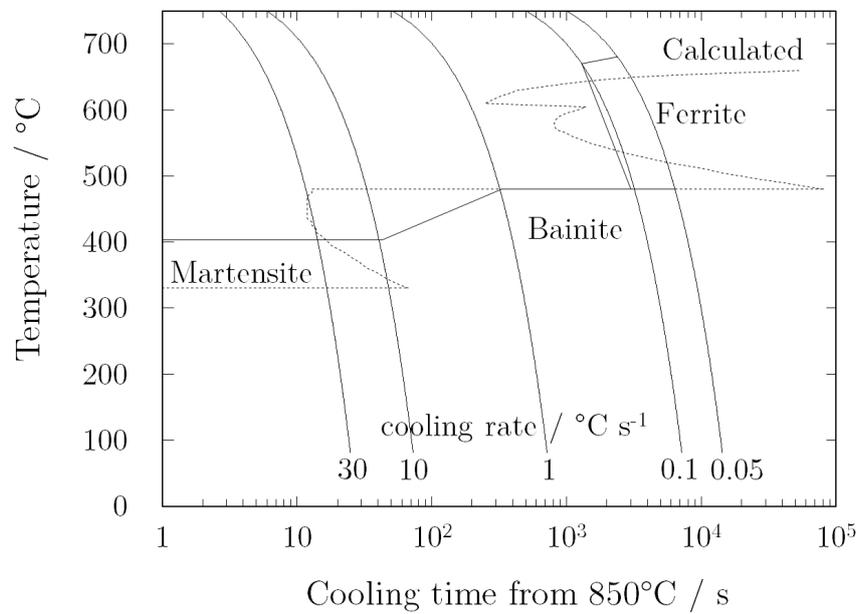
Fig. 4.5: Experimental CCT diagram compared with the calculated TTT diagram for Alloy 2.

(a) Alloy 1

(b) Alloy 2
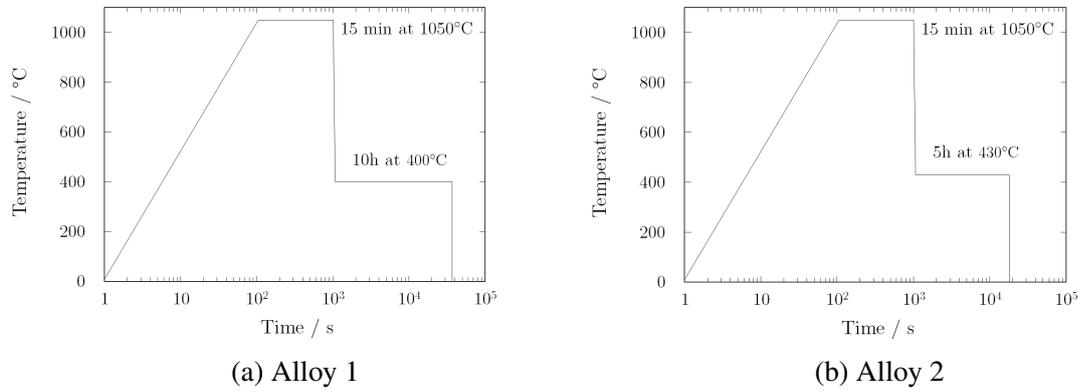
Fig. 4.6: Isothermal heat treatments that Alloy 1 and 2 were subjected to. The long holding times are not critical, and were selected to ensure the bainitic transformation would cease and the time required for it could be recorded.

(a) Alloy 1 - transformation at 400°C

(b) Alloy 2 - transformation at 430°C
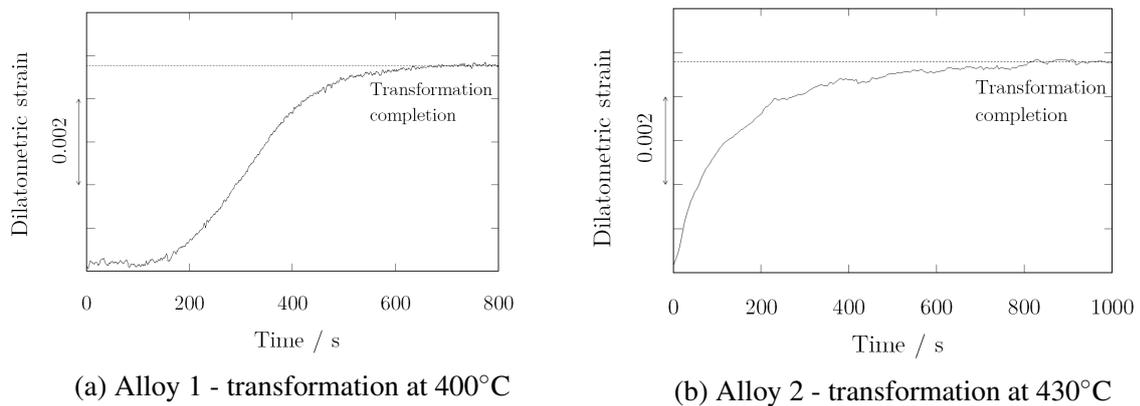
Fig. 4.7: Strain change with respect to time during the isothermal heat treatment.

4.3   Scanning electron microscopy

Scanning electron microscopy was then used to investigate the microstructure generated. All the figures presented in this section were obtained using secondary electrons, since they permit higher resolution imaging. The contrast in SEM micrographs arises due to the difference in packing efficiency of the austenitic and the ferritic phase. The bainitic ferrite, body-centred cubic, is less closely packed than the austenite, face-centred cubic, and therefore more of it is etched away, leading to a darker contrast in secondary electron imaging. At high magnification, this effect is clearer and the austenite phase appears to protrude from the sample surface. Fig. 4.8 exhibits the structure of Alloy 1. A typical bainitic structure is visible, with thin bainitic ferrite laths present, separated by thin films of retained austenite.

Bainitic ferrite uniformity

In Alloy 1, the structure is regular and rather uniform over large areas, as depicted in Fig. 4.9, showing medium and high magnification. It is also visible at low magnification. This is not the case for Alloy 2, which had a significantly more heterogeneous structure, as displayed in Fig. 4.10. Different scales of bainitic ferrite can be seen in each micrograph. Since the bainite laths are randomly oriented within the prior austenite grains, a part of this effect originates from the angle at which the surface of the sample, the viewing plane, intersects the bainite structure. This is shown schematically in Fig. 4.11. The smallest observable bainite thickness is therefore likely to be closer to the actual value of the bainite lath thickness. The visibly largest laths could be of a similar size but seen at a smaller angle between the viewing plane and the lath. The other effect that could be taking place simultaneously is the presence, at a single transformation temperature, a range of bainitic ferrite lath thickness, although it is unclear how to assess both effects separately. At higher magnification, at a grain boundary, the same trend is clear, and very pronounced in Alloy 2, as visible in Fig. 4.12. The average bainite plate thickness was measured for both alloys using the method proposed by Chang: the mean intercept perpendicular to the long axis of the bainitic ferrite plates is measured and multiplied by a factor of $2/\pi$ to find the actual plate thickness [173]. They were found to
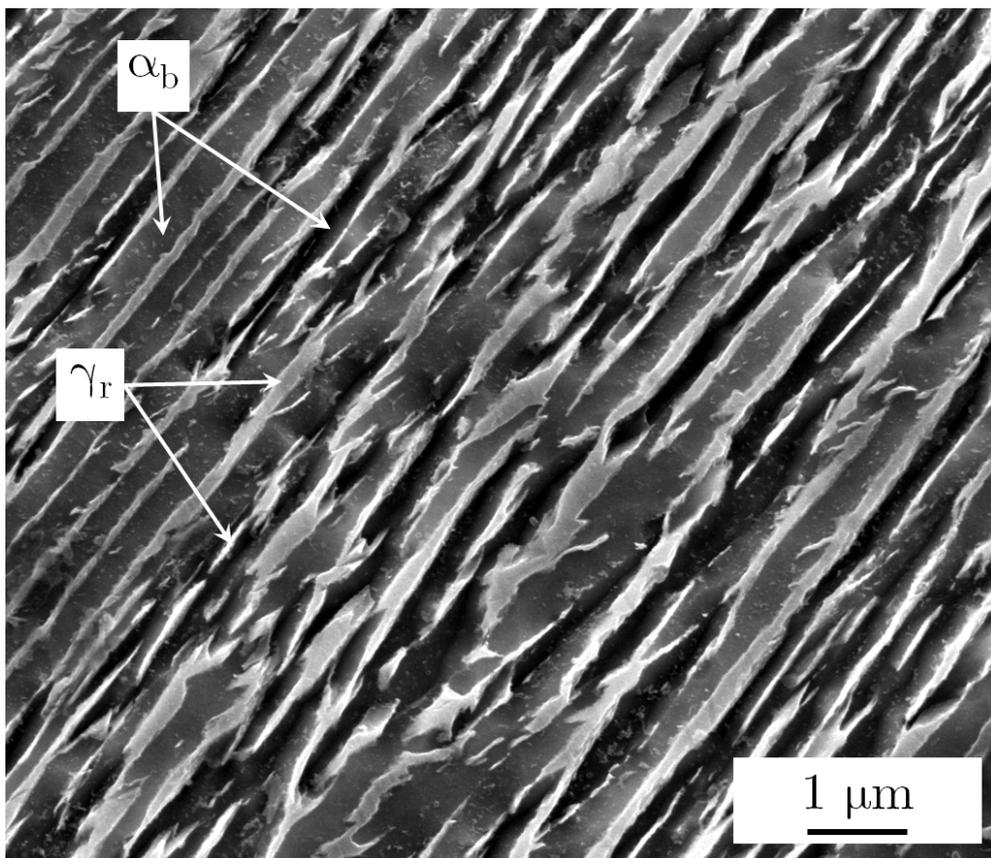
Fig. 4.8: Bainitic structure obtained in Alloy 1. The darker regions are bainitic ferrite, α_b, and the lighter regions are thin films of retained austenite, γ_r.

be: 175 ± 25 nm and 215 ± 30 nm for Alloy 1 and 2 respectively. These values for both alloys are slightly inferior to that anticipated from the relationship between transformation temperature and average plate thickness shown by Bhadeshia [117]. The sub-unit thickness was not measured because they were hard to distinguish.

Blocky austenite presence

The prior austenite grain boundaries remained untransformed in most of the samples. Some regions of blocky austenite are also visible in both alloys, and are much larger in Alloy 2. In order to quantify the size of those regions, the standard ASTM austenite grain size determination could not be used because of the presence of ferrite as the main phase in the microstructure [174]. Instead, the area of the largest visible austenite blocks, delimited by neighbouring ferrite or prior austenite grain boundary, were measured. Due to sectioning effect, they are not quantitatively representative of the actual volume of blocky austenite, because those regions are visibly not equiaxed, as visible in Fig. 4.12. Those values are therefore indicative of a general trend. The largest visible block of austenite and the average block size are presented in Table 4.2, alongside the measured bainite lath thickness. The retained austenite blocks were seen to be visibly larger in Alloy 2.

Table 4.2: Differences in the bainite lath thickness and blocky austenite size between Alloy 1 and Alloy 2.

	Alloy 1	Alloy 2
Bainite lath thickness / nm	175 ± 25	215 ± 30
Largest blocky austenite area / μm^2	150 ± 10	430 ± 15
Average blocky austenite area / μm^2	60 ± 55	280 ± 70

(a) Alloy 1, medium magnification

(b) Alloy 1, high magnification
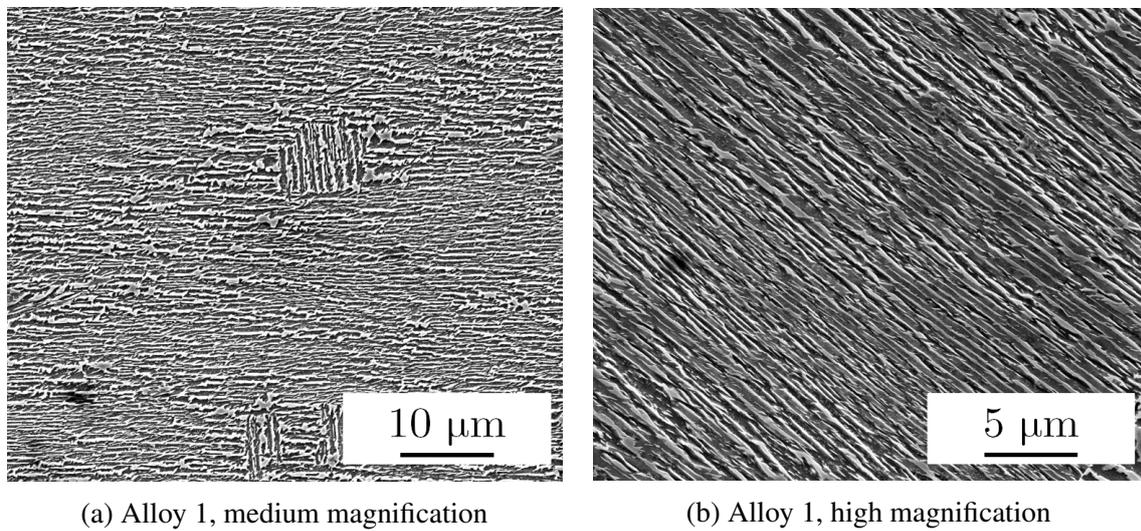
Fig. 4.9: Micrographs displaying the regularity of the bainitic structure in Alloy 1 at medium and high magnification.
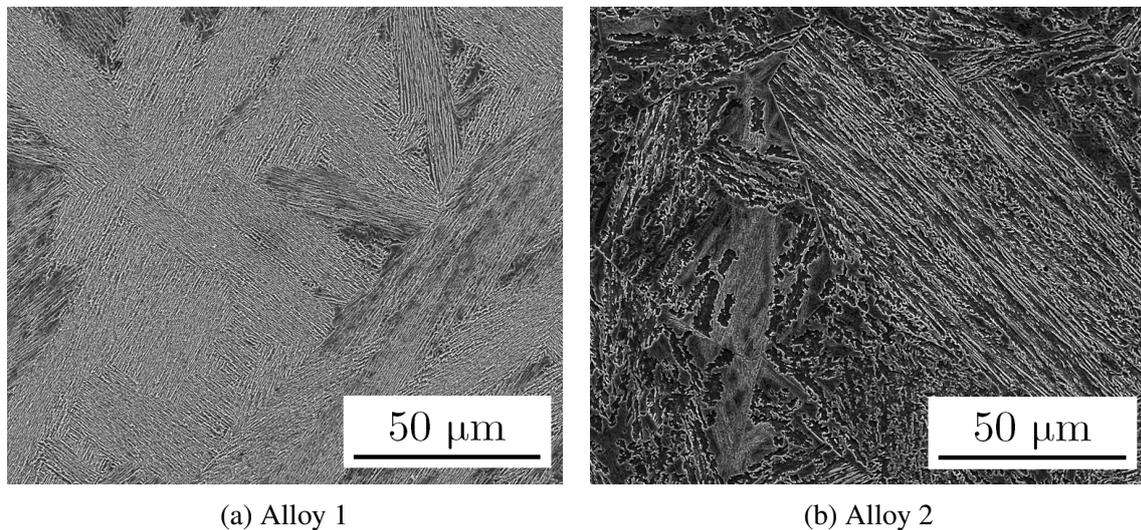
(a) Alloy 1

(b) Alloy 2

Fig. 4.10: Bainitic structure obtained in Alloy 1 and 2. The bainitic structure appeared more homogeneous in Alloy 1 than in Alloy 2.
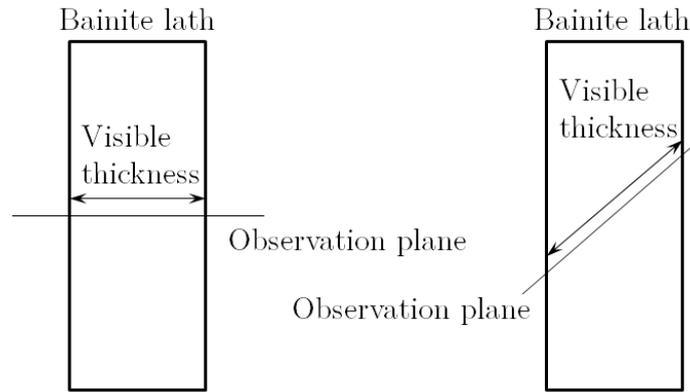
Fig. 4.11: Examples of observation planes intersection with bainite ferrite laths. The first example shows the minimum observable thickness corresponds to the actual lath thickness, while the second examples depicts an arbitrary intersection, showing a larger visible lath thickness. Figure inspired from Chang [173].

(a) Alloy 1   (b) Alloy 2
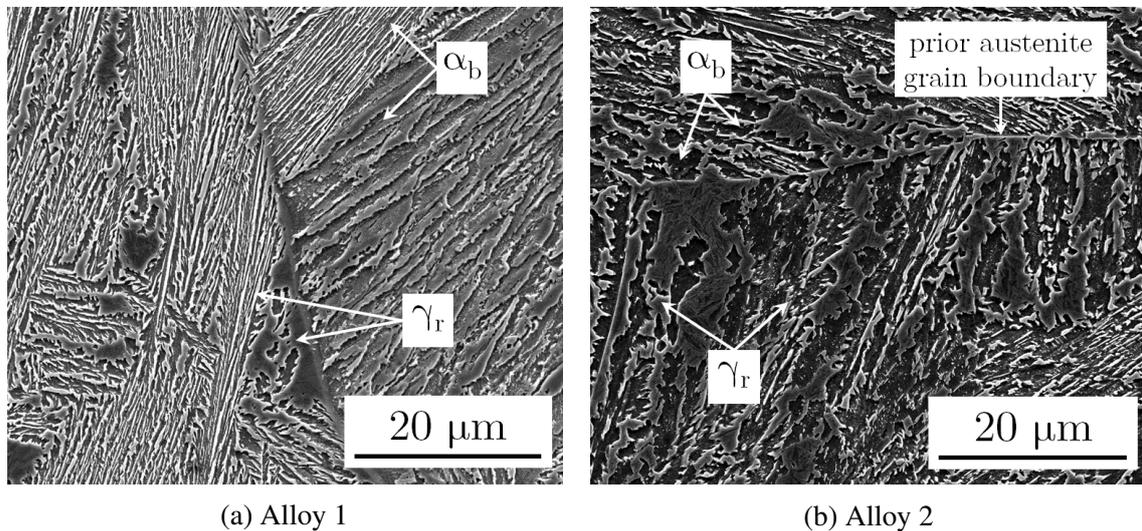
Fig. 4.12: Bainitic structures at prior austenite grain boundaries for Alloy 1 and 2. Large regions of blocky retained austenite were visible in Alloy 2. The lath thickness appeared different in neighbouring prior austenite grains, indicating growth of bainite in different orientations.

Austenite decomposition

The decomposition of the large regions of blocky austenite into martensite in Alloy 1, and into a mixture of bainite and martensite in Alloy 2, during cooling after the isothermal transformation ceased, was also revealed by SEM. This decomposition is a common feature of bainite, and is described in the literature [51]. In Alloy 2, this is visible at any magnification since the large regions of blocky austenite can be seen to have consistently transformed. In Alloy 1, the characteristic lenticular shape of the martensite is displayed in Fig. 4.13, alongside examples of areas in the microstructure where austenite decomposition was observed. In alloy 2, small retained austenite regions were seen to decompose into martensite exclusively, while larger regions would transform predominantly to bainitic ferrite. This bainitic ferrite obtained from austenite decomposition was observed to have a significantly smaller lath size than the bainitic ferrite formed during the isothermal transformation. Several regions in Alloy 2 were imaged, showing examples of austenite decomposition into only martensite, and gradually into mostly bainitic ferrite, presented in Fig. 4.14. In (a), only martensite is present. In (b), it is not clear what phase is forming, but it has characteristics of both martensite and bainite. In (c) and (d), bainite laths appeared in the austenite, and in (e) and (f), the largest regions of austenite had decomposed principally to bainite.

In order to prove this transformation only occurs during cooling in Alloy 1 and 2, the strain with respect to temperature was measured during cooling after the isothermal transformation, and Fig. 4.15 shows that the otherwise expected linear contraction was not observed, but instead, the strain plateaued despite the temperature drop. This demonstrates the formation of a ferritic phase from austenite upon cooling. The final structure of Alloy 2 resembles bainitic alloys with bimodal distribution of the bainitic ferrite lath thickness that can be obtained by two successive isothermal heat treatments, as described by Bhadeshia [93]. In those steels, the first, higher temperature, transformation step forms the coarser structure, and the second step produces a much finer structure.
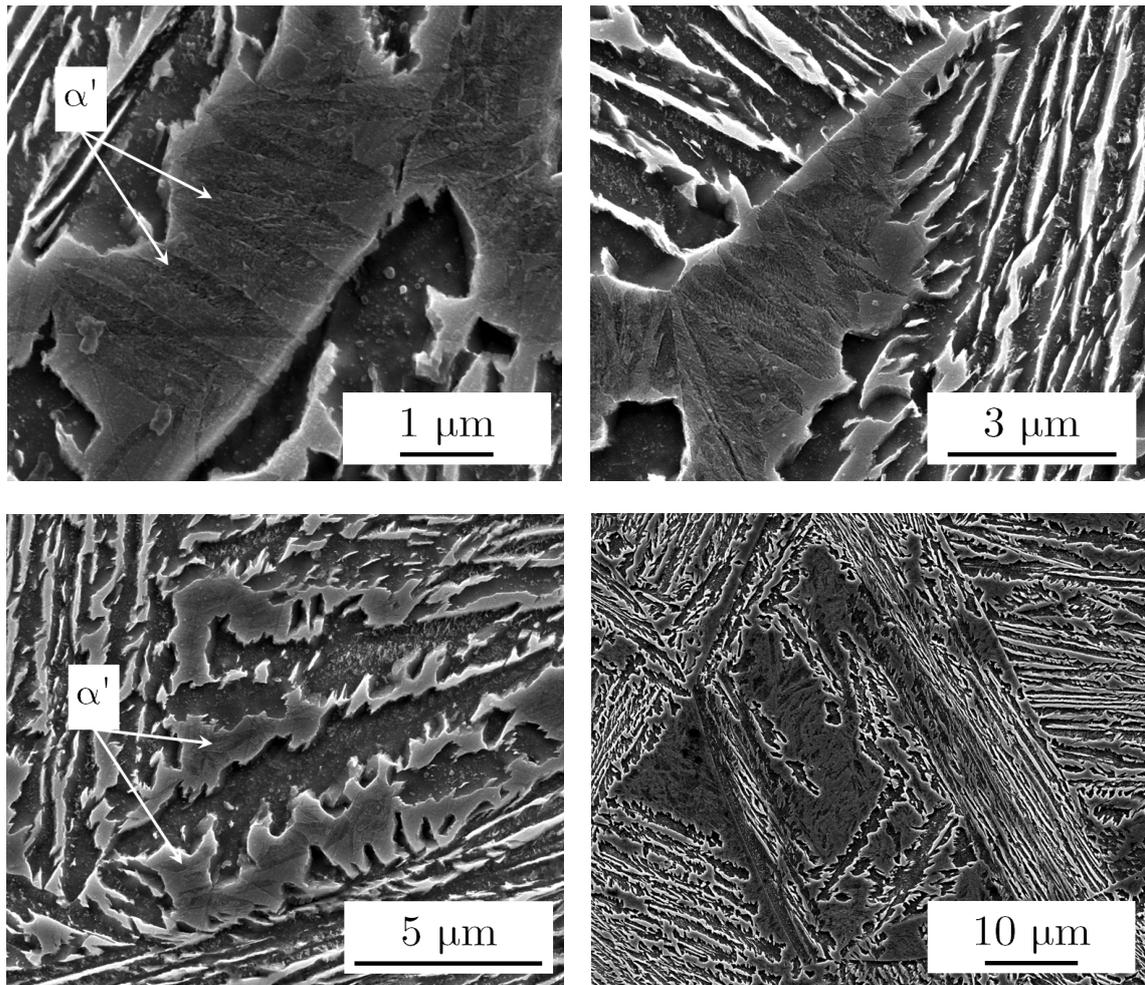
Fig. 4.13: Micrographs displaying the austenite decomposition into martensite (α') in Alloy 1, at varying magnifications.
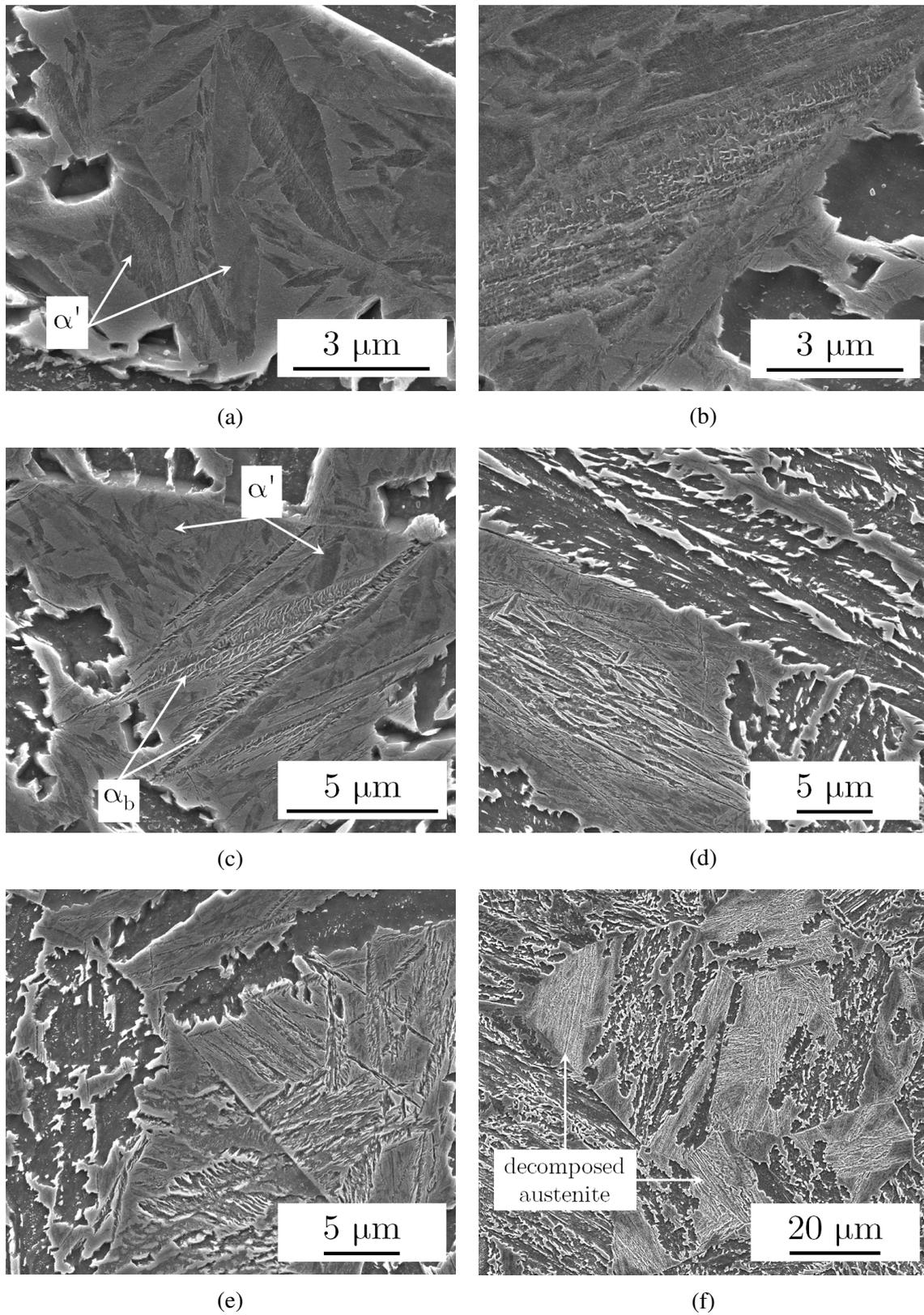
Fig. 4.14: Micrographs displaying the austenite decomposition into martensite (α') and bainite (α_b) in Alloy 2, at varying magnifications. The blocky austenite size influenced the nature of the phase it decomposed into.
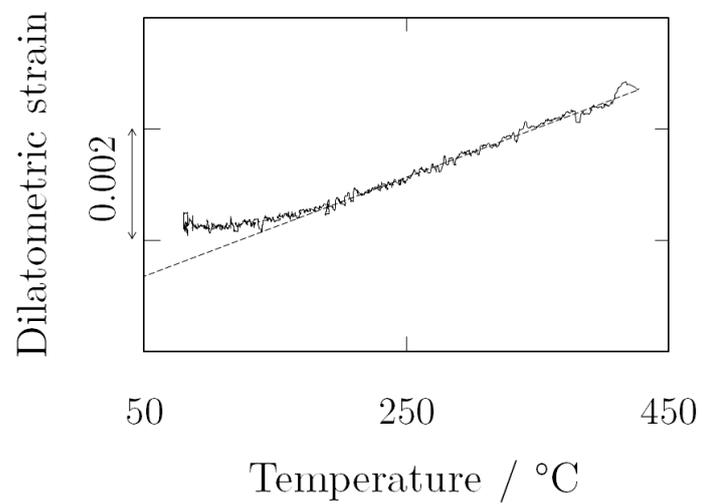
Fig. 4.15: Dilatometry measurement of the strain with respect to temperature upon cooling from 430°C, following the isothermal heat treatment of Alloy 2. The strain did not decrease linearly with temperature, but plateaued, indicating the decomposition of some austenite into a ferritic phase, martensite or bainite.

4.4   X-ray diffraction

In order to quantify the fraction of ferrite and austenite, XRD scans were obtained using the Cu K_{α_1} for both alloys between 40 and 125° 2θ. This allowed five ferrite peaks and six austenite peaks to appear, and ensured a reliable quantification of the phase fraction. Fig. 4.16 depicts the XRD pattern obtained for Alloy 1. Only a few peaks have been indexed for clarity. All peaks in the pattern were fitted using Rietveld refinement, described in Chapter 3, and as specified by McCusker [167]. Using the Highscore Plus software, an accuracy of $\pm$ 0.01 in the estimated phase fraction has been reported in steels when quantifying the austenite to ferrite ratio [163, 169, 175]. In order to confirm this error, the data obtained were fitted, and the fits were allowed to vary, until it was no longer accurate. This corresponded to a variation in phase fraction of approximately 0.01. The austenite fraction was estimated to be 0.11 $\pm$ 0.01 and 0.17 $\pm$ 0.01 for Alloy 1 and 2 respectively.
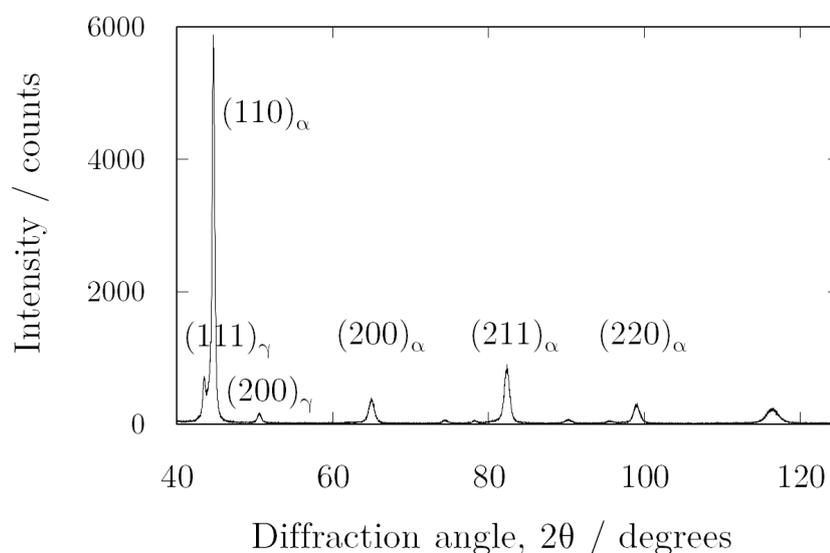
Fig. 4.16: XRD spectrum for Alloy 1. The austenite and ferrite peaks were fitted to determine the phase fraction of austenite, which was estimated to be 0.11 $\pm$ 0.01.

4.5   Hardness

The macroscopic Vickers hardness was measured using a 30 kg load. This ensured the heterogeneity of the structure on a large scale did not affect the measurements, but an average and reproducible value was obtained. Ten measurements were performed for each alloy. The measured values of hardness were 390 ± 8 HV30 and 355 ± 5 HV30 for Alloy 1 and 2 respectively. Those values correspond to the usual hardness of bainitic ferrite transformed at those temperatures [117]. The relatively close values between Alloy 1 and 2 can be explained from the significant austenite decomposition into fine bainite and martensite in Alloy 2. This means that despite having a significantly larger average bainite plate thickness, which would cause a lower hardness, the hardness is still close to that of Alloy 1. Indeed, the bainitic ferrite lath thickness is related directly to the strength of the alloys because the dislocation glide path is limited by the thickness of the lath [176]. The values of Vickers hardness using a 30 kg load were multiplied by 3.3 in order to estimate the equivalent ultimate tensile strength, because this relation has repeatedly been observed empirically [127, 156]. The values of strength were estimated to be 1290 MPa and 1170 MPa for Alloy 1 and 2 respectively, the former of which satisfies the desired target value of 1230 MPa. Table 4.3 summarises those results.

Table 4.3: Hardness and estimated yield strength (YS) and ultimate tensile strength (UTS) for both alloys. The ratio between hardness and UTS was estimated to be approximately 3.3 and the ratio between YS and UTS was estimated to be close to 0.7, as graphically presented in Fig. 2.1.

Alloy	Vickers hardness / HV30	Estimated YS / MPa	Estimated UTS / MPa
Requirements	370	860	1230
Alloy 1	390 ± 8	900	1290
Alloy 2	355 ± 5	820	1170

4.6   Carbide characterisation

4.6.1   SEM

SEM is not usually used for carbide characterisation, since it only provides qualitative information on the carbide morphology. Neither the crystal structure nor the phase fraction of carbides can be determined with SEM when the volume fractions involved are small. It was nevertheless used for Alloy 2 because TEM sample preparation was challenging. Carbides could only be identified with certitude in the regions of retained austenite that had decomposed to bainite during cooling after the isothermal heat treatment. Fig. 4.17 illustrates an example of the structure in such regions. Many carbides can be seen, growing at an angle of approximately 60° from the long axis of the bainitic ferrite, as is typical of carbides growing within bainite laths [93]. The apparent length of those carbides is measured to vary between 20 and 250 nm, although sectioning effects induce this observation. Their volume fraction was estimated using XRD. The higher carbon content in retained austenite compared to the average composition of the alloy is suggested as the reason why carbides were growing in larger numbers in those regions.

4.6.2   XRD

Cementite identification

For carbide identification, the scan range was 25 to 70° 2θ because the strongest carbide reflections are observed in that range. In the light of the small volume fraction expected, a long dwell time of 20 s was used in order to maximise the signal to noise ratio. The data were processed using Rietveld refinement in order to quantify the ferrite and austenite phases and provide an initial calculated pattern to fit the data. The additional peaks that did not fit this pattern were indexed by comparing the peak location of carbide phases in the different databases used. Only one or two peaks were detected in XRD, and they could only be attributed to cementite. It is common to use more peaks to identify phases with XRD, but the same cementite file, from Shimura [177], in the ICDD database, was fitted using more
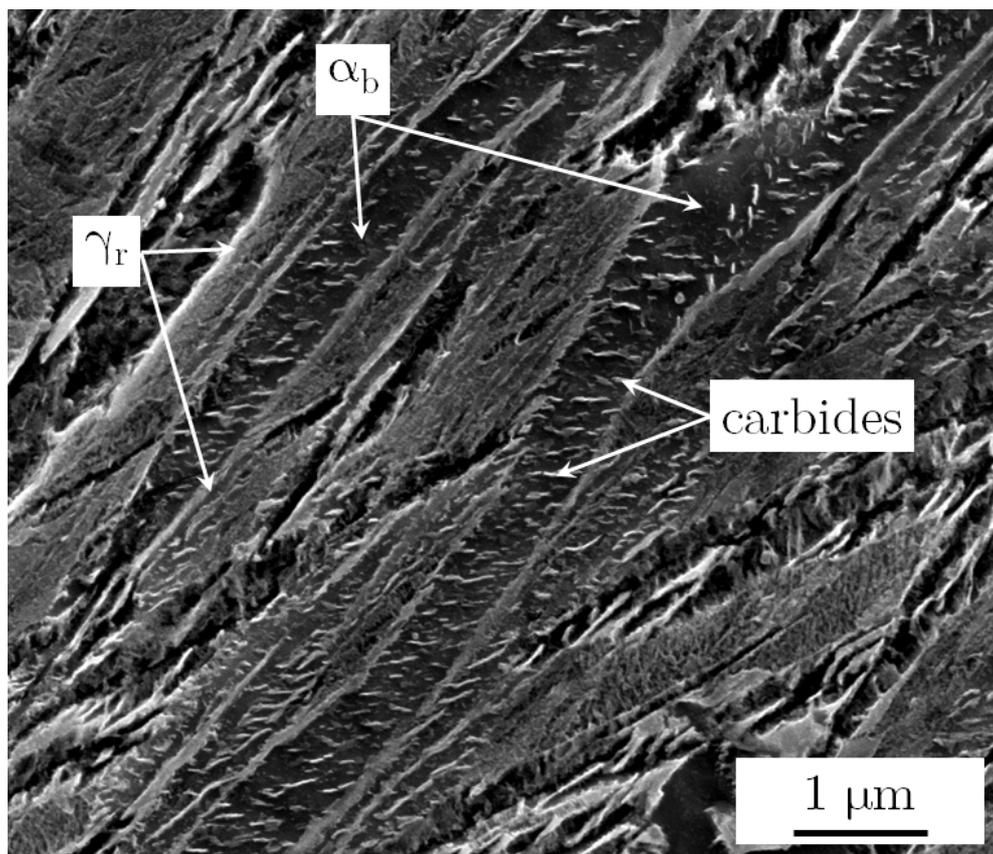
Fig. 4.17: Micrograph showing the presence of carbides within the bainitic ferrite, in a region of retained austenite that had decomposed to a mixture of bainite and carbides during cooling to room temperature, in Alloy 2.

peaks in larger scale alloys, with results presented in Chapter 6. Those results confirmed unequivocally the presence of cementite. Fig. 4.18 presents the indexed XRD scans realised for both alloys. The peak at 28.6° 2θ is probably due to contamination, but the source could not be identified. The peaks at 40.1° and 58.1° 2θ were both due to the Cu K_β X-rays satisfying the Bragg condition for the (110) and (200) ferrite planes respectively. Despite using the thickest available nickel filter, they were not fully removed. The identified cementite unit cell was orthorhombic with lattice parameters: a = 4.50 Å, b = 5.15 Å, c = 6.75 Å.

Phase fraction determination

The presence of a single sharp cementite peak, indexed as (111), signifies the presence of rather large diffracting crystals [162], which is consistent with the carbides of approximately 250 nm in length observed with SEM. The fact that only one or two peaks were observed was unexpected. In fact, calculating ideal XRD diffraction patterns from the cementite phase indicated that other peaks should be visible too, as shown in Fig. 4.19. When the (111) cementite peak was fitted, in the dashed line pattern, it appeared that the (200) and (121) reflections should also be visible. For clarity, the calculated scans were displayed until 45° 2θ only. Several other peaks also appeared in the calculated pattern, with the same interpretation applying. There can be two explanations for those reflections being absent from the experimental data:

1. Cementite crystals tend to align in a specific direction that make the set of (111) planes satisfy the Bragg condition rather than other planes. Since the cementite crystals were present in a randomly oriented bainitic ferrite matrix, texturing is not expected to be detectable with X-rays.

2. The cementite crystals are longer in the [111] direction, leading to more (111) planes satisfying the Bragg condition. It is not clear why this should be the case, but this behaviour was suggested as the cause of the presence of the sharp (111) peaks presence.

In order to quantify the fraction of cementite, an ideal XRD diffraction pattern was simulated, ensuring that no other peak than the (111) would be distinguishable from the background,
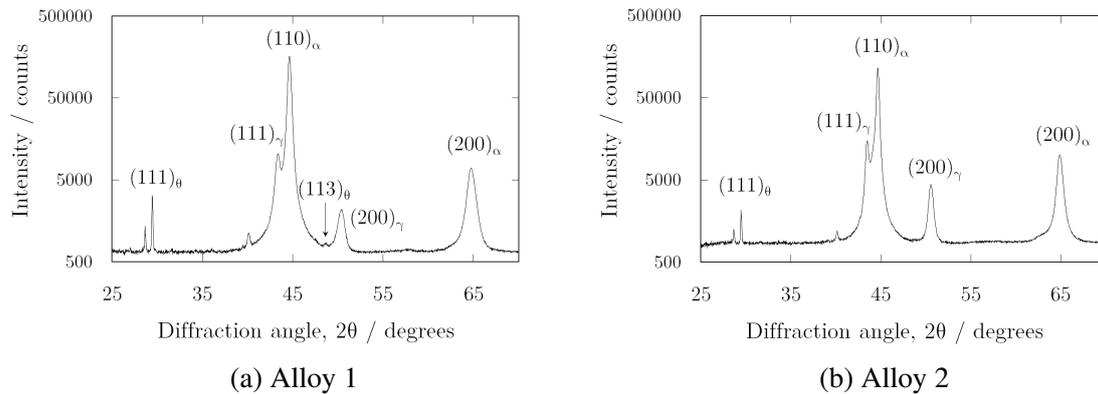
Fig. 4.18: XRD spectra used for carbide identification. Only one or two cementite (θ) peaks could be indexed in Alloy 1 and 2. The results presented in Chapter 6 confirmed the presence of cementite using additional indexed peaks.

shown as the dashed line in Fig. 4.19. In this case, the calculated (111) reflection was weaker than that in the experimental data. The cementite volume percent in both patterns was calculated as 1.73% and 0.26% for the pattern in which the (111) peak was fitted and the one in which it wasn't respectively. This gave the upper and lower limits of the actual cementite phase percent present in the alloy, since in the first case, many peaks are missing in the experimental data compared to the simulation and in the second case, the (111) peak is not fitted to the experimental data but no other peaks are visible, as is the case for the experimental pattern. The same process was realised for Alloy 2, in which case the cementite percent was estimated as 0.36-1.20%. Realistically, the amount of cementite is likely to be higher in Alloy 1 since two peaks are visible and the (111) peak appears more strongly.

4.6.3 TEM

Carbides characterisation

TEM was used to exhibit the carbides morphology using dark field imaging, and to confirm the crystal structure of the carbides identified as cementite using diffraction patterns. Two regions of interest were imaged in Alloy 1, Fig. 4.20 and 4.21. It was not possible to obtain satisfactory TEM samples from Alloy 2. The carbides appeared rod-shaped, and always present within the bainitic ferrite laths. No carbide was visible at the austenite ferrite boundary, where it could favour brittle fracture in hydrogen environments, indicating that
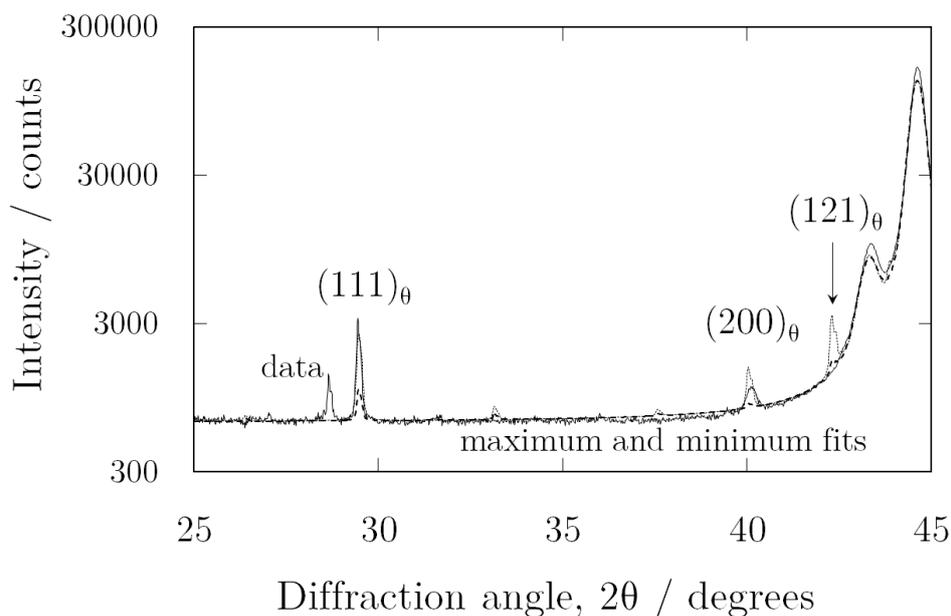
Fig. 4.19: XRD spectrum for Alloy 1 presented with the maximum and minimum fits. The maximum fit was calculated by fitting the experimental $(111)_\theta$ peak. The minimum fit was calculated by allowing the $(111)_\theta$ to be the only peak distinguishable from the background signal.

the silicon content was sufficient to prevent cementite precipitation from austenite. Indeed, Materkowski reported the interlath carbides as crack initiation sites in tempered martensitic steels with 0.30 wt% C, during Charpy impact tests [178]. Cementite was the only carbide that fitted the diffraction patterns retrieved from TEM. The calculated d-spacings from the diffraction pattern correspond to those of cementite, and the ferrite (101) type reflections and the cementite (103) type reflections are close in the diffraction patterns, which agrees with the Bagaryatskii and Isaichev orientation relationships [103]. Those are the common orientation relationships between ferrite and cementite growing within the bainite laths [93].

Consistency with XRD results

Both techniques led to the identification of the carbides as cementite. To confirm this result, d-spacings of the visible cementite reflections in the TEM diffraction patterns were calculated and compared to those d-spacings calculated using the unit cell lattice parameters identified by XRD. The results were consistent, and are presented in Table 4.4. Despite many peaks

missing from the XRD data, cementite could still be formally identified, using TEM as a complimentary technique.

Table 4.4: Comparison of the d-spacings obtained from diffraction patterns in TEM and from the cementite unit cell characterised by XRD. The errors in the TEM measurement were due to the size of the reflection spots.

Cementite diffracting planes	TEM measured d-spacing	XRD calculated d-spacing
(210)	2.07 ± 0.025	2.060
(103)	2.03 ± 0.03	2.010
(310)	1.43 ± 0.015	1.442

(a) Bright field

(b) Dark field

(c) Diffraction pattern
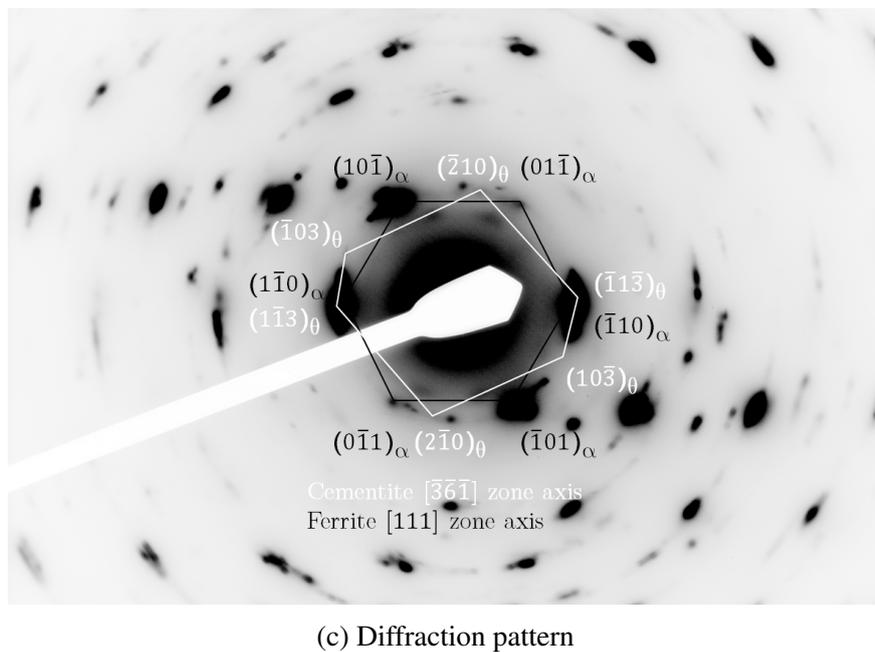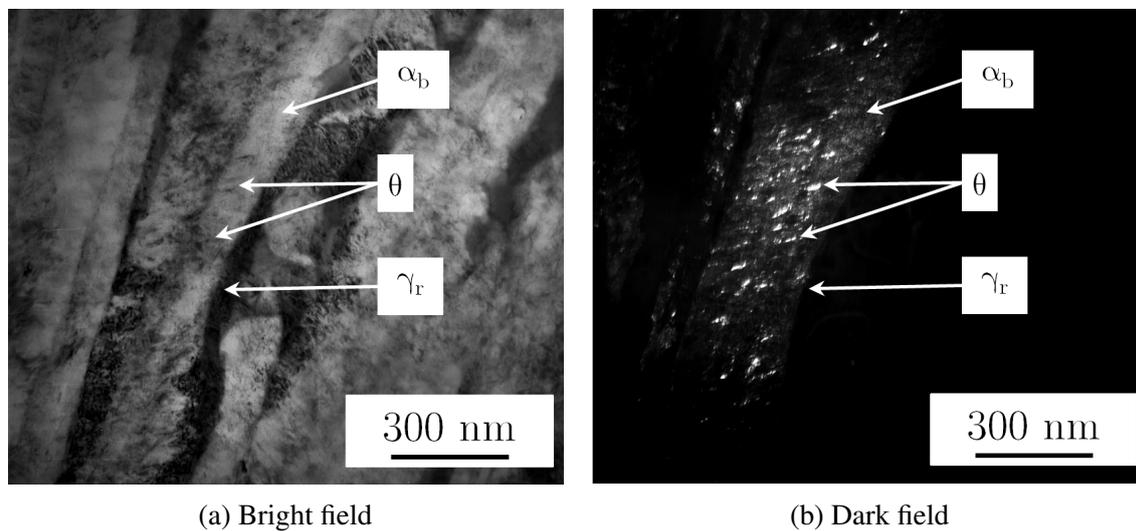
Fig. 4.20: TEM characterisation of cementite within the bainitic ferrite in Alloy 1, in the first region of interest. The diffraction pattern was obtained using a selected area aperture that encompassed the region of interest. The dark field image was formed using the indexed $(\bar{2}10)$ cementite reflection.
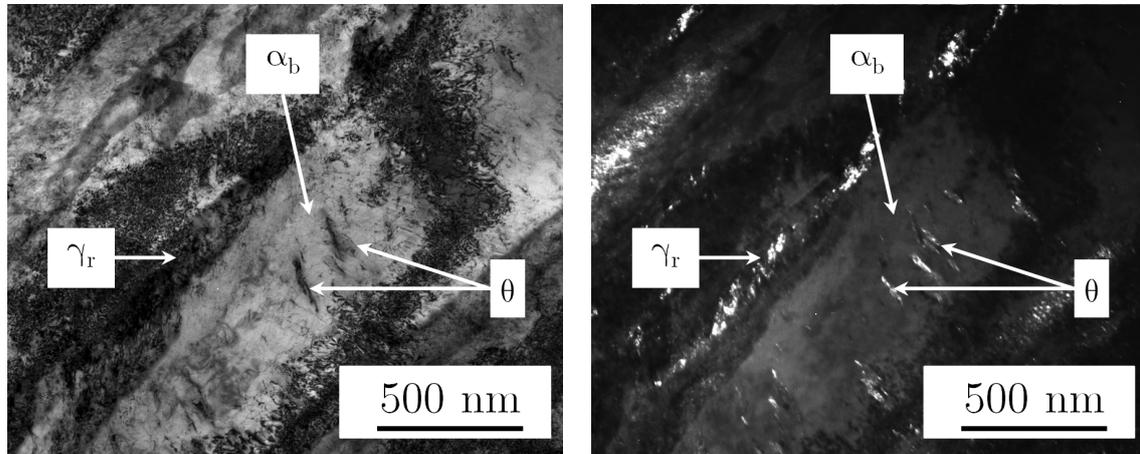
(a) Bright field

(b) Dark field
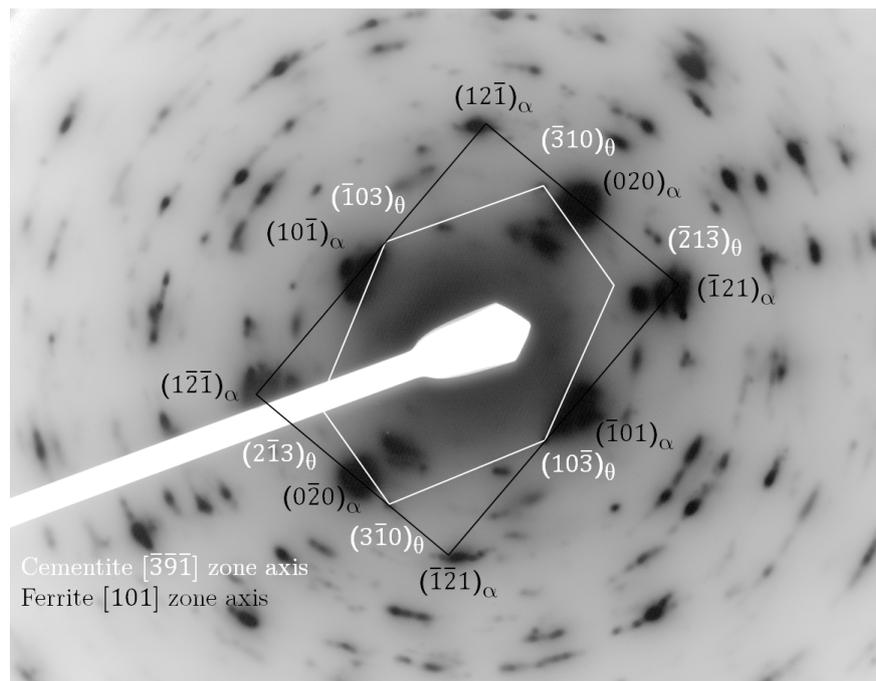
(c) Diffraction pattern

Fig. 4.21: TEM characterisation of cementite within the bainitic ferrite in Alloy 1, in the second region of interest. The diffraction pattern was obtained using a selected area aperture that encompassed the region of interest. The dark field image was formed using the indexed ($\bar{1}$03) cementite reflection. The objective aperture used was too large to allow only the carbide reflection to be used to form the final image, and a neighbouring austenite reflection was also partially visible.

4.7 Thermal Desorption Spectroscopy

The results presented in this section are only qualitative because only few samples of the laboratory scale alloys were available, and they all had significantly different geometries.

4.7.1 Experimental method

Aqueous hydrogen charging

First, the samples were ground gradually using P600, P1200 and P2500 grit SiC paper in order to reveal a fresh surface. An individual sample was then spot-welded onto a thin steel rod, and both the steel rod and the sample were covered in insulating paint, except for the charging area. For cylindrical samples, this area excluded the top and bottom faces. For sheet samples, this area excluded the thin edges. A 3.5 wt% NaCl and 0.3 wt% NH_4SCN (ammonium thiocyanate) charging solution was prepared. Ammonium thiocyanate serves as a hydrogen recombination poison, meaning the ability of atomic hydrogen formed electrochemically at the surface of the steel to form H_2 is hindered. This in turns favours ingress into the steel. The sample was then immersed in the solution, with a spiral-shaped platinum electrode previously placed along the edges of the container. Immediately, a Gamry Interface 1000 potentiostat in galvanostat mode was used to generate a current of $-1\,\mathrm{mA\,cm^{-2}}$ between the platinum counter electrode and the sample, the working electrode. This lead to the reduction of hydrogen ions in solution into atomic hydrogen at the surface of the steel. The solution was constantly stirred magnetically. The charging was performed for 48 hours. Only one sample was charged at a time, since practical experience showed that the differences in spot welding could lead to hydrogen charging discrepancies between identical samples charged in identical conditions.

Thermal desorption apparatus

Fig. 4.22 shows the TDS setup schematically. First, the gas chromatography detector was calibrated using a standard helium and hydrogen gas mixture with a 60 parts per million hydrogen. The helium carrier gas was then passed through the gas chromatograph in order to

quantify the hydrogen impurity level present in it. Two types of experiment were performed in order to assess the hydrogen trapping of the designed alloys. In both cases, samples were ground before being placed in the TDS furnace so that any oxide on the surface could be removed. In the first type of experiment, alloys were left in air after charging, so that all the diffusible hydrogen would escape the samples and only the strongly trapped hydrogen would be detected. In the second case, the TDS was performed directly after charging so that as much as possible of the hydrogen present in the steel at the end of the charging process could be detected. In that case, the furnace chamber was purged for twelve minutes before the signal could start being acquired because the oxygen and nitrogen present in air prevent the hydrogen from being detected. For both, the samples were heated at a rate of $100°C$ per hour, from room temperature until $300°C$. Above that temperature, the gas chromatography consistently detected the presence of hydrogen, even in tests without samples. This could be due to oxidation reactions from impurities, water, or other substances in the tube. The cause could not be identified and runs could not be performed above this temperature, although strong traps might only show above it. A solution to this problem is presented in Chapter 6, through the use of the complementary electrochemical permeation technique, in which strong traps can be detected.

4.7.2   Results

TDS after room temperature desorption

Initially, both alloys were tested after room temperature desorption, as this is a simple way to detect strong traps [95]. Removing diffusible hydrogen at room temperature before TDS can only show trends, since the trap binding energies can only be determined from the TDS peak temperature. Interpretation of the signal is easier since there is no diffusible hydrogen present in the samples, therefore all hydrogen evolved in this case is due to traps. Samples for this first experiment were cylindrical with a diameter of 8 mm and heights varying between 5 and 12 mm. Those dimensions are not ideal since in 48 hours, hydrogen saturation cannot be achieved in samples with this thickness. Yet, trapping behaviours could still be qualitatively investigated. No signal could be detected in Alloy 2. A weak signal was detected for Alloy 1,
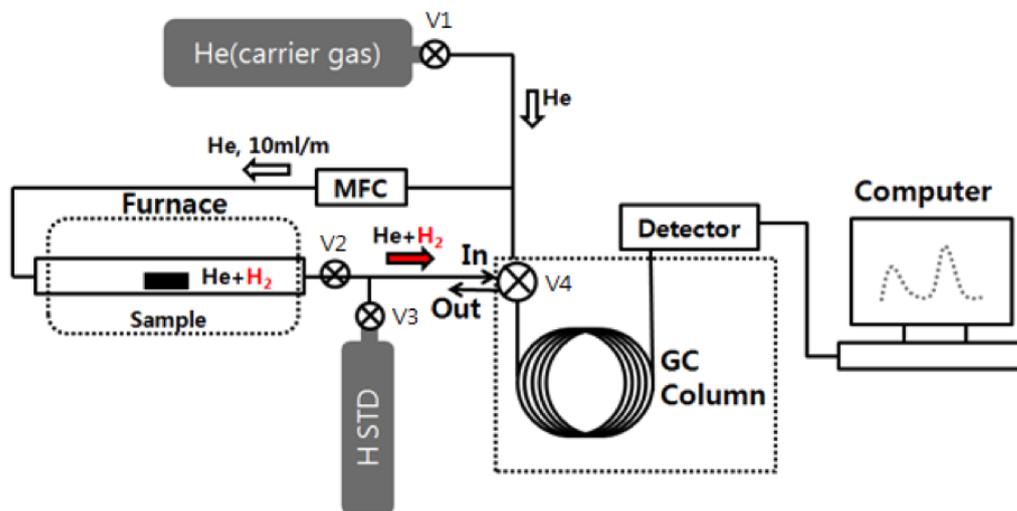
Fig. 4.22: Schematic of the TDS setup. A mass flow controller was used to ensure a constant flow of carrier gas. A pure He carrier gas was sent through the furnace where the sample was heated up and released previously charged hydrogen. The hydrogen and helium mixture was then sent to an Agilent technologies 7890B gas chromatography (GC) column that measured the quantity of hydrogen present compared to a standard reference. Diagram reproduced from Ryu [179].

which was quantified as 0.036 ppm of hydrogen. This showed the presence of weak traps, with trapping ability much below the most efficient strong traps known, such as vanadium carbides, that can trap up to a few ppm of hydrogen [95]. Two additional isothermal heat treatments were then performed for Alloy 1: 25 minutes and 1 hour at 400°C. The first time was chosen as it is close to the minimum required time for the full bainitic transformation to cease, and the second is somewhere between that and the initial 10 hour hold. Comparing the trapping ability of Alloy 1 following three different heat treatments could indicate whether the transformation time has a significant effect on trapping or not. Fig. 4.23 illustrates the TDS curves for all three samples. Trapping is seen to increase with increasing hold time. No hydrogen could be detected for the sample transformed for the shortest time. The TDS peak position on the temperature axis is strongly correlated to the trap binding energy [180]. The peak location for the sample transformed for 1 hour is approximately 165°C, while it is 115°C for the sample transformed for 10 hours. The trapped hydrogen quantity for the former was calculated to be 0.013 ppm. Those results suggest that stronger traps are present

in the sample transformed 1 hour but a significantly lower concentration is trapped. This indicates that the traps are fewer in number.

TDS directly after charging

Since the trapping was small for both alloys after room temperature degassing, TDS was performed directly after charging. In that case flat samples were used, with varying dimensions. The contribution of austenite to the overall behaviour of hydrogen in the alloys was investigated by comparing the TDS traces of samples with and without austenite. As part of the heating process, the furnace was set to reach 500°C, at which point it was seen from dilatometry that all the austenite should have decomposed. This way, the only microstructural difference between the two TDS experiments would be the presence of austenite during the first test, and the absence of it in the second one. XRD was used to confirm that the austenite fraction had decreased close to 0 after the initial TDS run. Fig. 4.24 and 4.25 illustrate those differences. The quantity of evolved hydrogen for the four samples was: A1 - 0.9 ppm with austenite, 1.0 ppm without austenite; A2 - 4.1 ppm with austenite, 2.3 ppm without austenite. Those values could not be used to draw any conclusions because different sample geometries were used due to the limited availability of laboratory-scale alloys, and because samples were not saturated with hydrogen. Nevertheless, two constant trends could be observed for both alloys:

1. The TDS peak temperature was higher when austenite was present. This indicates that the austenite and ferrite interface plays a significant part in the overall trapping behaviour, as described by Turnbull [50].

2. At temperatures above the peak temperature, there was always more hydrogen evolved in the sample with austenite, visible as the TDS curve of the sample with austenite being above the other curve at any given temperature above the peak temperature. This behaviour confirms that austenite can oppose the egress of hydrogen from the steel. It therefore implies that it must prevent the ingress of hydrogen into the steel.
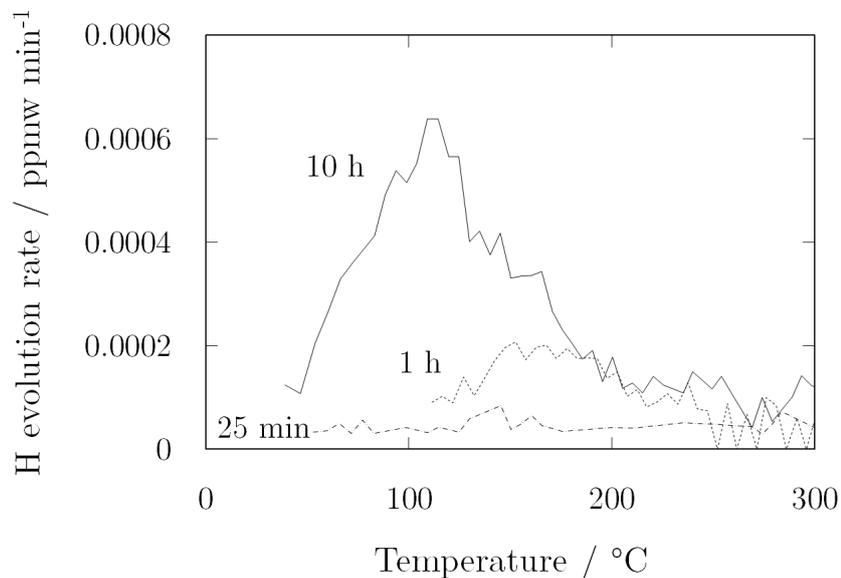
Fig. 4.23: TDS curves obtained after room temperature hydrogen desorption for samples of Alloy 1 isothermally transformed at 400°C for either 25 minutes, 1 hour or 10 hours. The amount of hydrogen released increased with transformation time. The values were all small and this trapping was not predicted to have a significant impact on a large scale.
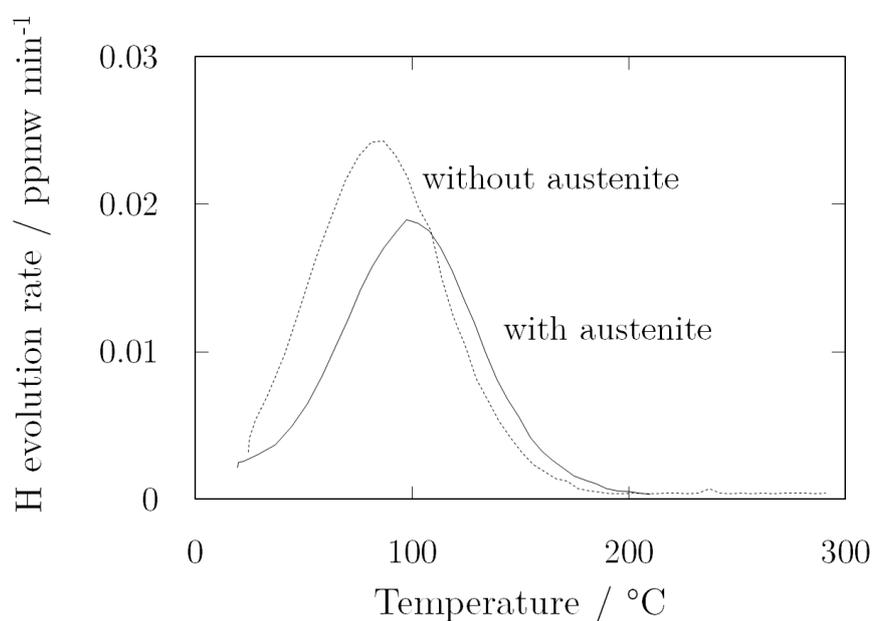
Fig. 4.24: TDS curves obtained directly after charging for Alloy 1. The difference between the TDS traces when austenite was present or absent confirmed the proposed hindrance of austenite to hydrogen diffusion.
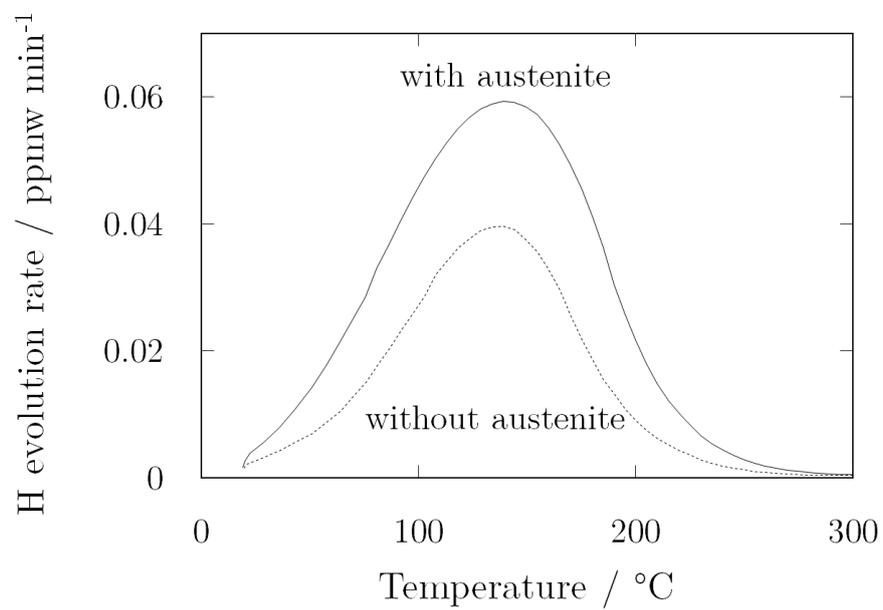
Fig. 4.25: TDS curves obtained directly after charging for Alloy 2. The difference between the TDS traces when austenite was present or absent confirmed the proposed hindrance of austenite to hydrogen diffusion.

4.8   Conclusions and determination of the composition of large scale alloys

Many characterisation techniques were used to investigate the structure and properties of the novel alloys. Table 4.5 summarises all the parameters and properties characterised for Alloy 1 and 2. They successfully met most of the required expectations: the hardness of Alloy 1 was satisfactory, both alloys possessed an austenite fraction comprised between 0.1 and 0.2, and cementite was shown to be only present within the bainite laths using TEM, although its phase fraction could not be characterised precisely. The austenite fraction above 0.1, measured with XRD, was shown using TDS to provide an effective barrier to hydrogen ingress. Still, a few modifications were made to the compositions of Alloy 1 and 2 for the manufacturing of large scale alloys, based on the results presented in this chapter.

Increase in carbon content

Alloy 2 displayed a microstructure composed of large areas of austenite that had decomposed to martensite and bainite. This structure was a direct cause of a carbon concentration too low, which forced a too high transformation temperature. This makes the structure hard to control by simple heat treatments. Additionally, the hardness of that alloy did not meet the set requirement. Conversely, the structure of Alloy 1 was considerably more homogeneous, and its hardness was satisfactory. Consequently, the lowest carbon concentration of the two large scale alloys was set to 0.35 wt%, close to that of Alloy 1. The highest one was selected as 0.45 wt%. This serves two purposes:

1. Two similar alloys can be empirically compared and the alloy with the most promising mechanical properties can be assessed and selected.

2. Since neither alloy displayed hydrogen trapping as desired, increasing the carbon content is expected to favour the formation of carbides and improve trapping ability.

Decrease in nickel and silicon content

Because of the unintended carbon content differences between both laboratory scale alloys,

the effect of a difference in nickel content was not clear. The composition was kept at 3 wt%
to limit the alloy costs. Silicon at 1 wt% was enough to prevent the formation of cementite at
the austenite ferrite interface. Since no ε-carbide could be characterised in either alloy, and
in order to optimise carbide formation within the bainitic ferrite laths, the silicon content was
lowered to 1 wt% for both alloys. The suggested compositions for the two large scale alloys
are presented in Table 4.6.

Table 4.5: Characteristics of Alloy 1 and Alloy 2.

Parameters and properties	Alloy 1	Alloy 2
Carbon content / wt%	0.36	0.31
Bainitic reaction range / °C	300-460	410-480
Selected transformation temperature / °C	400	430
Retained austenite fraction	0.11 ± 0.01	0.17 ± 0.01
Bainitic ferrite lath thickness / nm	175 ± 25	215 ± 30
Vickers hardness / HV30	390 ± 8	355 ± 5
Estimated yield strength / MPa	900	820
Estimated ultimate tensile strength / MPa	1290	1170
Identified carbide	cementite	cementite
Calculated carbide volume percent	0.263-1.73%	0.363-1.2%

Table 4.6: Nominal compositions in wt% of the two large scale novel bainitic steels designed,
compared to the actual compositions of Alloy 1 and Alloy 2.

Name	C	Si	Mn	Cr	Ni	Mo
Alloy 1 - actual	0.36	1.88	0.14	0.99	3.01	0.25
Alloy 2 - actual	0.31	1.03	0.11	0.99	3.57	0.22
Alloy 3	0.35	1	0.1	1	3	0.25
Alloy 4	0.45	1	0.1	1	3	0.25

Chapter 5

Characterisation of large scale novel alloys

5.1 Introduction

The purpose of the work presented in this chapter is to characterise the microstructure of the novel alloys produced as 100 kg melts. Several heat treatments were performed for each alloy. The aim was to achieve a mixture of satisfactory mechanical properties and hydrogen trapping abilities, and to assess the effect of heat treatments on those. The hydrogen behaviour and mechanical properties of both alloys are presented in Chapter 6 and 7 of this thesis respectively.

First, dilatometry was used to determine experimentally continuous cooling transformation diagrams for both alloys. Dilatometry was subsequently used to compare the extent of bainitic transformation at different isothermal transformation temperatures, seen as three different values of strain due to the phase transformation. The phase fractions were confirmed using X-ray diffraction, and the austenite carbon content was estimated using measured lattice parameters and a knowledge of the effect of dissolved carbon on these parameters. The consistency between those values and the expected retained austenite carbon content predicted using the MUCG program, was evaluated. The differences within the structures

were then assessed using SEM and energy dispersive X-ray spectroscopy. TEM was used to show typical structures.

5.2   Alloy manufacture

Both alloys were manufactured in Belgium, by OCAS NV, a company that has produced good quality alloys for other projects in the department of materials in Cambridge. The two improved alloys were cast in a vacuum induction furnace as 100 kg ingots. The cast head, which was approximately 45 kg, was removed and the ingots were cut into four equivalent blocks, with length and width of 125 mm and height of 95 mm. They were subsequently heated to 1100°C and hot rolled to a final thickness of 12 mm in eight passes of gradually decreasing operating temperature, the final pass taking place at 900°C. The plates were then transferred to coiling furnaces, where they were held at constant temperature for 15 hours. The holding temperatures were determined using the MUCG program, for which the time-temperature-transformation diagrams were predicted from the nominal compositions, illustrated in Fig. 5.1. The MUCG program estimates the bainite-start temperatures depending on whether the phase transformation is growth or nucleation-limited. Since the nucleation-limited temperature is the lowest of both [137], it was used as B_S, to ensure the bainite formation range predicted would not be larger than the actual range, in the case that the transformation is nucleation-limited. The isothermal transformation temperatures were selected as 15°C above the predicted M_S, in order to allow for inaccuracies in the compositions of the produced alloys that could raise the M_S value, while keeping the temperature as low as possible to prevent large blocks of retained austenite from being present in the structure, since they are larger at higher temperatures [173]. A fifteen hour hold ensured the reaction ceased before the samples were cooled down to room temperature, since the laboratory scale alloys with similar compositions were observed to reach that point within 20 minutes at temperatures of the order of 400°C.

The carbon content of the two alloys were determined by combustion and the other alloying elements compositions were determined by inductively coupled plasma optical emission spectrometry. The nominal and actual compositions are summarised in Table 5.1, and the alloys names were changed to reflect their carbon contents.
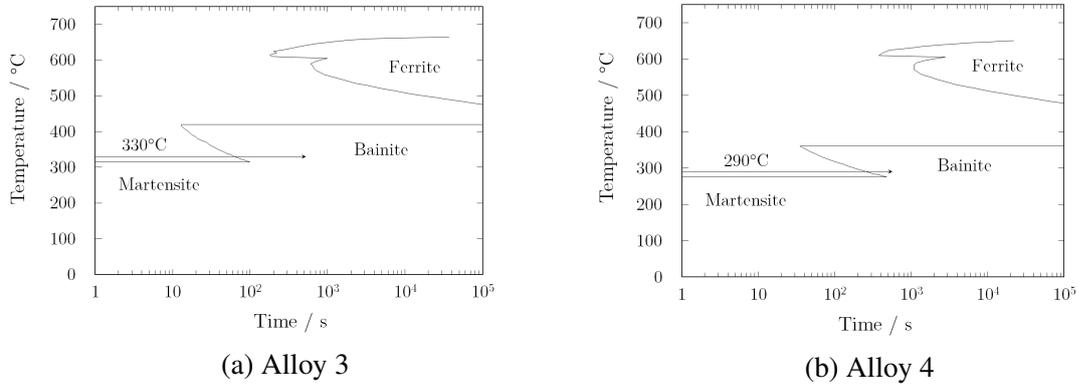
(a) Alloy 3

(b) Alloy 4

Fig. 5.1: MUCG predicted TTT diagrams for the nominal compositions of Alloy 3 and 4. In order to form bainite, Alloy 3 was transformed at 330°C and Alloy 4 was transformed at 290°C, as depicted by arrows above the martensite-start temperatures, indicating bainitic structures should be formed. The calculated bainite-start temperature shown was nucleation-limited.

Table 5.1: Nominal and actual compositions in wt% of the two large scale novel bainitic steels designed. Alloy 3 was renamed F34 and Alloy 4 was renamed F49, to reflect their respective carbon contents.

Alloy	C	Si	Mn	Cr	Ni	Mo
Alloy 3 - nominal	0.35	1	0.1	1	3	0.25
F34	0.34	1.04	0.15	1.31	3.09	0.23
Alloy 4 - nominal	0.45	1	0.1	1	3	0.25
F49	0.49	1.18	0.15	1.22	3.57	0.26

5.3   Dilatometry

5.3.1   Continuous cooling transformation diagram determination

This method, described in Chapter 3, was used to generate the continuous cooling transformation diagrams for F34 and F49. The results are presented in Fig. 5.2, compared with the MUCG predicted time-temperature-transformation diagrams, adjusted to the actual composition of both alloys. They indicated that the values of 290°C and 330°C satisfied the conditions for bainitic structures formation for F49 and F34 respectively. In order to explore the impact of heat treatment on mechanical properties and to assess the change in diffusivity of hydrogen as a function of austenite volume fraction, two other isothermal transformations were performed for samples of each alloy after another austenitising step. The lowest transformation temperature was selected to be as close to M_S as possible to obtain the highest strength and smallest austenite fraction. The highest temperature was selected to be slightly higher than the transformation temperature during manufacturing, and so that the three temperatures are separated by similar temperature ranges. For each alloy, the difference between the lowest and highest temperatures was 45°C. The transformation temperatures were: 305°C, 330°C and 350°C for F34 and 260°C, 290°C and 305°C for F49. Additionally, samples of both alloys were transformed by air-cooling after austenitising, since air-cooled bainitic alloys have recently been identified as having satisfactory combination of properties, and can simplify the manufacturing process [149]. In that case, microstructures of plates 16 mm thick were reported to have appropriate microstructures when transformed between $2°C\,s^{-1}$ and $0.1°C\,s^{-1}$ [94], which indicated that similar structures could be achieved for F34, since bainite was observed to form in that alloy at cooling rates below $0.5°C\,s^{-1}$, as showed in Fig. 5.2 (a). The F34 and F49 plates manufactured were 12 mm in thickness. For each alloy, two plates were attached together using steel wires and a thermocouple reader was placed between both plates. This resulted in an apparent plate thickness of 24 mm for the air-cooling treatment, which ensured slower cooling, and a temperature reading corresponding to the middle of the apparent 24 mm plate. The plates were austenitised to 850°C and

left to cool in air. Fig. 5.3 shows the cooling curves obtained this way. F49 transformed to a fully martensitic structure, which was confirmed by SEM, as displayed in Fig. 5.4. F34 on the contrary started transforming in the bainitic region, and finished transforming in a martensitic region. The sample subjected to this heat treatment was therefore also included in the characterisation, as F34-AC, indicating it was air cooled, along with the six isothermally transformed samples.

(a) F34   (b) F49
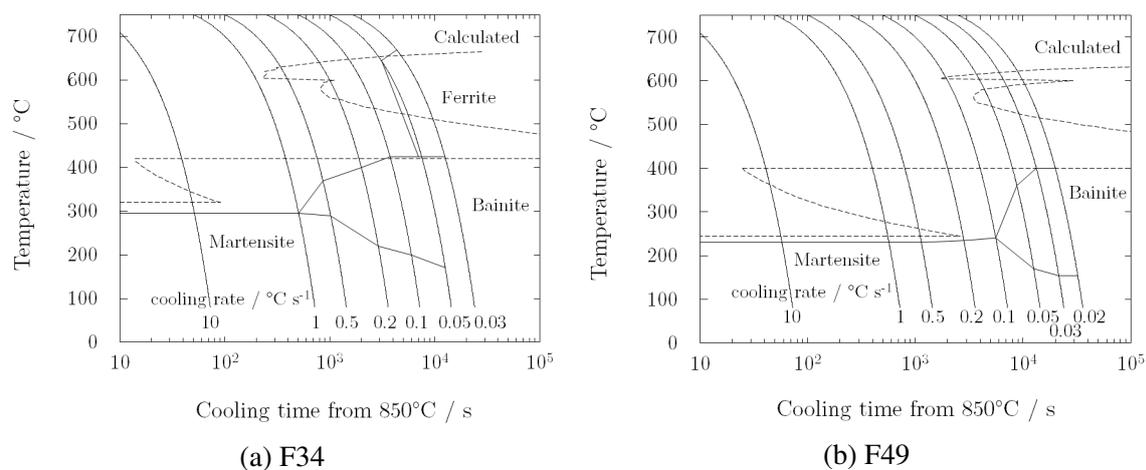
Fig. 5.2: Comparison between predicted TTT and experimental CCT diagrams for F34 and F49. Since the composition of both alloys were similar except for the carbon content, it was the main factor responsible for the differences in M_S, B_S and in the time required for the reaction to start. Only the initiation of reaction is shown.

(a) F34   (b) F49
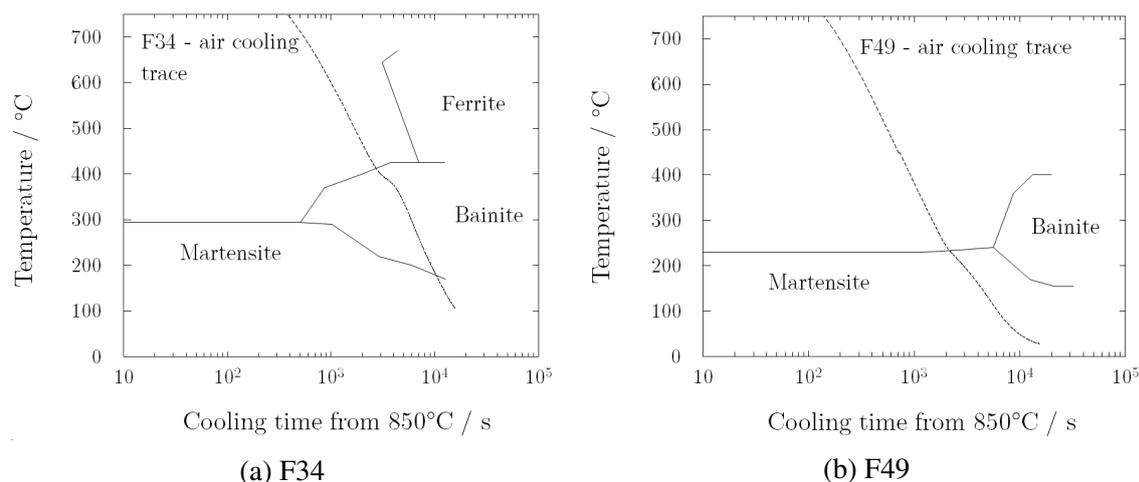
Fig. 5.3: Cooling traces for both alloys, with respect to the experimentally determined CCT diagrams. F34 could be seen to transform in the bainitic region while F49 transformed in the martensitic region.
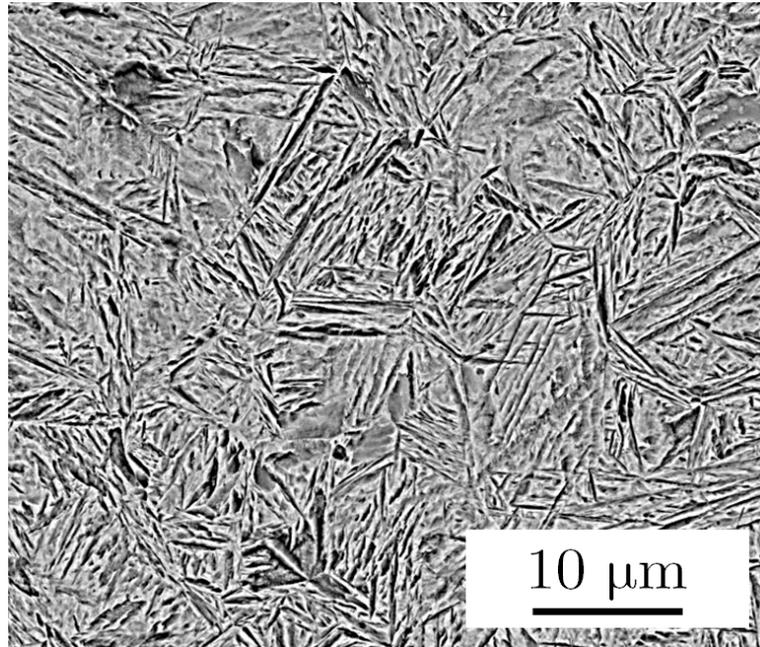
Fig. 5.4: Fully martensitic structure of an F49 air cooled sample. A fully martensitic structure is not suited for this project and air cooling of F49 was not a useful heat treatment.

5.3.2 Isothermal transformations

The strain changes form the austenite to bainitic ferrite phase transformation at the three transformation temperatures for each alloy are presented in Fig. 5.5. Opposite behaviours are visible, with the strain change increasing with transformation temperature in F34, and decreasing in F49. The strain change is proportional to the amount of bainite phase formed, meaning that higher strain indicates larger transformed bainite fractions [172]. A larger fraction of bainite forming at lower temperatures is consistent with the T_0' carbon content being higher at lower temperatures, thus indicating that the austenite can be enriched to higher carbon contents before the reaction should cease [93]. The behaviour in F49 is consistent with this theory. This is not the case for F34, although the strain difference between the transformation at 330°C and 350°C is rather small. The strain due to the transformation at 305°C appeared small. All curves exhibit a typical s-shape, except for the isothermal transformations of F34 at 305°C and F49 at 260°C, the lowest isothermal transformation temperatures for each alloy. In those two cases, the transformations started as soon as the transformation temperatures were reached. Table 5.2 summarises the strain measured and

the time required for the reaction to cease for each of the six isothermal transformations. The transformation temperature affected the transformation time strongly in F49 only. The transformation temperature affected the strain to similar extents in both alloys.

(a) F34   (b) F49
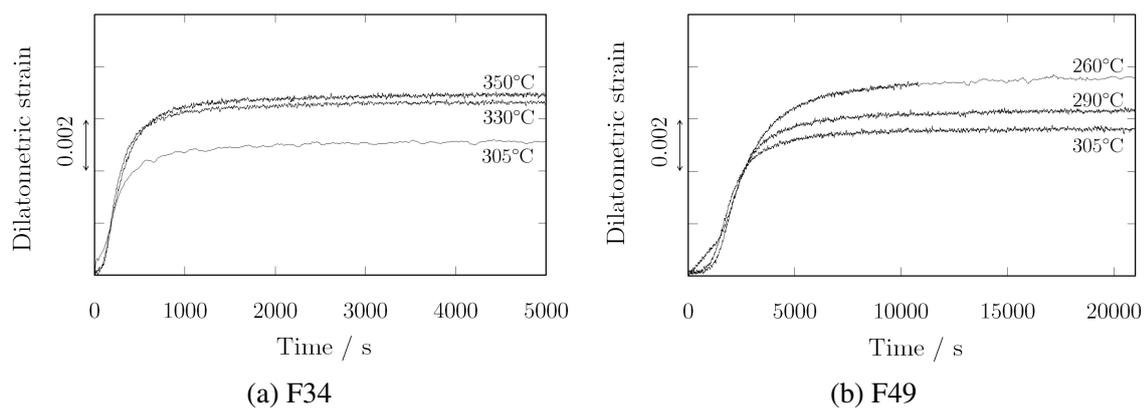
Fig. 5.5: Strain change due to the bainitic transformation at the three determined isothermal transformation temperatures for each alloy.

Table 5.2: Summary of the transformation time and strain due to the bainitic transformation at the three determined isothermal transformation temperatures for each alloy.

Alloy	Strain	Transformation time
F34-305C	0.0051	6500 s (1 h 45 min)
F34-330C	0.0065	5000 s (1 h 30 min)
F34-350C	0.0070	4800 s (1 h 20 min)
F49-260C	0.0071	22000 s (6 h 5 min)
F49-290C	0.0062	18000 s (5 h 0 min)
F49-305C	0.0053	16000 s (4 h 25 min)

5.4   X-ray diffraction

5.4.1   Austenite phase fraction

XRD was used to quantify the amount of austenite present in the seven described samples, using the method described in Chapter 3. Fig. 5.6 displays an example of an acquired and fitted XRD pattern, as well as a plot of the difference between the measured and calculated X-ray intensity. The quality of the fit provides evidence for the accuracy of the values of the austenite volume fraction and lattice parameter calculated. The $(200)_\alpha$ peak was not fitted as well as the other peaks because of the presence of martensite in the samples. In martensite, the (200) peak is the most significantly affected by the longer c-axis, and is seen in practice as a broadening of the peak to lower angles. The austenite lattice parameter was deduced from the XRD peak locations and an equivalent carbon content was suggested, using Dyson and Holmes [164]. All results are summarised in Table 5.3. The error on the austenite fraction is of the order of $\pm$ 0.01, as is standard when using Rietveld refinement in steels [163, 169, 175], and the error in the austenite lattice parameter is of the order of 0.0004 Å, as given by the highscore plus software used for analysis. The phase fraction error was verified after fitting data, and allowing the fit to vary until it became inaccurate, which corresponded indeed to a phase fraction difference of approximately 0.01. The XRD analysis confirmed the trend observed in dilatometry for F49 that the fraction austenite increases with increasing transformation temperature. F34-330C and F34-350C have similar austenite fractions, which is consistent with the dilatometry results, despite not agreeing with the theory that suggests the austenite fraction should increase with increasing transformation temperature. This indicates the transformation reaction might have started before the transformation temperature had been reached. The fraction austenite in F34-305C was found to be the smallest despite the dilatometry results showing the smallest isothermal transformation strain. The low austenite fraction in F34-305C agrees with the theory that suggests the austenite fraction should decrease with decreasing transformation temperatures [93]. In order to assess whether austenite decomposed significantly more to martensite for that sample, the

strain change upon cooling from the isothermal transformation temperature was compared to that in F34-330C, illustrated in Fig. 5.7. Both samples displayed a similar strain change upon cooling, indicating that a similar amount of austenite decomposition into martensite.
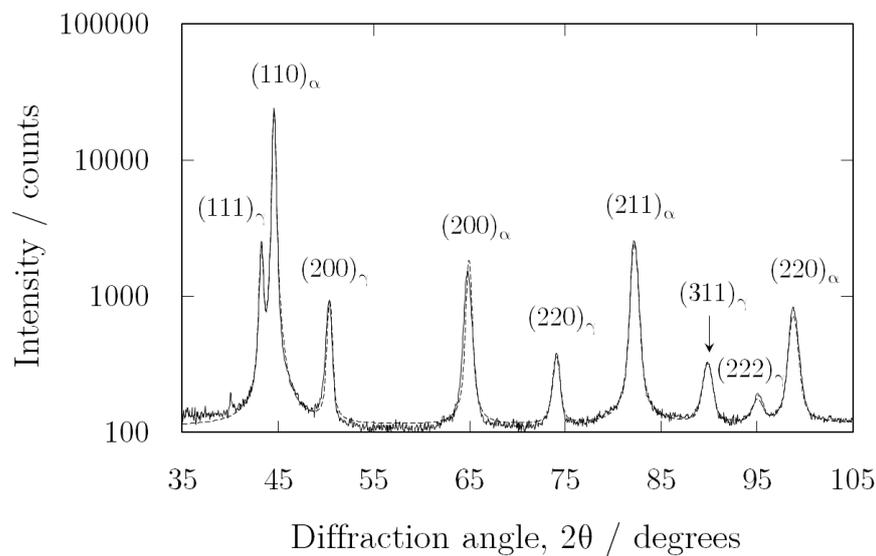
(a) XRD spectrum (solid line) and fit (dashed line)
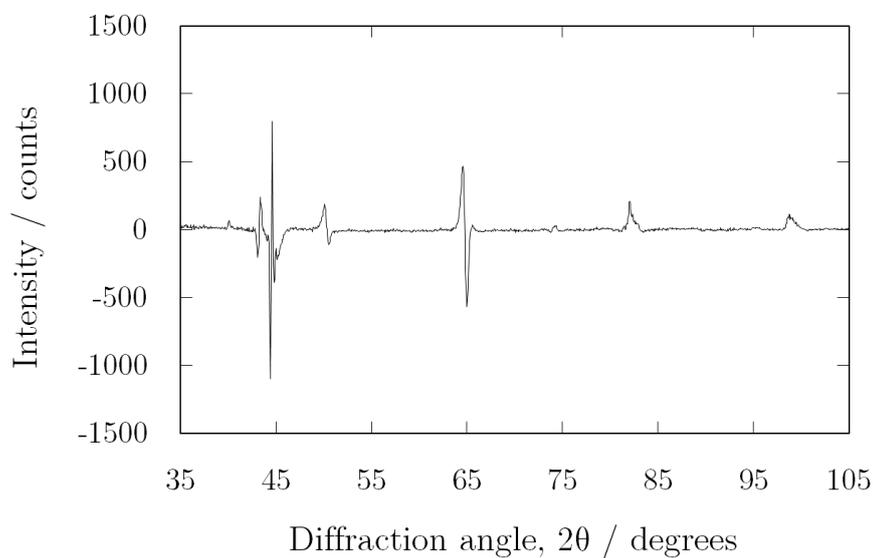
(b) Difference between the acquired and simulated spectra

Fig. 5.6: Example of a fitted XRD spectrum, for F34-330C. The quality of the fit can be assessed by plotting the difference between both spectra. A good fit ensures the the austenite fraction estimated is accurate.

5.4.2 Austenite carbon content

XRD was used to determine the carbon content present in the retained austenite, using the empirical relationship by Dyson and Holmes:

a_γ = 3.578 + 0.033 C + 0.00095 Mn - 0.0002 Ni + 0.0006 Cr +0.0031 Mo, where a_γ is the austenite lattice parameter in Å and the composition of alloying elements is expressed in wt% [164]. The results for F49 were consistent with the dilatometry and austenite fraction data, with the austenite lattice parameter increasing with decreasing transformation temperature, and thus indicating a larger carbon content, representative of the higher value of the T_0 line at lower temperature. These results are displayed in Fig. 5.8, where they are compared to the predicted T_0 carbon content using MUCG. In the case of F34, only at the lowest transformation temperature did the carbon content match the MUCG prediction. The carbon content deduced for F34-330C, the middle transformation temperature, was higher than for both other F34 samples, and despite not agreeing with the T_0 curve predicted, was nevertheless consistent with the higher austenite content detected in that alloy compared to the other two F34 samples.

Table 5.3: Summary of the measured austenite fractions, lattice parameters and calculated carbon contents for both novel alloys, using XRD.

Alloy	Austenite fraction	Lattice parameter / Å	C content / wt%
F34-305C	0.08 ± 0.01	3.6138	1.05
F34-330C	0.14 ± 0.01	3.6180	1.18
F34-350C	0.12 ± 0.01	3.6140	1.06
F34-AC	0.17 ± 0.01	3.6187	1.20
F49-260C	0.12 ± 0.01	3.6184	1.19
F49-290C	0.18 ± 0.01	3.6175	1.17
F49-305C	0.19 ± 0.01	3.6144	1.07
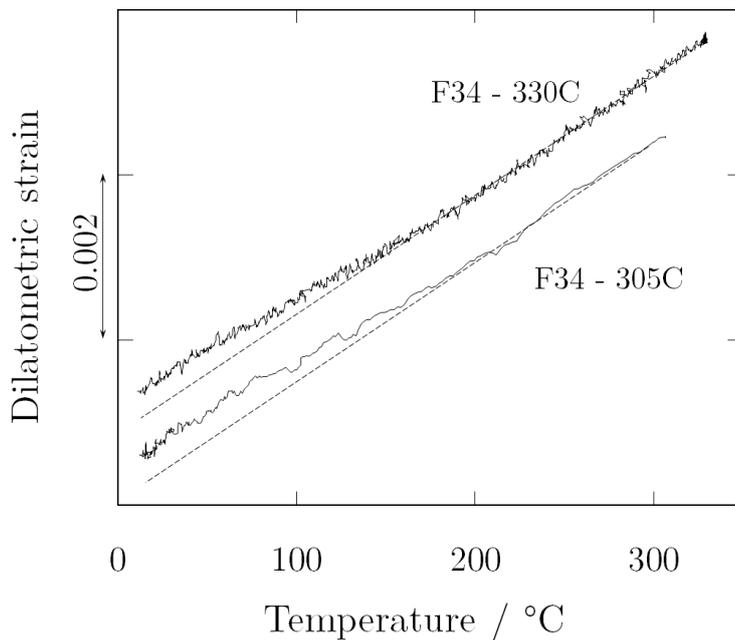
Fig. 5.7: Comparison between the strain change upon cooling after isothermal transformation at 330°C and 305°C for F34. The measured strains in both cases were similar.
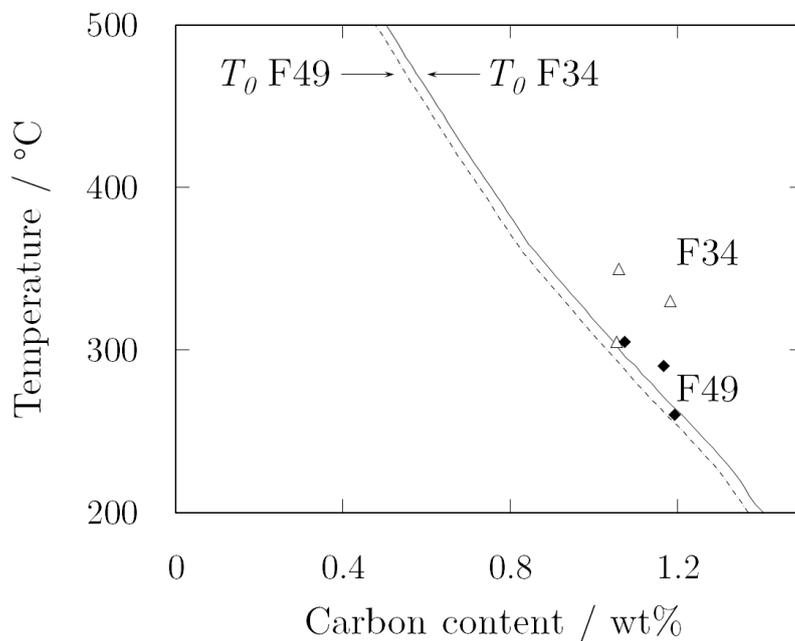
Fig. 5.8: Comparison between the MUCG calculated austenite carbon concentration as a function of temperature, given by the T_0 line, and the experimental data deduced from the measured austenite lattice parameter obtained from XRD.

5.5   Scanning electron microscopy

SEM was used to assess the differences in scale of the bainitic structure and blocky retained austenite at different transformation temperatures, to characterise the structure of the air cooled F34 sample and to identify regions of alloying element segregation in the plates due to the manufacturing process.

5.5.1   Structural characterisation

Retained austenite characterisation

The structures of the six isothermally transformed samples were typical bainitic structures, with bainite laths separated by films of retained austenite. An example of such microstructure, for F49-290C, is presented at high magnification in Fig. 5.9. In all plates, it was possible to see regions of blocky austenite decomposing into martensite. This behaviour is common in bainitic steels [145]. Fig. 5.10 displays examples of such decomposition for F49-290C and F34-330C. Based on the T_0 line presented in Fig. 5.8, it was predicted that, for each alloy, a decrease in transformation temperature would lead to more austenite transforming to bainite, and therefore a higher carbon content in austenite when the bainitic transformation finishes. This would also result in smaller regions of blocky austenite to remain untransformed, as bainite packets would grow and converge together [116]. Additionally because of slower kinetics, the bainite laths would be smaller at lower transformation temperatures [93]. The size of the largest blocks of retained austenite and the average size of retained austenite were calculated for all seven samples, as well as the bainite lath thickness and results are presented in Table 5.4. The results were almost all in agreement with the predictions. The effect of transformation temperature has a strong impact in F49, where the average retained austenite size increases from about 1.6 μm to 27.4 μm for an increase in temperature of 45°C. In F34, the blocky austenite size was more consistent, varying only between 4.6 μm and 14.3 μm for an equivalent temperature difference.

Fig. 5.11 depicts the strong visible change in blocky retained austenite size for F49, while

Fig. 5.12 shows more consistent structures, for F34. Those micrographs also revealed the presence of banded regions, described by Bhadeshia, which are regions with segregation of alloying elements cause by the hot rolling process [93]. Those regions are especially visible in the Fig. 5.11 (b) and (c) micrographs, as long dark and light stripes respectively. Both micrographs showed that blocky austenite was more present in such regions compared to the rest of the microstructure. This suggests banded regions could be rich in austenite-stabilising elements compared to other regions. Energy dispersive X-ray spectroscopy was used to identify the segregation. Fig. 5.13 showed the same result more clearly, at higher magnification, and in regions of banding. The air-cooled sample had a significantly different structure compared to the other six samples. The martensitic phase was consistently present in the banded regions, since the cooling rate was too fast to permit the bainitic transformation to finish.

Bainite lath thickness characterisation

Figs. 5.14 and 5.15 illustrate the lath thickness results presented in Table 5.4. All micrographs were taken of representative areas of the samples. The bainite lath thickness was considerably more affected by the transformation temperature in F49 compared to F34, with an increase from 81 μm to 130 μm between the two extreme transformation temperatures. For F34, there was little difference in the bainite lath thickness, with values within the error range of each other. F34-AC displayed the largest overall bainite lath thickness along with small austenite areas, due to the significant presence of martensite in the austenite-rich regions. It could be concluded that alloys with lower carbon content led to more consistent structures, irrespective of transformation temperature. Finally, when comparing the as-received F34 and F49 alloys, the difference in carbon content and transformation temperature led to a large difference in scale, as seen in Fig. 5.16.

5.5.2 Energy-dispersive X-ray spectroscopy (EDX)

EDX point analyses were performed to investigate the differences in composition between banded regions and other regions. Carbon was not investigated since EDX is not a reliable
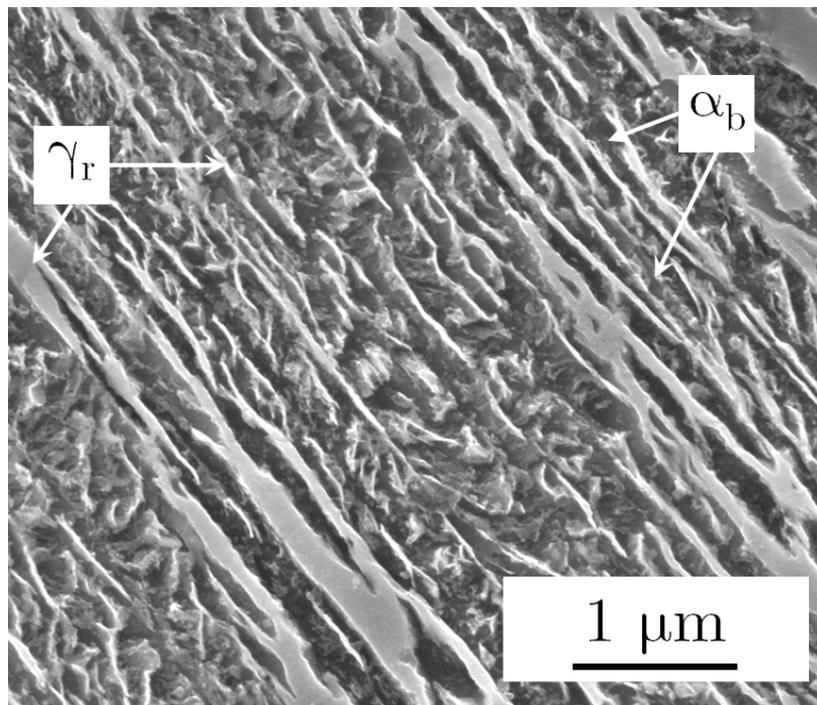
Fig. 5.9: F49-290C micrograph displaying a fine bainitic structure with intercalated thin sheets of retained austenite.
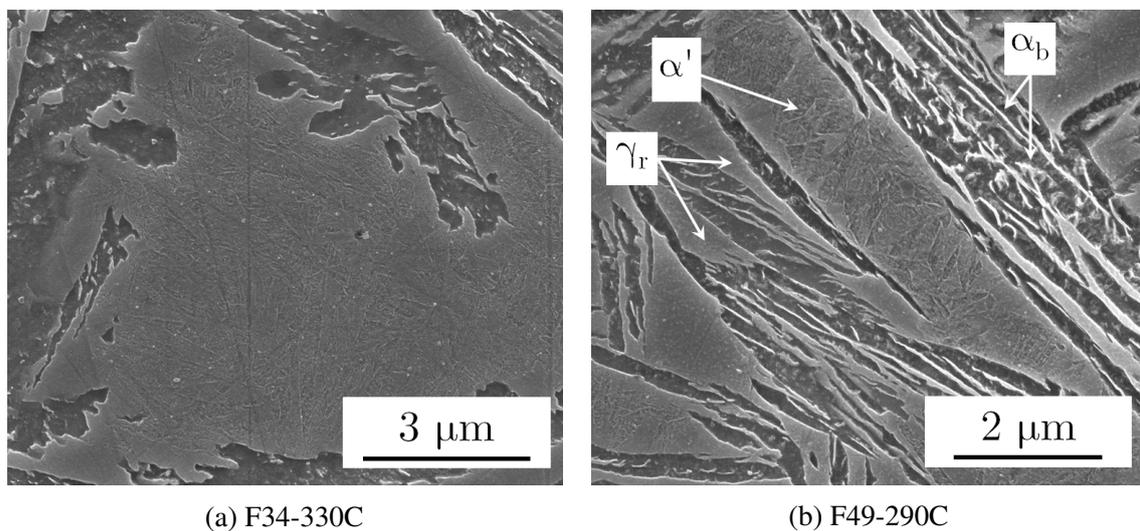
(a) F34-330C

(b) F49-290C

Fig. 5.10: Examples of regions of retained austenite that has decomposed into martensite, in F34-330C and F49-290C. In F49-290C, differences between decomposed austenite and retained austenite appeared clearly.

(a) F49-260C

(b) F49-290C

(c) F49-305C
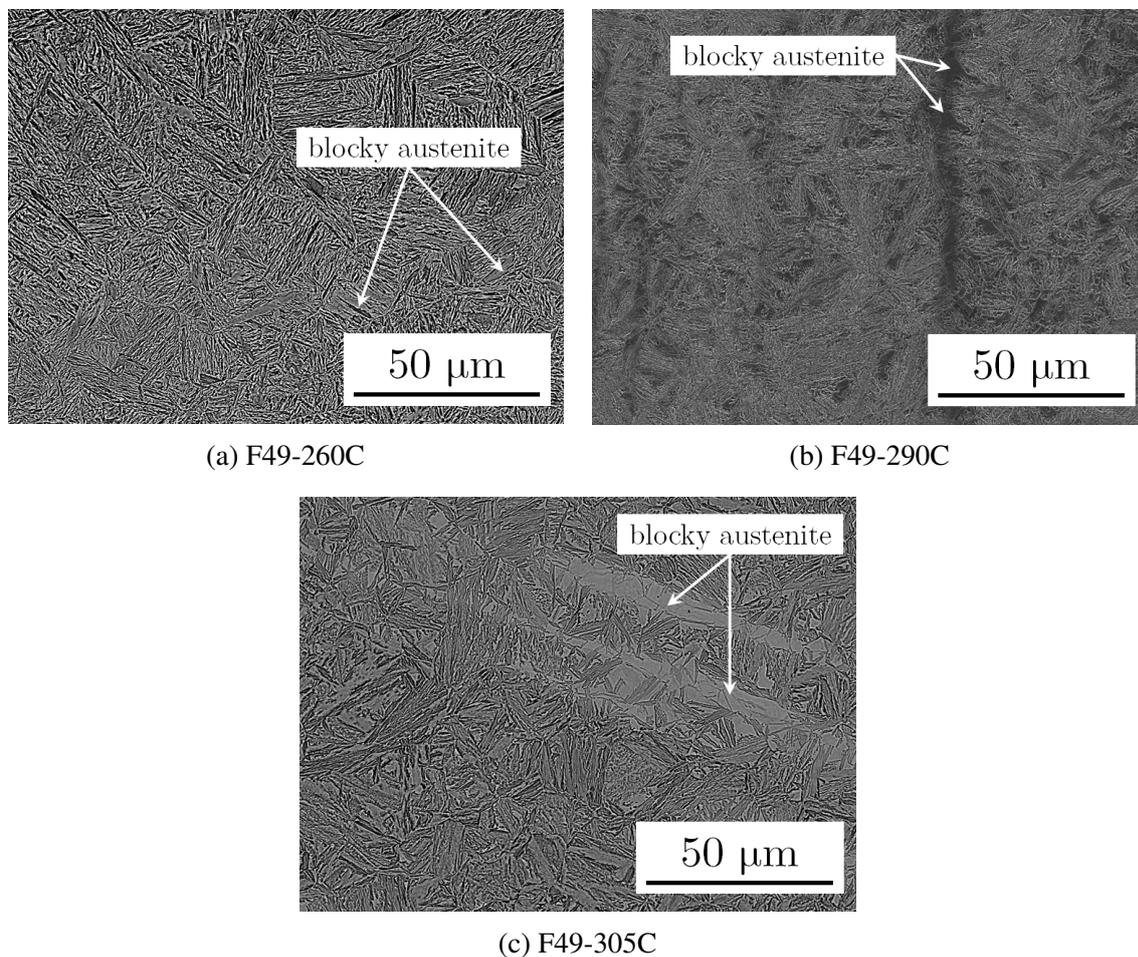
Fig. 5.11: Micrographs showing larger retained blocky austenite areas present in F49 samples transformed at higher temperatures.

Table 5.4: Differences in the bainite lath thickness and blocky austenite area between the seven samples characterised. The bainite lath thickness was similar in all the F34 samples, but it varied significantly in the F49 samples. The blocky austenite size was also more affected by the transformation temperature in F49 than in F34.

	F49			F34			
	F49-260C	F49-290C	F49-305C	F34-305C	F34-330C	F34-350C	F34-AC
Bainite lath thickness / nm	81 ± 15	113 ± 23	130 ± 22	153 ± 25	166 ± 29	164 ± 22	176 ± 27
Largest blocky austenite area / μm^2	3	19	50	10	61	27	10
Average blocky austenite area / μm^2	1.6 ± 0.7	7.6 ± 4.8	27.4 ± 10.6	4.6 ± 1.8	11.8 ± 3.7	14.3 ± 6.0	5.6 ± 2.2

(a) F34-305C

(b) F34-330C

(c) F34-350C

(d) F34-AC
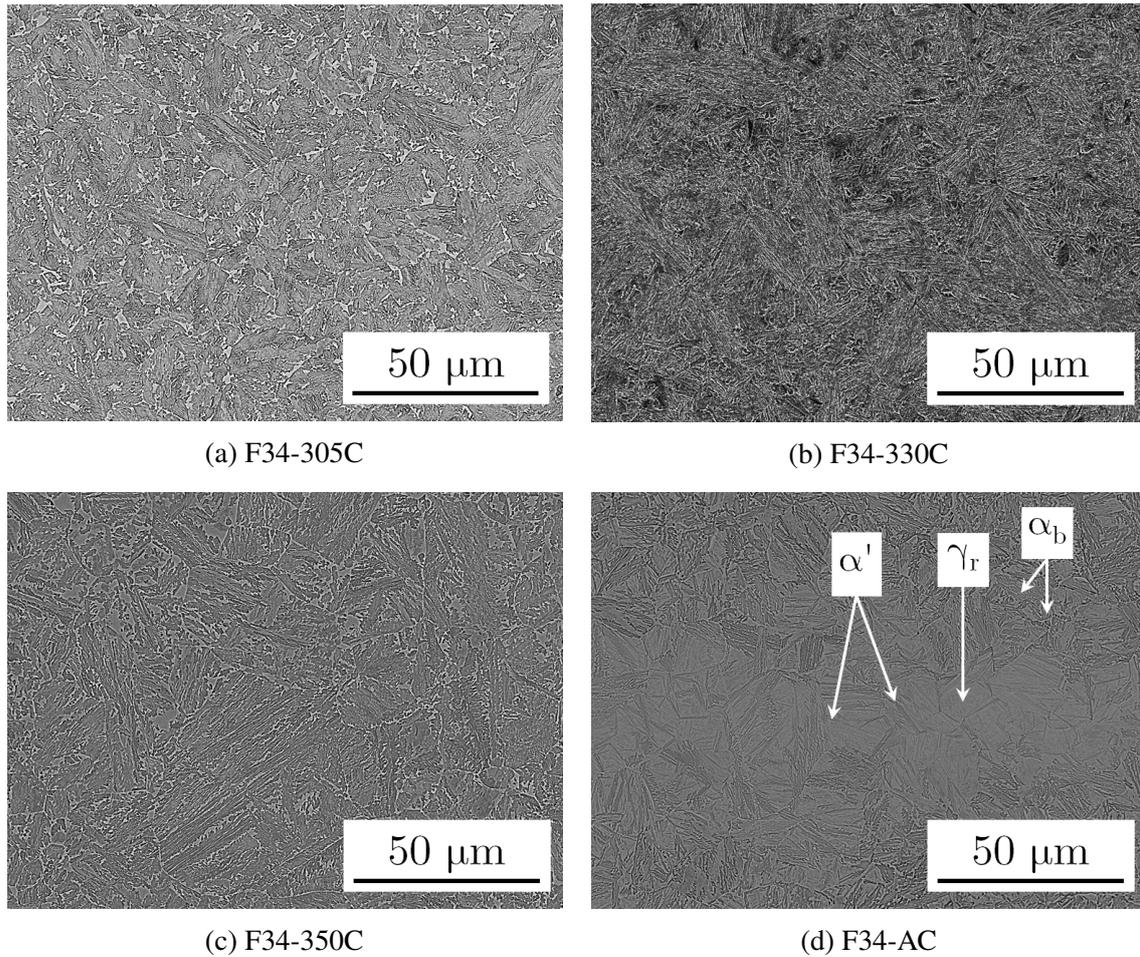
Fig. 5.12: Micrographs showing little difference in the retained blocky austenite size in F34 samples, irrespective of the transformation temperature.

(a) F49-260C

(b) F49-290C

(c) F49-305C

(d) F34-330C

(e) F34-AC
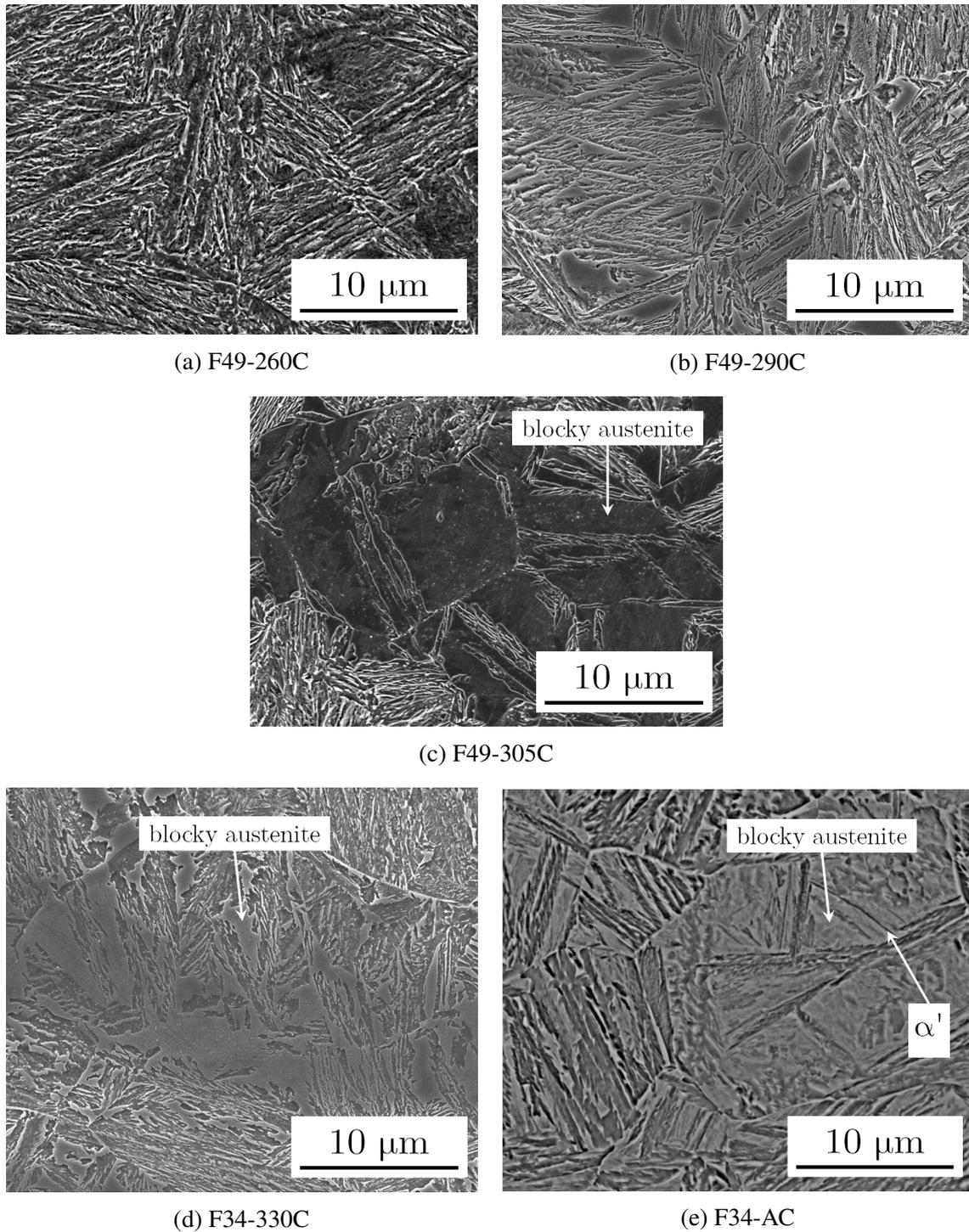
Fig. 5.13: Higher magnification micrographs showing the same effect in all F34 and F49 samples.

(a) F49-260C

(b) F49-290C

(c) F49-305C
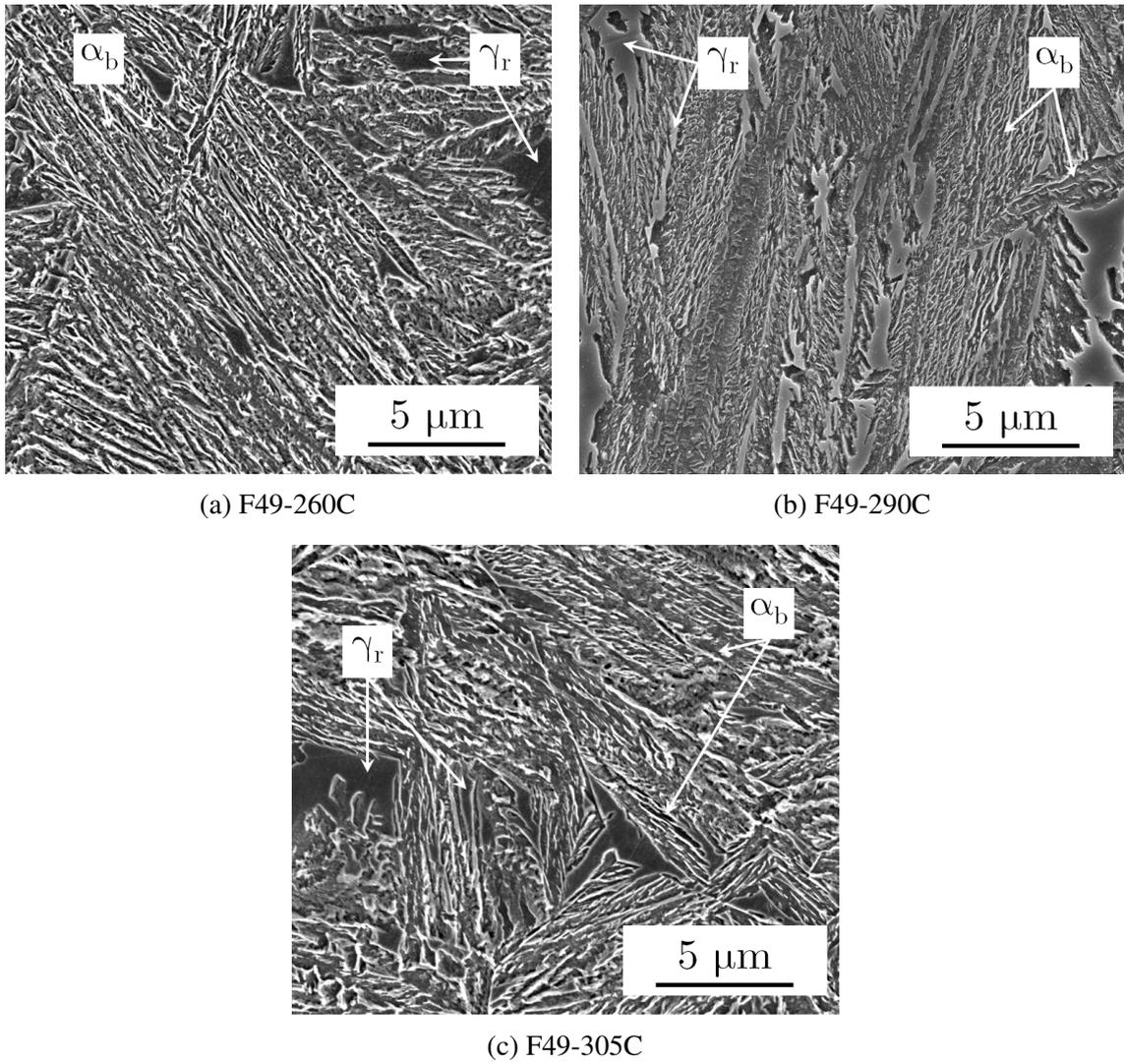
Fig. 5.14: Micrographs showing a finer bainite lath thickness with decreasing transformation temperatures in F49.

(a) F34-305C

(b) F34-330C

(c) F34-350C

(d) F34-AC
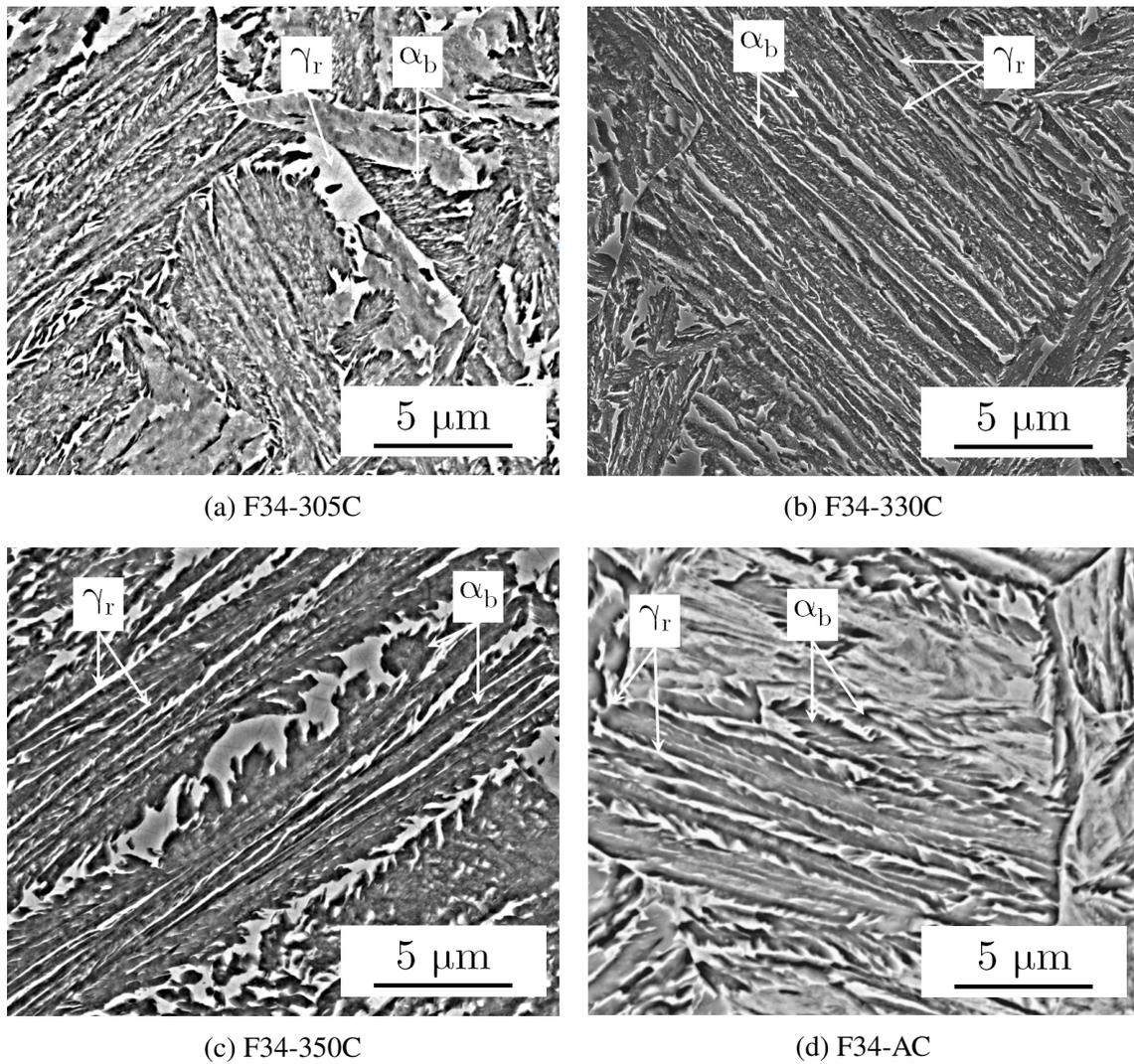
Fig. 5.15: Micrographs showing the bainite lath thickness was not significantly affected by the transformation temperature in F34.
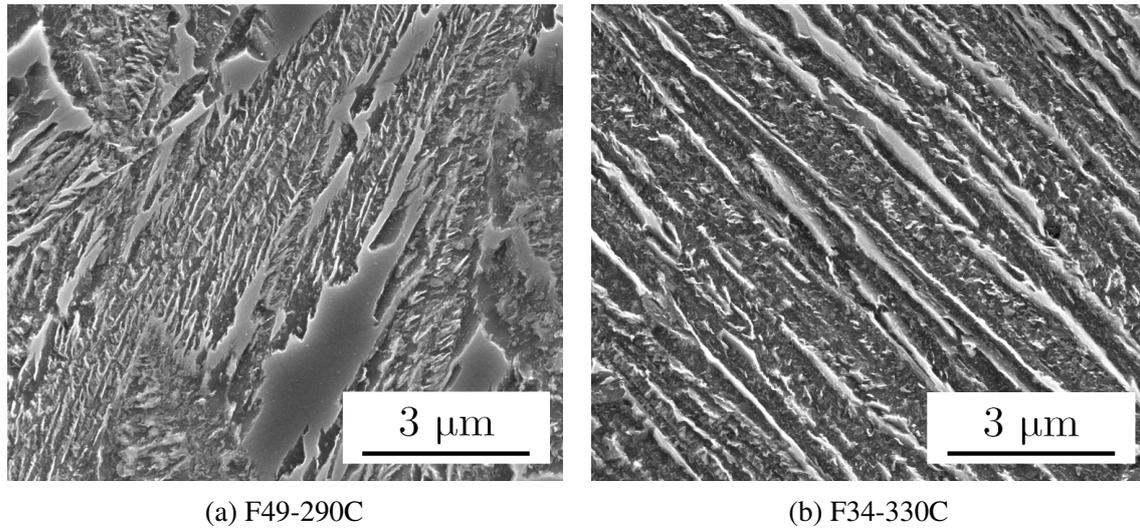
(a) F49-290C   (b) F34-330C

Fig. 5.16: Micrographs showing the difference in scale between F34-330C and F49-290C, the two alloys in their as-received conditions.

technique to identify carbon contents due to contamination [181]. Iron was also detected and was the balance in the the compositions reported in Table 5.5. The points were separated by 2.5 to 3 μm, since EDX resolution is reported as approximately 1 μm [181]. As displayed in Fig. 5.17, points 1, 6 and 7 assess the bulk composition and points 2, 3, 4 and 5 the banded region, with point 4 being most representative, since it is in the centre of the banded region. EDX revealed that in the banded region, the silicon, manganese and chromium contents were approximately double that of the bulk. The nickel content was of the same order. The most notable difference was in the molybdenum content, which was up to 8 times higher in the banded region compared to the bulk. These results are surprising because Ni and Mn, which are strong austenite stabilisers [116], are present in slightly larger concentrations, while Mo, which reduces all transformation temperatures [168], is present in a much larger quantity, yet the banded regions were mainly austenitic. The reason for this effect must therefore be kinetic rather than thermodynamic. In other words, the excess alloying elements in the banded regions cause austenite to transform to bainite slower, so the neighbouring austenite transforms first, enriching the banded regions in carbon. Once the carbon content reaches the T_0' line in the banded regions, those regions cannot transform to bainite.
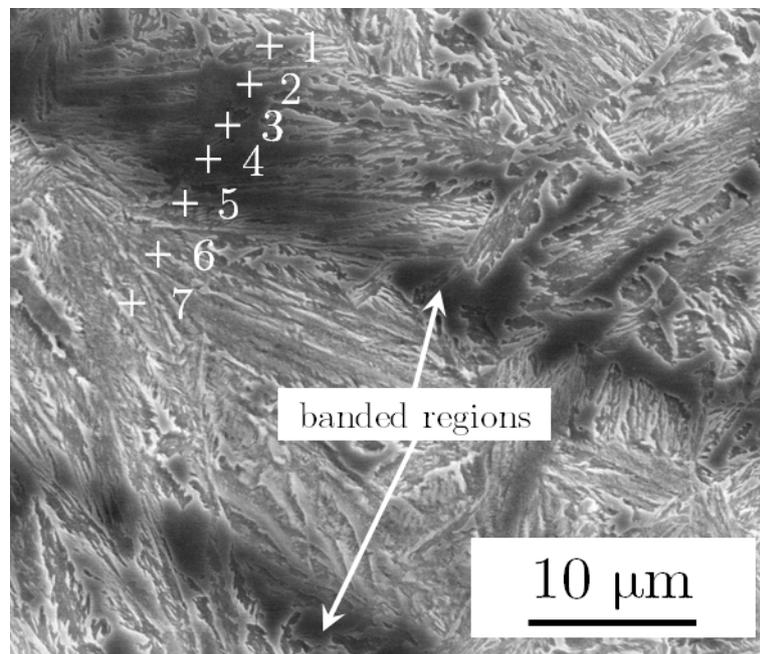
Fig. 5.17: F34-330C micrograph displaying the points at which EDX spectra were collected.

Table 5.5: EDX spectra showing the alloying element composition in a banded region of F34-330C, displayed in Fig. 5.17. Significant solute inhomogeneity was revealed, in particular for Mo, which was present in much larger quantities in those regions compared to the rest of the sample. The centre of the banded region corresponded to Point 4, which showed the highest alloying element disparity with the bulk.

Spectrum point	Si / wt%	Mn / wt%	Cr / wt%	Ni / wt%	Mo / wt%
Bulk	1.04	0.15	1.31	3.09	0.23
1	1.63 ± 0.04	0.16 ± 0.06	1.55 ± 0.05	3.87 ± 0.12	0.43 ± 0.10
2	2.00 ± 0.04	0.28 ± 0.06	1.75 ± 0.05	3.91 ± 0.12	1.03 ± 0.11
3	2.12 ± 0.04	0.23 ± 0.06	2.15 ± 0.06	3.74 ± 0.12	1.46 ± 0.11
4	$\mathbf{2.08 \pm 0.04}$	$\mathbf{0.35 \pm 0.06}$	$\mathbf{2.36 \pm 0.05}$	$\mathbf{3.78 \pm 0.12}$	$\mathbf{1.87 \pm 0.11}$
5	1.63 ± 0.04	0.18 ± 0.06	1.56 ± 0.05	3.59 ± 0.12	0.80 ± 0.10
6	1.28 ± 0.04	0	1.26 ± 0.05	3.36 ± 0.12	0.20 ± 0.09
7	1.15 ± 0.04	0	1.20 ± 0.05	3.30 ± 0.12	0.35 ± 0.10

5.6   Transmission electron microscopy

The results presented in this section do not include the alloys carbide characterisation, which is presented in Chapter 6 of this thesis, but permitted the structures presented in Section 5.5 to be viewed in a different light.

Fig. 5.18 visibly confirmed the scale difference of the bainitic laths between the two alloys. The bright field images show also dark stripes within the bainite laths in F49-290C, while in F34-330C, the bainite laths are more uniform in colour, indicating that the electron beam was not as strongly diffracted. This was due to a greater presence of dislocations in F49-290C, which was quantified in Section 6.3.3.

Fig. 5.19 displays large fully bainitic regions in the F34-AC sample, as well as the presence of twinned martensite, on a smaller scale.
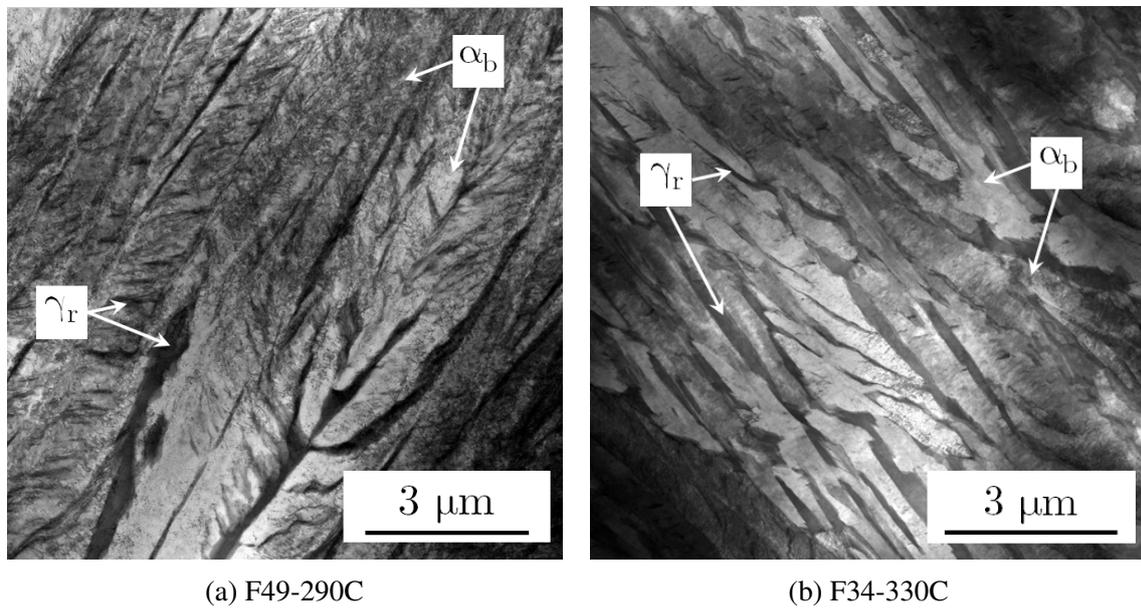
(a) F49-290C

(b) F34-330C

Fig. 5.18: Bright field micrographs showing the difference in bainite lath thickness between F34-330C and F49-290C.

(a) F34-AC bainitic structure

(b) F34-AC martensitic twinned structure
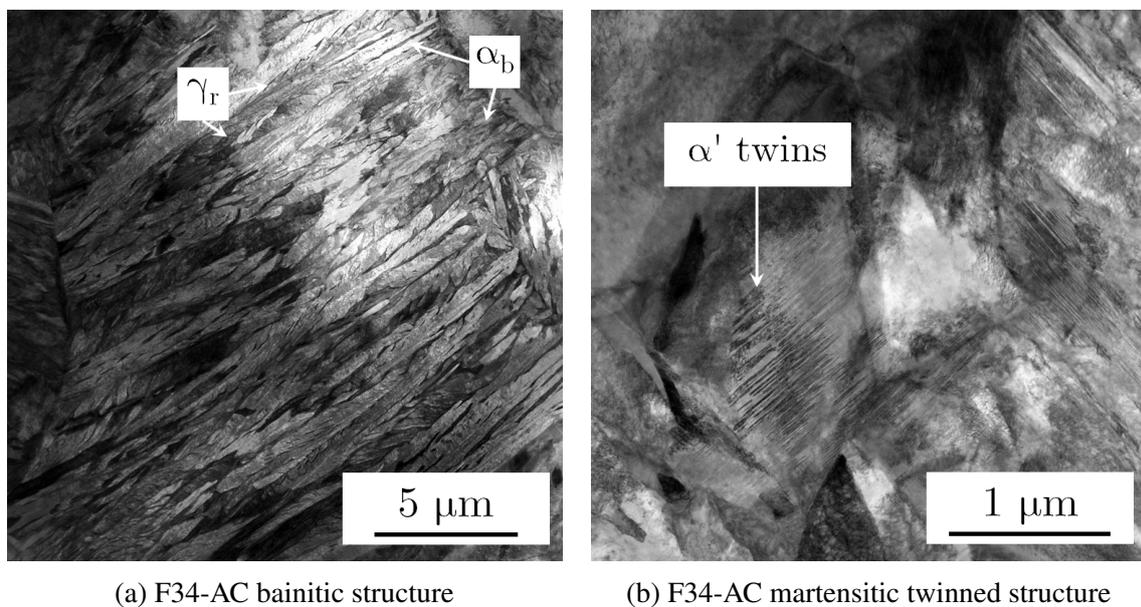
Fig. 5.19: Bright field micrographs showing the presence of bainite and martensite in F34-AC samples.

5.7   Conclusions

After having performed an in-depth structural characterisation of the novel alloys, it was observed that the higher carbon alloy, F49, had a finer structure that was more sensitive to the isothermal transformation temperature. It was observed that the bainite lath thickness as well as the blocky austenite size changed dramatically over a temperature range of 45°C, whereas little difference was observed in the bainite thickness in F34 over the same range. The lower carbon alloy, F34, had a coarser structure, but was less affected by a change in the transformation temperature. It was found that F34 could simply be air-cooled from austenisation temperature in order to form a new structure that contained bainite, and martensite in banded regions, which were austenite-rich. The same was not possible for F49. Almost all samples achieved an austenite fraction in excess of 0.1, with F34-305C being the only exception, with an austenite fraction of 0.08. Chapter 6 and 7 present the hydrogen behaviour in, and mechanical properties of the novel alloys respectively, as a consequence of the differences in their microstructures.

Chapter 6

Hydrogen behaviour in large-scale novel alloys

6.1   Introduction

The work presented in this chapter provides an insight into the behaviour of atomic hydrogen in the two alloys and seven samples subjected to different heat treatments characterised in-depth, as described in Chapter 5. An electrochemical permeation experiment was first employed to determine and compare the effective diffusivity of hydrogen in those samples, as a function of their retained austenite fraction. The contribution to trapping from reversible and irreversible traps was then estimated [182]. Most samples displayed similar effective diffusivity values, and for this reason only three of them were used for further characterisation: F34-330C, F34-AC and F49-290C, which are the two as-received alloys, and the air-cooled F34 sample, since its structure was significantly different from those of all other samples.

Based on the literature review and on the microstructural characterisation, three hydrogen traps were identified in the three samples:

1. Dislocations, for which the density was estimated using XRD and the Williamson-Hall method [165].

2. Iron carbides, characterised as cementite using TEM and XRD and for which a phase fraction was estimated by Rietveld analysis of XRD patterns.

3. The austenite/ferrite interface, the contribution of which was estimated by fitting the thermal desorption spectroscopy (TDS) spectra.

There were no microvoids in the current microstructures since no cold-work had been performed. There were indeed some grain boundaries, but they have been omitted as an independent trap, since it was observed with SEM that most grain boundaries were retained austenite, as shown extensively in Chapter 5, and thus were already taken into account as ferrite/austenite interfaces. Additionally, grain boundaries have been reported to have low binding energies and would not make a significant to the analysis presented [57].

The deeper characterisation of those three samples was used to predict a number density of corresponding hydrogen traps, that was then fitted to the TDS data using the model developed by Song in order to determine the cementite binding energy in the bainitic alloys and the interfacial trap density [49].

6.2   Electrochemical Permeation

The results presented in this section were obtained through a collaboration with Gaurav Joshi, at the University of Manchester, where all the permeation work was undertaken.

6.2.1   Experimental method

Cell description

The use of an electrochemical cell to measure the diffusivity of atomic hydrogen in palladium was first reported by Devanathan [34]. The setup used in this project relies on a similar cell, referred to as a Devanathan-Stachurski cell, composed of two electrochemical cells joined together where the specimen sits. Fig. 6.1, adapted from Turnbull, displays the setup used [183]. A current is applied on the reduction cell, on the left-hand side, in order to reduce hydrogen cations in solution to atomic hydrogen on the sample's surface. The hydrogen can then penetrate the steel. Atomic hydrogen travels through the sample to reach the oxidation cell, on the right-hand side, where it is oxidised back to ionic hydrogen in solution. The electrons generated in the process are monitored and the current output measured is then used to identify the hydrogen diffusivity in the sample. The following equations summarise this process:

$$\text{Reduction cell}: H^{+} + e^{-} \rightarrow H(atomic) \tag{6.1}$$

$$\text{Oxidation cell}: H(atomic) \rightarrow H^{+} + e^{-} \tag{6.2}$$
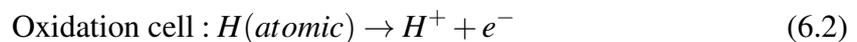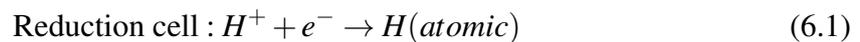
A voltage is applied between the counter electrode and the working electrode, the sample, on the oxidation cell. This ensures the sample is passivated, and results in a spike in the detected oxidation current, which subsequently decays to a stable background value [183]. When it is reached, galvanostatic charging of the reduction cell begins, which means a constant current is used to drive the reduction of ionic hydrogen into atomic hydrogen on the reduction side of the cell. This leads to a constant absorbed hydrogen concentration sub-surface, hence to a

Fig. 6.1: Schematic of the Devanathan-Stachurski permeation cell used, modified from Turnbull [183]. S_{in} and S_{out} show the solution flow in and out of the cell into a larger external container. CE represents the counter electrodes, while RE_R and RE_O are the reference electrodes on the reduction and oxidation side of the cell respectively. The sample was the working electrode for both sides of the cell. The whole setup was immersed in a deionized water bath at 30°C.

constant diffusion rate through the sample [183]. When hydrogen atoms start reaching the oxidation side of the cell, they are first detected as an increase in the oxidation current, until it plateaus, when a steady-state of hydrogen diffusion through the sample is achieved [182]. This particular oxidation current is called the "permeation transient".

Experimental setup

The samples were prepared by electromechanical discharge machining as samples of $70 \times 40 \times 1$ mm, with the length along rolling direction, from 10 mm thick plates. The samples were ground up to a 2500 SiC grit paper finish. The areas of the sample exposed to the solution were discs of 6.6 cm^2, meaning the radius of the discs were 14.5 mm. This satisfied the requirement that the ratio between radius and thickness should be at least 10:1 [182].

Many combinations of electrodes, solutions, applied potential and current, and sample thickness can be used, but they should meet the standard requirements set by Turnbull to ensure the validity of data acquired [183]. All parameters used are summarised in Table 6.1. The following targets had to be met:

- Avoiding crevice corrosion and pitting on the oxidation side of the sample. It is usually caused by ions, especially Cl$^-$ [182]. Hence the reference electrode used on that side of the cell was Hg | HgO.

- Ensuring the oxidation of hydrogen atoms is transport limited and represents the diffusion of hydrogen through the sample, rather than surface reactions. For this, Turnbull indicated a potential of +300 mV above the open-circuit potential measured using a saturated calomel electrode as satisfactory for most metals to meet this transport requirement [183]. This reference electrode contains Cl$^-$ ions, and could not be used, as described previously. Since Hg | HgO was used instead, its equivalent potential was set to +650 mV above the open-circuit potential.

- Minimising undesired surface reactions on the sample. Raising the pH of the reduction solution to 8.5 was proposed by Turnbull to mitigate surface reaction often observed in

NaCl [183]. A solution of 0.1 M NaOH was also reported to passivate the oxidation side when a potential of +650 mV above the open-circuit potential measured with Hg | HgO electrode [183].

- Minimising the reduction cell solution chemistry changes. Any changes in the solution will affect the reduction reaction, which will in turn modify the sub-surface hydrogen concentration and the diffusion kinetics measured [183]. In order to achieve this, the reduction cell was linked to a large container, and the solution was cycled through the cell and the container continuously throughout the experiment. Additionally, glass cells have been reported to release ions in solution, and polytetrafluoroethylene (PTFE) was selected as the cell material, with deionized water to avoid this problem [183]. Similarly, deaerated solutions with N_2 have been reported to be less prompt to chemistry changes and were used.

- Minimising other factors that could impact the oxidation current readings. The change in room temperature depending on the time of day has been shown to affect those readings, and the cell was submerged in a 30°C de-ionized water bath to maintain the temperature constant throughout the experiment [183].

Data quality verification

Before analysis, several steps were performed to ensure the validity of the collected data. The reduction cell charging current and oxidation cell hydrogen recombination rates need to be constant for the experiment to be valid [183]. Using galvanostatic charging ensured the first requirement was satisfied, and the recombination rate was assessed by monitoring the potential change on the reduction side over the time of the experiment. If confirmed to be small, the reduction is of constant surface conditions. A large potential change would indicate solution or surface changes on the electrode, and therefore invalidate the data [183]. The oxidation current change with time was normalised and compared to the current predicted by solving Fick's second law of diffusion, equation (6.3), which governs concentration changes time, in this case simplified to one dimension:

Table 6.1: Summary of the experimental setup used for electrochemical permeation.

Sample dimensions	$70 \times 40 \times 1$ mm
Cell temperature	30°C
Cell material	Polytetrafluoroethylene
Reduction solution	3.5 wt% NaCl at pH 8.5 in deionized water
Reduction solution volume	1.5 L
Oxidation solution	0.1 M NaOH in deionized water
Oxidation solution volume	300 mL
Minimum solutions deaeration time	5 h
Counter electrodes (CE)	Platinum
Reduction reference electrode (RE_R)	Saturated calomel electrode, Hg $\vert$ Hg$_2$Cl$_2$
Oxidation reference electrode (RE_O)	Mercury-mercury oxide, Hg $\vert$ HgO
Oxidation cell applied potential	+650 mV with respect to open-circuit current
Reduction cell charging current density	$-1\,\mathrm{mA\,cm}^{-2}$

$$\frac{\partial C}{t} = \frac{D\partial^2 C}{\partial x^2} \tag{6.3}$$

where C is the concentration of hydrogen atoms, D is the hydrogen diffusivity in the sample, t is time and x is the distance along the sample thickness.

The data should always have a steeper gradient than predicted by Fick's law, showing defects in the structure affecting the diffusion process. A shallow gradient would show that surface reactions dominate, and the hydrogen oxidation is not transport limited [182].

Data analysis

Two methods have been advanced by Devanathan to calculate the effective diffusivity, the breakthrough and time-lag methods [34]. Consistency between the values of diffusivity deduced using both methods is essential to prove well implemented experiments.

1. Breakthrough method. The time between the start of the galvanostatic charging of the reduction cell and the time when the initial rise in the oxidation current is observed is measured and the diffusivity is obtained using:

$$D_{Eff} = \frac{L^2}{15.3 \times t_b} \qquad (6.4)$$

where D_{Eff} is the hydrogen effective diffusivity, L is the sample thickness, and t_b is the breakthrough time.

2. Time-lag method. The time between the start of the galvanostatic charging of the reduction cell and that at which the oxidation current has reached 63% of the steady-state current value, background excluded, is measured and the diffusivity is obtained using:

$$D_{Eff} = \frac{L^2}{6 \times t_{lag}} \qquad (6.5)$$

where D_{Eff} is the hydrogen effective diffusivity, L is the sample thickness, and t_{lag} is the time-lag time.

The change in gradient between two successive runs can indicate qualitatively the presence of deep irreversible traps. During the first permeation experiment, both reversible and irreversible traps hinder the diffusion of hydrogen through the lattice. After the first experiment, the reversible traps release the trapped hydrogen while irreversible traps retain it. During the second experiment, only reversible traps participate in the retardation of hydrogen transport, which is seen as a less steep permeation transient, that also occurs earlier [182].

6.2.2   Results

Effective diffusivity

Due to time constraints, one of the seven samples could not be investigated. It was chosen to be F34-350C, since it was observed that its austenite fraction, bainite lath thickness and blocky austenite size were close to that of F34-330C and would likely give similar permeation results. Table 6.2 summarises all the values of D_{Eff} calculated from permeation using the breakthrough and time-lag methods, and compares those values to the retained austenite fraction (V_γ) presented in Fig. 5.3 for each sample. For all samples, the consistency

between D_{Eff} calculated using the time-lag and breakthrough methods indicate that the permeation experiments were performed well. For F34-305C, the only sample with V_γ below the percolation limit of 0.1, the diffusivity was significantly faster than for all other samples. Interestingly, despite the many microstructural differences between all the samples, the values of D_{Eff} calculated were all close, comprised between 0.9 and $1.1 \, \mathrm{m^2 \, s^{-1}}$, with the exception of F49-305C, for which it was $0.8 \, \mathrm{m^2 \, s^{-1}}$.

All breakthrough data were then plotted against austenite fraction, in order to compare them with the data from Fielding and Kazum, which are the only two published results of hydrogen diffusivity in nanostructured bainitic steels containing retained austenite [76, 184]. The reported charging current densities used were: $-0.1 \, \mathrm{mA \, cm^{-2}}$ for Fielding and $-2 \, \mathrm{mA \, cm^{-2}}$ for Kazum. Since those values are close to the ones used for this project, the resulting values of effective diffusivity are expected to be consistent together. Fielding was the first to ever report a decrease in D_{Eff} with increasing austenite fraction, especially above the austenite percolation limit. Due to the inconsistencies between the time-lag and breakthrough values presented by Fielding, only the breakthrough diffusivity values could be trusted, since shorter times are required to acquire such data, over which surface reactions are less likely to occur and affect the results. All data were plotted as diffusivity versus V_γ, in Fig. 6.2. The data collected followed the trend observed by Fielding and were also consistent with the work presented by Kazum. Fig. 6.2 reveals that after the initial drop in diffusivity when V_γ increases from 0 to 0.1, the values of D_{Eff} plateau, for austenite fractions comprised between approximately 0.1 and 0.18, before decreasing again over 0.19. Below a volume fraction of 0.1, any increase in V_γ can be conceptualised as a significant increase in the hydrogen path tortuosity, thus observed as a decrease in D_{Eff}. At $V_\gamma = 0.1$, the hydrogen path has to cross at least 1 austenite barrier. It is possible that up to 0.18 V_γ, there is no significant increase in the tortuosity of the hydrogen path with increasing V_γ, because many other paths that involve crossing one austenite barrier become available. Above 0.18 V_γ, it may be that the hydrogen path needs to cross more than one austenite barrier, thus decreasing D_{Eff} further. In order to test that hypothesis, additional permeation tests are needed to be run with samples possessing

a bainitic structure with intercalated austenite, and with V_γ in excess of 0.2.

Because of the similar diffusivity values found, it was expected that most samples would display similar TDS curves. Only three samples were analysed further using TDS, to determine the cementite binding energy in bainite, and to determine the hydrogen trapping ability of the samples. Those were the two as received alloys, F34-330C and F49-290C, as well as F34-AC, for which the microstructure was unique compared to all other heat treated samples.

Deep trapping investigation

This was investigated by performing two successive permeation experiments and observing the differences in permeation transient slope and start time. Because this process is only qualitative, it was only performed on a few samples, which all displayed very similar behaviours, shown in Fig. 6.3 for F34-305C. The transient that would occur following Fick's second law was also plotted using the data provided in the British standard ISO 17081 [182]. Both transients are steeper than the one that fits Fick's law, which verified the transport-limited hydrogen oxidation and certified the quality of the data. It also confirmed the presence of traps in the alloy, without which the sample transients would superimpose onto the transient obtained from Fick's second law. The first transient rose slightly later than the second one, with a slightly steeper slope, indicating a low deep trap presence [182]. The three selected samples were tested with TDS after room temperature hydrogen degassing in order to quantify those deep traps, with results presented in Section 6.5.2.

Table 6.2: Summary of all effective diffusivity (D_{Eff}) values obtained from permeation together with the XRD measured austenite fractions for the samples investigated. The potential changes measured were small enough to ensure the validity of the data collected, as could be confirmed by the close agreement of the values calculated using the time-lag and the breakthrough methods.

| Alloy	Austenite fraction	Time-lag D_{Eff} / $m^2\,s^{-1}$	Breakthrough D_{Eff} / $m^2\,s^{-1}$	Potential change / mV
F34-305C	0.08	1.41×10^{-11}	1.43×10^{-11}	30
F34-330C	0.14	1.11×10^{-11}	0.97×10^{-11}	40
F34-AC	0.17	0.89×10^{-11}	0.95×10^{-11}	80
F49-260C	0.12	1.02×10^{-11}	1.03×10^{-11}	20
F49-290C	0.18	0.91×10^{-11}	0.99×10^{-11}	15
F49-305C	0.19	0.79×10^{-11}	0.82×10^{-11}	15
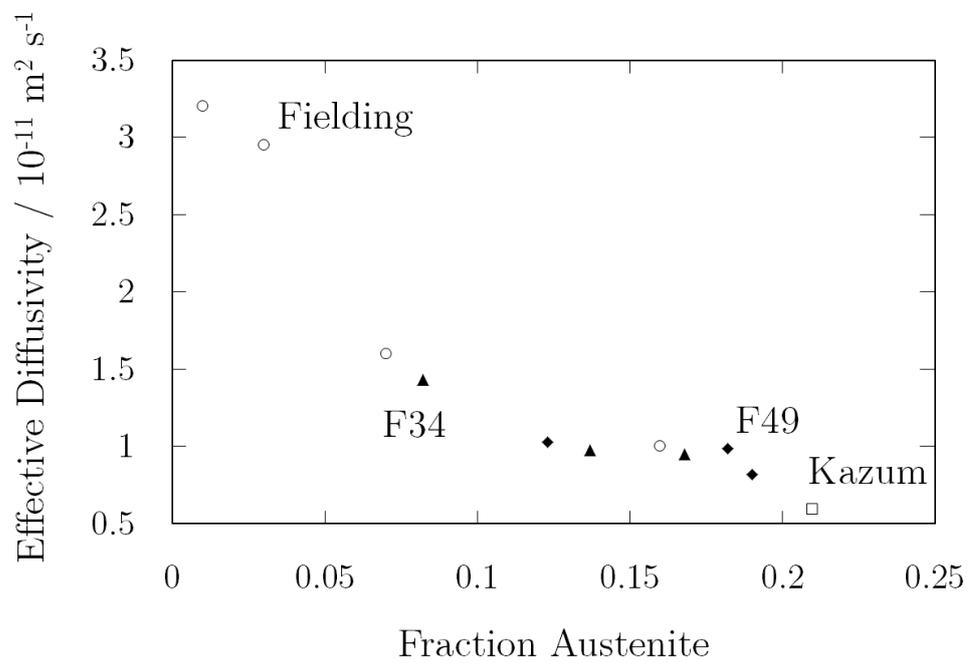
Fig. 6.2: Comparison of all breakthrough data with the work of Fielding and Kazum [76, 184]. The new data fit well in the trend reported for bainitic alloys, and provided evidence for the presence of a plateauing of D_{Eff} when V_γ was comprised between 0.1 and 0.18.
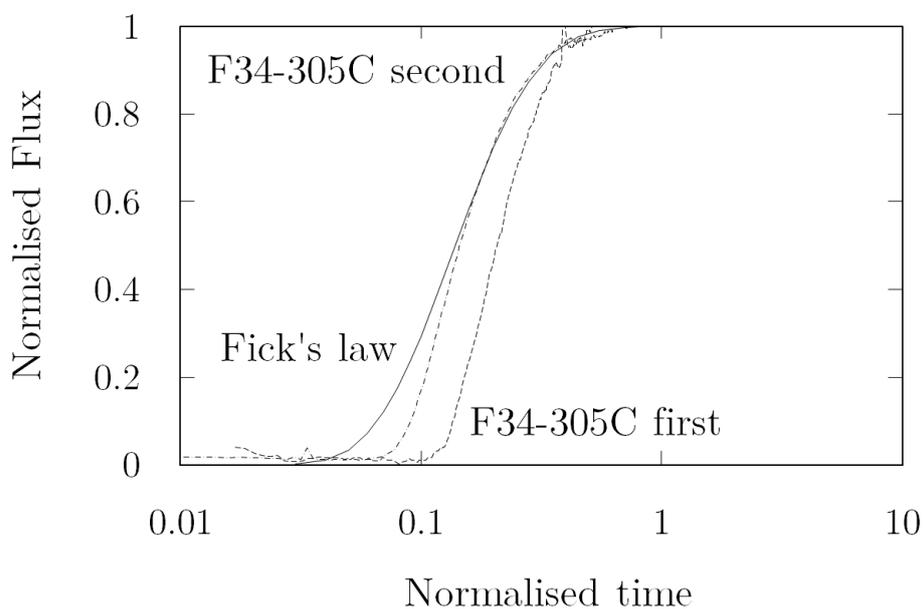
Fig. 6.3: Experimental F34-305C successive transients compared to Fick's law, plotted using data provided in the British standard ISO 17081 [182]. The small but noticeable change in the transient gradient and start time indicate a small density of strong traps. The normalised flux was obtained by dividing the hydrogen flux by the steady-state flux and the normalised time was obtained by multiplying the time measured from the start of the galvanostatic charging by D_{Eff} and divided by the thickness of the sample squared. Both are therefore unitless.

6.3   Dislocation density characterisation

6.3.1   Introduction

The dislocation contribution to trapping in the three selected samples could be predicted from the dislocation density, which determines the number density of hydrogen traps at the core of dislocations [23]. Combining this information with the dislocation binding energy reported in the literature permitted the TDS data to be fitted. Several methods have been proposed for assessing dislocation density, including dilatometry [185], XRD [186], TEM [186] or an empirically derived formula by Bhadeshia [93]. It is commonly accepted that XRD is the simplest method for this analysis [93, 186], and it was performed exclusively.

With XRD, the peak broadening is used to determine dislocation density. As explained by Cullity, there are in total three contributions to peak broadening, one from the instrument, and two from the sample [162]:

1. The instrument contribution, which has to be first estimated using a standard sample, presently LaB_6.

2. The contribution from small crystallite size, which occurs at length below 100 nm and are due to small diffracting lattices.

3. The contribution from internal strains, which can be uniform or not, and modify the d-spacing of the lattice in the vicinity of the strains. Fig. 6.4 represents those effects schematically. Dislocations cause non-uniform strains in samples and cause a peak broadening.

6.3.2   Data Analysis

In order to subtract the instrument contribution from the peak broadening, the peak profile had to be known. In practice the XRD peaks are neither purely Gaussian or Lorentzian, but a
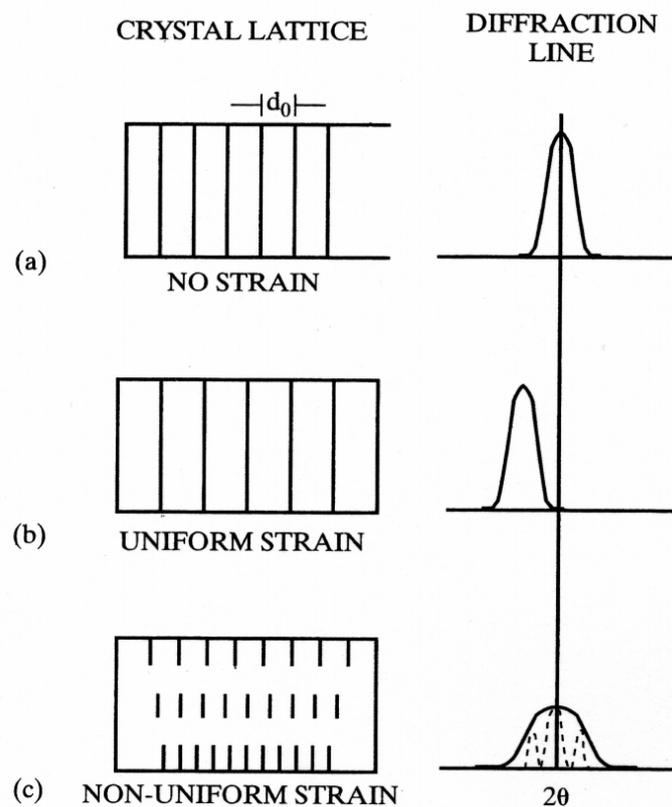
Fig. 6.4: Schematic representation of the effect of internal stresses on XRD peaks, from Cullity [162]. In the case of dislocations, non-uniform strains are present around the dislocation core, which modify the d-spacings of neighbouring planes of atoms unevenly, and are seen as a peak broadening in the XRD spectra.

linear mixture of both, called pseudo-Voigt. For purely Lorentzian and Gaussian profiles, the instrument contribution to broadening is expressed according to equations (6.6) and (6.7) respectively [162]:

$$\text{Lorentzian profile: } B_{total} = B_{instrument} + B_{sample} \tag{6.6}$$

$$\text{Gaussian profile: } B_{total}^2 = B_{instrument}^2 + B_{sample}^2 \tag{6.7}$$

where B_{total} is the total peak breadth, $B_{instrument}$ is the instrument contribution, and B_{sample} is the sample contribution.

There is no accurate formula for pseudo-Voigt profiles, but it is possible to realise that the instrument contribution can be removed in the two extreme cases, for purely Lorentzian and Gaussian peak profiles, and state the real case scenario would be within both cases [168]. Fig. 6.5 and Fig. 6.6 show an XRD pattern fitted assuming purely Gaussian or purely Lorentzian peaks respectively. The peaks can be seen to be almost purely Gaussian, and the squared stripping of the instrument contribution was performed according to equation (6.7). The sample crystallite size and microstrain contributions to broadening had to be separated. The Williamson-Hall plot, which displays peak breadth versus peak diffraction angle was used for this effect, as it enabled calculation of the strain within the sample as the slope of the graph, and crystal size as the offset [165]. In the present work, the four first ferrite peak breadths were plotted versus the tangent of half the diffraction angle at which they occur, which lead to a slope equivalent to four times the strain in the sample, using equation (6.8) derived by Stokes [187]:

$$B_{sample} = 4\varepsilon \times \tan\theta \tag{6.8}$$

where B_{sample} is the sample broadening, ε is the microstrain and θ is half the diffraction angle.
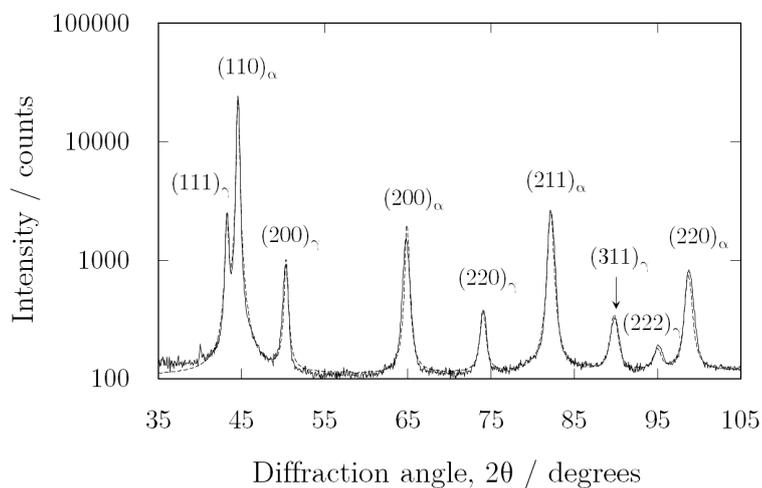
(a) XRD spectrum (solid line) and fit (dashed line) assuming purely Gaussian peaks
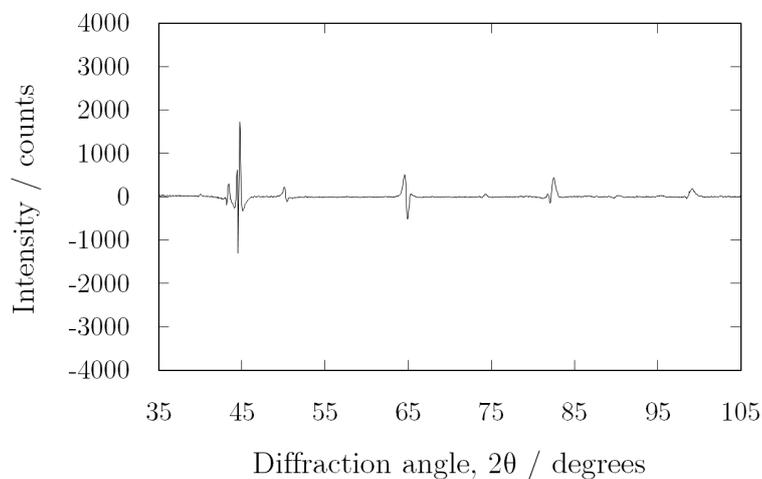

(b) Difference between the acquired and simulated spectra

Fig. 6.5: Example of XRD pattern fitted assuming purely Gaussian peaks, for F34-330C. The fit is good and close to the fit obtained using Pseudo-Voigt peaks, presented in Fig. 5.6, indicating the peaks were almost purely Gaussian.
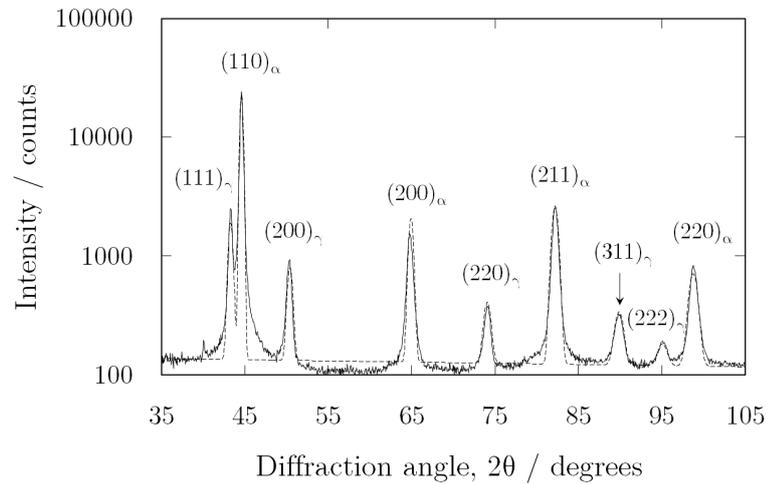
(a) XRD spectrum (solid line) and fit (dashed line) assuming purely Lorentzian peaks
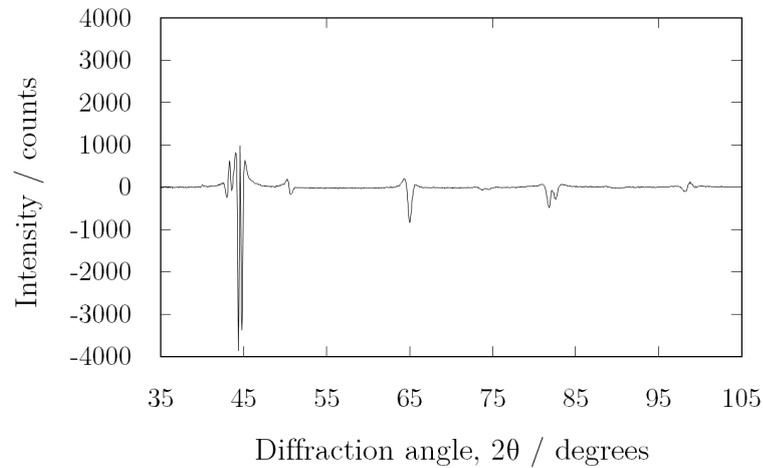
(b) Difference between the acquired and simulated spectra

Fig. 6.6: Example of XRD pattern fitted assuming purely Lorentzian peaks, for F34-330C. The fit is not good, indicating the peaks were not Lorentzian.

The dislocation density was then deduced using equation (6.9) derived by Williamson, for body-centred cubic phases [188]:

$$\rho = 14.4 \frac{\varepsilon^2}{\frac{\sqrt{3}a}{2}^2} \qquad (6.9)$$

where ρ is dislocation density in m^{-2}, ε is the microstrain, a is the lattice parameter, and $\frac{\sqrt{3}a}{2}$ is the Burgers vector of dislocations in body-centred cubic phases.

6.3.3 Results

First, the instrument broadening was measured using a standard LaB$_6$ powder, with the same apparatus setup that was also used for the dislocation density measurements. The receiving slit was 0.1 mm and the divergence slit was variable, with a fixed illumination length of 10 mm. A 0.012 mm Ni filter was used, and the 35 to 105 degrees range was covered, with a dwell time of 0.5 s and a step of 0.05 degrees for samples and 0.01 degrees for the standard LaB$_6$ powder. The peak breadth versus diffraction angle was plotted for the standard, and a second degree polynomial equation was fitted. This way, the instrument contribution could be estimated at the ferrite peak positions in the samples. The XRD scans were then performed on the three samples. The integral breadth, which represents the width of a rectangle of same height and area as the peak investigated, was used as a measure of the peak breadth because of the necessity to use this value with equation (6.7) [162]. Fig. 6.7 shows the Williamson-Hall graph obtained for F34-330C. All three graphs were similar, with the second data point, which corresponds to the (200) ferrite peak always inconsistent with the rest of the data. This is due to the presence of martensite in all three samples, which has a longer c axis than bainitic ferrite. Consequently, the (002) martensite peak appeared at a lower 2θ diffraction angle compared to the (200) ferrite peak. Because of the small difference in the c axis value between martensite and ferrite, both peaks cannot be resolved, but appeared as a broader peak than if only ferrite had been present. This second data point was ignored when fitting the data points, and the slope of the best fit line was used to find the microstrain. Equation (6.9) was then used to find the dislocation density, using the lattice

parameter determined by XRD. The values of dislocation density were also compared to the empirical equation proposed by Bhadeshia, equation (6.10) which estimates the dislocation density of a bainitic alloy solely based on its isothermal transformation temperature [93]:

$$\log \rho = 9.2848 + \frac{6880}{T} - \frac{1780360}{T^2} \tag{6.10}$$

where ρ is the dislocation density in m^{-2} and T is the isothermal transformation temperature in Kelvin.

All the calculated dislocation densities are summarised in Table 6.3. All values are close, and agree reasonably well with the simple relation provided by Bhadeshia. The dislocation densities are also consistent with those reported by Fondekar, where 0.34 wt% C alloys were transformed to bainitic structures at 300 and 360°C and for which the dislocation densities obtained using XRD were 6.3 and 4.7 $\times 10^{15}$ m^{-2} respectively [189]. Since the dislocation densities are of similar orders, it is expected that dislocation in all three samples should contribute to hydrogen trapping in a similar fashion.

Table 6.3: Dislocation densities ρ calculated using XRD and estimated from the empirical relation provided by Bhadeshia [93].

Alloy	XRD calculated ρ / m^{-2}	Estimated ρ using [93] / m^{-2}
F34-330C	$4.5 \pm 1.5 \times 10^{15}$	6.3×10^{15}
F34-AC	$5.0 \pm 2.7 \times 10^{15}$	N/A
F49-290C	$5.8 \pm 2.3 \times 10^{15}$	7.7×10^{15}
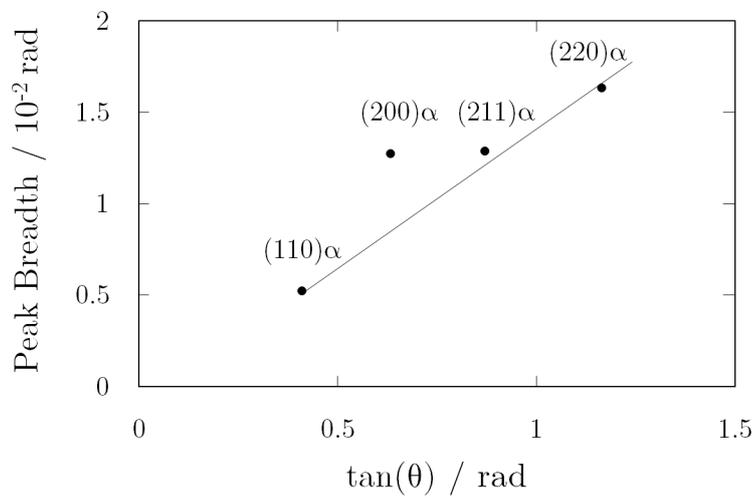
Fig. 6.7: Williamson-Hall plot for F34-330C. The $(200)_\alpha$ point was not aligned with all other points because the martensite present in the sample caused a significant broadening of this peak due to its shorter c parameter compared to bainitic ferrite. The slope was equal to four times the microstrain present in the sample [187].

6.4   Carbide characterisation

Carbides were first imaged and characterised using TEM. XRD was then used to quantify the phase fraction of carbides in the samples. The very low fraction of carbide present in the samples made it challenging to quantify, and it was only possible to do so with F49-290C, for which a phase fraction of cementite of 0.001 ± 0.0001 was quantified. This value is smaller than ever reported in the literature for similar alloys, using XRD.

6.4.1   TEM

The experimental details described in Chapter 3 were used in order to obtain the data presented in this subsection. From the carbide reflection spots in the diffraction patterns, cementite could always be identified undoubtedly. Figs. 6.8, 6.9 and 6.10 show the different morphology that cementite was observed to possess within the different samples. At the highest transformation temperature, in F34-330C, the cementite particles were significantly coarser and longer than in the other two allows. In F49-290C, the cementite particles were substantially finer and more dispersed within the ferrite laths. For the air-cooled sample, F34-AC, the cementite morphology was within the two other cases. This is consistent with the observation by Bush that cementite is coarser at higher transformation temperatures in bainitic structures [190].

6.4.2   XRD

Experimental method

Determining the initial setup parameters was complicated because of the low cementite content present in the samples investigated, as well as the presence of iron oxides in the samples and the inability to remove completely the Cu K_β radiation. This beta radiation generated peaks due to diffraction with the highest intensity (110) ferrite and (111) austenite peaks, at the exact location where cementite peaks are usually present and therefore completely hide those peaks, which renders the phase quantification more complicated [177]. After many
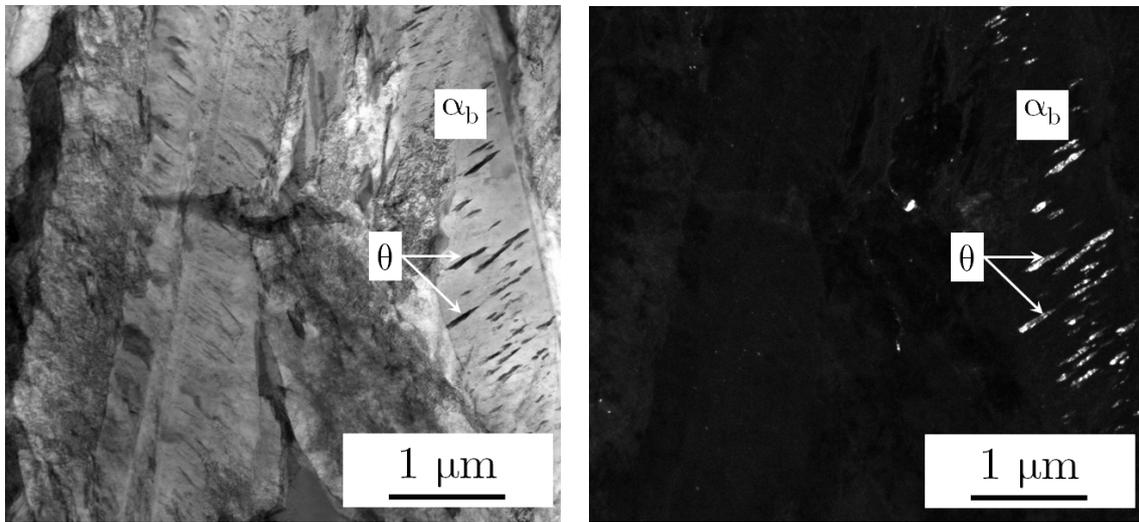
(a) Bright field

(b) Dark field
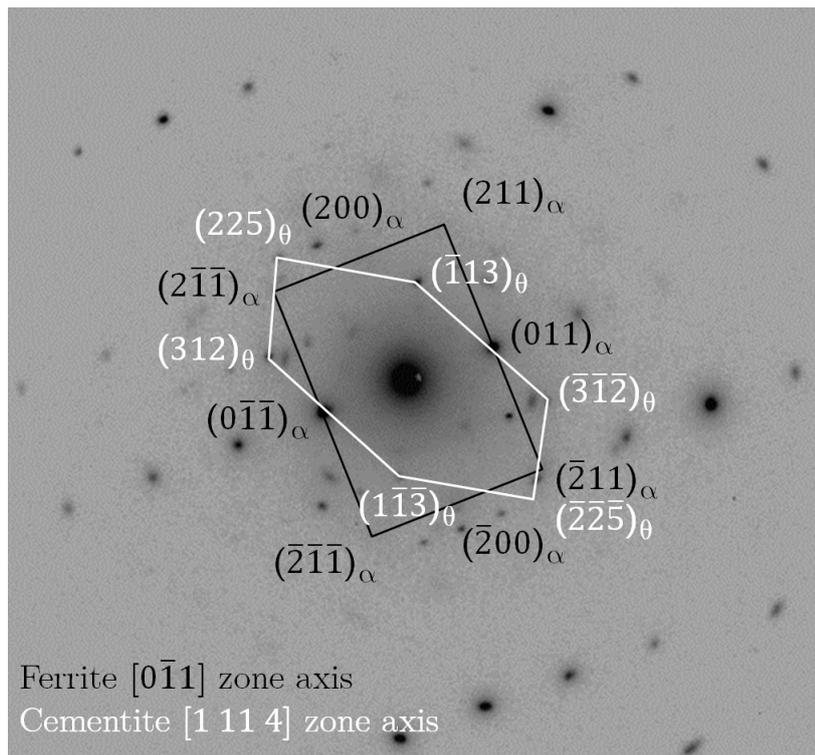
(c) Diffraction pattern

Fig. 6.8: TEM characterisation of cementite (θ) within the bainitic ferrite in F34-330C. The diffraction pattern was obtained using a selected area aperture that encompassed the region of interest. The dark field image was formed using the indexed (312) cementite reflection.

(a) Bright field
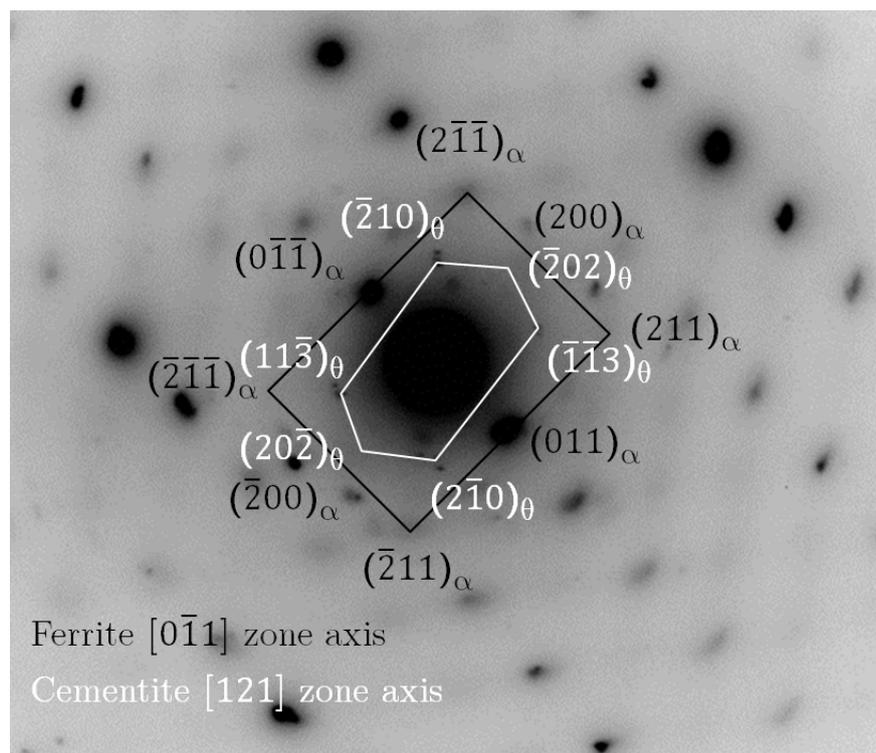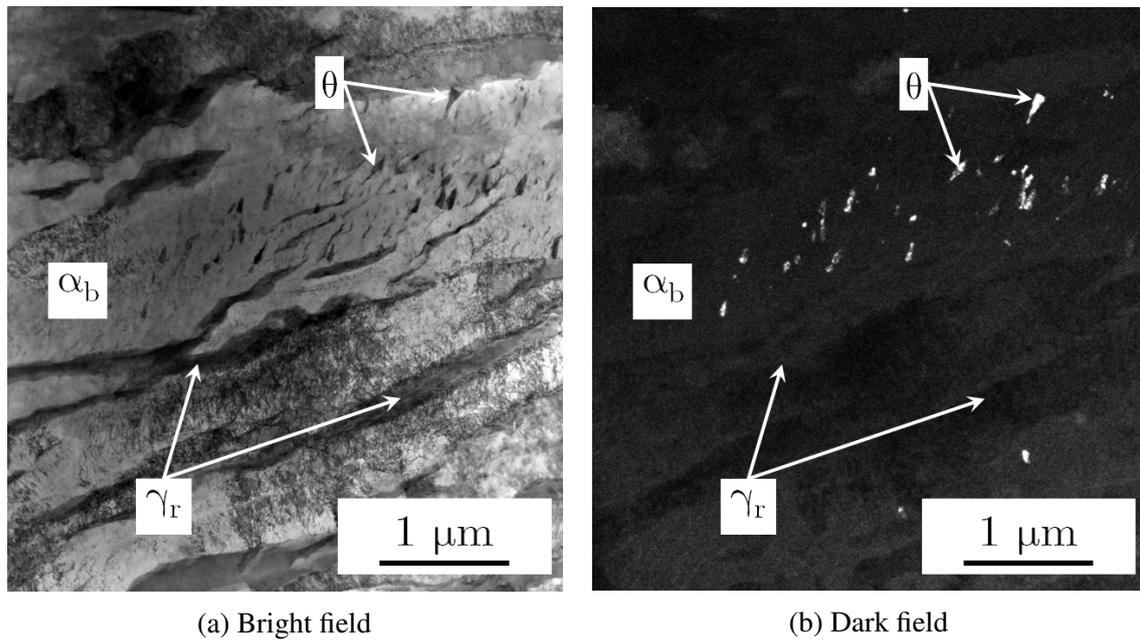
(b) Dark field

(c) Diffraction pattern

Fig. 6.9: TEM characterisation of cementite within the bainitic ferrite in F34-AC. The diffraction pattern was obtained using a selected area aperture that encompassed the region of interest. The dark field image was formed using the indexed $(\bar{1}\bar{1}3)$ cementite reflection.

(a) Bright field
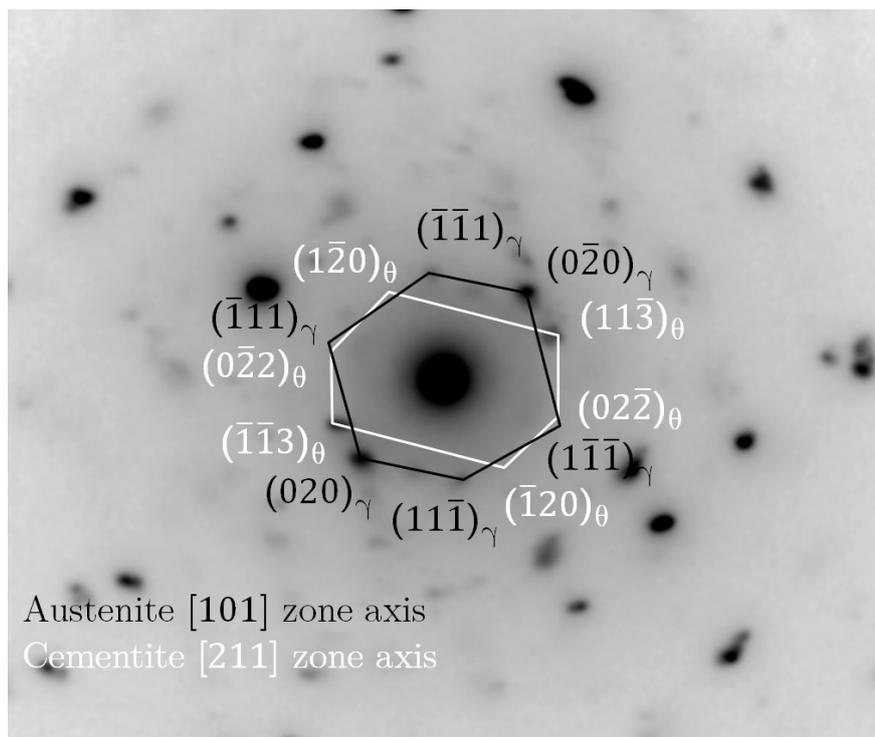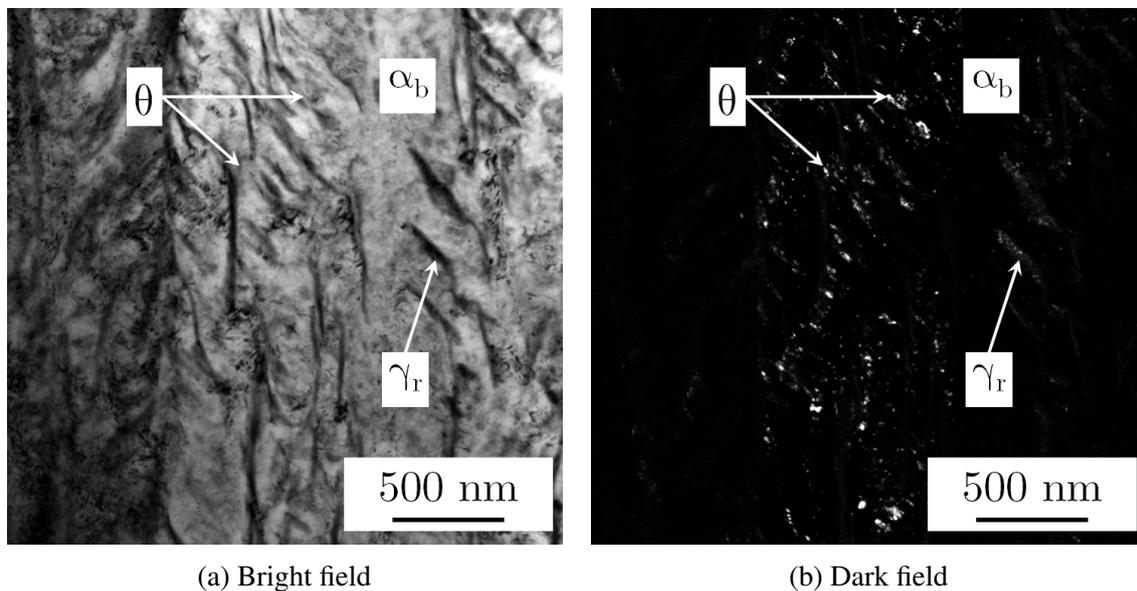
(b) Dark field

(c) Diffraction pattern

Fig. 6.10: TEM characterisation of cementite within the bainitic ferrite in F49-290C. The diffraction pattern was obtained using a selected area aperture that encompassed the region of interest. The dark field image was formed using the indexed $(11\bar{3})$ cementite reflection.

attempts, the following parameters were chosen for carbide detection optimisation: 0.1 mm receiving slit, variable divergence slit with 10 mm fixed illuminated length, 0.02 mm Ni filter, 25-70 degrees range, with a dwell time of 22.5 s and a step of 0.015 degrees. The nickel filter was kept because many other parasitic radiations caused additional peaks to appear when it was removed, which prevented the cementite peaks from being visible. Cementite was only detected and therefore quantified accurately in F49-290C. For the other two samples, the maximum cementite fraction was determined by simulating the point at which the phase fraction of cementite would be large enough for it to become visible in the diffraction pattern.

Data analysis

In order to ensure only cementite was present, the following steps were always taken to index all peaks present in the acquired patterns:

1. All beta peaks were identified and ignored for the analysis.

2. All oxide peaks were identified and ignored for the analysis. Both Fe_2O_3 and Fe_3O_4 were detected.

3. The last unindexed peaks were fitted with all possible iron carbide data files present in the ICDD, ICSD and crystalmet databases. Only cementite was found to fit the experimental data, with the best fit being using the cementite file from Shimura [177]. One peak remained unidentifiable, it fitted some SiO_2 patterns, but not in a unequivocal manner.

Results

The final XRD scan for F49-290C is presented in Fig. 6.11. Most of the scan contained peaks from oxides and beta radiation that could not be used for cementite quantification. At angles between 25 and 40 degrees, Fig. 6.12, the (111) cementite peak was clearly visible. By fitting this peak, it appeared that two other cementite peaks, (020) and (112) were also just discernible from the background. This pattern was fitted using the cementite file by Shimura to simulate an ideal pattern from this phase [177]. The unit cell was found to be: a = 4.50 Å,

b = 5.15 Å, c = 6.75 Å. The fit and the experimental data are both shown in Fig. 6.12. After initially fitting and quantifying the ferrite and austenite phases, the cementite phase was also quantified as 0.1% using Rietveld analysis [167]. The error on that phase quantification was estimated by allowing the fraction of cementite to vary and observe the effect on a simulated ideal pattern. Fig. 6.13 shows the slight variations in simulated pattern when changing the volume percent of cementite by 0.01%. Despite this low number, it is still possible to see in the pattern that above 0.11% cementite, all visible simulated peaks have too high intensities, while below 0.09% cementite, the (111) simulated peak has a too low intensity, although the (020) peak is still reasonably fitted.

When fitting the diffraction patterns for F34-330C and F34-AC, the visibility limit of cementite was found to be 0.01% and 0.02% respectively, signifying the cementite phase percent must be inferior to that. It is not clear why the quantity of cementite was observed to be much larger in the laboratory scale alloys, where they were of the order of 0.2-1.7%. One reason could be due to the higher heterogeneity of laboratory manufactured alloys compared to large scale produced ones. A summary of the amount of cementite contained in the three samples is presented in Table 6.4.

Table 6.4: Cementite phase fraction characterised using XRD for the three samples.

| Alloy	cementite phase fraction
F34-330C	< 0.0001
F34-AC	< 0.0002
F49-290C	0.001 ± 0.0001
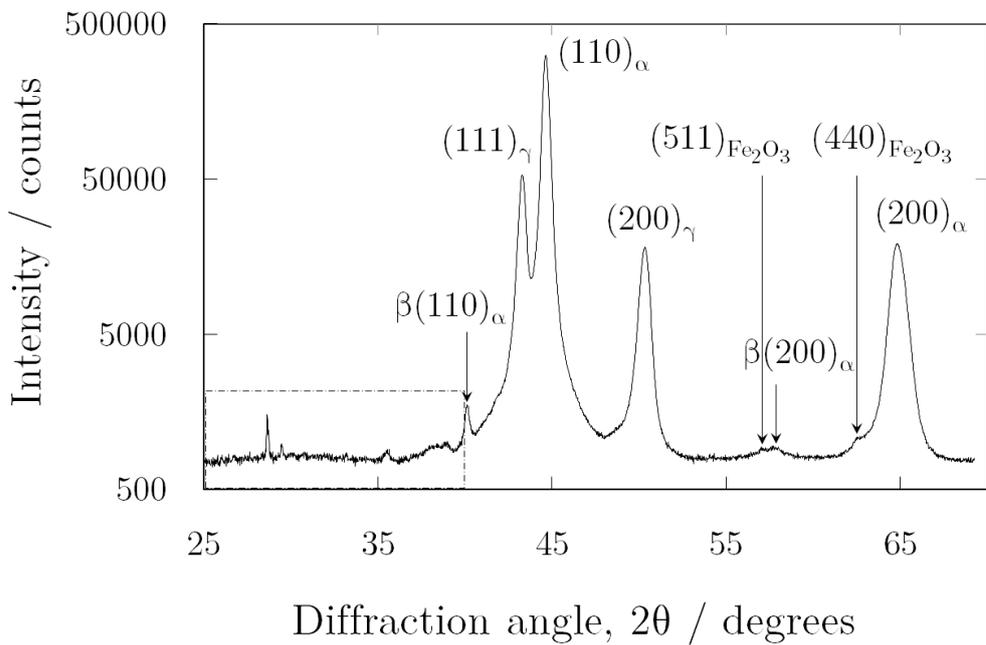
Fig. 6.11: XRD spectrum for F49-290C displaying the presence of oxides, cementite, and β reflections from iron.
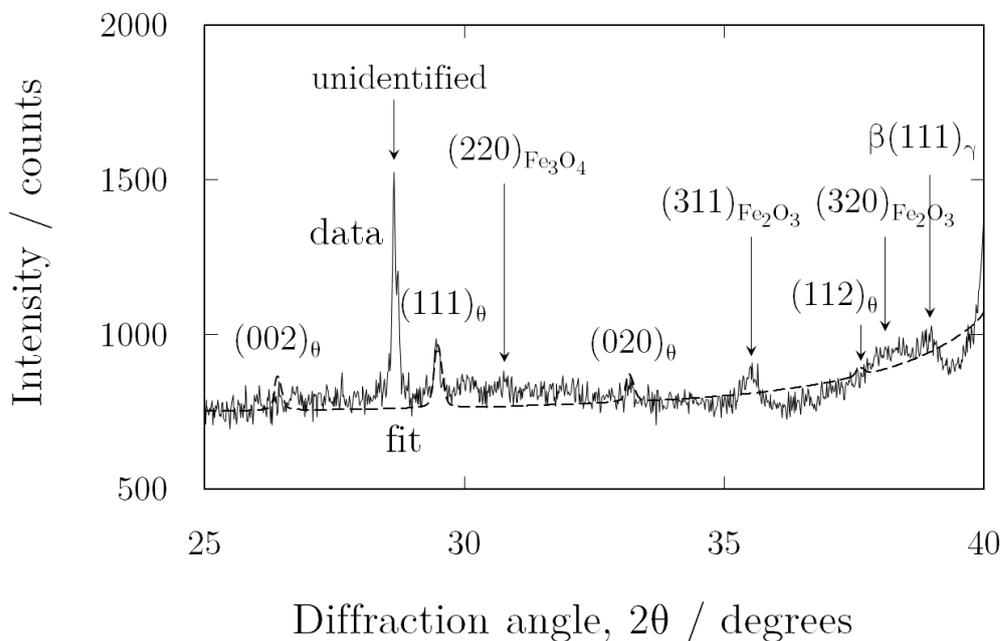

Fig. 6.12: Dashed portion of Fig. 6.11. In this portion of the scan, the $(111)_\theta$, $(020)_\theta$ and $(112)_\theta$ peaks used for quantifying the amount of cementite can be seen, along with a simulated pattern, obtained using the cementite file from Shimura [177].
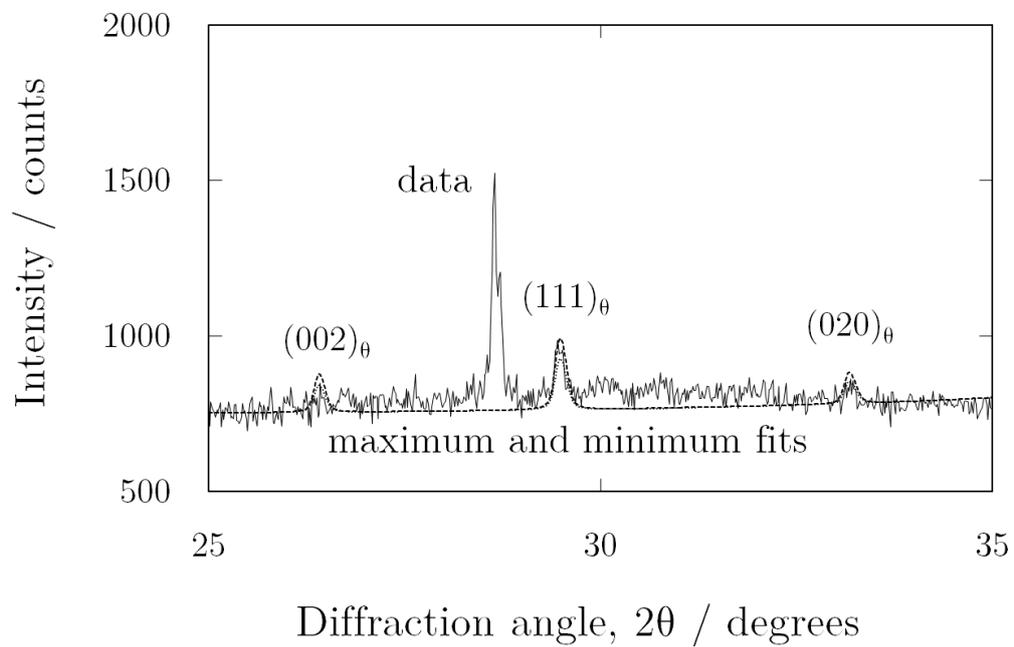
Fig. 6.13: The same pattern was used to determine the error in the quantification. The (111) and (020) peaks were fitted to extremes, where the fits became inaccurate. Those extremes corresponded to 0.09 and 0.11% cementite.

6.5 Thermal Desorption Spectroscopy

Experimental setup

The experimental method described in Section 4.7.1 was used to acquire and treat the thermal desorption spectroscopy (TDS) spectra. In the current chapter, the sample dimensions were $60 \times 10 \times 2$ mm, with the thickness along the rolling direction, which is most representative of the microstructure [191]. The heating rate was $50°$C h^{-1} for all samples except for the tempered F49-290C sample, for which it was $100°$C h^{-1}. Since the effective diffusivity of the three investigated samples was comprised between 0.9 and 1.1 $\times 10^{-11}$ m^2 s^{-1}, the time required to penetrate 2 mm into the samples was obtained from diffusion theory as L^2/D_{Eff}, that is between 101 and 123 hours [183]. Since charging occurred from both sides of the samples simultaneously, the ingress may actually need to cover only 1 mm, which would equate to charging times of 25 to 31 hours. In order to ensure saturation, even if one side of the sample had oxidised, the charging time was selected as 100 hours. This charging time appeared to be too high and sometimes led to oxidation of samples, which meant the experiments had to be restarted.

6.5.1 Parameters used to fit experimental data

The local equilibrium computer model developed by Song was used to fit the experimental data in order to assess the binding energy of cementite and the number density of the three traps investigated: dislocations, cementite, and the ferrite/austenite interface. In order to fit experimental data, several parameters are needed. All parameters were estimated from the literature, with the exception of the trap densities, which were estimated experimentally. A list of all those parameters, along with their physical significance and estimated value is presented:

- Q - hydrogen lattice activation energy. It has been reported in pure iron to be of the order of 7.5 kJ mol^{-1} [35, 39, 42]. This value was used.

- D_0 - hydrogen lattice diffusion pre-exponential factor. In pure iron, it has been reported as $10^{-7}\,\mathrm{m^2\,s^{-1}}$ [35, 42, 192]. The model used for fitting was developed using Oriani theory of local equilibrium, in single phase alloys [49]. To reflect the presence of two phases with different hydrogen diffusivity in the samples investigated, D_0 was lowered, as suggested previously by Turnbull in other duplex alloys [50]. The value of D_0 selected for fitting was $1.25 \times 10^{-8}\,\mathrm{m^2\,s^{-1}}$.

- C_0 - initial sample hydrogen concentration sub-surface. The value of the solubility of hydrogen in ferrite at room temperature, presented by San-Martin, is approximately 0.025 ppm [193]. Since C_0 is dependant on experimental setup, 0.025 ppm was chosen as the ideal maximum value. For F49-290C, this value was lowered to 0.0125 ppm to match the experimental data behaviour.

- N_L - hydrogen lattice site density. Those are the twelve tetrahedral interstitial sites per unit cell. Song reported a value of $5.2 \times 10^{29}\,\mathrm{m^{-1}}$ in fully bainitic alloys [49]. Since the samples analysed had significant austenite fractions, this number was multiplied by the phase fraction of bainitic ferrite.

- E_{B_D} - Dislocation binding energy. As presented in Chapter 1, the value of $25\,\mathrm{kJ\,mol^{-1}}$ reported by Oriani [23], and confirmed by Ramasubramaniam and Choo, as 26 and $27\,\mathrm{kJ\,mol^{-1}}$ respectively, was used [57, 58].

- E_{B_C} - Cementite binding energy. The model fitting was used to obtain this value.

- E_{B_I} - Ferrite/austenite interface binding energy. As presented in Chapter 1, the value of $52\,\mathrm{kJ\,mol^{-1}}$ reported by Turnbull was used [50].

- N_{T_D} Dislocation trap density. It was calculated as described by Oriani [23]. One atom of hydrogen was assumed to sit per dislocation line per atomic plane. Dividing the dislocation density, which is a dislocation length per unit volume, by the number of planes perpendicular to that line, in other word by the Burgers vector of the the dislocation led to the trap density. The Burgers vector for all three samples was $b = \frac{\sqrt{3}}{2}a$ with a = 2.87 Å, giving a value of b = 2.49 Å.

- N_{T_C} Cementite trap density. Zhu demonstrated using atom-probe tomography that hydrogen atoms are present within epsilon-carbides, rather than exclusively at the interface, as displayed in Fig. 6.14 [29]. Because of the similar structures between epsilon-carbide and cementite reported in Section 1.5.2, it was assumed that both structures would trap hydrogen in similar fashion. In other words, the assumption used for the calculation of N_{T_C} is that hydrogen is trapped at the cementite interstitial sites rather than at the interface with ferrite. There are four equivalent, most stable, octahedral interstices that hydrogen can occupy in cementite [64]. The cementite trap density was therefore calculated as four times the carbide volume fraction in the sample divided by the volume of the cementite cell, both presented in Section 6.4.2.

- N_{T_I} Ferrite/austenite interface trap density. The model fitting was used to obtain this value. Since F49-290C has the smallest bainite lath size and the highest austenite fraction, it was expected that it would have the highest value of N_{T_I} out of the three samples. F34-330C and F34-AC both have similar bainite lath thickness but F34-330C has a lower austenite fraction, therefore it was expected to have the smallest value of N_{T_I} out of the three samples.

The values of those input parameters are summarised in Table 6.5.

6.5.2   Results

TDS curves obtained after hydrogen room temperature degassing

After room temperature hydrogen degassing, no hydrogen could be detected in any of the three samples. This is typical of microstructures that do not contain deep traps. The reversibly trapped hydrogen is allowed to escape with the diffusible hydrogen, and no hydrogen stays trapped in the sample. This is consistent with the permeation experiments during which only little irreversible trapping could be detected. Nevertheless, one example of degassing experiment is presented in Fig. 6.15, for F49-290C. The total amount of hydrogen present in the sample was calculated to be 3.0 parts per million (ppm) and it took approximately 2800 minutes, or 47 hours for all the hydrogen to escape the sample.
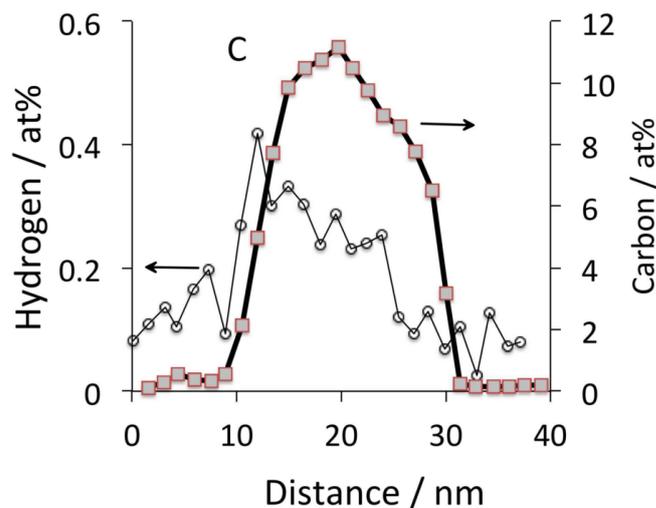
Fig. 6.14: Atom-probe tomography showing hydrogen trapped within epsilon-carbide, rather than exclusively at its interface with ferrite. The diagram was from Bhadeshia, adapted from Zhu [2, 29].

Table 6.5: Summary of all parameters used as an input for the TDS curve fitting. The dislocation and cementite trap densities were determined experimentally and all other parameters were obtained from the literature. The cementite binding energy and α/γ interface trap density were investigated using the fitting procedure.

| Parameter	Alloy	Value
Q / kJ mol^{-1}	All	7.5
D_0 / m^2 s^{-1}	All	1.25×10^{-8}
E_{B_D} / kJ mol^{-1}	All	25
E_{B_C} / kJ mol^{-1}	All	-
E_{B_I} / kJ mol^{-1}	All	52
C_0 / ppm	F34-330C	0.025
C_0 / ppm	F34-AC	0.025
C_0 / ppm	F49-290C	0.0125
N_L /m^{-3}	F34-330C	4.472×10^{29}
N_L /m^{-3}	F34-AC	4.316×10^{29}
N_L /m^{-3}	F49-290C	4.264×10^{29}
N_{T_D} / m^{-3}	F34-330C	18×10^{24}
N_{T_D} / m^{-3}	F34-AC	20×10^{24}
N_{T_D} / m^{-3}	F49-290C	23×10^{24}
N_{T_C} / m^{-3}	F34-330C	$<3 \times 10^{24}$
N_{T_C} / m^{-3}	F34-AC	$<5 \times 10^{24}$
N_{T_C} / m^{-3}	F49-290C	25×10^{24}
N_{T_I} / m^{-3}	All	-
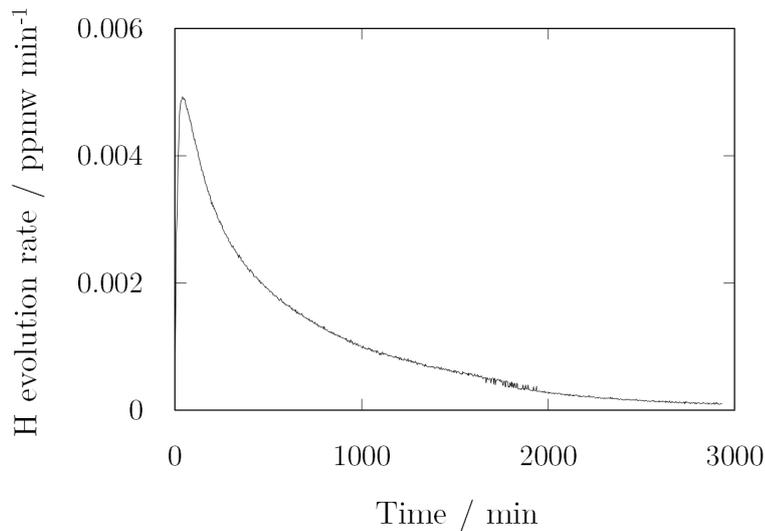
Fig. 6.15: Example of room temperature degassing for F49-290C.

TDS curves obtained directly after hydrogen charging

Fig. 6.16 displays the TDS traces collected for all three samples. The three traps contribution cannot be resolved into separate peaks, but a trend in TDS peak position is nevertheless noticeable between the three samples. In fact the peak position for F49-290C, which was predicted to have the highest cementite trap density, is seen to be at a higher temperature than the other two samples, agreeing with that prediction. The density of traps at the ferrite/austenite interface could also be higher in this sample due to a finer bainite lath thickness and higher overall austenite content, and be the reason for this peak shape. The peak position for F34-330C, which was predicted to have the lowest trap density from dislocations and cementite was observed to be the lowest of all three samples, also being consistent with that prediction. The calculated total amount of hydrogen present in the samples were 1.7, 1.9 and 1.9 ppm for F34-330C, F34-AC and F49-290C respectively. The difference in the quantity of evolved hydrogen between the two F49-290C samples (3 and 1.9 ppm respectively) are due to the experimental charging step, which was not always reproducible due to occasional sample oxidation.

Determination of the cementite binding energy

It was not possible to fit the three TDS curves while conserving the predicted cementite trap

density. The cementite trap density predicted for F49-290C was used as a starting point for fitting, because cementite was characterised with little error by XRD for that sample only. The cementite binding energy and interface trap density were obtained by optimising the quality of the fit between the data and the model. Keeping the same cementite binding energy, the experimental data for F34-330C and F34-AC were then fitted. In the fit optimisation step, it became apparent that a higher cementite binding energy than initially attempted led to better fits. This refinement process was repeated several times until a good agreement between the experimental data and the simulations was obtained for all three samples. The final values of the cementite binding energy and of the dislocation, cementite and interface trap densities are presented in Table 6.6, and the three fitted TDS curves are shown in Fig. 6.17. As predicted, both the cementite and the interface trap density were highest for F49-290C and lowest for F34-330C. The cementite trap density was significantly different from that predicted for F34-330C and F34-AC. Because of the extremely low fraction of cementite and the limited penetration of X-rays in steel, it is possible that sampling error led to the inconsistencies between the predicted and modelled cementite trap densities. The cementite binding energy was found to be 37.5 kJ mol^{-1}. This value is consistent with the work of Robertson, which was described as the most experimentally rigorous cementite binding energy assessment in Section 1.3.4, in which it was found to be 36 kJ mol^{-1} [37]. It is also close to the cementite octahedral site trapping energy calculated from first principles by Kawakami, who proposed a value of 41 kJ mol^{-1} [64].

Table 6.6: List of parameters that produced a good match between the experimental data and the simulated fits.

Parameter	F34-330C	F34-AC	F49-290C
E_{B_C} – Cementite binding energy / kJ mol^{-1}	37.5	37.5	37.5
N_{T_D} – Dislocation trap density / m^{-3}	18×10^{24}	20×10^{24}	23×10^{24}
N_{T_C} – Cementite trap density / m^{-3}	18×10^{24}	19×10^{24}	26.5×10^{24}
N_{T_I} – α/γ interface trap density / m^{-3}	0.6×10^{24}	0.9×10^{24}	1.4×10^{24}
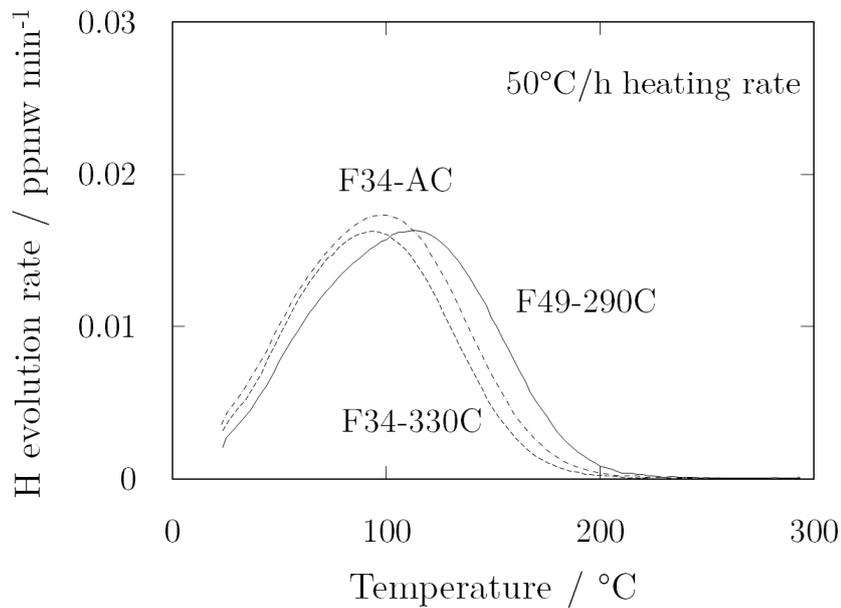
Fig. 6.16: TDS curves obtained directly after charging the all three samples.

Investigation of austenite decomposition effect on hydrogen trapping

A F49-290C sample was tempered at 500°C for 30 minutes to decompose the austenite into a mixture of ferrite and carbides, after it was confirmed using MTDATA that, at equilibrium, there should be 1% austenite in that sample at 400°C and 0% at 500°C. As explained by Bhadeshia, the dislocation density should remained unchanged while transforming at 500°C in times shorter than 1 hour [93]. Indeed, during bainitic transformation, recovery is seen to occur simultaneously as the reaction proceeds, and further recovery usually occurs at higher temperatures or when samples are tempered for longer times.

The dislocation density and carbide quantification characterisation steps previously described were repeated in order to find the new dislocation and cementite trap densities. As predicted, the dislocation density had not changed, although the Williamson-Hall plot revealed another feature, visible in Fig. 6.18. Unlike it was the case in untempered samples, the (200) peak breadth was this time consistent with other peaks, indicating that the martensite present in the sample had transformed to ferrite during the tempering step. The cementite fraction was calculated to have increased from 0.001 to 0.0035 ± 0.0020, and the austenite fraction
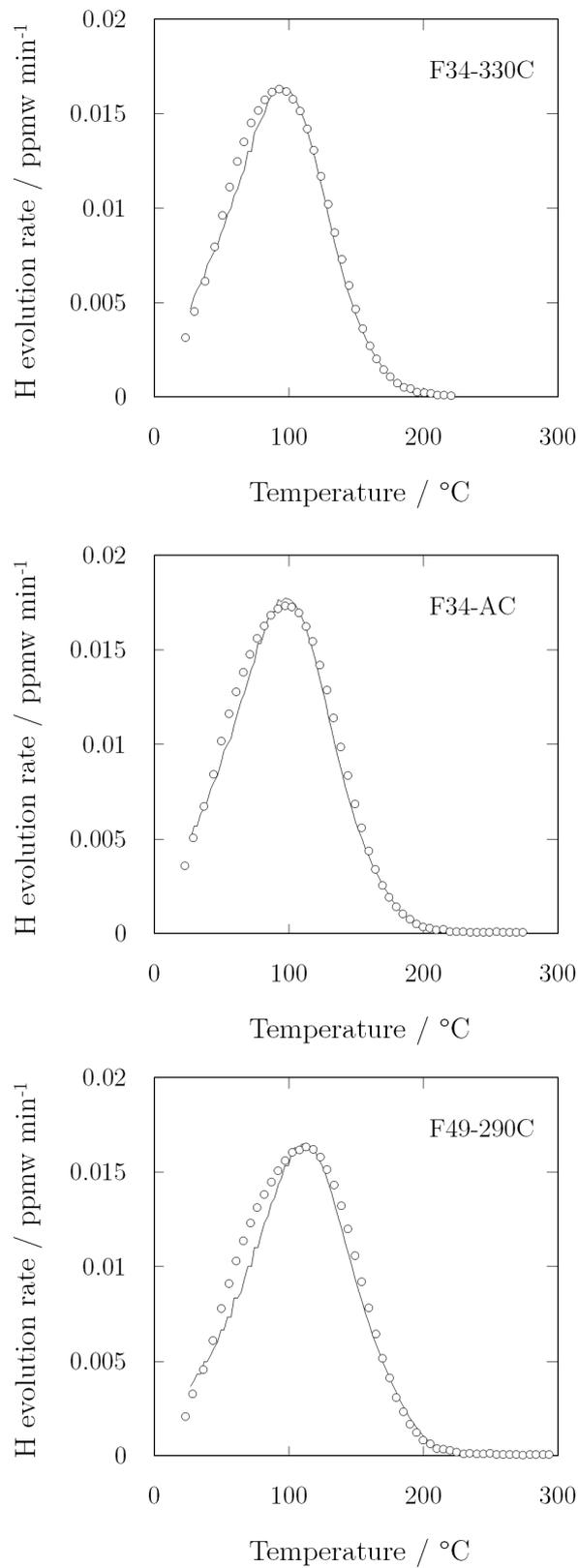
Fig. 6.17: Comparison between the experimental TDS data (circles) and simulations (lines) obtained using the computer model developed by Song [49].

was observed to have decreased from 0.18 to 0.09. Since the film retained austenite is more enriched in carbon than bulky austenite due to the surrounding ferrite rejecting into it its own excess carbon, this austenite is less thermally stable than its bulky counterpart, in other words, the driving force for decomposition into ferrite and cementite is larger [93, 116, 194]. If half the austenite has decomposed it is possible that most of the austenite that contributed to the interfacial trap has decomposed and only bulky austenite is left in the structure.

The fitted data are displayed in Fig. 6.19, and the fitting parameters are compared to those of F49-290C in Table 6.7. The fitting parameters for both samples were surprisingly close, the only difference being a slight increase in the cementite trap density, from 26.5×10^{24} to 28.5×10^{24} m^{-3}. Those results suggest a substantially smaller increase in cementite fraction than expected. The XRD sampling error was again suggested as a potential reason for the inconsistencies between predicted and fitted values of cementite trap density. The austenite trap density did not change between both samples. It is possible that the tempering time was too short to cause a significant change in the microstructure. The total evolved hydrogen from this sample was 2.0 ppm, which is only a slight increase from the 1.9 ppm observed in the untempered F49-290C sample.

Table 6.7: Comparison of the fitting parameters used for F49-290C before and after tempering.

| Parameter	F49-290C	F49-290C tempered
E_{B_C} – Cementite binding energy / kJ mol^{-1}	37.5	37.5
N_{T_D} – Dislocation trap density / m^{-3}	23×10^{24}	23×10^{24}
N_{T_C} – Cementite trap density / m^{-3}	26.5×10^{24}	28.5×10^{24}
N_{T_I} – α/γ interface trap density / m^{-3}	1.4×10^{24}	1.4×10^{24}
C_0 – Initial hydrogen concentration sub-surface / ppm	0.0125	0.0125
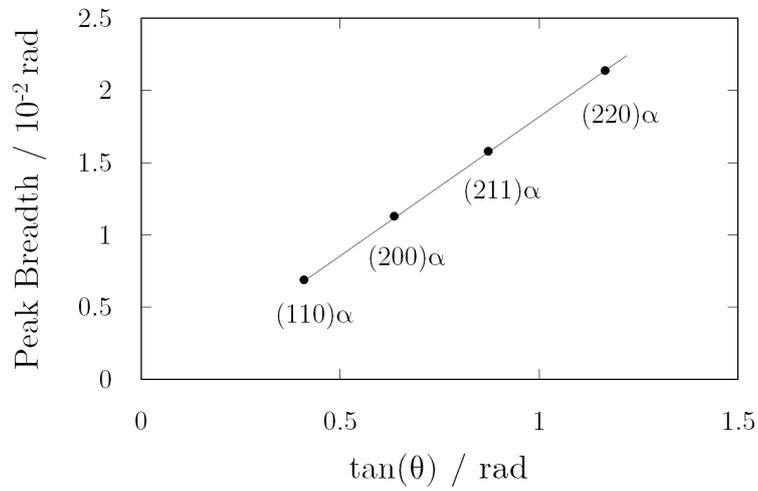
Fig. 6.18: Williamson-Hall plot for the tempered F49-290C sample, displaying the $(200)_\alpha$ point aligned with other points, indicating the removal of martensite from the microstructure.
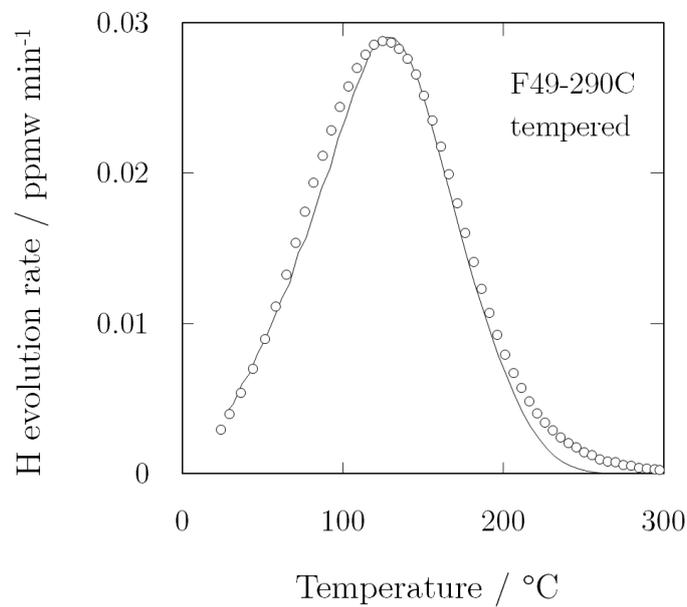

Fig. 6.19: Comparison between the experimental TDS curve (circles) and the fit (line) obtained for the tempered F49-290C sample.

6.6   Conclusions

It has been shown that the six samples investigated displayed similar behaviour of hydrogen diffusion through their lattice. The effective diffusivities calculated using electrochemical permeation were all comprised in the range of 0.8-1.4 $\times 10^{-11}$ m^2 s^{-1}. It was shown that the values of effective diffusivity plateau between austenite fractions of 0.1 to 0.18. Little irreversible trapping was observed when performing successive permeation transients. This lack of deep traps was confirmed in TDS when almost no hydrogen could be detected after room temperature degassing of the samples over two days. Both results suggest cementite was not a strong trap. The binding energy of cementite was found to be 37.5 kJ mol^{-1} in bainitic ferrite, by fitting several TDS spectra. Tempering of bainite for 30 minutes at 500°C was shown to remove the martensite from the sample, but had little impact on the overall microstructure and on the hydrogen behaviour of the sample. XRD has been used to quantify the lowest levels of cementite ever reported in steels, of a value of 0.1 $\pm$ 0.01 % cementite, for F49-290C. The dislocation density was characterised in all samples using Williamson-Hall plots, the maximum cementite fraction was also suggested for all samples and the trap densities from both traps was predicted.

Chapter 7

Mechanical properties of novel alloys

7.1 Introduction

The work presented in this chapter reports the mechanical properties of the designed alloys in relation to their microstructures. Both alloys had to achieve a yield strength above 860 MPa, an elongation to failure of at least 15% and a Charpy fracture energy in excess of 25 J at room temperature. Tensile and Charpy tests were performed to confirm that both alloys met those requirements. Additionally, the stability of austenite and its role towards ductility were explored by cryogenic cooling and by performing tensile tests at constant temperature, ranging from 20 to 300°C. Finally, the susceptibility of F34-330C to sulphide stress cracking, the most common form of hydrogen embrittlement in sour environments, was investigated using an in-situ four-point bend test.

7.2 Tensile tests

7.2.1 Experimental method

The tensile tests were run in accordance to the E8/E8M standard [195]. In tensile tests, samples are fixed on a machine that pulls both ends at a constant rate until the sample fractures. The initial response of the material is elastic, it transitions into plastic deformation past the yield point, and deforms until fracture. Flat specimens were initially tested, but produced very unreproducible results, indicating that the alloys were sensitive to the presence of surface notches. The dimensions of the samples used are displayed in Fig. 7.1. Those dimensions were chosen because they were the largest possible machinable cylindrical samples that could be obtained from the rolled plates of both alloys F34 and F49, thus representative of the effect of the microstructural heterogeneity of the alloys on the outcome of the tensile tests. The samples were tested in a machine with threaded grips, and the elongation was measured with extensometers. The six different isothermally transformed microstructures were tested in three orientations: at 0, 45 and 90° relative to the rolling direction. This way it was possible to detect any anisotropy in the tensile strength. Each test condition was performed in duplicate, with two different cross-head speeds of 0.01 and 0.001 $\mathrm{mm\,s^{-1}}$. The tests were all run at room temperature. Additionally one sample of F34-AC was tested at room temperature, the other samples of F34-AC were used for higher temperature tests in order to assess austenite stability.
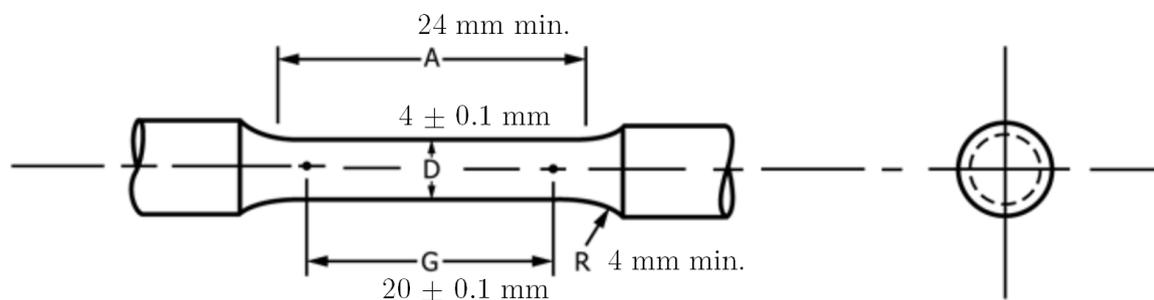

Fig. 7.1: Tensile test specimen dimensions described in the E8/E8M standard [195]. The samples used were cylindrical, with the gauge length being five times longer than the diameter.

7.2.2 Results

Fig. 7.2 displays an example of a tensile curve obtained, for F34-305C. The 0.2% yield strength (0.2% YS) was obtained by drawing a line parallel to the initial stress-strain curve response, corresponding to the elastic deformation of the sample, from the point with coordinates (0.2 , 0). The yield strength was measured at the point of intersection between this line and the stress-strain curve. The ultimate tensile strength (UTS) corresponds to the maximum strength value of the stress-strain curve. The elongation was obtained by drawing a line parallel to the initial stress-strain curve response, from the point of fracture. The elongation was measured at the point of intersection between this line and the x-axis. Table 7.1 shows all the tensile test results for F34 and F49. The strain rate or orientation of samples did not cause a significant change in the properties of the samples, indicating that the properties are isotropic. All F34 samples achieved the strength and elongation to failure goals, and only F49-260C did not for F49. For this sample, the elongation to failure was not satisfactory, but it had the highest ultimate tensile strength compared to all samples, and its yield strength greatly exceeded the set requirement.
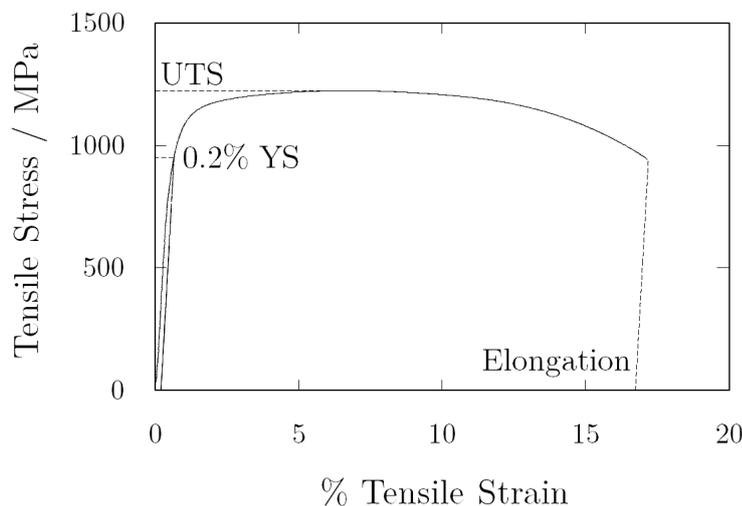

Fig. 7.2: Stress-strain curve for F34-305C, tested along the rolling direction, at $0.01\,\mathrm{mm\,s^{-1}}$. The locations where the values of the 0.2% yield strength (0.2% YS), ultimate tensile strength (UTS) and elongation can be measured are indicated.

Table 7.1: Tensile test results for F34 and F49 presented with the bainite thickness and austenite fraction (V_γ). There was little dependence of mechanical properties on orientation or strain rate. The ultimate tensile strength is abbreviated to UTS and the yield stress to YS.

Alloy	Orientation / °	Crosshead rate / mm s^{-1}	YS / MPa	UTS / MPa	Elongation / %	Bainite thickness / nm	V_γ
Requirements	-	-	860	1230	15	-	-
F34-305C	0	0.01	951	1224	17	153 ± 25	0.08 ± 0.01
F34-305C	0	0.001	846	1232	18	153 ± 25	0.08 ± 0.01
F34-305C	45	0.01	952	1225	17	153 ± 25	0.08 ± 0.01
F34-305C	45	0.001	983	1234	18	153 ± 25	0.08 ± 0.01
F34-305C	90	0.01	969	1241	18	153 ± 25	0.08 ± 0.01
F34-305C	90	0.001	902	1233	17	153 ± 25	0.08 ± 0.01
F34-330C	0	0.01	949	1281	19	166 ± 29	0.14 ± 0.01
F34-330C	0	0.001	822	1268	19	166 ± 29	0.14 ± 0.01
F34-330C	45	0.01	949	1279	20	166 ± 29	0.14 ± 0.01
F34-330C	45	0.001	887	1279	20	166 ± 29	0.14 ± 0.01
F34-330C	90	0.01	986	1314	18	166 ± 29	0.14 ± 0.01
F34-330C	90	0.001	928	1309	17	166 ± 29	0.14 ± 0.01
F34-350C	0	0.01	857	1367	18	164 ± 22	0.12 ± 0.01
F34-350C	0	0.001	868	1358	18	164 ± 22	0.12 ± 0.01
F34-350C	45	0.01	870	1327	17	164 ± 22	0.12 ± 0.01
F34-350C	45	0.001	820	1335	18	164 ± 22	0.12 ± 0.01
F34-350C	90	0.01	879	1363	18	164 ± 22	0.12 ± 0.01
F34-350C	90	0.001	878	1394	18	164 ± 22	0.12 ± 0.01
F34-AC	0	0.01	920	1412	24	175 ± 27	0.17 ± 0.01
F49-260C	0	0.01	1344	1762	12	81 ± 15	0.12 ± 0.01
F49-260C	0	0.001	1211	1739	12	81 ± 15	0.12 ± 0.01
F49-260C	45	0.01	1229	1706	13	81 ± 15	0.12 ± 0.01
F49-260C	45	0.001	1270	1704	11	81 ± 15	0.12 ± 0.01
F49-260C	90	0.01	1308	1742	13	81 ± 15	0.12 ± 0.01
F49-260C	90	0.001	1403	1731	13	81 ± 15	0.12 ± 0.01
F49-290C	0	0.01	1006	1427	20	113 ± 23	0.18 ± 0.01
F49-290C	0	0.001	1045	1441	21	113 ± 23	0.18 ± 0.01
F49-290C	45	0.01	1058	1468	18	113 ± 23	0.18 ± 0.01
F49-290C	45	0.001	988	1448	21	113 ± 23	0.18 ± 0.01
F49-290C	90	0.01	999	1424	22	113 ± 23	0.18 ± 0.01
F49-290C	90	0.001	928	1413	29	113 ± 23	0.18 ± 0.01
F49-305C	0	0.01	1149	1561	15	130 ± 22	0.19 ± 0.01
F49-305C	0	0.001	1005	1579	14	130 ± 22	0.19 ± 0.01
F49-305C	45	0.01	1101	1530	15	130 ± 22	0.19 ± 0.01
F49-305C	45	0.001	1220	1530	15	130 ± 22	0.19 ± 0.01
F49-305C	90	0.01	1258	1565	16	130 ± 22	0.19 ± 0.01
F49-305C	90	0.001	1168	1574	15	130 ± 22	0.19 ± 0.01

Strength

Fig. 7.3 shows the elongation versus ultimate tensile strength relationship for both alloys. While F34 data are seen as a cluster, F49 data display a more typical behaviour for tensile tests results, with elongation decreasing with increasing tensile strength [51]. In steels, strength arises from features in the microstructure that hinder the flow of dislocations, such as interstitials or grain boundaries [51]. The average bainite lath thickness was presented alongside the tensile results in Table 7.1 to show the general trend that strength increases with decreasing bainite lath thickness, hence with impeded dislocation motion. In the case of bainite, the lath size is fine and the strength has been reported to be proportional to the inverse of the bainite lath thickness [93]. Fig. 7.4 confirmed this trend graphically. For F34, the values of strength had a large spread, possibly due to the impact of martensite from austenite decomposition in isothermally transformed samples. The martensite present in F34-AC also contributed to strength in that sample and is not accounted for in Fig. 7.4.

Ductility

In two-phase steels, it usually is the case that the ferritic phase provides strength while the austenitic one provides ductility [51]. Sandvik suggested that the elongation achieved in tensile tests is a function of the austenite fraction in the alloys [196]. That relation was plotted in Fig. 7.5, and the general trend was confirmed for the different microstructures of each alloy. In fact, F34-305C, which has a fraction of austenite of 0.08, has a higher elongation to failure than all the F49-260C and F49-305C samples, which have higher austenite fractions. Fig. 7.5 also shows that despite the presence of untempered martensite in F34-AC, this sample has a higher elongation to failure than most other F34 samples. This demonstrates the efficacy of using a bainitic structure with retained austenite to achieve both the required strength and ductility. In F49, the total elongation is significantly lower after transformation at 305°C compared to 290°C, although the austenite fraction is higher in F49-305C. The likely cause of this effect is the presence of large regions of blocky austenite, as shown in Fig. 5.11 (c). After transformation to martensite in the initial stages of the tensile test, through the TRIP effect, large areas of brittle martensite would be present [51]. They could become propitious
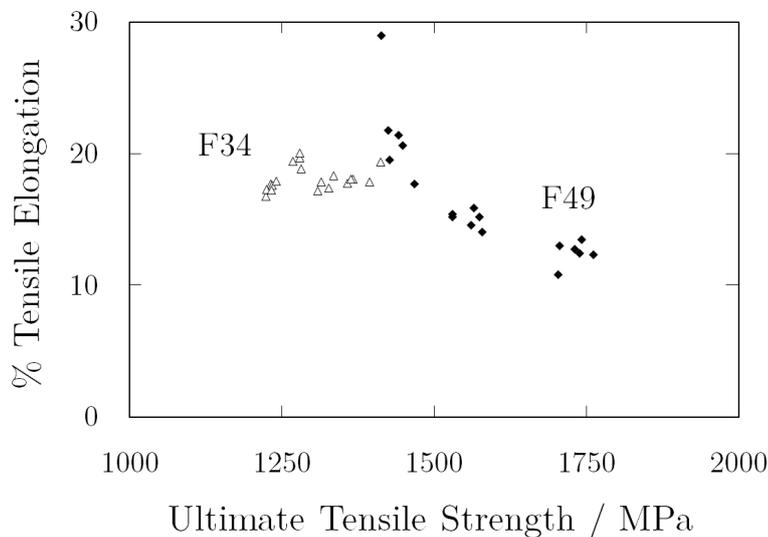
Fig. 7.3: Elongation to failure plotted against UTS for all samples. F34 samples displayed similar properties, irrespective of heat treatment, while F49 samples exhibited a wider range of properties.
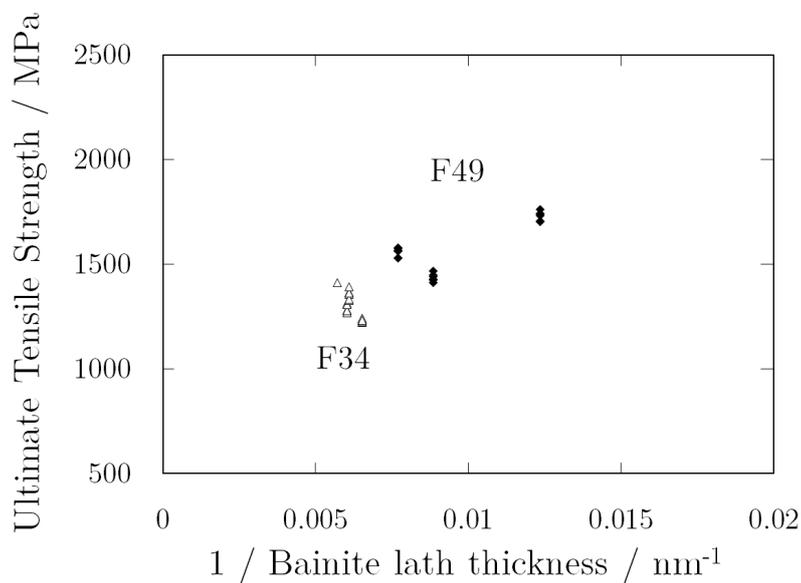

Fig. 7.4: UTS plotted against the inverse of the bainite lath thickness for all samples. The general trend that strength increases with decreasing lath thickness was observed.

areas for crack nucleation and growth, and lead to a lower total elongation. This interpretation also agrees with the observed higher strength of F49-305C compared to F49-290C, although the respective bainite thicknesses of 130 and 113 nm would suggest the opposite.

Comparison to published data

The elongation versus ultimate tensile strength data have also been plotted alongside the data for many commercial steels, in Fig. 7.6. The published data were provided by Bhadeshia [51]. The novel alloys appear to have the highest combination of strength and elongation, omitting nanostructured steels, which have high carbon contents, of approximately 1 wt% C, and would not meet the target fracture toughness set for this project. For isothermally transformed samples, the strength versus transformation temperature was also plotted in comparison with data from the literature, in Fig. 7.7. Again, the new alloys fit previous data behaviour well. Finally, the new data were plotted as ultimate tensile strength versus transformation time and transformation temperature versus transformation time. In both cases, the transformation time used is the time determined from dilatometry for the bainitic reaction to cease. In both graphs, Bhadeshia identified regions of existence using a neural network, and it was confirmed, in Fig. 7.8 that the new data fit the predicted values accurately.


Fig. 7.5: Elongation to failure plotted against V_γ for all samples. Both F34 and F49 alloys individually showed an increase in elongation with increasing V_γ, except for F49-305C.

Fig. 7.6: Plot of elongation to failure versus UTS for both novel alloys and compared to common commercial steels. The data were provided by Bhadeshia [51].
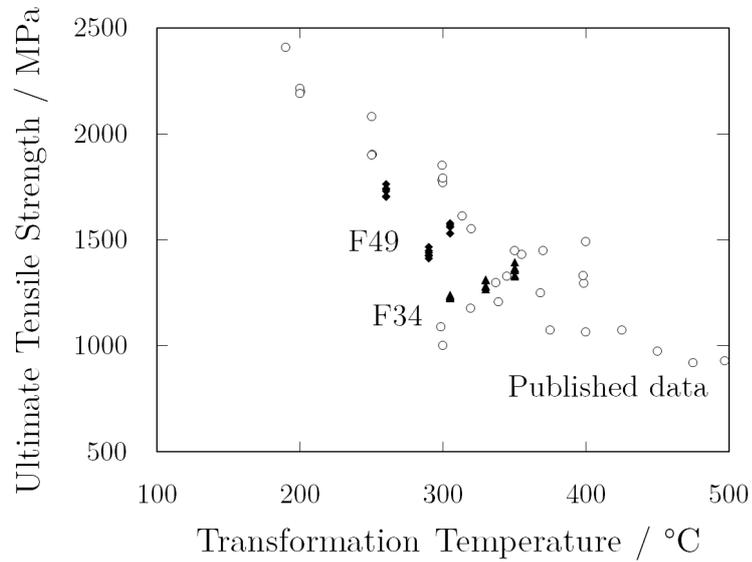
Fig. 7.7: UTS plotted against transformation temperature for the novel alloys and compared to the data used for the alloy design, presented in Fig. 2.2. The published data were collected from [93, 120, 123–125].


(a)   (b)
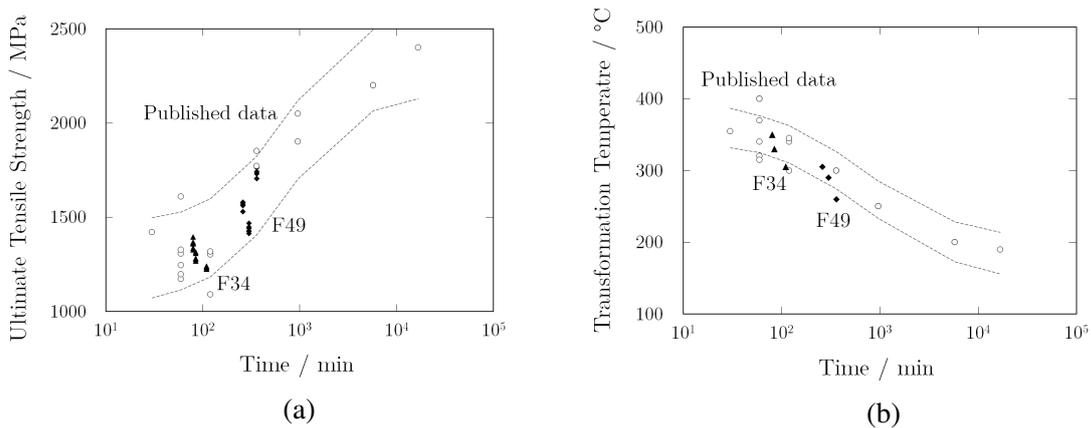
Fig. 7.8: Neural network predicted region of existence of data for (a) UTS versus transformation time and (b) transformation temperature versus transformation time, formulated by Bhadeshia [51]. The transformation times were presented in Table 5.2. The current data fit the predicted range precisely, with only two data points sitting outside it.

7.3   Charpy impact tests

7.3.1   Experimental method

The Charpy impact tests were run in accordance to the European Standard - EN 10 045-1 [197]. In Charpy tests, a sample is notched and placed on the route of a heavy swinging pendulum, with the pendulum hitting the un-notched side of the specimen, in the alignment of the notch. When the pendulum hits the sample, the sample fractures and absorbs some of the energy of the pendulum. This is recorded as the fracture toughness, or Charpy energy of the specimen. The sample dimensions were as defined by the standard, and shown schematically in Fig. 7.9, reproduced from Hulme-Smith [116]. All tests were performed at room temperature except one, for each of F34-330C and F49-290C, which was performed at -40°C. This was to observe any difference in behaviour at low temperatures. Since the typical applications for the present alloys does not include low temperature operation, the ductile to brittle transition temperature was not investigated thoroughly. The samples were cut from the parent plates in three orientations: at 0, 45 and 90° from the rolling direction, to assess the isotropy of the fracture toughness. Each test condition was performed once.
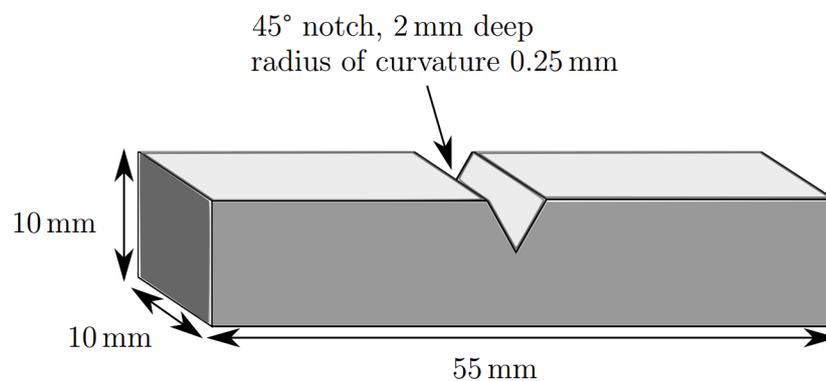

Fig. 7.9: Charpy impact test specimen dimensions, as defined by the European Standard - EN 10 045-1 [197]. The schematic was reproduced from Hulme-Smith [116].

7.3.2   Numerical results

Table 7.2 displays all the results of the Charpy impact tests, as well as the values of ultimate tensile strength, tested at 0.01 mm s^{-1}. The bainite thickness and austenite fraction are also included for reference. Excluding F34-350C, the fracture toughness of F34 samples are significantly higher than those of F49. The difference in carbon content is the main explanation for this difference, as described by Irvine in upper and lower bainite [198]. Higher carbon alloys tend to suffer from the presence of carbides that have high strengths and are brittle, and can cause crack initiation, hence decreasing the observed fracture toughness [93]. This negative effect is mitigated by having the carbides present within the bainitic ferrite laths, as shown in Fig. 6.6, 6.7 and 6.8, where the crack propagation is limited [84]. In the current study, the lower Charpy energy of F49-290C can be linked to the cementite fraction being at least one order of magnitude larger than in F34-330C, as characterised in Chapter 6, thus having many more locations for crack initiation. It is not clear why F34-350C displays poor fracture toughness, and the result could not be explained from the microstructural characterisation. The fracture toughness appeared to be isotropic for all samples. Brozzo claims that the toughness in bainitic alloys with carbon weight percent below 0.5 is controlled by the bainite lath size [199], but this is not consistent with the data presented here, as illustrated in Fig. 7.10. The Charpy energy versus ultimate tensile strength was plotted in Fig. 7.11 and reveals the F34-305C and F34-330C have the best combination of properties. The values of Charpy energy for F34-330C and F49-290C at -40°C were similar to those at room temperature, indicating that the ductile to brittle transition temperature was below -40°C.

Table 7.2: Charpy test results for F34 and F49 presented with the bainite thickness and austenite fraction (V_γ). The value of ultimate tensile strength (UTS) for the crosshead rate of 0.01 mm s^{-1} is indicated for reference.

| Alloy	Orientation / °	Charpy energy / J	UTS / MPa	Bainite thickness / nm	V_γ
Requirements	-	25	1230	-	-
F34-305C	0	58	1224	153 ± 25	0.08 ± 0.01
F34-305C	45	61	1225	153 ± 25	0.08 ± 0.01
F34-305C	90	71	1241	153 ± 25	0.08 ± 0.01
F34-330C	0	65	1281	166 ± 29	0.14 ± 0.01
F34-330C	45	62	1279	166 ± 29	0.14 ± 0.01
F34-330C	90	66	1314	166 ± 29	0.14 ± 0.01
F34-330C at -40°C	0	61	-	166 ± 29	0.14 ± 0.01
F34-350C	0	34	1367	164 ± 22	0.12 ± 0.01
F34-350C	45	28	1327	164 ± 22	0.12 ± 0.01
F34-350C	90	34	1363	164 ± 22	0.12 ± 0.01
F34-AC	0	41	1412	175 ± 27	0.17 ± 0.01
F34-AC	45	41	-	175 ± 27	0.17 ± 0.01
F34-AC	90	33	-	175 ± 27	0.17 ± 0.01
F49-260C	0	31	1762	81 ± 15	0.12 ± 0.01
F49-260C	45	27	1706	81 ± 15	0.12 ± 0.01
F49-260C	90	27	1742	81 ± 15	0.12 ± 0.01
F49-290C	0	45	1427	113 ± 23	0.18 ± 0.01
F49-290C	45	29	1468	113 ± 23	0.18 ± 0.01
F49-290C	90	41	1424	113 ± 23	0.18 ± 0.01
F49-290C at -40°C	0	31	-	113 ± 23	0.18 ± 0.01
F49-305C	0	33	1561	130 ± 22	0.19 ± 0.01
F49-305C	45	27	1530	130 ± 22	0.19 ± 0.01
F49-305C	90	28	1565	130 ± 22	0.19 ± 0.01
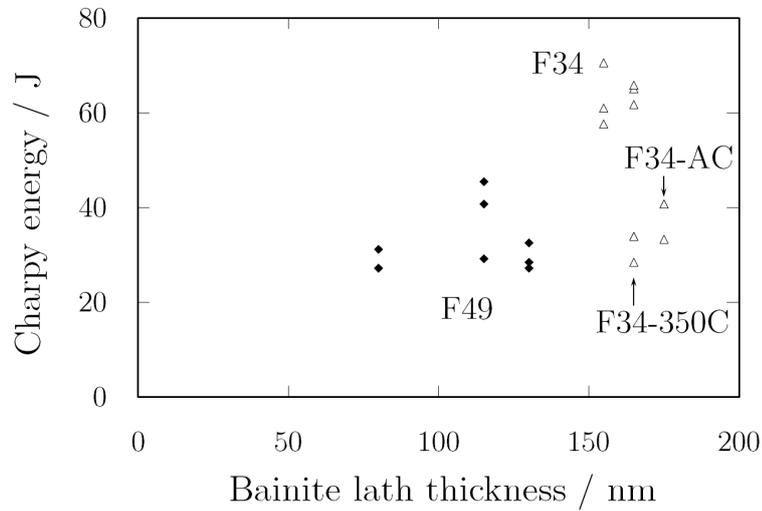
Fig. 7.10: Charpy energy plotted against the bainite lath thickness. No correlation was apparent.
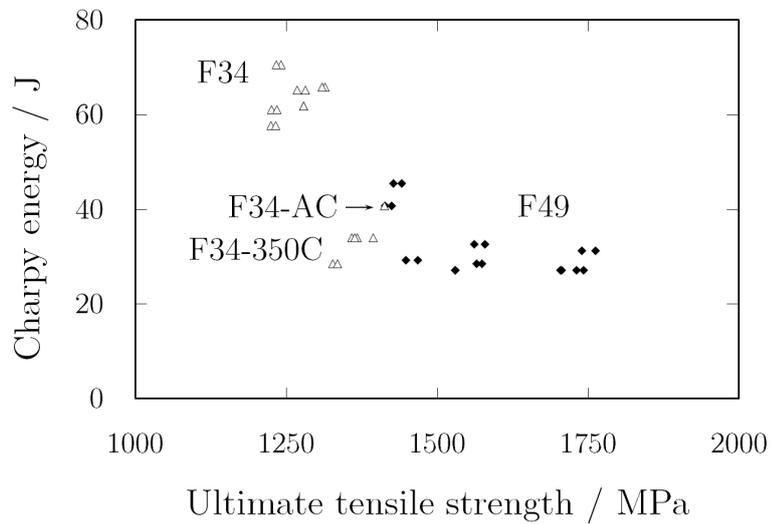
Fig. 7.11: Charpy energy plotted against UTS. F34-305C and F34-330C appeared to have the best combination of properties.

7.3.3 Fracture analysis

Fracture surfaces

The fracture surface analysis was performed using scanning electron microscopy with secondary electron imaging. It did not reveal any significant differences between the various samples. A comparison between the fracture surfaces of F34-330 and F49-290C is presented in Fig. 7.12. The central regions of the Charpy samples displayed characteristics of both brittle and ductile fracture modes, while the edges were fully ductile. The dimple size in the fully ductile regions appear smaller in F49-290C compared to F34-330C. Both regions, as well as the transition region, were imaged at the same resolution for F34-330C, and presented in Fig. 7.13. All three regions contain small dimples but the mixed region displays large regions without dimples. Those dimples form characteristically at non-metallic inclusions like sulphides or silicates or at carbides [51], although those inclusions are not visible in Fig. 7.13. In the central region, void coalescence could have played a significant role in fracture, indicated by the presence of large regions without dimples. The transition region between fully ductile fracture and mixed fracture displayed dimples as well as large smooth fracture surfaces.

Sub-surface secondary cracks

Fractured Charpy specimens were cut in half, perpendicular to the v-notch, as illustrated in Fig. 7.14, and etched in 2% nital in order to reveal the microstructure. The sub-surface crack path was imaged using backscattered electrons, which show a difference in contrast between the austenite and the ferrite phase. The sub-surface crack path can be seen not to follow prior austenite grain boundaries in Fig. 7.15. In (b) and (c) particularly, the crack path appears tortuous. In (a) and (d), the crack path is linear with sharp angles, and still appears to cut through prior austenite grains. The transgranular nature of the secondary cracks as well as the tortuous paths indicate the crack paths are complex and result in alloys that are not brittle. Fig. 7.16 illustrates examples of sub-cracks in F34-AC. In (a), the crack path can be seen to be going through the martensite phase specifically, indicating that this brittle phase contributes to crack nucleation or growth. (b) shows that large cracks do not necessarily go

(a) F34-330C - fully ductile region

(b) F49-290C - fully ductile region

(c) F34-330C - mixed region

(d) F49-290C - mixed region

(e) F34-330C - mixed region

(f) F49-290C - mixed region
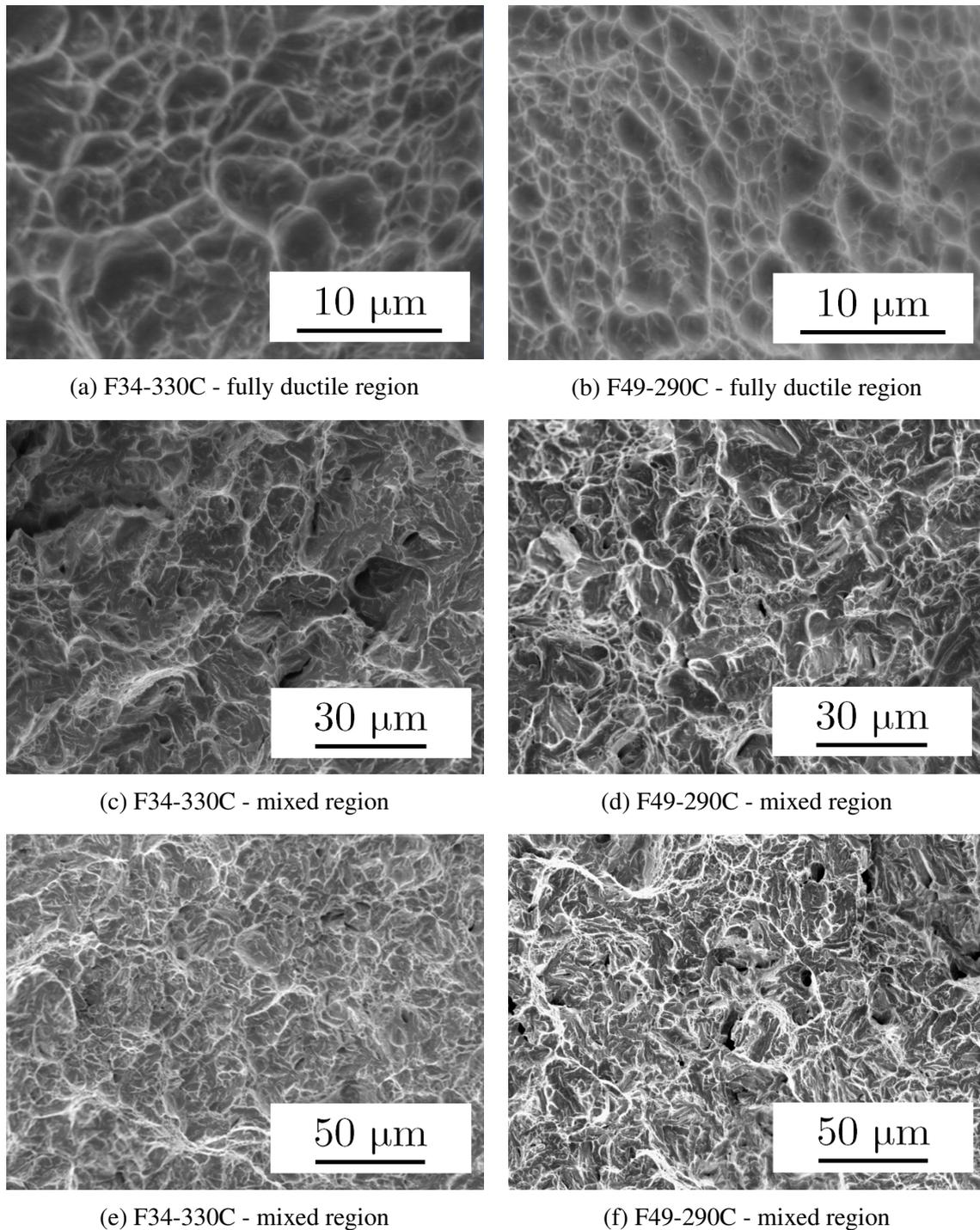
Fig. 7.12: Micrographs showing the fracture surfaces of F34-330C and F49-290C. The dimple size in the fully ductile regions appeared smaller in F49-290C compared to F34-330C. In other regions, both alloy fractures appeared similar.

(a) Mixed region

(b) Fully ductile region

(c) Transition region
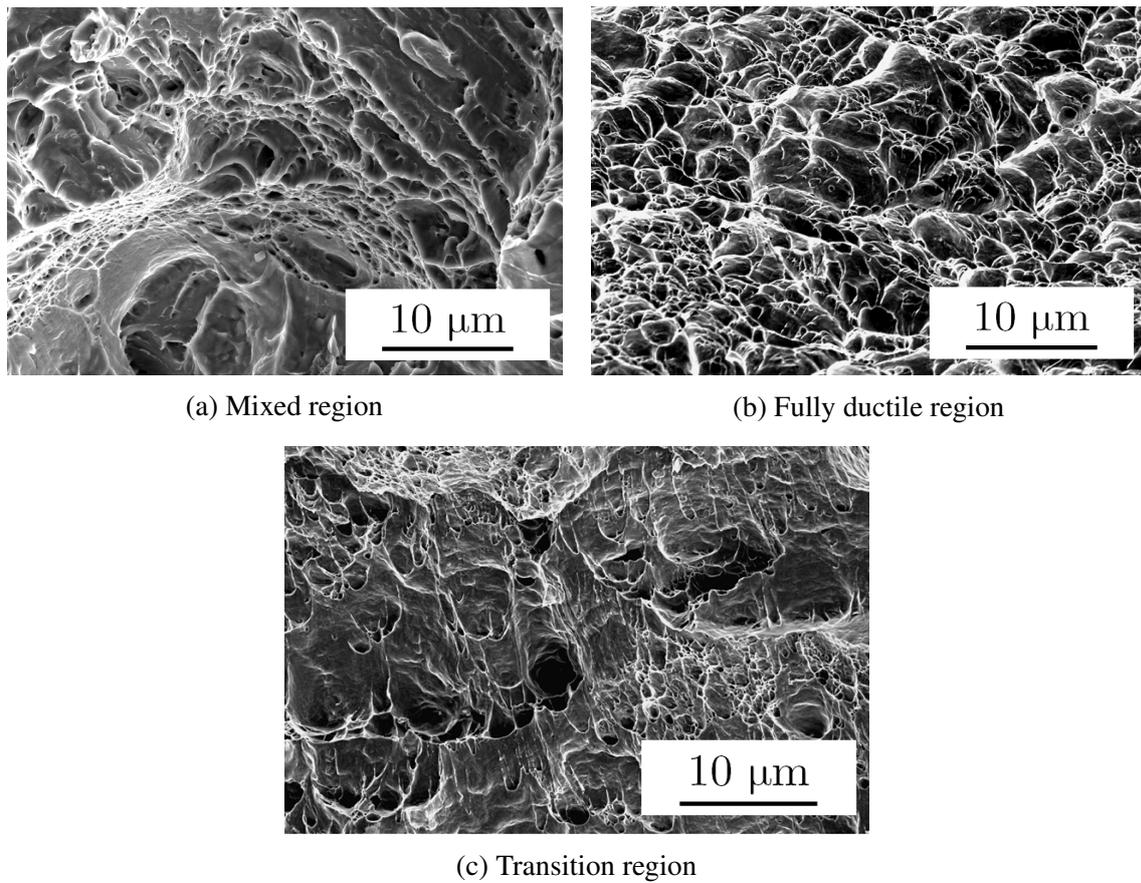
Fig. 7.13: Micrographs exposing the differences in fracture surfaces at identical magnification in F34-330C.

through the martensitic phase, thus reinforcing the numerical results that the presence of martensite is not significantly detrimental to the fracture toughness of F34-AC. At higher magnifications, it was possible to observe the crack path ramification to be almost exclusively in the ferritic phase, as displayed in Fig. 7.17. This suggests that cracks are initiated in that phase and grow through it before progressing to and through the austenitic phase.
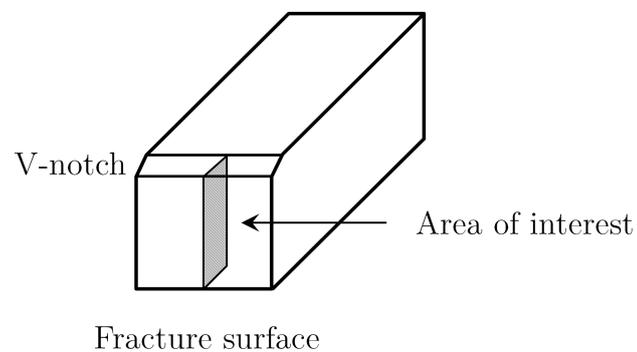

Fig. 7.14: Schematic representation of the area of interest for imaging secondary cracks.

(a) F34-330C

(b) F49-290C
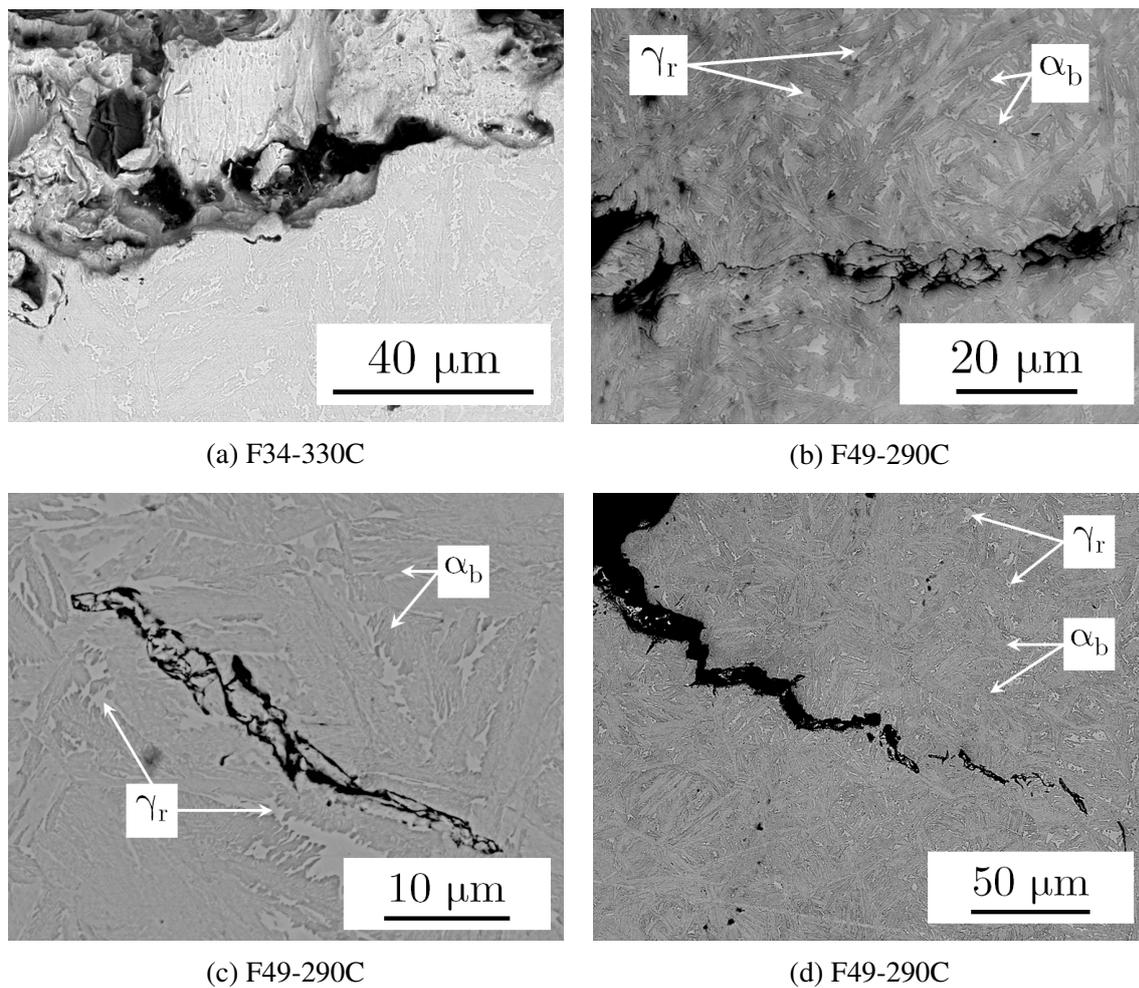
(c) F49-290C

(d) F49-290C

Fig. 7.15: Micrographs showing that the secondary cracks did not seem to follow prior austenite grain boundaries in either F34-330C or F49-290C.
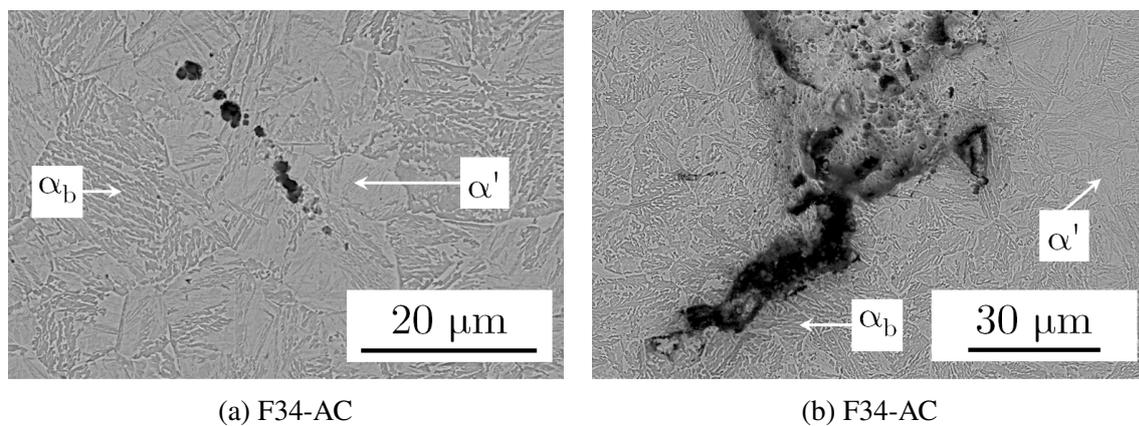

(a) F34-AC

(b) F34-AC

Fig. 7.16: Micrographs showing that the secondary cracks could grow in the martensite regions of F34-AC but were also present in bainitic regions close to martensite.

(a) F49-290
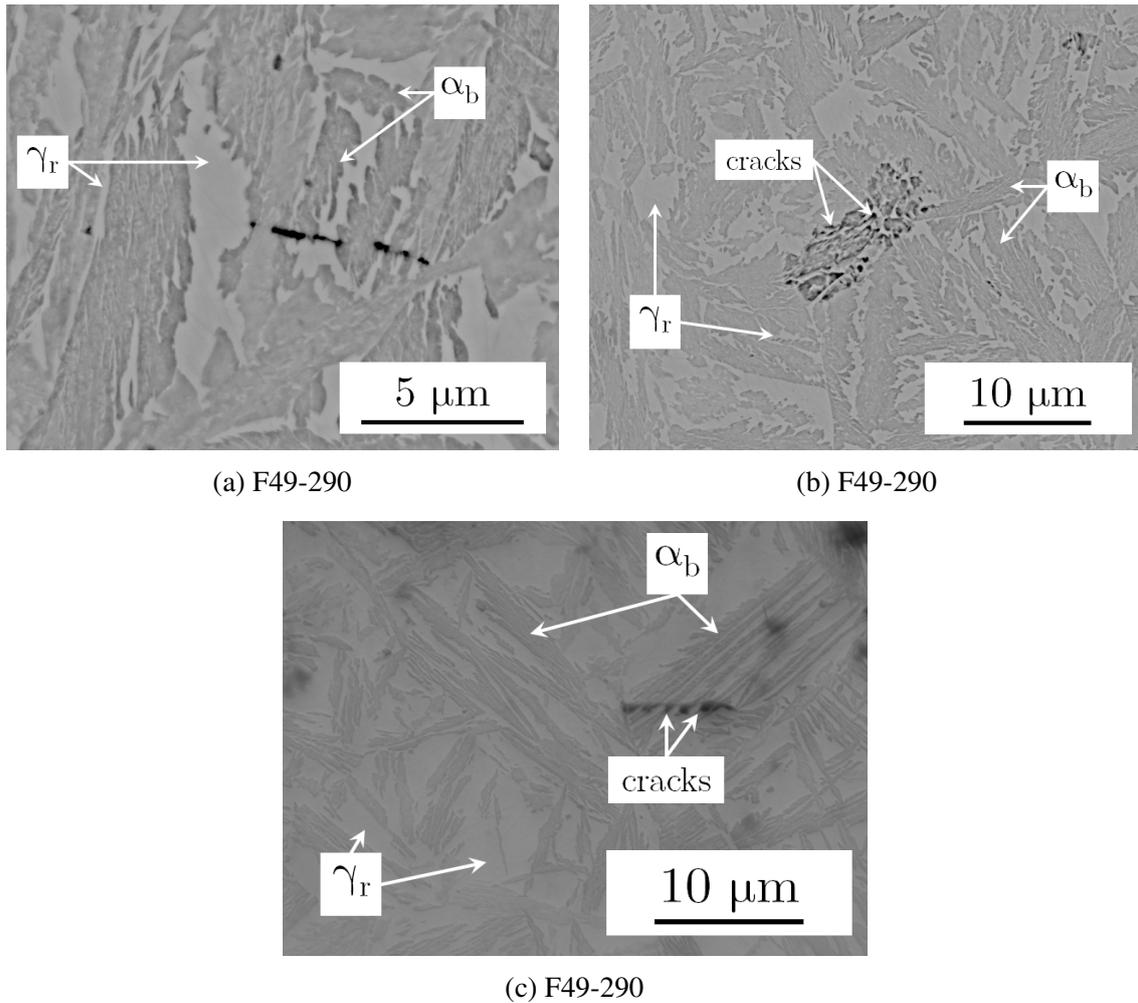
(b) F49-290

(c) F49-290

Fig. 7.17: Micrographs showing that the secondary cracks were preferentially growing in ferrite compared to austenite in F49-290C.

7.4   Austenite stability

The austenite phase was demonstrated to provide toughness and ductility in bainitic alloys, it is therefore essential to have a stable austenite phase that does not transform to martensite due to small external stimuli [93]. Conversely, the austenite should not be stable to the extent that the transformation-induced plasticity (TRIP) effect does not occur. At this point, the austenite would not either fulfil its designed role. The austenite stability was therefore assessed over a wide temperature range and under stress.

7.4.1   Low temperature austenite stability

The austenite stability at cryogenic temperatures was investigated. F34-330C, F34-AC and F49-290C samples were submerged in liquid nitrogen, of temperature -196°C, for 168 hours (one week), and their austenite fractions were compared before and after this heat treatment. The fraction of austenite was measured as reported in Chapter 5, using XRD. The austenite fractions measured are presented in Table 7.3. Little difference in the austenite content before and after submersion in liquid nitrogen was observed, indicating a good stability at low temperatures. This compared positively to high carbon martensitic alloys with retained austenite. Two examples in the literature reported microstructures obtained by air-cooling that contained 0.17 and 0.25 retained austenite for which the austenite decomposed fully to martensite after leaving samples in liquid nitrogen for 36 hours [200, 201].

Table 7.3: Austenite fractions measured using XRD, before and after submerging samples in liquid nitrogen for 168 hours. The small differences indicated a stable austenitic phase in all samples.

Alloy	Prior austenite fraction	Final austenite fraction
F34-330C	0.14 ± 0.01	0.13 ± 0.01
F34-AC	0.17 ± 0.01	0.16 ± 0.01
F49-290C	0.18 ± 0.01	0.18 ± 0.01

7.4.2 High temperature austenite stability under stress

The austenite stability was investigated by performing four tensile tests at temperatures 20, 100, 200 and 300°C for F34-AC. The sample dimensions were as described in Section 7.2.1. and the only difference in test machine is the presence of a 3 zone split furnace that samples were placed in. The fraction austenite remaining after the tensile tests was measured using XRD below the fracture surface, as close to it as possible, schematically illustrated in Fig. 7.18. The four stress-strain curves obtained are compared in Fig. 7.19 and all the numerical results are presented in Table 7.4. The ultimate tensile strength values were similar but there were significant differences in the elongation to failure values. The two lower temperature tests, 20 and 100°C, displayed lower plasticity than the other two tests. The fracture surfaces of the four broken samples are displayed in Fig. 7.20. The fracture surfaces confirm the similarity in fracture behaviour for the tests performed at 20 and 100°C. They both display ductile areas around the edges of the specimen, that appear as small dimples at high magnification, and a central region that has components of ductile and brittle fracture. The 200°C sample displayed only ductile regions, although appeared irregular macroscopically. The 300°C sample was also fully ductile, and had the typical cup and cone fracture mode [202]. A significant reduction in sample diameter was also visible for that sample compared to all others.
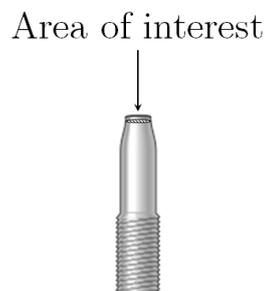

Fig. 7.18: Schematic location of the area exposed to XRD for measuring the austenite content after tensile testing. Broken tensile specimens were cut as close to the fracture surface as possible. The schematic was adapted from [203].
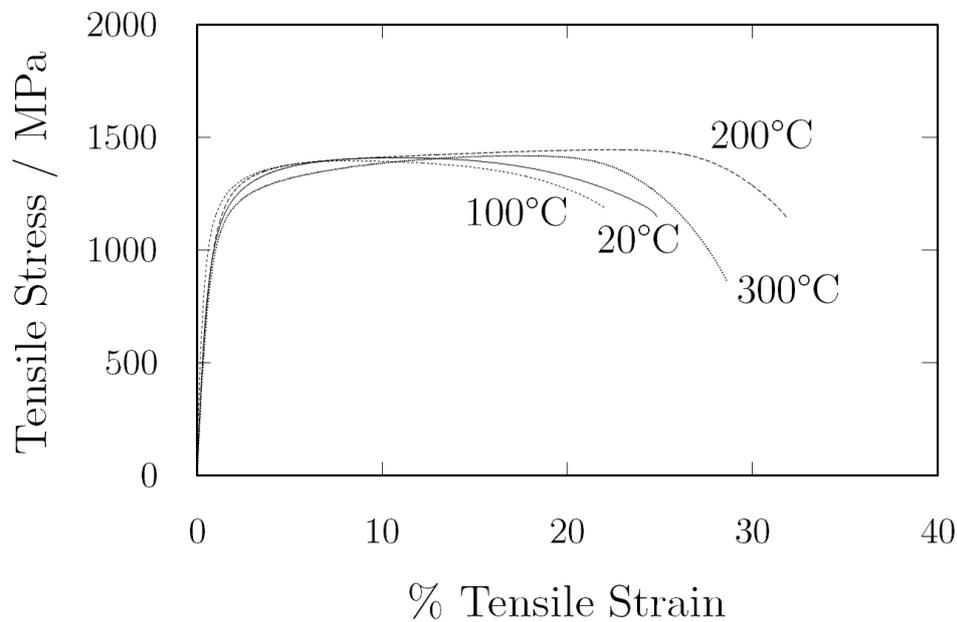
Fig. 7.19: Stress-strain curves for F34-AC. The tensile tests were performed at constant temperatures of 20, 100, 200 and 300°C.

Table 7.4: Comparison of the mechanical properties and austenite fraction below the fracture surface of F34-AC samples in tensile tests performed at varying temperatures.

| Test temperature / °C	UTS / MPa	Elongation / %	Prior austenite fraction	Final austenite fraction
20	1412	24	0.17 ± 0.01	0.09 ± 0.01
100	1397	22	0.17 ± 0.01	0.09 ± 0.01
200	1446	31	0.17 ± 0.01	0.01 ± 0.01
300	1420	28	0.17 ± 0.01	0.00 ± 0.01

(a) 20°C

(b) 100°C

(c) 200°C

(d) 300°C
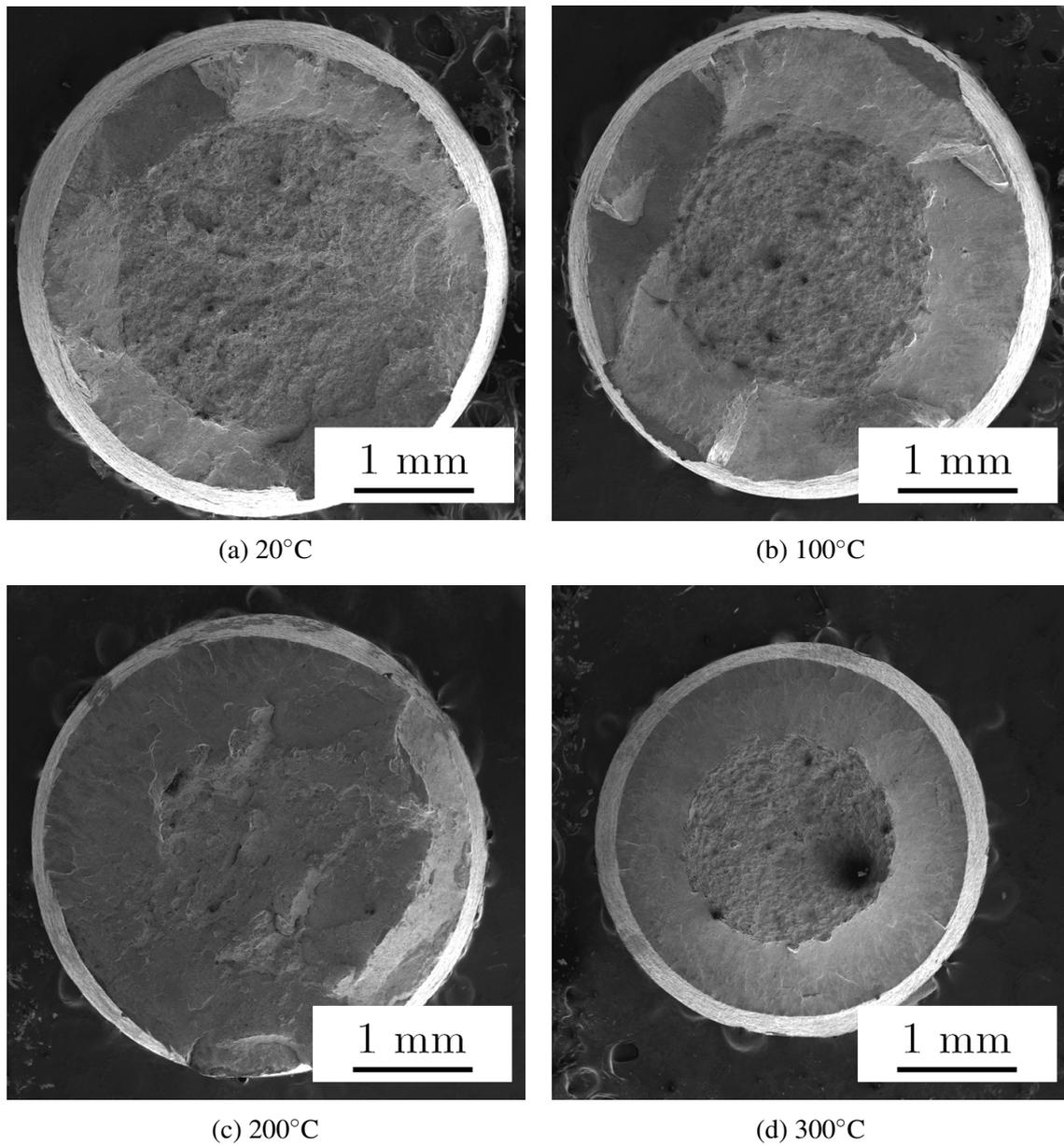
Fig. 7.20: Fracture surfaces of the four broken F34-AC tensile specimens. The two lower temperature specimens exhibited a mixture of ductile and brittle fractures while the two higher temperature ones had fully ductile fractures.

Significance of austenite percolation

The data presented in Table 7.4 confirmed the theory hypothesised by Bhadeshia that the fraction retained austenite should be superior to 0.10 in order for it to percolate the microstructure, and therefore for the austenite properties to be effective microscopically [204]. Fig. 7.21 illustrates those results graphically. The fracture in specimens tested at 20 and 100°C occurred when the austenite fraction descended below 0.10, indicating that the austenite could not provide ductility after losing percolation. This behaviour was not observed at higher temperatures. A possible explanation for that difference is the ability of the ferrite phase to soften due to facilitated, thermally activated, dislocation motion. This way, cracks did not initiate in the ferritic phase as they would at lower temperatures, and the austenite could fulfil its role even below the percolation threshold, and result in specimens that broke after their austenite fractions had reached 0.01 or 0. Consequently, those specimens reached larger elongations to failure.

Comparison to transformation-induced plasticity (TRIP) steels

No example of such analysis in bainite containing retained austenite has been reported in the literature. Chatterjee presented similar analyses done for a δ-TRIP steel, which also contains a mixture of a ferritic phase (δ-ferrite) and retained austenite [123]. For that steel, the stability of austenite was seen to increase dramatically between 20 and 100°C, resulting in a significant loss of ductility, as depicted in Fig. 7.22. The austenite was so stable, the final and initial austenite volume fractions were identical, and the austenitic phase could not provide ductility in the alloy. The novel alloys did not display that diminution in ductility and lack of austenite transformation at higher transformation temperatures, indicating a potential advantage of bainitic alloys for operating at high temperatures.

Sherif used TRIP steel data to create a model predicting the stability of austenite under plastic deformation, at any temperatures [205]. Those steels have typical compositions of 0.15 wt% C, 1.5 wt% Si and 1.5 wt% Mn, and usually contain about 70% allotriomorphic
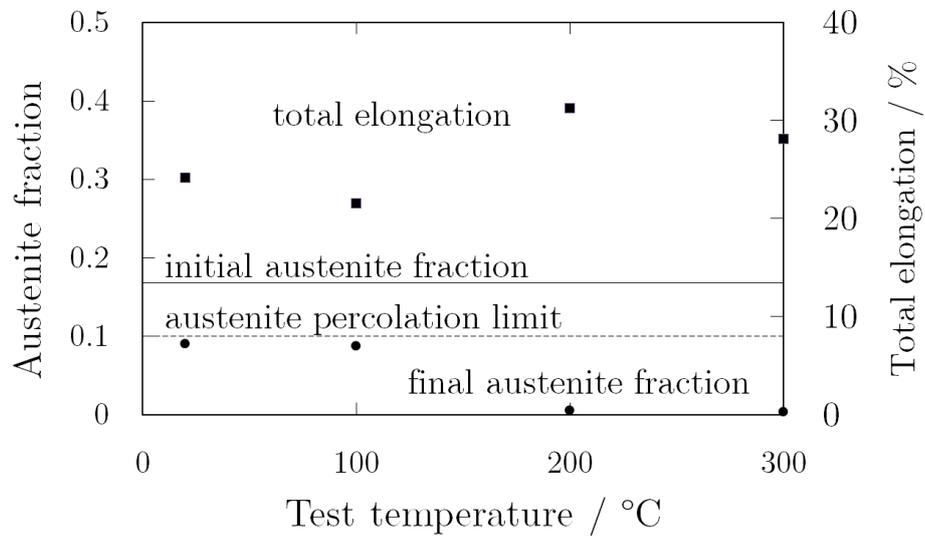
Fig. 7.21: Austenite fraction (circles) of F34-AC samples after fracture plotted against test temperature. At lower temperatures, the final austenite fraction was just beneath the austenite percolation limit, while at higher temperatures, it was close to 0. The elongation to failure (squares) is shown for reference.
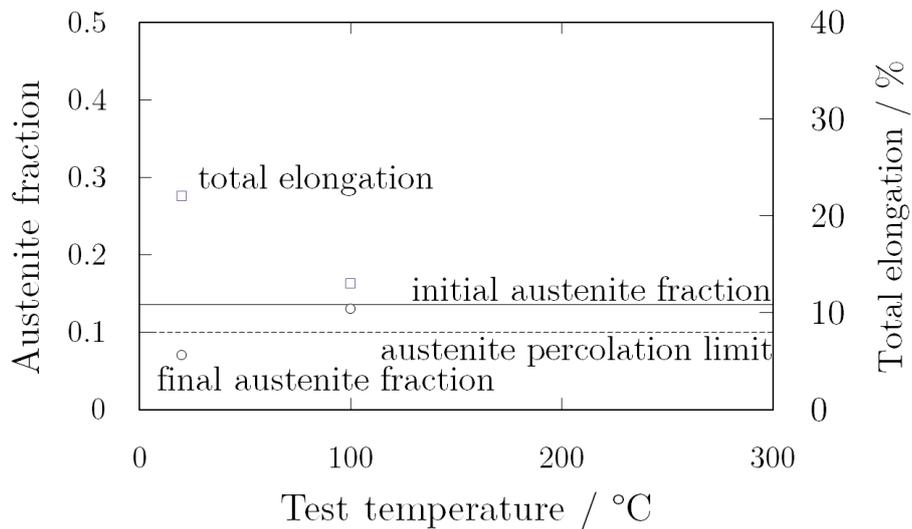

Fig. 7.22: Austenite fraction (circles) of a δ-TRIP steel after fracture, plotted against test temperature, from [123]. In this δ-TRIP steel, there was a significantly higher austenite stability at 100°C, which was detrimental to the ductility of the alloy. The elongation to failure (squares) is shown for reference.

ferrite, 20% bainite and 10% retained austenite. The relation between initial and final austenite contents was obtained from rearranging Equation (3) presented by Sherif [205]:

$$V_\gamma = \exp(\ln V_\gamma^0 - 0.00446\Delta G^{\alpha'\gamma}\varepsilon) \qquad (7.1)$$

where V_γ is the final austenite fraction, V_γ^0 is the initial austenite fraction, $\Delta G^{\alpha'\gamma}$ is the free energy change between the austenite and the martensite phase in $\mathrm{J\,mol^{-1}}$, and ε is the strain. The factor 0.00446 was found by Sherif empirically.

In the current study, the free energy change from austenite to martensite was calculated using the MTDATA software [136], with the NPL-plus database, to reproduce consistently all steps performed by Sherif. The austenite carbon composition was calculated from X-ray diffraction and presented in Table 5.3 and the alloying elements composition was measured using energy-dispersive X-ray spectroscopy, presented in Table 5.5, using point 4, which was most representative of the austenite region. The composition used for the simulation was: Fe-1.20C-2.08Si-0.35Mn-2.36Cr-3.78Ni-1.87Mo in wt%. The predicted final austenite fraction was plotted against strain in Fig. 7.23. By locating the total elongation achieved in the tensile tests on the x-axis, the model should indicate the final austenite fraction. The model only predicted accurately the final austenite fraction for the test run at 200°C, while all other results were significantly off their predicted values. The difference in chemical compositions between TRIP steels and the current alloys is not expected to cause inconsistencies between the predictions and the results presented in this subsection because the free energy difference term in Eq. (7.1) takes into account the chemical composition of the alloys for predicting the austenite stability. It is possible that the model can not describe accurately the austenite stability in bainitic microstructures. It is believed that the model failed to predict accurately the austenite fraction because the TRIP steels investigated by Sherif commonly had austenite fractions below or close to the percolation limit [206, 207], which could cause them to behave differently to the current alloys that have austenite fractions above it. For the current alloys, at 20 and 100°C, reaching the austenite percolation limit was significant for the overall test performance.
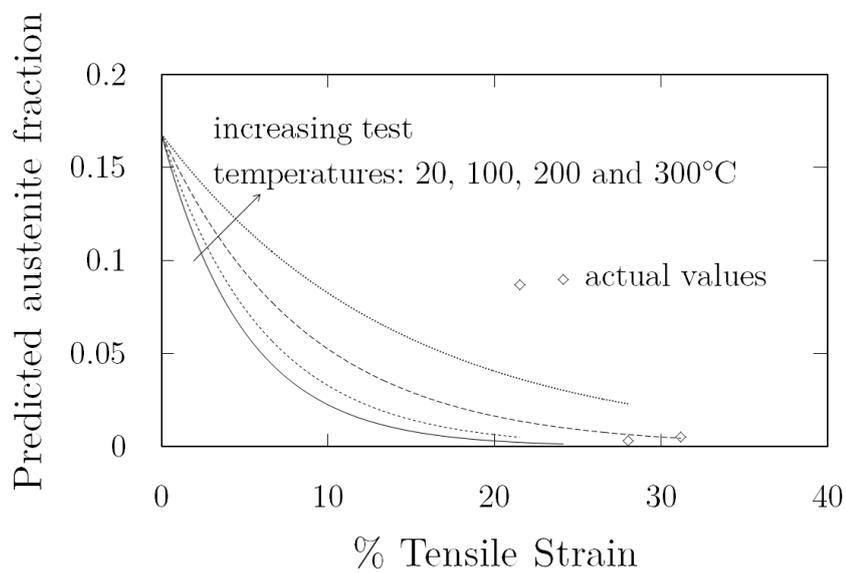
Fig. 7.23: Predicted austenite fraction depending on tensile strain, at varying temperatures for F34-AC, using the model developed by Sherif, and the MTDATA software with the NPL-plus database [136, 205]. The prediction at 200°C fitted the experimental datum. All other predictions were significantly off the experimental results.

7.5   In-situ four-point bend test

After having proved the novel alloys had matched the mechanical requirements imposed, their susceptibility to sulphide stress cracking, the main form of hydrogen embrittlement in sour environments, was assessed using a four-point bend test. Only F34-330C was tested because of its better suitability for industrial use compared to other alloys developed in this project; it achieved a great combination of toughness, ductility and strength, while having consistent properties for many different heat treatments. It also showed a reasonable hydrogen trapping ability. Four-point bend tests are used to validate or invalidate alloys before operation in sour environments. In the presence of hydrogen, microstructural inhomogeneity such as $M_{23}C_6$ and M_3C carbides, where M is a combination of alloying elements, have been reported to be crack initiation sites [83]. This effect is dramatic when such carbides are present at the grain boundaries. The microstructure investigated did not possess microstructural inhomogeneity that could be definitely anticipated to cause sulphide stress cracking.

7.5.1   Experimental method

The four-point bend test was performed in accordance to the International Standard NACE TM0316-2016/ 21404 [71]. The sample size and apparatus are described in Fig. 7.24. The sample sits in an environment designed to replicate the sour environment that the alloy should be exposed to. The sour domain map presented in the literature review was used to select the partial pressure of H_2S and the pH of the solution to be used [208]. The test condition was picked to be moderate sour conditions, in domain 1 of Fig 7.25, with a pH of 5.5 and a partial pressure of H_2S of 1 kPa, with CO_2 balance. The NACE TM0177 solution C was used, and kept at constant pH using 5 gl^{-1} CH_3COOH in deionised water. The solution contained no Cl^- ions. The test involved applying a stress equal to 100% of the yield strength of the alloy, 945 MPa, for 30 days. Two samples were investigated simultaneously. Tests are considered passed if no sub-surface crack longer than 50 μm can be seen at the end of the test.
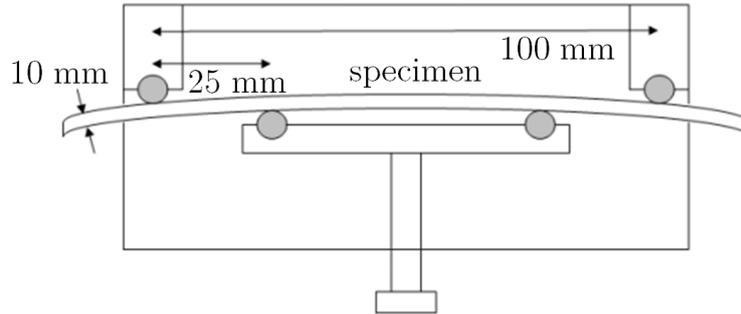
Fig. 7.24: Schematic representation of the four-point bend test setup and sample dimensions, adapted from [71]. The sample was placed in a closed environment containing a solution simulating sour operating conditions.
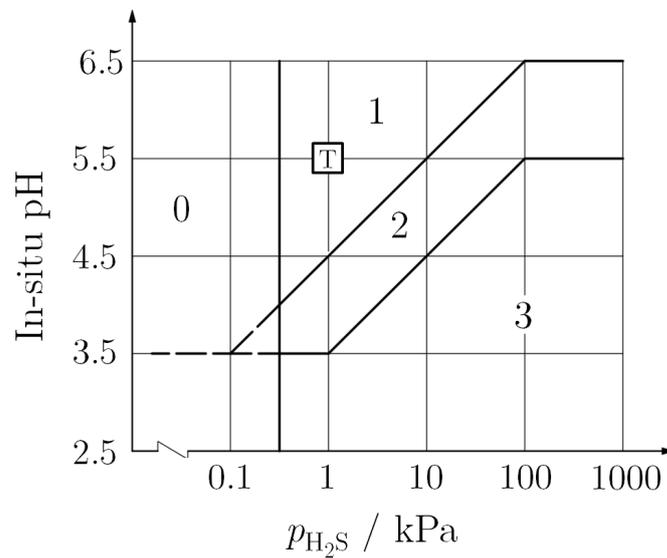

Fig. 7.25: Sour domain map defined in the International Standard ANSI/NACE MR0175/ ISO 15156-2 [208]. The domains are labelled 0 to 3, with 0 representing non-sour conditions and 3 extremely sour conditions. The T box represents the test condition used. p_{H_2S} is the partial pressure of hydrogen sulphide.

7.5.2 Results

Both samples fractured in half, indicating they failed the test. Subsequent metallographic analysis revealed the samples fractured due to pitting, as shown in Fig. 7.26. It is common that pitting initiates at inclusions in high stress steels, and subsequently propagates due to brittle carbides along grain boundaries or hydrogen atmosphere around dislocations, which prevent normal plasticity [83]. Since F34-330C does not possess interlath carbides, the second mechanism was suggested as the crack propagation mechanism. The four-point bend test did not appear to be a good test to assess carbide trapping, because the quantity of hydrogen inserted in the steel from this method amounted to 56 ppm, which is considerably larger than the hydrogen trapping ability described in Chapter 6. Additionally, tensile tests revealed that F34-330C samples were susceptible to fracture due to surface notches, and the four-point bend test is very likely to create some notches at the four points of contact. High strength steels have been reported to be very susceptible to sulphide stress cracking. The highest strength carbon steel ever produced that did not suffer sulphide stress cracking in domain 2 of the sour domain map, had a yield strength of 860 MPa, and was designed after decades of improvements [83]. It is possible that the significantly higher yield strength of the novel alloy, 945 MPa, made it unsuited for this particular test.


(a) F34-330C - sample 1   (b) F34-330C - sample 2
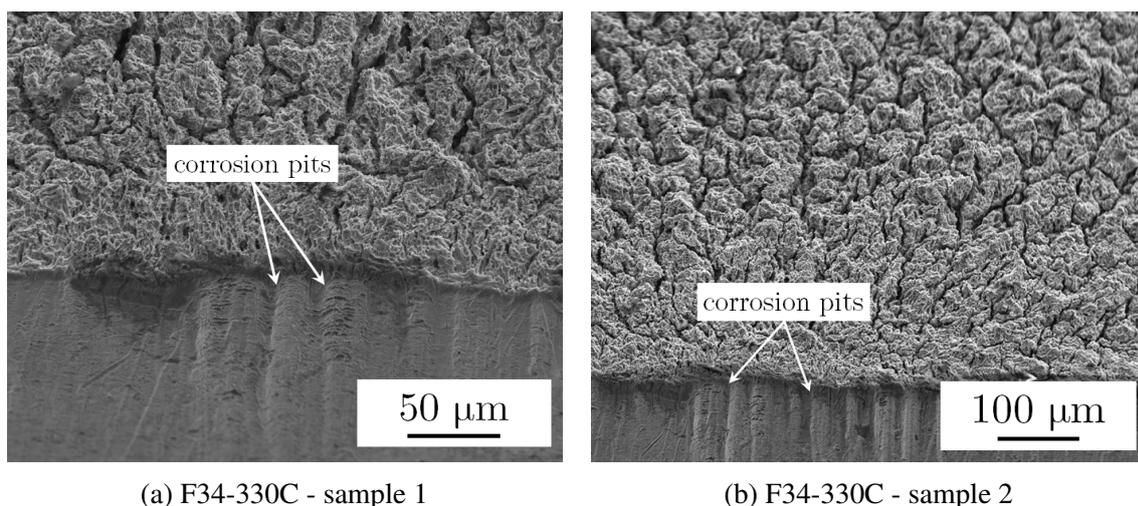
Fig. 7.26: SEM images of the fracture surfaces of the four-point bend test specimens, displaying the presence of corrosion pits at the crack initiation sites.

7.6   Conclusions

The mechanical properties of the novel alloys met the set requirements. F34 samples had very consistent strength and ductility, independent of heat treatment, whereas F49 samples properties were very dependent on heat treatment. F49 samples displayed lower fracture toughness than F34 samples. Both results indicated that F34 was more suited for industrial application. The austenite stability in both alloys was excellent at low temperatures, and was not inhibiting the transformation induced plasticity mechanism in F34-AC at high temperature and under stress. It was observed that the austenite lost its role as a ductile phase below the percolation limit of 10% below 100°C, but not above 200°C. In sour environment, F34-330C displayed sulphide stress cracking.

Chapter 8

General conclusions and future work

8.1   General conclusions

This thesis presented the design of novel bainitic alloys for hydrogen embrittlement resistance. It described the structural characterisation of four alloys, two produced at a laboratory scale and two produced at a large scale, and outlined the differences between them. The bainite lath thickness and retained austenite area were investigated as a function of isothermal transformation temperatures, and revealed that only the alloy with 0.49 wt% C, was sensitive to them. The austenite decomposition mechanism was investigated. All alloys displayed a decomposition of austenite to martensite, except for the alloy with 0.31 wt% C, transformed at $430°C$, where it decomposed to a mixture of bainite and martensite.

The hydrogen behaviour in large scale alloys was presented using the data acquired from electrochemical permeation and thermal desorption spectroscopy. The electrochemical permeation data revealed the change in effective diffusivity of hydrogen with respect to volume fraction austenite. Up to $0.1\ V_\gamma$, a linear decrease is observed, which plateaus until $0.18\ V_\gamma$, before decreasing again. This demonstrated the theorised austenite percolation limit suggested as $0.1\ V_\gamma$. Thermal desorption spectroscopy indicated that the binding energy of cementite was 37.5 kJ mol^{-1}, when present with the bainitic ferrite laths. Both techniques were used to prove that cementite is not a strong hydrogen trap. The suggested use of austenite as a

barrier to hydrogen ingress was also demonstrated using thermal desorption spectroscopy, by observing a shift in peak temperature to lower temperatures in samples where austenite was absent. Tempering of the novel alloys for short times did not appear to have a significant influence on the hydrogen behaviour.

This thesis described the optimisation of the X-ray diffraction technique for quantifying carbides. A volume fraction of cementite of 0.001, the lowest ever reported in steels using this technique, could be quantified.

The mechanical properties of the designed alloys were observed to meet all the set requirements. The alloy with 0.34 wt% C was identified as better suited for industrial used because it had consistent strength and ductility regardless of the heat treatment it was subjected to. Its strength was always inferior to that of the alloy with 0.49 wt% C, which indicated a lower susceptibility to hydrogen embrittlement. Despite the alloy not displaying any known microstructure that are prone to hydrogen embrittlement, it did not pass the standard test qualifying alloys for use in sour environments, owing to its high strength compared to commercially available martensitic steels.

The high-temperature stability of austenite tests provided another demonstration of the theorised austenite percolation limit. V_γ was observed to be 0.1 at the fracture locations of tensile tests below 100°C. The ferrite phase was also shown to be less brittle above 200°C, as demonstrated by V_γ reaching 0, indicating that the ductility provided by the austenite was still effective below the percolation threshold.

8.2   Future work

Many conceptual advantages of bainite over martensite were confirmed in this thesis. It would therefore be valuable to pursue further work in developing bainitic alloys so they become a viable alternative to martensitic ones in hydrogen-containing environments.

- It is suggested that lower strength alloys should be used. It was probably overly ambitious to try and develop a hydrogen-resistant alloy with strength much in excess of the current best performing alloys. Since high strength is a crucial factor in hydrogen susceptibility, lower strength alloys should be tested first.

- Since it was shown that cementite cannot be used for effective hydrogen trapping, other carbides should be investigated for that purpose. Transition iron carbides could be investigated, although they are unstable and have a tendency to transform to cementite. It would therefore be essential to prevent this transformation.

- Another strategy would be to use carbides that have already been characterised as strong hydrogen traps, such as vanadium, niobium or titanium carbides. This strategy would require a tempering step to be added in the alloy manufacturing, to permit carbide precipitation. In order to benefit from the advantages of the bainitic structure, the composition would have to be adapted so that the austenite does not decompose during the tempering step. Both aspects would cause an increase in the cost of the novel alloys, since more energy would be needed for production and expensive alloying elements such as nickel would be present in large quantities to stabilise the austenite.

- The effect of austenite on effective diffusivity can be investigated further. The current work characterised their correlation up to 0.2 V_γ, but it would be interesting to assess how this behaviour changes beyond that volume fraction. It may be that the number of austenite barriers needed to be crossed increase significantly with austenite fraction above that point, which would mean the alloys would experience a significantly slower hydrogen ingress rate. The austenitic phase configuration should be as presented in

this thesis, thin films intercalated between bainite laths. Large bulky areas of austenite would not be useful in the microstructure, even at high V_γ.

Bibliography

[1] W. H. Johnson. On some remarkable changes produced in iron and steel by the action of hydrogen and acids. *Proceedings of the Royal Society of London*, 23:168–179, 1874.

[2] H. K. D. H. Bhadeshia. Prevention of Hydrogen Embrittlement in Steels. *ISIJ International*, 56:24–36, 2016.

[3] R. Kirchheim and A. Pundt. *Hydrogen in Metals (Fifth Edition)*. Elsevier, 2014.

[4] S. P. Lynch. Metallographic and Fractographic Contributions to Understanding Environmentally Assisted Cracking. *Microscopy and Microanalysis*, 20:2160–2161, 2014.

[5] M. Nagumo. Hydrogen related failure of steels – a new aspect. *Materials Science and Technology*, 20:940–950, 2004.

[6] M. Nagumo. *Fundamentals of Hydrogen Embrittlement*. Springer, Singapore, 2016.

[7] D. H. R. Fors and G. Wahnström. Nature of boron solution and diffusion in α -iron. *Physical Review B - Condensed Matter and Materials Physics*, 77:3–6, 2008.

[8] J. G. Speer, D. V. Edmonds, F. C. Rizzo, and D. K. Matlock. Partitioning of carbon from supersaturated plates of ferrite, with application to steel processing and fundamentals of the bainite transformation. *Current Opinion in Solid State and Materials Science*, 8:219–237, 2004.

[9] J. R. G. da Silva and R. B. McLellan. Diffusion of carbon and nitrogen in B.C.C. iron. *Materials Science and Engineering*, 26:83–87, 1976.

[10] Y. Itsumi and D. Ellis. Electronic bonding characteristics of hydrogen in bcc iron: Part I. Interstitials. *Journal of Materials Research*, 11:2206–2213, 1996.

[11] L. B. Pfeil. The Effect of Occluded Hydrogen on the Tensile Strength of Iron. *Proceedings of the Royal Society of London*, 112:182–195, 1926.

[12] J. C. Slater. Atomic Radii in Crystals. *The Journal of Chemical Physics*, 41:3199–3204, 1964.

[13] H. K. Birnbaum. Mechanical Properties Of Metal Hydrides. *Journal of the Less Common Metals*, 104:31–41, 1984.

[14] C. D. Beachem. A new model for hydrogen-assisted cracking (hydrogen "embrittlement"). *Metallurgical Transactions*, 3:441–455, 1972.

[15] H. K. Birnbaum and P. Sofronis. Hydrogen-enhanced localized plasticity - a mechanism for hydrogen-related fracture. *Materials Science and Engineering A*, 176:191–202, 1994.

[16] T. Tabata and H. K. Birnbaum. Direct observations of hydrogen enhanced crack-propagation in iron. *Scripta Metallurgica*, 18:231–236, 1984.

[17] S. P. Lynch. A fractographic study of gaseous hydrogen embrittlement and liquid-metal embrittlement in a tempered-martensitic steel. *Acta Metallurgica*, 32:79–90, 1984.

[18] J. Song and W. A. Curtin. Atomic mechanism and prediction of hydrogen embrittlement in iron. *Nature materials*, 12:145–151, 2013.

[19] R. L. S. Thomas, J. R. Scully, and R. P. Gangloff. Internal hydrogen embrittlement of ultrahigh-strength AERMET 100 steel. *Metallurgical and Materials Transactions A*, 34:327–344, 2003.

[20] C. San Marchi and B. P. Somerday. Technical reference on hydrogen compatibility of materials. *SAND2008-1163, Sandia National Laboratories, Livermore CA*, 2008.

[21] B. J. Berkowitz and F. H. Heubaum. The Role of Hydrogen in Sulfide Stress Cracking of Low Alloy Steels. *Corrosion*, 40:240–245, 1984.

[22] N. Eliaz, A. Shachar, B. Tal, and D. Eliezer. Characteristics of hydrogen embrittlement, stress corrosion cracking and tempered martensite embrittlement in high-strength steels. *Engineering Failure Analysis*, 9:167–184, 2002.

[23] R. A. Oriani. the Diffusion and Trapping of Hydrogen in Steel. *Acta Metallurgica*, 18:147–157, 1970.

[24] G. M. Pressouyre and I. M. Bernstein. An Example of the Effect of Hydrogen Trapping on Hydrogen Embrittlement. *Metallurgical Transactions A*, 12:835–844, 1981.

[25] J. Takahashi, K. Kawakami, and T. Tarui. Direct observation of hydrogen-trapping sites in vanadium carbide precipitation steel by atom probe tomography. *Scripta Materialia*, 67:213–216, 2012.

[26] G. M. Pressouyre. A Classification of Hydrogen Traps in Steel. *Metallurgical and Materials Transactions A*, 10:1–3, 1979.

[27] R. Gemma, T. Al-Kassab, R. Kirchheim, and A. Pundt. Analysis of deuterium in V-Fe5 at% film by atom probe tomography (APT). *Journal of Alloys and Compounds*, 509:S872–S876, 2011.

[28] J. Takahashi, K. Kawakami, Y. Kobayashi, and T. Tarui. The first direct observation of hydrogen trapping sites in TiC precipitation-hardening steel through atom probe tomography. *Scripta Materialia*, 63:261–264, 2010.

[29] X. Zhu, W. Li, T. Y. Hsu, S. Zhou, L. Wang, and X. Jin. Improved resistance to hydrogen embrittlement in a high-strength steel by quenching-partitioning-tempering treatment. *Scripta Materialia*, 97:21–24, 2015.

[30] J. Y. Lee and S. M. Lee. Hydrogen trapping phenomena in metals with b.c.c. and f.c.c. crystal structures by the desorption thermal analysis technique. *Surface and Coatings Technology*, 28:301–314, 1986.

[31] Y. D. Park, I. S. Maroef, A. Landau, and D. L. Olson. Retained Austenite as a Hydrogen Trap in Steel Welds. *Welding Journal*, 81:27–35, 2002.

[32] H. Asahi, D. Hirakami, and S. Yamasaki. Hydrogen Trapping Behavior in Vanadium-added Steel. *ISIJ International*, 43:527–533, 2003.

[33] J. S. Kim, Y. H. Lee, D. L. Lee, K. T. Park, and C. S. Lee. Microstructural influences on hydrogen delayed fracture of high strength steels. *Materials Science and Engineering A*, 505:105–110, 2009.

[34] M. A. V. Devanathan and Z. Stachurski. The Adsorption and Diffusion of Electrolytic Hydrogen in Palladium. *Proceedings of the Royal Society of London A*, 270:90–102, 1962.

[35] H. Hagi and Y. Hayashi. Effect of dislocation trapping on hydrogen and deuterium diffusion in iron. *Transaction of the Japan Institute of Metals*, 28:368–374, 1987.

[36] A. J. Kumnick and H. H. Johnson. Deep Trapping for Hydrogen Iron. *Acta Metallurgica*, 28:33–39, 1980.

[37] W. M. Robertson and A. W. Thompson. Permeation measurements of hydrogen trapping in 1045 steel. *Metallurgical Transactions A*, 11:553–557, 1980.

[38] A. McNabb and P. K. Foster. A New Analysis of the Diffusion of Hyrogen in Iron and Ferritic Steels. *Transactions of the Metallurgical Society of AIME*, 227:618–627, 1963.

[39] O. D. Gonzalez. The measurement of hydrogen permeation in alpha iron-an analysis of the experiments. *Transactions of the Metallurgical Society of AIME*, 245:607–612, 1969.

[40] W. Beck, J. O. Bockris, J. McBreen, and L. Nanis. Hydrogen Permeation in Metals as a Function of Stress, Temperature and Dissolved Hydrogen Concentration. *Proceedings of the Royal Society of London A*, 290:220–235, 1966.

[41] G. W. Simmons, P. S. Pao, and R. P. Wei. Fracture mechanics and surface chemistry studies of subcritical crack growth in AISI 4340 steel. *Metallurgical Transactions A*, 9:1147–1158, 1978.

[42] H. Hagi, Y. Hayashi, and N. Ohtani. Diffusion Coefficient of Hydrogen in Iron Between 230 and 300 K. *Journal of the Japan Institute of Metals*, 42:801–807, 1978.

[43] A. J. Griffiths and A. Turnbull. On the effective diffusivity of hydrogen in low alloy steels. *Corrosion Science*, 37:1879–1881, 1995.

[44] H. E. Kissinger. Variation of peak temperature with heating rate in differential thermal analysis. *Journal of Research of the National Bureau of Standards*, 57:217–221, 1956.

[45] H. E. Kissinger. Reaction Kinetics in Differential Thermal Analysis. *Analytical Chemistry*, 29:1702–1706, 1957.

[46] E. J. Song. *Hydrogen Desorption in Steels*. Ph.D. thesis, Pohang University of Science and Technology, 2015.

[47] Y. A. Du, J. Rogal, and R. Drautz. Diffusion of hydrogen within idealized grains of bcc Fe: A kinetic Monte Carlo study. *Phys. Rev. B*, 86:174110, 2012.

[48] L. S. Darken and R. P. Smith. Behaviour of Hydrogen in Steel During and After Immersion in Acid. *Corrosion*, 5:1–16, 1948.

[49] E. J. Song, D. W. Suh, and H. K. D. H. Bhadeshia. Theory for hydrogen desorption in ferritic steel. *Computational Materials Science*, 79:36–44, 2013.

[50] A. Turnbull and R. Hutchings. Analysis of hydrogen atom transport in a two-phase alloy. *Materials Science and Engineering: A*, 177:161–171, 1994.

[51] H. K. D. H. Bhadeshia and R. W. K. Honeycombe. *Steels: Microstructure and Properties (Fourth edition)*. Butterworth-Heinemann, 2017.

[52] Y. Fukai. *The metal-hydrogen system: basic bulk properties*, volume 21. Springer Science & Business Media, 2006.

[53] E. J. Song, H. K. D. H. Bhadeshia, and D. W. Suh. Effect of hydrogen on the surface energy of ferrite and austenite. *Corrosion Science*, 77:379–384, 2013.

[54] R. Nazarov, T. Hickel, and J. Neugebauer. First-principles study of the thermodynamics of hydrogen-vacancy interaction in fcc iron. *Physical Review B*, 82:224104, 2010.

[55] K. Kawakami and T. Matsumiya. Numerical Analysis of Hydrogen Trap State by TiC and V_4C_3 in bcc-Fe. *ISIJ International*, 52:1693–1697, 2012.

[56] J. P. Hirth. Effects of hydrogen on the properties of iron and steel. *Metallurgical Transactions A*, 11:861–890, 1980.

[57] W. Y. Choo and J. Y. Lee. Thermal Analysis of Trapped Hydrogen in Pure Iron. *Metallurgical Transactions A*, 13:135–140, 1982.

[58] A. Ramasubramaniam, M. Itakura, and E. A. Carter. Interatomic potentials for hydrogen in α–iron based on density functional theory. *Physical Review B*, 79:174101, 2009.

[59] I. M. Bernstein. The effect of hydrogen on the deformation of iron. *Scripta Metallurgica*, 8:343–349, 1974.

[60] F. G. Wei, T. Hara, and K. Tsuzaki. Precise determination of the activation energy for desorption of hydrogen in two Ti-added steels by a single thermal-desorption spectrum. *Metallurgical and Materials Transactions B*, 35:587–597, 2004.

[61] G. M. Pressouyre and I. M. Bernstein. A quantitative analysis of hydrogen trapping. *Metallurgical transactions A*, 9:1571–1580, 1978.

[62] G. W. Hong and J. Y. Lee. The interaction of hydrogen and the cementite-ferrite interface in carbon steel. *Journal of Materials Science*, 18:271–277, 1983.

[63] K. Takai and R. Watanuki. Hydrogen in Trapping States Innocuous to Environmental Degradation of High-strength Steels. *ISIJ International*, 43:520–526, 2003.

[64] K. Kawakami and T. Matsumiya. Ab-initio Investigation of Hydrogen Trap State by Cementite in bcc-Fe. *ISIJ International*, 53:709–713, 2013.

[65] F. G. Wei and K. Tsuzaki. Response of hydrogen trapping capability to microstructural change in tempered Fe-0.2C martensite. *Scripta Materialia*, 52:467–472, 2005.

[66] K. Ono and M. Meshii. Hydrogen detrapping from grain boundaries and dislocations in high purity iron. *Acta Metallurgica Et Materialia*, 40:1357–1364, 1992.

[67] T. Asaoka, G. Lapasset, M. Aucouturier, and P. Lacombe. Observation of hydrogen trapping in Fe-0.15 wt% Ti alloy by high resolution autoradiography. *Corrosion*, 34:39–47, 1978.

[68] T. Yokota and T. Shiraga. Evaluation of Hydrogen Content Trapped by Vanadium Precipitates in a Steel. *ISIJ International*, 43:534–538, 2003.

[69] P. R. Rhodes. Environment-assisted cracking of corrosion-resistant alloys in oil and gas production environments: A review. *Corrosion*, 57:923–966, 2001.

[70] P. R. Rhodes, L. A. Skogsberg, and R. N. Tuttle. Pushing the limits of metals in corrosive oil and gas well environments. *Corrosion*, 63:63–100, 2007.

[71] Standard Test Method: Four-Point Bend Testing of Materials for Oil and Gas Applications. *International Standard NACE TM0316-2016/21404*, 2016.

[72] L. D. Wang, F. L. Liu, Q. Y. Zhao, and H. B. Wu. CO2 Corrosion and Grooving Corrosion Behavior of the ERW Joint of the Q125 Grade Tube Steel. *Journal of Iron and Steel Research International*, 22:943–948, 2015.

[73] N. S. Stoloff, L. Klein, and J. E. Grossman. Hydrogen embrittlement of an aligned γ/γ'-δ eutectic alloy. *Scripta Metallurgica*, 10:889–893, 1976.

[74] K. Nose and H. Asahi. Effect of microstructure on corrosion resistance of a martensitic stainless linepipe. NACE-00145. In *Corrosion*. NACE International, 2000.

[75] K. Kondo, H. Amaya, T. Ohmura, and K. Moriguchi. Effect of cold work on retained austenite and on corrosion performance in low carbon martensitic stainless steels. NACE-03094. In *Corrosion*. NACE International, 2003.

[76] L. C. D. Fielding, E. J. Song, D. K. Han, H. K. D. H. Bhadeshia, and D. W. Suh. Hydrogen diffusion and the percolation of austenite in nanostructured bainitic steel. *Proceedings of the Royal Society A*, 470:1–32, 2014.

[77] B. Miao, D. O. Northwood, L. C. Lim, and M. O. Lai. Microstructure of tempered AISI 403 stainless steel. *Materials Science and Engineering A*, 171:21–33, 1993.

[78] J. Kolts. Alloy 718 for the Oil and Gas Industry. In E. A. Loria, editor, *Superalloy 718- Metallurgy and Applications*, pages 329–344. Warrendale, PA: The Minerals, Metals, and Materials Society [TMS], 1989.

[79] A. Turnbull and G. Hinds. Hydrogen Diffusion in Corrosion Resistant Alloys. NACE-04469. In *Corrosion*. NACE International, 2004.

[80] H. Asahi, Y. Sogo, M. Ueno, and H. Higashiyama. Metallurgical Factors Controlling SSC Resistance of High-Strength, Low-Alloy Steels. *Corrosion*, 45:519–527, 1989.

[81] G. P. Echaniz, T. E. Perez, C. Pampillo, R. C. Newman, R. P. M. Procter, and G. W. Lorimer. The effect of microstructure on SSC resistance of low alloy carbon steels. CONF-970332. NACE International, 1997.

[82] M. Watkins and R. Ayer. *Microstructure – the critical variable controlling the SSC resistance of low-alloy steels*. CONF-950304. NACE International, 1995.

[83] T. Omura, M. Numata, T. Takayama, Y. Arai, A. Souma, T. Ohe, H. Amaya, and M. Ueda. Super-high Strength Low Alloy Steel OCTG with Improved Sour Resistance. *Nippon Steel & Sumitomo Metal Technical Report No. 107*, pages 18–23, 2015.

[84] B. D. Craig and G. Krauss. The structure of tempered martensite and its susceptibility to hydrogen stress cracking. *Metallurgical Transactions A*, 11:1799–1808, 1980.

[85] T. Omura, T. Ohe, T. Abe, M. Ueda, P. I. Nice, and J. W. M. Sulfide Stress Cracking (SSC) Resistance Limits For A 125 Ksi Grade High Strength Low Alloy Steel Octg Developed For Mildly Sour Service. NACE-10307. In *NACE Corrosion*. NACE International, 2010.

[86] Y. Torii, K. Shimogori, K. Kitahata, and T. Hosoda. Effect of fine carbo-nitride precipitates on SCC resistance of high strength low alloy steels. In *Corrosion*. 1985.

[87] F. G. Caballero, H. K. D. H. Bhadeshia, K. J. A. Mawella, D. G. Jones, and P. Brown. Very strong low temperature bainite. *Materials Science and Technology*, 18:279–284, 2002.

[88] T. W. Thorpe, P. M. Scott, A. Rance, and D. Silvester. Corrosion fatigue of BS 4360:50D structural steel in seawater. *International Journal of Fatigue*, 5:123–133, 1983.

[89] J. A. Gordon, J. P. Hirth, A. M. Kumar, and N. E. Moody. Effects of Hydrogen on the Mixed Mode I / III Toughness of a High-Purity Rotor Steel. *Metallurgical Transactions A*, 23:1013–1020, 1992.

[90] D. L. Sponseller and J. A. Straatman. Tubular high strength low alloy steel for oil and gas wells, US 4533405 A, 1985.

[91] S. D. Zhu, J. F. Wei, Z. Q. Bai, G. S. Zhou, J. Miao, and R. Cai. Failure analysis of P110 tubing string in the ultra-deep oil well. *Engineering Failure Analysis*, 18:950–962, 2011.

[92] M. Liu, C. D. Yang, G. H. Cao, A. M. Russell, Y. H. Liu, X. M. Dong, and Z. H. Zhang. Effect of microstructure and crystallography on sulfide stress cracking in API-5CT-C110 casing steel. *Materials Science & Engineering A*, 671:244–253, 2016.

[93] H. K. D. H. Bhadeshia. *Bainite in steels*. IOM Communications Ltd, London, 1992.

[94] G. Gomez, T. Pérez, and H. K. D. H. Bhadeshia. Air cooled bainitic steels for strong, seamless pipes Part 1 - alloy design, kinetics and microstructure. *Materials Science and Technology*, 25:1501–1507, 2009.

[95] B. A. Szost, R. H. Vegter, and P. E. J. Rivera-Díaz-del Castillo. Hydrogen-Trapping Mechanisms in Nanostructured Steels. *Metallurgical and Materials Transactions A*, 44:4542–4550, 2013.

[96] I. Gutierrez, J. Aranzabal, F. Castro, and J. J. Urcola. Homogeneous formation of epsilon carbides within the austenite during the isothermal transformation of a ductile iron at 410 °C. *Metallurgical and Materials Transactions A*, 26:1045–1060, 1995.

[97] B. P. J. Sandvik. The Bainite Reaction in Fe-Si-C Alloys: The Primary Stage. *Metallurgical Transactions A*, 13:777–787, 1982.

[98] L. Yakel. Crystal Structures of Stable and Metastable Iron-Containing Carbides. *International Metals Reviews*, 30:17–40, 1985.

[99] S. Nagakura. Study of Metallic Carbides by Electron Diffraction Part III. Iron Carbides. *Journal of the Physical Society of Japan*, 14:186–195, 1959.

[100] J. H. Jang, I. G. Kim, and H. K. D. H. Bhadeshia. First-principles calculations and the thermodynamics of Cementite. *Materials Science Forum*, 642:3319–3324, 2010.

[101] K. H. Jack. Structural Transformations in the Tempering of High-Carbon Martensitic Steels. *Journal Iron and Steel Institute*, 169:26–36, 1951.

[102] D. H. Huang and G. Thomas. Metallography of bainitic transformation in silicon containing steels. *Metallurgical Transactions A*, 8:1661–1674, 1977.

[103] K. W. Andrews. The structure of cementite and its relation to ferrite. *Acta Metallurgica*, 11:939–946, 1963.

[104] W. C. Leslie, R. M. Fisher, and N. Sen. Morphology, Precipitates, and Crystal Structure of Carbides from Solid Solution in Alpha Iron. *Acta Metallurgica*, 7:632–644, 1969.

[105] S. Murphy and A. Whiteman. The precipitation of epsilon-carbide in twinned martensite. *Metallurgical Transactions*, 1:843–848, 1970.

[106] V. I. Voronin, I. F. Berger, Y. N. Gornostyrev, V. N. Urtsev, A. R. Kuznetsov, and A. V. Shmakov. Composition of cementite in the dependence on the temperature. In situ neutron diffraction study and Ab initio calculations. *Journal of Experimental and Theoretical Physics Letters*, 91:143–146, 2010.

[107] M. H. Hong, W. T. Reynolds, T. Tarui, and K. Hono. Atom probe and transmission electron microscopy investigations of heavily drawn pearlitic steel wire. *Metallurgical and Materials Transactions A*, 30:717–727, 1999.

[108] L. Battezzati, M. Baricco, and S. Curiotto. Non-stoichiometric cementite by rapid solidification of cast iron. *Acta Materialia*, 53:1849–1856, 2005.

[109] B. D. Craig. On the elastic interaction of hydrogen with precipitates in lath martensite. *Acta Metallurgica*, 25:1027–1030, 1977.

[110] G. Y. Lai. On the precipitation of epsilon-carbide in lower bainite. *Metallurgical and Materials Transactions A*, 6:1469–1471, 1975.

[111] V. T. T. Miihkinen and D. V. Edmonds. Microstructural examination of two experimental high-strength bainitic low-alloy steels containing silicon. *Materials Science and Technology*, 3:422–431, 1987.

[112] B. V. Narasimha Rao and G. Thomas. Structure property relations and the design of Fe-4Cr-C base structural steels for high strength and toughness. *Metallurgical Transactions A*, 11:441–457, 1980.

[113] B. P. J. Sandvik. The bainite reaction in Fe-Si-C alloys: the secondary stage. *Metallurgical Transactions A*, 13:789–800, 1982.

[114] S. J. Matas and R. F. Hehemann. The structure of bainite in hypoeutectoid steels. *Transactions of the Metallurgical Society of AIME*, 221:179–185, 1961.

[115] H. K. D. H. Bhadeshia and D. V. Edmonds. The Bainite Transformation in a Silicon Steel. *Metallurgical Transactions A*, 10:895–907, 1979.

[116] C. N. Hulme-Smith. *The thermal stability of bulk nanocrystalline steels*. Ph.D. thesis, University of Cambridge, 2016.

[117] H. K. D. H. Bhadeshia. Nanostructured bainite. *Proceedings of the Royal Society A: Mathematical, Physical and Engineering Sciences*, 466:3–18, 2010.

[118] F. G. Caballero, H. K. D. H. Bhadeshia, K. J. A. Mawella, D. G. Jones, and P. Brown. Design of novel high strength bainitic steels: Part 2. *Materials Science and Technology*, 17:517–522, 2001.

[119] K. Sugimoto, M. Misu, M. Kobayashi, and H. Shirasawa. Effects of second phase morphology on retained austenite morphology and tensile properties in a trip-aided dual-phase steel sheet. *ISIJ International*, 33:775–782, 1993.

[120] Y. Tomita and T. Okawa. Effect of microstructure on mechanical properties of isothermally bainite-transformed 300M steel. *Materials Science and Engineering A*, 172:145–151, 1993.

[121] G. Gomez, T. Pérez, and H. K. D. H. Bhadeshia. Strong bainitic steels by continuous cooling transformation. *New Developments on Metallurgy and Applications of High Strength Steels*, 1:1–12, 2008.

[122] W. M. Garrison. The Effect of Silicon and Nickel Additions on the Sulfide Spacing and Fracture Toughness of a 0.4 Carbon Low Alloy Steel. *Metallurgical transactions A*, 17A:669–678, 1986.

[123] S. Chatterjee, M. Murugananth, and H. K. D. H. Bhadeshia. δ TRIP steel. *Materials Science and Technology*, 23:819–827, 2007.

[124] C. Garcia-Mateo and F. G. Caballero. Ultra-high-strength Bainitic Steels. *ISIJ International*, 45:1736–1740, 2005.

[125] G. Eggbauer and B. Buchmayr. High-Strength Bainitic Steels for Forged Products. *Berg-und Hüttenmännische Monatshefte*, 160:209–213, 2015.

[126] C. G. Lee, S. J. Kim, T. H. Lee, and S. Lee. Effects of volume fraction and stability of retained austenite on formability in a 0.1C-1.5Si-1.5Mn-0.5Cu TRIP-aided cold-rolled steel sheet. *Materials Science and Engineering A*, 371:16–23, 2004.

[127] H. K. D. H. Bhadeshia. High performance bainitic steels. *Materials Science Forum*, 501:63–74, 2005.

[128] C. N. Hulme-Smith, I. Lonardelli, A. C. Dippel, and H. K. D. H. Bhadeshia. Experimental evidence for non-cubic bainitic ferrite. *Scripta Materialia*, 69:409–412, 2013.

[129] C. N. Hulme-Smith, M. J. Peet, I. Lonardelli, A. C. Dippel, and H. K. D. H. Bhadeshia. Further evidence of tetragonality in bainitic ferrite. *Materials Science and Technology*, 31:254–256, 2015.

[130] H. K. D. H. Bhadeshia. Carbon in Cubic and Tetragonal Ferrite. *Philosophical Magazine*, 93:3417–3429, 2013.

[131] J. H. Jang, H. K. D. H. Bhadeshia, and D. W. Suh. Solubility of carbon in tetragonal ferrite in equilibrium with austenite. *Scripta Materialia*, 68:195–198, 2013.

[132] D. J. C. Mackay. Probable networks and plausible predictions — a review of practical Bayesian methods for supervised neural networks. *Network: Computation in Neural Systems*, 6:469–505, 1995.

[133] H. K. D. H. Bhadeshia. Neural networks in materials science. *ISIJ International*, 39:966–979, 1999.

[134] S. Kang, M. Kim, and S. J. Lee. Microstructural and mechanical characteristics of novel 6% Cr cold-work tool steel. *Metals*, 7:1–7, 2017.

[135] M. P. Phaniraj, Y. M. Shin, J. Lee, N. H. Goo, D. I. Kim, J. Y. Suh, W. S. Jung, J. H. Shim, and I. S. Choi. Development of high strength hot rolled low carbon copper-bearing steel containing nanometer sized carbides. *Materials Science and Engineering A*, 633:1–8, 2015.

[136] R. H. Davies, A. T. Dinsdale, J. A. Gisby, J. A. J. Robinson, and S. M. Martin. MTDATA - thermodynamic and phase equilibrium software from the national physical laboratory. *Calphad*, 26:229–271, 2002.

[137] H. K. D. H. Bhadeshia. Thermodynamic analysis of isothermal transformation diagrams. *Metal Science*, 16:159–165, 1982.

[138] S. A. Khan and H. K. D. H. Bhadeshia. The bainite transformation in chemically heterogeneous 300M high-strength steel. *Metallurgical Transactions A*, 21:859–875, 1990.

[139] H. K. D. H. Bhadeshia. Hard bainite. *The Minerals, Metals & Materials Society*, 1:469–484, 2005.

[140] S. Yamasaki and H. K. D. H. Bhadeshia. M4C3 precipitation in Fe-C-Mo-V steels and relationship to hydrogen trapping. *Proceedings of the Royal Society A: Mathematical, Physical and Engineering Sciences*, 462:2315–2330, 2006.

[141] M. Soliman and H. Palkowski. Ultra-fine Bainite Structure in Hypo-eutectoid Steels. *ISIJ International*, 47:1703–1710, 2007.

[142] G. R. Speich and W. C. Leslie. Tempering of Steel. *Metallurgical Transactions*, 3:1043–1054, 1972.

[143] W. C. Leslie and G. C. Rauch. Precipitation of Carbides in Low-Carbon Fe-Al-C Alloys. *Metallurgical transactions A*, 9:343–349, 1978.

[144] J. Hoon, I. Gee, and H. K. D. H. Bhadeshia. ε-carbide in Alloy Steels : First-principles Assessment. *Scripta Materialia*, 63:121–123, 2010.

[145] H. K. D. H. Bhadeshia and D. V. Edmonds. Bainite in silicon steels: new composition–property approach Part 1. *Metal Science*, 17:411–419, 1983.

[146] I. Olefjord. Temper embrittlement. *International Metals Reviews*, 23:149–163, 1978.

[147] H. I. Aaronson, H. A. Domian, and G. M. Pound. Thermodynamics of the austenite pro-eutectoid ferrite transformation. Pt. 1. Fe-C alloys. *Transactions of the Metallurgical Society of AIME*, 236:753–767, 1966.

[148] A. A. Chulkina, A. I. Ulyanov, A. V. Zagainov, A. L. Ulyanov, and E. P. Yelsukov. Formation of Chromium Alloyed Cementite in the Process of Mechanosynthesis and Subsequent Annealings. *The Physics of Metals and Metallography*, 116:309–317, 2015.

[149] G. Gomez, T. Pérez, and H. K. D. H. Bhadeshia. Air cooled bainitic steels for strong, seamless pipes Part 2 - properties and microstructure of rolled material. *Materials Science and Technology*, 25:1508–1512, 2009.

[150] L. A. Norström and O. Vingsbo. Influence of nickel on toughness and ductile-brittle transition in low-carbon martensite steels. *Metal Science*, 13:677–684, 1979.

[151] C. Garcia-Mateo, F. G. Caballero, and H. K. D. H. Bhadeshia. Acceleration of Low-temperature Bainite. *ISIJ International*, 43:1821–1825, 2003.

[152] W. S. Owen. The effect of silicon on the kinetics of tempering. *Transactions of the American Society for Metals*, 46:812–829, 1954.

[153] F. G. Caballero, M. K. Miller, and C. Garcia-Mateo. Atom probe tomography analysis of precipitation during tempering of a nanostructured bainitic steel. *Metallurgical and Materials Transactions A: Physical Metallurgy and Materials Science*, 42:3660–3668, 2011.

[154] J. H. Jang, I. G. Kim, and H. K. D. H. Bhadeshia. Substitutional solution of silicon in cementite: A first-principles study. *Computational Materials Science*, 44:1319–1326, 2009.

[155] W. Steven and A. G. Haynes. The temperature of formation of martensite and bainite in low-alloy steels. *Journal of the Iron and Steel Institute*, 183:349–359, 1956.

[156] H. K. D. H. Bhadeshia and D. V. Edmonds. Bainite in silicon steels: new composition–property approach Part 2. *Metal Science*, 17:420–425, 1983.

[157] L. Yuan, D. Ponge, J. Wittig, and P. Choi. Nanoscale austenite reversion through partitioning, segregation and kinetic freezing: Example of a ductile 2GPa Fe–Cr–C steel. *Acta Materialia*, 60:2790–2838, 2012.

[158] L. K. Perry, D. H. Ryan, and R. Gagnon. Studying surfaces and thin films using Mössbauer spectroscopy. *Hyperfine Interactions*, 170:131–143, 2006.

[159] H. K. D. H. Bhadeshia. Anomalies in carbon concentration determinations from nanostructured bainite. *Materials Science and Technology*, 31:758–763, 2015.

[160] H. K. D. H. Bhadeshia. *The Geometry of Crystals*. Institute of Metals, London, 1987.

[161] C. A. Schneider, W. S. Rasband, and K. W. Eliceiri. NIH Image to ImageJ: 25 years of image analysis. *Nature Methods*, 9:671–675, 2012.

[162] B. D. Cullity and S. R. Stock. *Elements of X-ray diffraction*. Upper Saddle River, N.J.: Prentice Hall, 3rd edition, 2001.

[163] C. Garcia-Mateo, F. G. Caballero, M. K. Miller, and J. A. Jimenez. On measurement of carbon content in retained austenite in a nanostructured bainitic steel. *Journal of Materials Science*, 47:1004–1010, 2012.

[164] D. J. Dyson and B. Holmes. Effect of alloying additions on the lattice parameter of austenite. *Journal Of The Iron And Steel Institute*, 208:469–474, 1970.

[165] G. K. Williamson and W. H. Hall. X-ray Line Broadening from Filed Aluminium and Wolfram. *Acta Metallurgica*, 1:22–31, 1953.

[166] D. B. Wiles and R. A. Young. A new computer program for Rietveld analysis of X-ray powder diffraction patterns. *Journal of Applied Crystallography*, 14:149–151, 1981.

[167] L. B. McCusker, R. B. Von Dreele, D. E. Cox, D. Louër, and P. Scardi. Rietveld refinement guidelines. *Journal of Applied Crystallography*, 32:36–50, 1999.

[168] M. Y. Sherif. *Characterisation and development of nanostructured, ultrahigh strength, and ductile bainitic steels*. Ph.D. thesis, University of Cambridge, 2006.

[169] L. C. D. Fielding. *Understanding toughness and ductility in novel steels with mixed microstructures*. Ph.D. thesis, University of Cambridge, 2014.

[170] H. S. Yang and H. K. D. H. Bhadeshia. Uncertainties in dilatometric determination of martensite start temperature. *Materials Science and Technology*, 23:556–560, 2007.

[171] H. S. Yang and H. K. D. H. Bhadeshia. Austenite grain size and the martensite-start temperature. *Scripta Materialia*, 60:493–495, 2009.

[172] H. K. D. H. Bhadeshia, S. A. David, J. M. Vitek, and R. W. Reed. Stress induced transformation to bainite in Fe–Cr–Mo–C pressure vessel steel. *Materials Science and Technology*, 7:686–698, 1991.

[173] L. C. Chang and H. K. D. H. Bhadeshia. Austenite films in bainitic microstructures. *Materials Science and Technology*, 11:874–882, 1995.

[174] Standard Test Methods for Determining Average Grain Size. *ASTM International E112-12*, 2012.

[175] W. Solano-Alvarez, H. F. G. Abreu, M. R. Da Silva, and M. J. Peet. Phase quantification in nanobainite via magnetic measurements and X-ray diffraction. *Journal of Magnetism and Magnetic Materials*, 378:200–205, 2015.

[176] F. G. Caballero, H. K. D. H. Bhadeshia, K. J. A. Mawella, D. G. Jones, and P. Brown. Design of novel high strength bainitic steels: Part 1. *Materials Science and Technology*, 17:512–516, 2001.

[177] S. Shimura. A study on the structure of cementite. *Proceedings of the Japan Academy*, 6:269–271, 1930.

[178] J. P. Materkowski and G. Krauss. Tempered martensite embrittlement in SAE 4340 steel. *Metallurgical Transactions A*, 10:1643–1651, 1979.

[179] J. H. Ryu. *Hydrogen Embrittlement in TRIP and TWIP Steels*. Ph.D. thesis, Pohang University of Science and Technology, 2012.

[180] R. Kirchheim. Bulk Diffusion-Controlled Thermal Desorption Spectroscopy with Examples for Hydrogen in Iron. *Metallurgical and Materials Transactions A*, 47:672–696, 2016.

[181] J. Goldstein, D. E. Newbury, P. Echlin, D. C. Joy, A. D. Romig Jr, C. E. Lyman, C. Fiori, and E. Lifshin. *Scanning electron microscopy and X-ray microanalysis: a text for biologists, materials scientists, and geologists*. Springer Science & Business Media, 2012.

[182] Method of measurement of hydrogen permeation and determination of hydrogen uptake and transport in metals by an electrochemical technique. *British Standard ISO 17081:2014*, 2014.

[183] A. Turnbull. Standardisation of hydrogen permeation measurement by the electrochemical technique. In *Hydrogen Transport and Cracking in Metals*, pages 129–141. Institute of Materials, 1994.

[184] O. Kazum, H. Beladi, I. B. Timokhina, Y. He, and M. Bobby Kannan. Hydrogen Permeation in Nanostructured Bainitic Steel. *Metallurgical and Materials Transactions A: Physical Metallurgy and Materials Science*, 47:4896–4903, 2016.

[185] C. Garcia-Mateo, F. G. Caballero, C. Capdevila, and C. G. de Andres. Estimation of dislocation density in bainitic microstructures using high-resolution dilatometry. *Scripta Materialia*, 61:855–858, 2009.

[186] J. Pešička, R. Kužel, A. Dronhofer, and G. Eggeler. The evolution of dislocation density during heat treatment and creep of tempered martensite ferritic steels. *Acta materialia*, 51:4847–4862, 2003.

[187] A. R. Stokes and A. J. C. Wilson. The diffraction of X rays by distorted crystal aggregates - I. *Proceedings of the Physical Society*, 56:174–181, 1944.

[188] G. K. Williamson and R. E. Smallman. III. Dislocation densities in some annealed and cold-worked metals from measurements on the X-ray debye-scherrer spectrum. *Philosophical Magazine*, 1:34–46, 1956.

[189] M. K. Fondekar, A. M. Rao, and A. K. Mallik. Strain tempering of bainite. *Metallurgical Transactions*, 1:885–890, 1970.

[190] M. E. Bush and P. M. Kelly. Strengthening mechanisms in bainitic steels. *Acta Metallurgica*, 19:1363–1371, 1971.

[191] E. J. Pickering. *Macrosegregation in Steel Ingots*. Ph.D. thesis, University of Cambridge, 2014.

[192] A. J. Kumnick and H. H. Johnson. Hydrogen transport through annealed and deformed armco iron. *Metallurgical Transactions*, 5:1199–1206, 1974.

[193] A. San-Martin and F. D. Manchester. The Fe-H (Iron-Hydrogen) system, edited by Okamoto, H. *Bulletin of Alloy Phase Diagrams*, 11:173–184, 1990.

[194] A. Saha Podder. *Tempering of a Mixture of Bainite and Retained Austenite*. Ph.D. thesis, University of Cambridge, 2011.

[195] Standard Test Methods for Tension Testing of Metallic Materials. *ASTM International E8/E8M - 15a*, 2015.

[196] B. P. J. Sandvik and H. P. Nevalainen. Structure-property relationships in commercial low-alloy bainitic-austenitic steel with high strength, ductility, and toughness. *Metals Technology*, 8:213–220, 1981.

[197] Metallic materials — Charpy impact test — Part 1 : Test method. *European Standard - EN 10 045-1*, 1990.

[198] K. J. Irvine, F. B. Pickering, W. C. Heselwood, and M. Atkins. The physical metallurgy of low–carbon, low–alloy steels containing boron. *Journal of the Iron and Steel Institute*, 186:54–67, 1957.

[199] P. Brozzo, G. Buzzichelli, A. Mascanzoni, and M. Mirabile. Microstructure and cleavage resistance of low-carbon bainitic steels. *Metal Science*, 11:123–130, 1977.

[200] K. Amini, A. Akhbarizadeh, and S. Javadpour. Investigating the effect of the quench environment on the final microstructure and wear behavior of 1.2080 tool steel after deep cryogenic heat treatment. *Materials and Design*, 45:316–322, 2013.

[201] A. Shokrani, V. Dhokia, P. Muñoz-Escalona, and S. T. Newman. State-of-the-art cryogenic machining and processing. *International Journal of Computer Integrated Manufacturing*, 26:616–648, 2013.

[202] V. Tvergaard and A. Needleman. Analysis of the Cup-Cone Round Tensile Fracture. *Acta Metallurgica*, 32:157–169, 1984.

[203] R. Austin. Materials Chapter 2 Powerpoint presentation, Michigan State University - http://slideplayer.com/slide/10251422/.

[204] H. K. D. H. Bhadeshia. Properties of fine-grained steels generated by displacive transformation. *Materials Science and Engineering A*, 481-482:36–39, 2008.

[205] M. Y. Sherif, C. G. Mateo, T. Sourmail, and H. K. D. H. Bhadeshia. Stability of retained austenite in TRIP-assisted steels. *Materials Science and Technology*, 20:319–322, 2004.

[206] Y. Sakuma, D. K. Matlock, and G. Krauss. Intercritically annealed and isothermally transformed 0.15 Pct C steels containing 1.2 Pct Si-1.5 Pct Mn and 4 Pct Ni: Part II. effect of testing temperature on stress-strain behavior and deformation-induced austenite transformation. *Metallurgical & Materials Transactions A*, 23A:1221–1232, 1992.

[207] D. Vanderschueren, M. D. Meyer, B. C. D. Cooman, and K. E. Y. Wor. The influence of the substitution of Si by Al on the Properties of Cold Rolled C-Mn-Si TRIP Steels. *ISIJ International*, 39:813–822, 1999.

[208] Petroleum and natural gas industries — Materials for use in H2S-containing environments in oil and gas production — Part 2: Cracking-resistant carbon and low-alloy steels, and the use of cast irons Industries. *International Standard ANSI/NACE MR0175/ ISO 15156-2*, 2009.